

**ORIENTATION AND THERMAL STABILITY  
OF ADVANCED RECORDING MEDIA**

**JESSADA CHUREEMART**

SUBMITTED FOR THE DEGREE OF DOCTOR OF PHILOSOPHY

**THE UNIVERSITY OF YORK**

DEPARTMENT OF PHYSICS

AUGUST 2013

---

## ABSTRACT

This study is focused on the characterisation of advanced perpendicular recording media. In particular, the distribution of the effective easy axis orientation and the effect of silica ( $\text{SiO}_2$ ) content on the magnetic properties have been investigated via magnetic measurements. The variation of coercivity ( $H_C$ ) as a function of angle has been used to determine the easy axis distribution. Due to the efficiency of the  $\text{SiO}_2$  segregation at the grain boundaries leading to intergranular exchange decoupling, the magnetisation reversal of each single domain particle can be described by a numerical simulation using Stoner Wohlfarth theory. The standard deviation of a Gaussian distribution of easy axis orientations in the calculations replicates the magnetic easy axis distribution in thin film media.

Three types of media; granular, exchange coupled composite (ECC) and the combination of exchange coupled composite and a coupled granular continuous (CGC) film have been studied. The crystallographic orientation was also measured via X-ray rocking curves for a comparison to be made. It was found that the ECC media which have their grains almost completely segregated by  $\text{SiO}_2$  give an excellent fit to the simulation with  $\sigma_\phi = 5^\circ$ . The results for granular and ECC/CGC media do not fit to the same level of accuracy. In-plane and cross-section TEM analysis of both samples show far from perfect segregation leading to intergranular exchange coupling.

The activation volume has been used to study the effect of  $\text{SiO}_2$  content in ECC media.  $V_{act}$  and the physical grain volume have been investigated for identical structures with three different levels of  $\text{SiO}_2$ . Time dependence measurements have been used to determine  $V_{act}$ . TEM analysis has been also carried out to investigate the grain size distribution and to examine the grain boundaries.  $V_{act}$  and the single grain volume are in excellent agreement for the sample with the highest  $\text{SiO}_2$  content, indicating complete exchange decoupling.

---

---

**TABLE OF CONTENTS**

<b>Abstract</b> .....	<b>2</b>
<b>List of Figures</b> .....	<b>7</b>
<b>List of Tables</b> .....	<b>13</b>
<b>Acknowledgements</b> .....	<b>14</b>
<b>Declaration</b> .....	<b>15</b>
<b>1 Introduction</b> .....	<b>16</b>
<b>2 Fundamental of Recording Media</b> .....	<b>19</b>
2.1 Magnetic Properties of Thin Film Media . . . . .	19
2.1.1 Magnetic Anisotropy in Thin Film Media . . . . .	19
2.1.1.1 Magnetocrystalline Anisotropy . . . . .	19
2.1.1.2 Other Anisotropies . . . . .	21
2.1.2 Demagnetising Field . . . . .	23
2.1.3 Limitations of Recording Media . . . . .	26
2.2 Magnetisation Reversal in Thin Film Media . . . . .	31
2.2.1 Single Domain Particles . . . . .	31
2.2.2 Stoner-Wohlfarth Theory . . . . .	34
2.2.3 Coherent and Incoherent Reversal Processes . . . . .	37
2.3 Interaction Mechanisms in Thin Film Media . . . . .	40
2.3.1 Exchange Interaction . . . . .	40
2.3.2 Dipolar Interaction . . . . .	42
2.3.3 Multilayered Interaction . . . . .	43
2.4 Time-Dependence of Magnetisation . . . . .	45

---

---

2.4.1	Energy Barrier . . . . .	45
2.4.2	Thermal Activation . . . . .	47
2.4.3	Magnetic Viscosity . . . . .	49
2.4.4	The Fluctuation Field and Activation Volumes . . . . .	52
<b>3</b>	<b>Advanced Recording Media . . . . .</b>	<b>56</b>
3.1	History of Recording Media . . . . .	57
3.1.1	Transition to Perpendicular Recording Media . . . . .	57
3.1.2	Perpendicular Recording . . . . .	60
3.2	Alternative Perpendicular Recording Media . . . . .	64
3.2.1	Coupled Granular Continuous Recording Media (CGC) . . . . .	64
3.2.2	Exchange Coupled Composite Media (ECC) . . . . .	67
3.2.3	ECC and CGC Media . . . . .	69
3.3	Future Recording Media . . . . .	70
3.3.1	Bit Patterned Media . . . . .	70
3.3.2	Heat Assisted Magnetic Recording (HAMR) . . . . .	72
3.3.3	Microwave Assisted Magnetic Recording (MAMR) . . . . .	73
<b>4</b>	<b>Experimental Techniques . . . . .</b>	<b>75</b>
4.1	Magnetic Characterisations . . . . .	75
4.1.1	The Vibrating Sample Magnetometer . . . . .	75
4.1.2	Magneto-Optical Kerr Effect(MOKE) . . . . .	78
4.1.2.1	Geometry of the MOKE Experiment . . . . .	80
4.1.3	Angular Dependent MOKE . . . . .	83
4.2	Magnetic Measurements . . . . .	86
4.2.1	Magnetisation Curve . . . . .	86
4.2.2	Remanence Curves . . . . .	88

---

---

4.2.3	Angular Measurements . . . . .	92
4.2.4	Time Dependence Measurements . . . . .	93
4.2.5	Determination of Fluctuation Field and Activation Volume . . . . .	94
4.3	Physical Structure Characterisation . . . . .	97
4.3.1	X-Ray Rocking Curves . . . . .	97
4.3.2	Transmission Electron Microscopy (TEM) . . . . .	99
4.3.3	Scanning Transmission Electron Microscopy (STEM) . . . . .	102
4.3.4	In-plane and Cross-section Sample Preparation . . . . .	106
4.3.4.1	In-plane Sample Preparation . . . . .	106
4.3.4.2	Cross-sectional Sample Preparation . . . . .	108
4.3.5	Grain Size Analysis . . . . .	110
4.4	Simulation of Easy Axis Distribution . . . . .	114
4.4.1	Stoner-Wohlfarth Simulation . . . . .	114
<b>5</b>	<b>Experimental Results . . . . .</b>	<b>118</b>
5.1	Structure of Advanced Recording Media . . . . .	118
5.2	Magnetic Properties of Thin Film Media . . . . .	123
5.2.1	Granular Media with Different Oxide Levels . . . . .	124
5.2.2	ECC Media with Different Oxide Levels . . . . .	126
5.2.3	ECC/CGC Media with Different Thicknesses . . . . .	128
5.3	Easy Axis Distributions . . . . .	130
5.3.1	Experimental Studies . . . . .	130
5.3.2	Theoretical Calculations . . . . .	133
5.3.3	Coercivity of Complex Structures . . . . .	139
5.3.4	The Easy Axis Distribution by the Variation of $H_{cr}$ . . . . .	141
5.4	Time Dependence in Thin Film Media . . . . .	144
5.4.1	Time Dependence of Magnetisation . . . . .	144

---

---

5.4.2	Determination of the Fluctuation Field and Activation Volumes . .	147
5.4.3	Correlation of Activation and Physical Grain Volumes . . . . .	150
<b>6</b>	<b>Conclusions and Future Work . . . . .</b>	<b>155</b>
6.1	Conclusions . . . . .	155
6.2	Future Work . . . . .	157
	<b>Publications and Presentations . . . . .</b>	<b>159</b>
	<b>List of Symbols . . . . .</b>	<b>161</b>
	<b>Bibliography . . . . .</b>	<b>166</b>

---

---

**LIST OF FIGURES**

1.1	The growth of the areal density for HDD technology . . . . .	17
2.1	Schematic of a single crystalline structure; a) bcc structure, b) fcc structure and c) hcp structure . . . . .	20
2.2	Typical cross-section TEM image showing the shape structure of a grain in a granular medium . . . . .	22
2.3	Schematic diagram of a) the magnetisation of a single domain particle with the demagnetising field and b) the global and local demagnetising field	24
2.4	Schematic diagram of read/write system in PRM and the transition width for different grain sizes . . . . .	27
2.5	Schematic diagram of a) the media-trilemma problem b) the quadrilemma problem . . . . .	30
2.6	Schematic diagram of the single domain structures of a uniaxial crystal .	32
2.7	Variation of coercivity with particle size for Fe and Co . . . . .	33
2.8	Schematic diagram of variation of the intrinsic coercivity with particle diameter . . . . .	33
2.9	Schematic diagram of cross-section and typical in-plane TEM image for ECC media . . . . .	34
2.10	Schematic of prolate spheroid single domain particle with magnetisation and applied field . . . . .	35
2.11	Magnetisation curves of the Stoner-Wohlfarth theory . . . . .	36
2.12	Schematic diagram of the reversal modes a) coherent reversal b) incoherent reversal . . . . .	38
2.13	Schematic diagram of a mechanism of reversal in a polycrystalline film in LRM . . . . .	39
2.14	Typical high resolution transmission electron microscope of advanced recording media . . . . .	41

---

---

2.15	Schematic of the interacting dipoles as a) long distance and b) short distance	43
2.16	Schematic illustration of exchange multi-layer of a) CGC model and b) ECC model	44
2.17	Schematic of the reversal process in the presence of an energy barrier	47
2.18	Schematic of thermal activation in a single grain	48
2.19	Schematic of a) a narrow distribution of energy barriers and b) the calculated variation of magnetisation decay with $\ln t$ in different regions of $f(\Delta E)$	51
3.1	a) Image of a hard disk drive and b) schematics of the read and write heads for LRM and PRM and a conventional recording media	57
3.2	Schematic diagram of the areal density evolution for HDD and flash memory products	58
3.3	Schematic diagram of antiferromagnetically couple film	60
3.4	Schematic diagram of PRM with the read/write head	61
3.5	a) Schematic diagram of a typical layer structure and a cross-sectional image of a perpendicular recording medium b) Schematic diagram of the magnetic grains with different grain boundary widths compared to an in-plane TEM image.	63
3.6	Schematic diagram of CGC media with a multi-layer and a thin continuous layer	65
3.7	Dependence of $K_U V / k_B T$ as a function of the interlayer exchange field for a CGC structure with various values of $K_U$	66
3.8	Schematic diagram of the geometry of tilted and conventional PRM	67
3.9	Schematic diagram of the switching process of ECC media	68
3.10	Schematic diagram of spin moments in a) ECC media and b) ECC/CGC media	69
3.11	Schematic diagram of a) bit patterned media with nano-islands and b) comparison of media structure between conventional PRM and BPM	71

---

---

3.12 Schematic diagram of a) the HAMR write process with the relationship between $H_C$ and T and b) a HAMR system with laser, write/read head and medium . . . . .	73
3.13 Schematic diagram of microwave assisted magnetic recording . . . . .	74
4.1 Schematic diagram of the vibrating sample magnetometer . . . . .	76
4.2 The magnetisation curve for an ECC/CGC thin film . . . . .	77
4.3 Schematic of MOKE effect . . . . .	78
4.4 Schematic diagram of polar MOKE . . . . .	80
4.5 Hysteresis loop for ECC/CGC media from MOKE (black dots) and VSM (red dots) . . . . .	81
4.6 Schematic of the MOKE setup . . . . .	82
4.7 The polar magneto-optic Kerr effect magnetometer . . . . .	83
4.8 Schematic diagram of the MOKE system . . . . .	84
4.9 The rotation system with sample holder . . . . .	85
4.10 Schematic of angular dependent MOKE at Seagate Media Research in Fremont CA . . . . .	86
4.11 Schematic diagram of hysteresis loop from the MOKE magnetometer for an ECC/CGC medium . . . . .	87
4.12 Schematic diagram of the demagnetising field in PRM . . . . .	88
4.13 Schematic of the energy barrier distribution at $H_C$ . . . . .	89
4.14 Schematic of the DCD curve . . . . .	90
4.15 Schematic of the IRM curve . . . . .	90
4.16 Typical DCD curve for an ECC/CGC sample . . . . .	91
4.17 Schematic of the distribution of the energy barriers a) a normal granular or ECC medium and b) an ECC/CGC medium . . . . .	93
4.18 Schematic of a group of time dependence magnetisation decay measurements for the waiting time method . . . . .	94

---

---

4.19	Schematic of a) the magnetisation decay with $\ln(t)$ and b) the variation of reverse field versus $\ln(t)$ . . . . .	95
4.20	a) Schematic of the magnetisation reversal in different applied fields and b) magnetisation curve measured using the VSM for the ECC/CGC sample	96
4.21	a) Geometry of a $\theta$ - $2\theta$ angle measurement. b) Typical X-ray rocking curve of a (0002) recording layer peak . . . . .	98
4.22	Cross-section HR-TEM image showing the interface structure between a Co-alloy and Ru intermediate layer and a schematic of the medium structure.	99
4.23	Schematic of a conventional transmission electron microscopy (left) and the process of an e-beam interaction with the sample surface (right) . . .	100
4.24	a) A comparison of TEM configurations in imaging mode and b) diffraction pattern mode . . . . .	101
4.25	Schematic of a STEM with two pairs of scanning coils . . . . .	103
4.26	Typical cross-section STEM image with a line scan image and EDX mapping for a range of elements in the film (courtesy of Dr. L. Lari). . . . .	105
4.27	a) Typical BF-HRTEM cross-sectional image and b) High angle annular dark field (HAADF)-STEM (courtesy of Dr. L. Lari) . . . . .	106
4.28	Schematic of the sample structure for in-plane imaging . . . . .	107
4.29	Typical in-plane TEM image with damaged and undamaged regions . . .	107
4.30	Schematic of cross-section TEM sample preparation . . . . .	108
4.31	Schematic of the complete dimple specimen . . . . .	109
4.32	Schematic of a dimple sample with the milling angle . . . . .	109
4.33	Schematic of perpendicular recording media cross-section TEM image . .	110
4.34	Typical in-plane TEM images for ECC/CGC, ECC and granular samples	111
4.35	Typical in-plane TEM image of ECC media and the measured log-normal distribution. . . . .	113
4.36	Typical HRTEM image of ECC sample with center to center distances marked . . . . .	113

---

---

4.37	Schematic of a film whose grains have an easy axis distribution . . . . .	115
4.38	Schematic of the easy axis distribution and the applied field . . . . .	116
4.39	The S-W calculation of the variation of $H_C(\theta)/H_C(0)$ for $\sigma_\phi = 0$ to 10 degrees . . . . .	116
5.1	Schematic of the structures and typical cross-section TEM images for the three types of media. . . . .	119
5.2	a) Schematic of the magnetisation reversal in different applied fields and b) the magnetisation curve measured using a VSM for sample ECO1 <sub>h</sub> . .	123
5.3	Magnetisation curves $M(H)$ of the granular samples a) good easy axis orientation and b) poor easy axis orientation. . . . .	125
5.4	Magnetisation curves of ECC samples a) good easy axis orientation and b) poor easy axis orientation . . . . .	126
5.5	Magnetisation curves of ECC/CGC samples a) good easy axis orientation and b) poorer easy axis orientation . . . . .	128
5.6	Typical magnetisation curves $M(H)$ at different angles for sample ECO2 <sub>h</sub>	131
5.7	The Stoner Wohlfarth calculation of the variation of $H_C(\theta)/H_C(0)$ for $\sigma_\phi = 0$ to 10 degrees (courtesy of P. Chureemart) . . . . .	134
5.8	Angular variation of $H_C$ from the experimental (dot) and numerical results (line) of granular samples; a) GPO at the different levels of SiO <sub>2</sub> and b) GO and GPO at low SiO <sub>2</sub> . . . . .	135
5.9	Angular variation of $H_C$ from the experimental (dot) and numerical results (line) for the various structures with high SiO <sub>2</sub> . . . . .	136
5.10	Bright Field (BF) in-plane images and normalised grain size distributions a) granular media, GO <sub>h</sub> , b) ECC media, EO <sub>h</sub> and c) ECC/CGC media, ECO2 <sub>h</sub> . . . . .	138
5.11	Angular variation of $H_C$ from the experimental (dot) and numerical results (line) for ECO samples with the different thickness ratios and high SiO <sub>2</sub> content . . . . .	139
5.12	Schematic of the distribution of the energy barriers for a) a normal granular of ECC media, b) the ECC/CGC medium . . . . .	140

---

---

5.13	Typical DCD curves at different angles $\theta$ for sample ECO3 <sub>h</sub> . . . . .	142
5.14	Angular variation of $H_{cr}$ from the experimental data and numerical results for ECO samples with different thicknesses of the CGC layer . . . . .	143
5.15	Typical time dependence of magnetisation decay for sample EO <sub>h</sub> . . . . .	145
5.16	The variation of the time dependent magnetisation with t . . . . .	146
5.17	The variation of the time dependent magnetisation with ln(t) . . . . .	147
5.18	The variation of the reverse field with ln(t) for all samples . . . . .	148
5.19	BF in-plane image and normalised grain size distributions for ECC sam- ples with good orientation and different oxide levels. . . . .	151
5.20	Comparison between activation volumes, $V_{act}$ and $V_{TEM}$ . . . . .	152
5.21	a) Typical BF-HR-STEM cross-section image and b) high angle annular dark field (HAADF)-STEM for sample EO <sub>h</sub> (courtesy of Dr. L. Lari) . . .	154
6.1	a) Comparison between Voronoi simulation grains and the recording grains and b) angular variation of $H_C$ from experimental results, S-W and Monte Carlo calculations provided by P. Chureemart and R.W. Chantrell. . . . .	158

---

---

**LIST OF TABLES**

5.1	Summary of granular sample parameters. . . . .	120
5.2	Summary of ECC sample parameters. . . . .	121
5.3	Summary of ECC/CGC sample parameters. . . . .	122
5.4	Summary of the magnetic properties of granular samples. . . . .	125
5.5	Summary of the magnetic properties of ECC samples. . . . .	127
5.6	Summary of the magnetic properties of ECC/CGC samples. . . . .	129
5.7	Coercivity at different angles for granular samples. . . . .	132
5.8	Coercivity at different angles for ECC samples. . . . .	132
5.9	Coercivity at different angles for ECC/CGC samples. . . . .	133
5.10	Comparison of $H_C$ and $H_{cr}$ at different angles for the ECO samples. . . . .	142
5.11	Summary of physical properties, $H_f$ and $V_{act}$ . . . . .	148
5.12	Summary of magnetic properties of ECC set. . . . .	148

---

## ACKNOWLEDGEMENTS

I would like to use this opportunity to express my sincere gratitude and appreciation to the many people who have introduced, guided, suggested and supported me to the study of magnetism throughout my PhD student. First and foremost I would like to express my deepest gratitude to my supervisor, Professor Kevin O'Grady who give me a great opportunity to work in the best magnetism group. I deeply appreciate for the generous level of discussion, precious supervision, and helpful guidance during the period of my graduate studies in University of York. It has been a great privilege and pleasure to be his student. I would like to thank again my great supervisor who has inspired me, without whom this work would not be possible.

During this work, I would like to extend my special thank to Dr.Tom Nolan and Dr.Janson Pressesky from Seagate Media Research, Fremont for the supply of advanced recording media and also give a great opportunity to visit and use a high quality angular MOKE at Seagate. Moreover, I would like to give special thank to Dr.Atsumi Hirohata for a useful discussion and suggestion and also Dr.Leonardo for his help with STEM work. I am grateful for the IEEE magnetics society for providing the opportunity to attend the 2011 summer school in New Orleans and also giving a student travel grant for 12<sup>th</sup> Joint MMM/Intermag conference 2013 at Chicago USA.

I am very extremely fortunate to be part of magnetism group, **SO20 team**. I would like to thank all the members past and present. Of course special thanks must be made to Luke, Alex and Rob who made my PhD life so enjoyable and valuable in UK.

I would like to gratefully acknowledge the financial support by the Royal Thai Government for the great scholarship. It has been a big present in my life that gives me the possibility to study in University of York. Importantly, my parents who have always supported me since I have left from Thailand must be special thanked for their endless love. Last, but not least, I would like to deeply thank my wife **Phanwadee** who has been always a part of my life for her love, continual support, enthusiasm and encouragement. I am very obliged to you THANKS!

---

## DECLARATION

I hereby declare that the following work presented in this thesis is based purely on my own research and effort, unless otherwise stated, and has not been submitted for a degree in either this or any other university.

Signed

Jessada Chureemart

August 2013

---

---

## CHAPTER I

### Introduction

The feasibility of achieving an areal density beyond 1 Tbit/in<sup>2</sup> on conventional perpendicular recording media is in doubt. It is a considerable challenge for hard disk drive technology. The evolution of magnetic hard disk drives (HDD) originated in 1957 when IBM launched the random access method of accounting and control (RAMAC) known as the IBM305 RAMAC to record information on magnetic disks. The first disks supported an areal density of only 2 kbits/in<sup>2</sup>. HDD technology has evolved in order to achieve as high an areal density as possible at low cost. The key factors to fulfil this aim are related to three components; the **write head** which generates a strong magnetic field to write data onto the medium, the **read head** which converts the stray field from the medium into a signal and the **recording medium** which stores the data. The achievement of the increase in areal density towards 1 Tbit/in<sup>2</sup> is attributed to the developments of all components of a HDD such as the invention of magneto resistive (MR) and subsequently giant magnetoresistance for the read head [1] [2] and the major paradigm shift from longitudinal to perpendicular recording media [3] [4]. In current HDD storage the areal density has seen enormous growth of about 500 million times from the initial stage.

Figure 1.1 shows a diagram of the growth of areal density for conventional recording media from 1980 to date. The compound growth rate (CGR) of conventional recording media has reduced from ~60%-100%/annum in the 1990s to ~20%-30%/annum currently. The density limit is mainly due to thermal stability of the magnetisation of the media due to the reduction of the grain size. The information must be stable for 10 years [5]. The advantage of reducing the grain size is that it can improve the signal to noise ratio (SNR) due to the narrow width of transitions. In order to sustain a high density the energy barrier to reversal must be able to withstand the demagnetising field. This has been achieved by increasing the anisotropy constant of the material  $K \geq 2\pi M_S^2$  [6]. A medium with such a high anisotropy to achieve thermal stability causes another issue of the writability of the medium. Therefore, writability, SNR and thermal

---

stability are intertwined such that the improvement of one parameter can lead to the deterioration of another. Therefore there are significant challenges to be overcome to increase the areal density beyond 1 Tbit/in<sup>2</sup>.

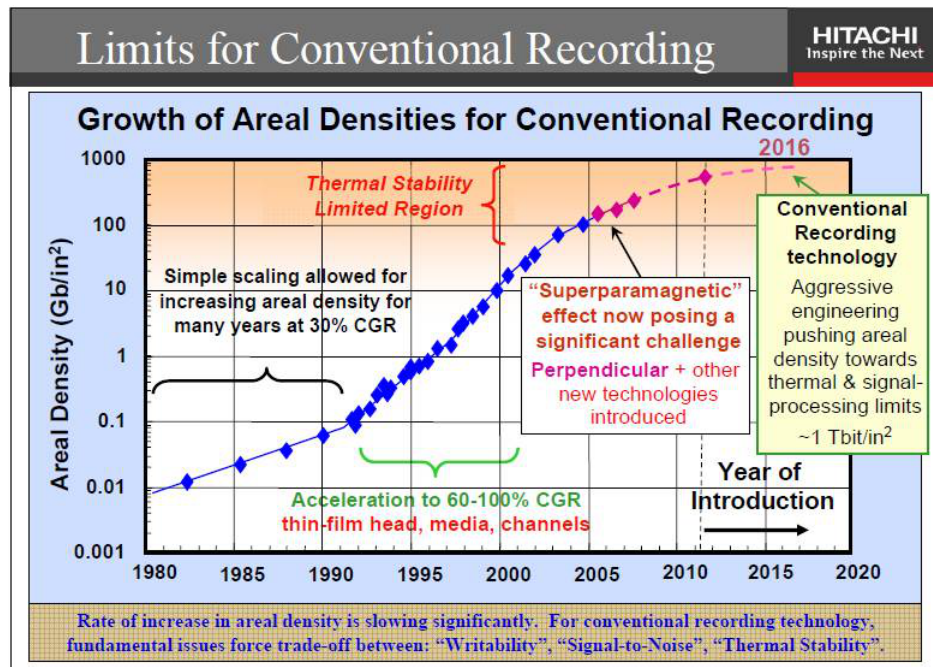


Figure 1.1: The growth of the areal density for HDD technology [7]

There are two proposed alternative approaches to overcome these limitations. The first is heat-assisted magnetic recording (**HAMR**) [8]. The fundamental concept of this technology is based on a *heat assist* for the writing process. A medium with a small grain size and a very high anisotropy constant is heated to a temperature close to its Curie temperature,  $T_C$  by a tiny laser spot. The reduction of the coercivity is sufficient for it to be switched by a low writing field.

The second technology is bit patterned media (**BPM**) [9]. The recording medium is patterned into discrete magnetic islands which represent a single bit. The increased volume of an individual bit, which is much larger than a grain in perpendicular recording media (PRM), improves the thermal stability of BPM. Unfortunately, the disadvantages of this technology are the writing error and the wide switching field distribution [10].

The difficulties of these novel technologies are not only a new design of a new write head but also the nanofabrication process. Therefore, new designs of conventional perpendicular recording media are still the favoured option. Coupled granular contin-

uous (**CGC**) media [11] and exchange coupled composite (**ECC**) media [12] [13] have been proposed to overcome the limitation of the write field. Medium design can reduce the switching field by half via the magnetisation reversal mechanism. Recently, a new composite media design was introduced using the advantages of CGC and ECC media to improve the performance of recording media further. This is known as ECC/CGC media [14]. In order to achieve high performance with the new media design the complex structure must be optimised by studying the magnetic properties and understanding the complex physics in such systems.

Therefore, the magnetic characterisation of these proposed media is the main purpose of this study. The fundamental understanding of magnetic behaviour of recording media can be understood from the magnetic properties. Advanced magnetic measurement techniques have been used to obtain the intrinsic properties of the new structures. These include remanence curves and time dependent behaviour. The study of the dispersion of easy axis orientation, which strongly affects the switching field distribution [15] and the thermal stability, are principle foci of this work.

---

---

## CHAPTER II

### Fundamental of Recording Media

#### 2.1 Magnetic Properties of Thin Film Media

##### 2.1.1 Magnetic Anisotropy in Thin Film Media

The shape of the magnetisation curve (M vs H) differs depending on the direction in which it is measured. The factor which gives a preferential orientation is the *magnetic anisotropy*. This is a very important factor for magnetic recording media design with high areal density. The easy axis orientation of data stored via the magnetisation is now perpendicular to the film surface. The main anisotropy contributing to the magnetic properties of disk recording media is *magnetocrystalline anisotropy*.

##### 2.1.1.1 Magnetocrystalline Anisotropy

The factor which makes one crystal direction more easily magnetised than the others is a crystalline structure effect. This effect is an intrinsic property of the material known as *magnetocrystalline anisotropy* or *crystal anisotropy*. The origin of this anisotropy comes from the spin-orbit coupling in the crystal lattice. The strongest coupling comes from the orbit-lattice coupling due to the orientation of the orbits fixed strongly to the lattice by the atomic bond. The orbital orientation is then in a fixed direction which cannot be realigned. The basis of magnetocrystalline anisotropy is then the spin-orbit electron coupling. If the spin moment of each electron is to be aligned to a new orientation due to an applied field, the spin-orbit coupling must be overcome. The energy required for the spin rotation is known as the *magnetocrystalline anisotropy energy*,  $E_K$ . The energy can be expressed in terms of the direction of magnetisation relative to the crystal axes. For a uniaxial structure this is given by

$$E_K = K_0 + K_1 \cdot \sin^2\theta + K_2 \sin^4 \cdot \theta + \dots \quad (2.1)$$


---

where,  $K_0$ ,  $K_1$  and  $K_2$  are the anisotropy constants and  $\theta$  is the angle between the magnetisation direction and the easy axis orientation. The direction of the spontaneous magnetisation in a crystal tends to lie along a preferred crystallographic direction with the lowest potential energy in the demagnetised state. This direction is known as the easy axis. Therefore, different structures provide different easy and hard axes. Fig.2.1 shows the easy, medium and hard axes for the different crystal structures such as bcc, fcc and hcp.

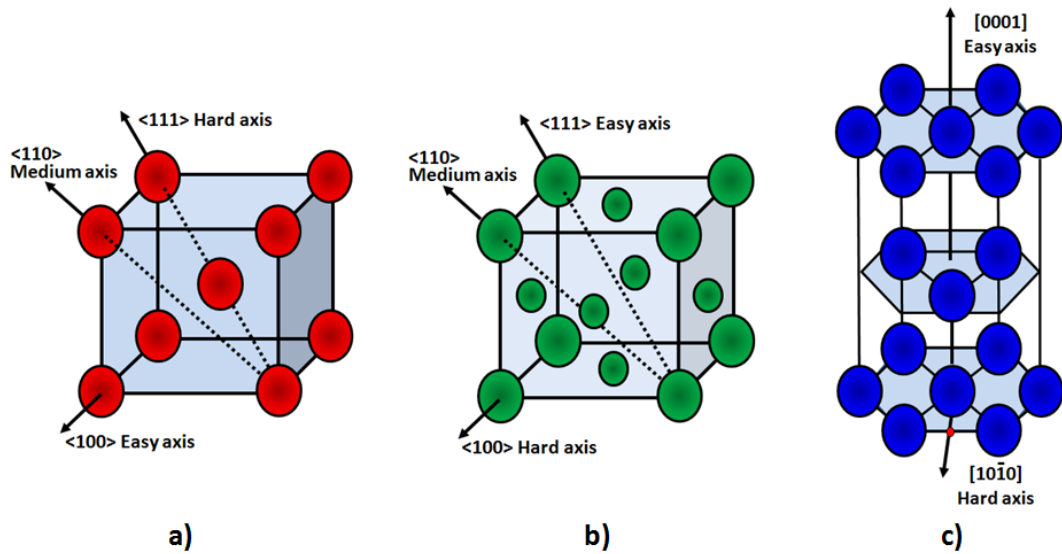


Figure 2.1: Schematic of a single crystalline structure; a) bcc structure, b) fcc structure and c) hcp structure

In recording media the materials used for the storage layer are based on Co-alloy materials such as CoCr, CoCrPt, CoCrTa, CoCrPtTa and CoCrPtB [16–19]. The crystalline structure is hexagonal close-packed (hcp) as shown in fig.2.1 c). In the demagnetised state the spontaneous magnetisation lies along the  $c$ -axis ([0001] axis) and all directions in the basal plane are equally hard to magnetise. Increasing the crystal anisotropy energy is a requirement for high thermal stability.  $K_2$  and higher terms are of negligible magnitude. Additive elements can be used to increase  $K_1$  in Co-alloys as can certain underlayer materials. Materials have been used such as Ru, Pd and Pt. In particular the amount of Pt added to the CoCr alloy strongly increases  $K_1$  up to  $8 \times 10^6$  ergs/cc. [20] [21]

### 2.1.1.2 Other Anisotropies

Magnetic anisotropy can originate from other effects such as sample shape and the effect of stress and strain. Shape anisotropy is associated with the self-demagnetising field,  $H_D$  due to the physical shape of the grains. It leads to a dipole interaction dependent on the shape of the grains called *shape anisotropy*. The shape effect can be clearly obtained by the consideration of the magnetised grain in different directions. In the case of a prolate spheroid, it is easier to magnetise the particle along its long axis, in which the demagnetising field is minimum, than a short axis.

Shape anisotropy energy is determined from  $H_D$  in terms of the magnetostatic energy,  $E_{ms}$ . In the case of a prolate spheroid,  $E_{ms}$  is

$$E_{ms} = \frac{1}{2} \cdot M^2 N_c + \frac{1}{2} \cdot (N_a - N_c) M^2 \sin^2 \theta \quad (2.2)$$

where,  $N_a$  and  $N_c$  are the demagnetising factors along the short and long axes respectively and  $\theta$  is the angle between the magnetisation  $M$  and the long axis. From the expression for the magnetostatic energy the shape anisotropy constant  $K_S$  can be defined as

$$K_S = \frac{1}{2} \cdot (N_a - N_c) M_S^2 \quad \text{or} \quad \frac{1}{2} \cdot \Delta N M_S^2 \quad (2.3)$$

From equation 2.3, the shape anisotropy constant is directly proportional to the geometric structure ( $N_a - N_c$ ) and the square of the magnetisation. In advanced recording media single-domain particles are formed due to the efficiency of the  $\text{SiO}_2$  segregation. Figure 2.2 shows a typical cross-sectional bright field high resolution transmission electron microscopy (BF-HRTEM) image of granular media. The grain diameter and the layer thickness are approximately 7 nm and 11 nm respectively. The layer thickness is the length of the long axis of the cylindrical grains. The axial ratio  $c/a \sim 1.5$ , the value of ( $N_a - N_c$ ) is 1.89 and the saturation magnetisation of the CoCrPt-alloy is 500 emu/cc. The shape anisotropy constant has been calculated from equation 2.3 and is about  $2 \times 10^5$  emu/cc. This value is less than 10 % of the magnetocrystalline anisotropy and hence the shape effect is a perturbation on the total anisotropy. Given that the grains are cylindrical and elongated along the  $c$ -axis, the shape anisotropy will add to the magnetocrystalline term and will not generate any multi-axial behaviour. Perpendicular recording media (PRM) is required to have low magnetisation to minimise the effect of the demagnetising field which is proportional to  $M$ . Therefore,  $K_S$  is not a significant factor compared to the magnetocrystalline anisotropy.

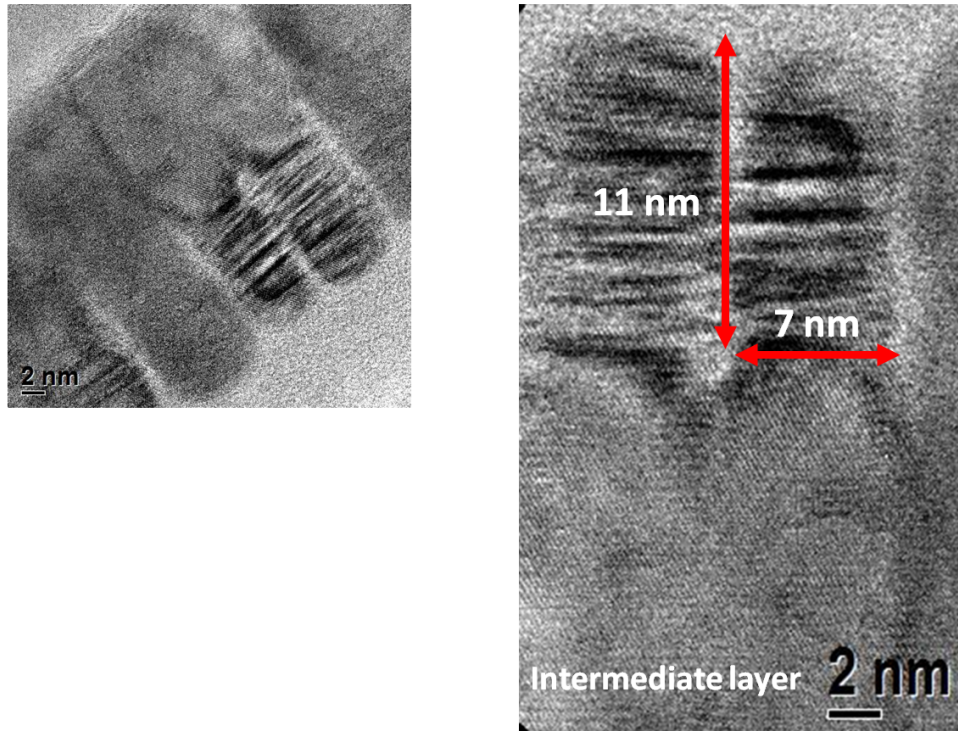


Figure 2.2: Typical cross-section TEM image showing the shape structure of a grain in a granular medium

Stress anisotropy directly relates to the strain effect known as magnetostriction ( $\lambda$ ). It can be described by the ratio of the fractional change of length ( $\Delta l/l$ ). The fractional change in length is caused by the difference in stress between the ordered phase of a domain in the demagnetised state and the saturated state due to an applied field. As a result stress leads to a change of magnetocrystalline anisotropy. The sign of  $\lambda$  indicates the direction in which the strain is measured. A positive value implies that the the strain is measured parallel whereas a negative value indicates an effect perpendicular to the direction of magnetisation.

The inverse effect of magnetostriction can also change the anisotropy. This phenomenon is known as *stress induced anisotropy* [22]. An applied tensile stress,  $\sigma$  can create a torsional effect in the material leading to a change of the magnetic behaviour. Due to the applied stress  $\sigma$ , the simple form of a magnetoelastic energy,  $E_{ms}$  and the resulting anisotropy from the magnetoelastic effect,  $K_{me}$  are

$$E_{me} = \frac{3}{2} \lambda_{me} \sigma \sin^2 \theta_{me} \quad (2.4)$$

and

$$K_{me} = -\frac{3}{2}\lambda_{me}\sigma \quad (2.5)$$

where,  $\theta_{me}$  is the angle between the magnetisation and  $\sigma$ ,  $\lambda_{me}$  is the magnetostriction constant. In thin films, the effect of stress and strain can be induced from dislocations induced in the deposition process. If the lattices of two materials are not matched, a tensile strain in one material and a compressive strain in the other are introduced in order to match the in-plane lattice [23]. Misfit dislocations are thickness dependent. Therefore, this effect also contributes to the magnetic anisotropy in thin film media.

For longitudinal recording media (LRM) an underlayer of an alloy Cr was deposited under the recording layer in order to make the crystallographic orientation of the Co  $c$ -axes alloy parallel to the film plane. Several works reported that the effect of in-plane stress differences induced a stress anisotropy of about  $\sim 1 \times 10^6$  ergs/cc which was large enough to contribute to the magnetic anisotropy [24] [25] [26]. However in perpendicular media there is no need for an exact lattice match to a seed layer as Co-alloys grow naturally with their  $c$ -axes perpendicular to the plane. At the time of writing there are no known reports of stress effects in perpendicular media.

### 2.1.2 Demagnetising Field

One of the critical factors which affects the magnetic properties and data density of thin film media is the *demagnetising field*. The major paradigm shift from longitudinal to perpendicular recording generates a strong demagnetising field. This factor is difficult to correct accurately in magnetic measurements and also affects the ability of the medium to store data. The origin of the demagnetising field lies in the law of continuity of flux. Fig.2.3 a) shows a typical single domain particle magnetised by an applied field,  $H_A$ . North and south poles are formed at the top and bottom of a body respectively along the applied field direction and the flux lines pass from north to south poles. The induced field is also present inside the body and is in the opposite direction to the magnetisation. It tends to demagnetise or reverse the magnetisation of the particle. This self-demagnetising field is denoted  $H_D$ .

---

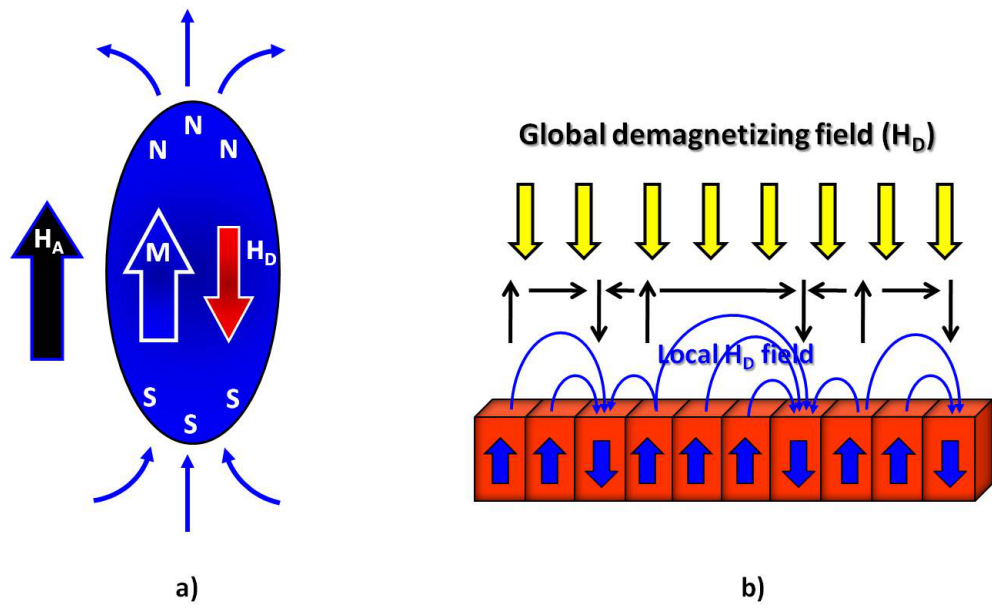


Figure 2.3: Schematic diagram of a) the magnetisation of a single domain particle with the demagnetising field and b) the global and local demagnetising field

The demagnetising field also has a shape effect. It can be written via the demagnetising factor,  $N_D$  and the value of magnetisation of the specimen as

$$H_D = -N_D \cdot M \quad (2.6)$$

The calculation of  $H_D$  is determined by the distribution of free poles around the surface. A full derivation of the demagnetising field can be found in Cullity and Graham [6]. In the case of perpendicular media the geometry is similar to an oblate spheroid with  $a \neq b = c$  and  $c/a = r$ . The demagnetising coefficients of oblate spheroids are  $N_a = 4\pi$  for perpendicular orientation and  $N_b = N_c = 0$  as  $r$  approaches infinity. Therefore  $N_D$  is equal to  $4\pi$  for perpendicular media.

$$N_D = N_a + N_b + N_c \quad (2.7)$$

For the characterisation of perpendicular recording media the correction for  $H_D$  is complicated if the magnetisation is non-uniform as fig.2.3 b).  $H_D$  consists of two components; the global demagnetising field and the local demagnetising field which depends on the orientation of the magnetisation of each grain. The magnitude of the local demagnetising field depends on the orientation of magnetisation across the grain and the exchange coupling between them.

Techniques for the magnetic characterisation of LRM cannot be used for PRM due to the presence of  $H_D$ . There have been a number of attempts using both theoretical and experimental techniques to correct for demagnetising effects in PRM. One simple approach is to extract  $H_D$  via the calculation of the internal field  $H_i$ . The demagnetising field is taken into account to correct the applied field  $H_A$  during measurements at each field step. The internal field is continuously changing with time due to the change of magnetisation. Therefore the internal field is

$$H_i = H_A - N_D \cdot M \quad (2.8)$$

Samwel *et al* [27] were the first group that tried to correct for  $H_D$  by calculating the internal field. Alumite media with magnetic columns of Fe, Co or Ni were used. The internal field was calculated from equation 2.8.  $N_D$  was found using the slope of the hysteresis loop at the coercivity. Several measurements such as the magnetisation curve, dc-demagnetisation curve (DCD) and iso-thermal remanent magnetisation curve (IRM) were investigated with uncorrected and corrected field values. They found that the measurements as a function of the internal field have limited use because of the sensitivity of the correction for the demagnetising coefficient. They also proposed the *recoil lines method* to describe the reversal behaviour due to the effect of  $H_D$ .

The internal field was also investigated by removing the global demagnetising field from  $H_A$  as proposed by Wu *et al* [28]. The correction was carried out in real time during measurements with a constant coefficient equal to  $4\pi$ . The corrected results distorted the loop shape leading to an over-corrected loop [29], [30] for CoCrPt alloys due to strong intergranular exchange coupling. In order to obtain a reasonable loop  $H_D$  had to be  $(0.1)4\pi M$ . This method was used to characterise perpendicular exchange-coupled composite (ECC) media by Deakin *et al* [29] [30]. The DCD curve was measured with correction at every field step. The shape of the hysteresis loop and the remanence curve changed significantly leading to a reduction of  $H_C$  and the remanent coercivity ( $H_{cr}$ ) by between 10-15 %. The approximation of  $N_D = 4\pi$  is not valid for PRM especially in the presence of strong intergranular exchange coupling.

Another approach to calculate  $N_D$  was used by Van der Veerdonk *et al* [31] [32]. The technique was based on recoil loop measurements originally proposed by Samwel *et al.* to obtain a DCD curve. The internal field from each recoil loop was corrected with the assumption of a constant value of  $N_D$ . The correction can be taken into account via a mean-field model on systems where long-range magnetostatic interactions dominate. The

iterative process was repeated in order to determine the value of  $N_D$  so that a remanence curve can be fitted to the switching field distribution assuming a log-normal distribution. The iterative method was used to correct  $H_D$  for magnetic viscosity measurements on PRM by Le Phan and Lodder [33]. A relaxation curve or time dependent measurement was measured with a corrected value for  $H_D$

$$H_{control}(t) = H_A + N \cdot [M(t) - M(0)] \quad (2.9)$$

where,  $H_{control}(t)$  is the corrected applied field,  $H_A$  is the applied field at the first iteration, and  $M(t)$  and  $M(0)$  are the magnetisation at time  $t$  and at the start of the relaxation respectively. The measurements were repeated until  $H_i$  was constant during the whole measurement. The limitation is that the correction of  $H_D$  is valid only for the specific condition that the PRM has intergranular exchange decoupling. The time dependent demagnetising field is more complicated due to the presence of the local demagnetising field from the orientation of the neighbouring grains as shown in fig.2.3 b).

### 2.1.3 Limitations of Recording Media

The key factor to achieve an increase in areal density for disk drive media is a reduced bit size or the transition width parameter, ( $a_o$ ). The transition width parameter represents the length of the magnetic transition with moments in opposite directions either up or down as a binary data storage of 1 or 0. In 1999, Richter [34] introduced the first analytic calculation of the transition width parameter for longitudinal recording media based on an analytical model of the write process defined by Williams and Comstock [35]. The transition width for perpendicular media ( $a_{WC}$ ) was also determined using similar assumptions. The approximate expression for  $a_{WC}$  is

$$a_{WC} = -\frac{\delta}{4} + \frac{z_0 [SFD + M_R/H_{cr}]}{\pi Q_{\perp}} + \left[ \left( \frac{z_0 (SFD + M_R/H_{cr})}{\pi Q_{\perp}} - \frac{\delta}{4} \right)^2 + \frac{z_0 \cdot SFD \cdot \delta}{\pi Q_{\perp}} \right]^{1/2} \quad (2.10)$$

where,  $a_{WC}$  is a Williams-Comstock transition width,  $\delta$  is the thickness of medium,  $z_0 = (d + \frac{\delta}{2})$ ,  $d$  is the magnetic spacing between the medium and the write head,  $M_R$  is the remanent magnetisation,  $H_{cr}$  is the remanent coercivity,  $SFD = (1 - S^*)$  which is related to the width of the switching field distribution [36],  $S^*$  is the coercive squareness calculated from the gradient of the magnetisation curve, and  $Q_{\perp}$  is proportional to the

head field gradient over the writing location

$$Q_{\perp} = -\frac{z_0}{H_{cr}} \cdot \frac{dH_{H,z}}{dx} \quad (2.11)$$

From equation 2.10, the main requirements to reduce the value of  $a_o$  are decreasing  $M_R$  and  $\delta$  and increasing  $H_{cr}$ . In reality the transition width can be easily approximated by the microstructure of the grains or the average grain diameter,  $D_{av}$ , and the exchange interaction between the grains. An approximation of the transition width in terms of  $a_{WC}$  and  $D_{av}$  [37] is

$$a_o \cong \sqrt{0.35a_{WC}^2 + \left(\frac{D_{av}}{2}\right)^2} \quad (2.12)$$

From equation 2.12, the transition width is directly proportional to the average grain diameter. Therefore high areal density can be achieved by reducing the grain size. Figure 2.4 shows a schematic of the storage process in PRM. The medium is magnetised normal to the surface by a single pole write head. The transition region will run through the grain boundary. Therefore large grain sizes with strong exchange coupling between the grains will broaden the transition region. If the grains are small the transition can be narrower as shown in fig.2.4. Therefore the medium must be engineered to reduce the grain size, the grain size distribution and exchange decouple the grains.

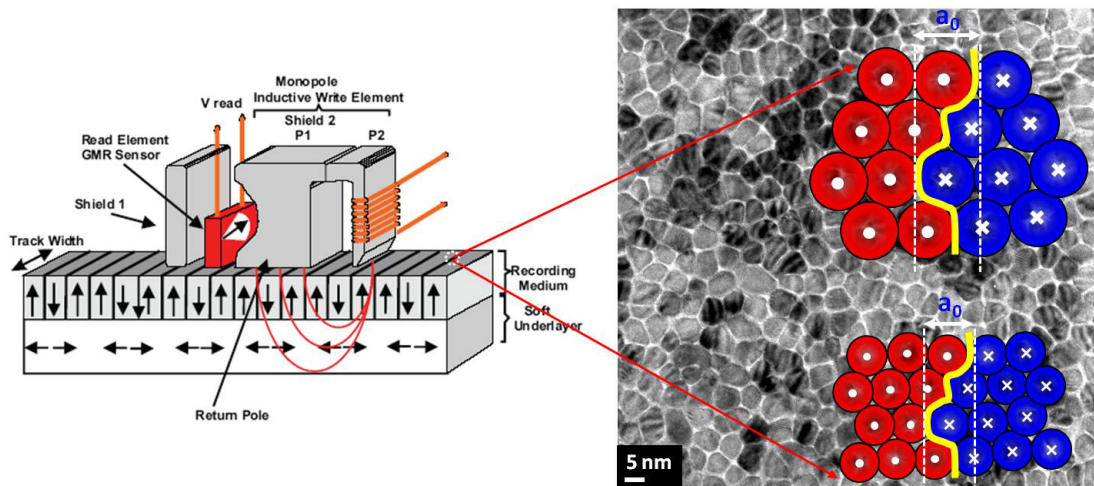


Figure 2.4: Schematic diagram of read/write system in PRM and the transition width for different grain sizes

In magnetic recording media, the critical factor for thermal stability is the energy barrier. It is proportional to the total anisotropy constant,  $K_u$ , the grain volume in the medium  $V$ , and the anisotropy field,  $H_K$

$$\Delta E = K_U V \left(1 - \frac{H}{H_K}\right)^2 \quad (2.13)$$

and

$$H_K = \frac{2K_U}{M_S} \quad (2.14)$$

where  $H$  is the external field and  $M_S$  is the saturation magnetisation. The anisotropy field is very significant for the thermal stability of the data. The coercivity can be approximated to  $H_K$  when there is no thermal energy. In order to achieve thermal stability  $H_K$  should be as high as possible. From eq.2.14 this can be accomplished by increasing the anisotropy constant and decreasing  $M_S$ . Moreover, the demagnetising field strongly influences the reversal of the magnetisation in PRM.  $H_D$  is dependent on the saturation magnetisation and the shape of specimen. Given that  $H_D$  is  $\sim 4\pi M_S$ , the saturation magnetisation affects both  $H_D$  and  $H_K$ . The criterion for perpendicular orientation is

$$H_K > H_D \quad (2.15)$$

or

$$M_S < \left(\frac{K_U}{2\pi}\right)^{1/2} \quad (2.16)$$

The energy barrier prevents the reversal of the magnetisation due to thermal energy and the self-demagnetising field, resulting in data loss. The reduction of grain size to achieve higher recording density leads to a deterioration of the thermal stability. As the areal density increases, if the anisotropy constant is fixed, the reduction of the grain volume leads to a decrease of the energy barrier. In the case of  $\Delta E$  being less than  $40k_B T$ , thermal energy will reverse the magnetisation in less than the specified 10 years [5]. The magnetisation at any time of an ensemble of grains

$$-\frac{dM}{dt} = f_o M e^{-\Delta E/k_B T} \quad (2.17)$$

where,  $f_o$  is a frequency factor which has a value of  $10^9 \text{ s}^{-1}$  [38]. The time at which the magnetisation decreases to  $1/e$  or 37% of its original value is given by the Néel-Arrhenius law

$$\frac{1}{\tau} = f_o e^{-\Delta E/k_B T} \quad (2.18)$$

where,  $\tau$  is the relaxation time. Hence, high areal density can be achieved in CoPt alloys by increasing the amount of Pt in the alloy [20], [21]. The thermal energy can be described in terms of a fictitious field known as the fluctuation field,  $H_f$ . The magnetisation decreases as a function of  $\ln(t)$  due to thermal energy. The details of the time dependence of magnetisation will be discussed in section 2.4.3. The increase in anisotropy also causes another limitation which is the writability through an increase in  $H_K$ . This is a serious problem for writing information due to the limit of the writing field,  $H_W$ .  $H_W$  depends on the capability of the write head material and its saturation magnetisation. De Witte *et al.* also showed that the frequency of the switching field gives rise to larger values of the switching field,  $H_S$  for measurements on short time scales [39].

$$H_W > H_S = H_K \left[ 1 - \left( \frac{\ln(t \cdot f_o) k_B T}{K_U V} \right)^{1/2} \right] \quad (2.19)$$

From equation 2.19, the coercivity is inversely proportional to the time scale,  $t$  which is the time taken for the magnetisation to cross zero after the application of a field probe. It indicates that if the time scale for the writing process is very short, the coercivity becomes larger than for a long time scale. This is a significant feature of the time or frequency dependence for the HDD. The write field operates at extremely high frequencies at  $\sim$  **GHz** levels. It leads to the large switching field. Therefore the write field must be greater than the switching field at the write frequency.

There is one factor which intertwines the thermal stability and writability required to improve the performance of hard disk drives. Signal to noise ratio (SNR) is a critical factor for the improvement of the read back signal from the medium. An approximate expression for SNR is [3]

$$SNR \approx \frac{0.31 PW_{50} \cdot B \cdot W_{read}}{a_o^2 D (1 + \sigma^2)} \quad (2.20)$$

where,  $PW_{50}$  is the width of the signal pulse at 50% amplitude,  $B$  is the bit length,  $W_{read}$  the read width of the head,  $\sigma$  is the standard deviation of the normalised grain size distribution and  $D$  is the diameter of the grains. This equation indicates that reducing the grain size ( $D$ ) would help to increase the SNR. However, if the anisotropy is not high enough to stabilise the magnetisation, some of small grains can be reversed by thermal energy. This contribution will be a source of noise [16].

The key factors which limit the growth of areal density are thermal stability, writability and SNR. This problem is known as the *media-trilemma* [40]. The reduction of grain size and the increase of the write field can be solved by **Heat Assisted Magnetic Recording** (HAMR) [8], [41]. If a medium with very high magnetocrystalline anisotropy is heated so that the anisotropy decreases, this allows the write process to succeed. The medium will then be cooled back to its normal state. The thermal fluctuation in the material due to the heating leads to the problem of *write error* or *bit error rate* (BER). This limitation of BER for future advances in magnetic recording media was introduced by Evans *et al.* [42]. They specifically addressed this problem for advanced recording media consisting of a combination of bit patterned media and HAMR. This factor is also intertwined to the three components of the trilemma. This design of the problem in recording media is called the *quadrilemma* problem. Fig.2.5 shows a schematic of the media-trilemma problem for conventional PRM and the quadrilemma problem for future advanced media.

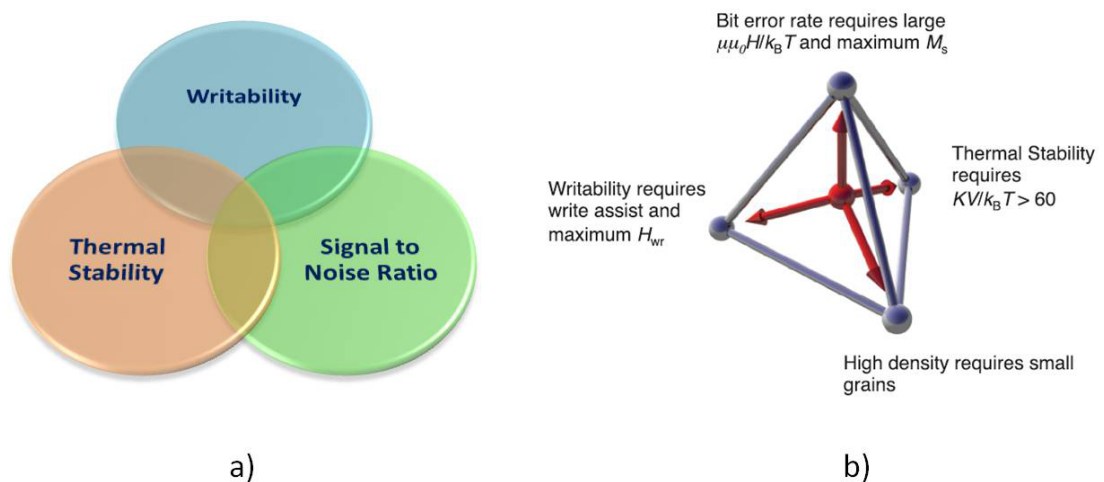


Figure 2.5: Schematic diagram of a) the media-trilemma problem b) the quadrilemma problem [42]

## 2.2 Magnetisation Reversal in Thin Film Media

Magnetisation reversal in thin film media is the fundamental process of information storage. This section describes the basis of all magnetic storage media which is the single domain particle. The mechanism of magnetisation reversal is described in terms of coherent reversal processes described by Stoner-Wohlfarth theory [15].

### 2.2.1 Single Domain Particles

The basis of the magnetic properties of ferromagnetic materials such as the shape of a magnetisation curve or the mechanism of hysteresis was first described by Weiss in terms of a molecular field theory and magnetic domains in 1906. A *magnetic domain* is a small region of a material where atomic magnetic moments have the same direction. In small particles it is energetically favourable for only one domain to exist with a saturation magnetisation,  $M_S$ .

The size of the single domain can be determined directly from the minimisation of the magnetostatic energy or the self-energy,  $E_{ms}$  and the wall energy,  $E_{wall}$  used to form a wall in a material. The direction of magnetisation within a single domain is along the  $c$ -axis due to the presence of the crystal structure of the Co alloy with uniaxial anisotropy. The magnetostatic energy can be determined from

$$E_{ms} = \frac{1}{8\pi} \int H_D^2 dv \quad (2.21)$$

where,  $H_D$  is the demagnetising field which depends on the sample shape and the orientation of the grains and  $v$  is the grain volume. From equation 2.21,  $E_{ms}$  can be written in a simplified form as

$$E_{ms} = \frac{1}{2} H_D M = \frac{1}{2} N_D M_S^2 \quad (2.22)$$

where,  $N_D$  is the demagnetising factor. In a bulk material if one domain splits into many domains in opposite directions as shown in fig 2.6, the magnetostatic energy will be decreased due to the magnetic north and south poles being closer to each other and the reduction in the spatial extent of the field. The domain cannot be divided to an unlimited degree due to the limitation of the wall energy. This leads to an equilibrium domain size. Therefore, the smallest size for a single domain is determined from the minimisation of  $E_{ms}$  and  $E_{wall}$ . From eq.2.22, the  $E_{ms}$  of a cubic structure can be

---

expressed by

$$E_{ms} = \frac{2}{3}\pi M_S^2 L \quad (2.23)$$

where  $L$  is the length of domain. This energy per unit area can be approximated by

$$E_{ms} = 0.85 M_S^2 D \quad (2.24)$$

In the case of the wall energy it can be represented by the relationship between the domain wall energy per unit area of the wall,  $\sigma$ , and the domain structure

$$E_{wall} = \sigma \frac{D}{L} \quad (2.25)$$

where,  $D$  is the width of the domain wall. The critical size for a single domain to form can be approximated by the differentiation of the total energy between  $E_{ms}$  and  $E_{wall}$  as a function of  $D$  at minimum energy. It is estimated as

$$D = \sqrt{\frac{\sigma L}{0.85 M_S^2}} \quad (2.26)$$

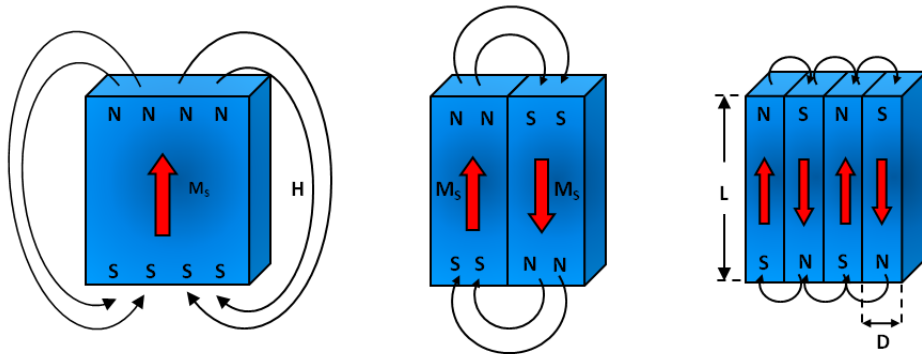


Figure 2.6: Schematic diagram of the single domain structures of a uniaxial crystal

For single domain particles magnetisation reversal is only possible by rotation. This rotation occurs over an energy barrier created by the anisotropy energy derived from either magnetocrystalline or shape effects or a combination of both. In certain cases and particularly for elongated particles, the atomic spins may not remain parallel during rotation leading to what are known as incoherent reversal mechanisms. These

effects were investigated in detail in the 1960s and 70s with the defining experimental work published by Luborsky [43]. He studied the variation of coercivity with particle size for Fe and Co particles. This work reproduced below, shows that the onset of incoherent reversal occurs above 20 nm for spherical particles.

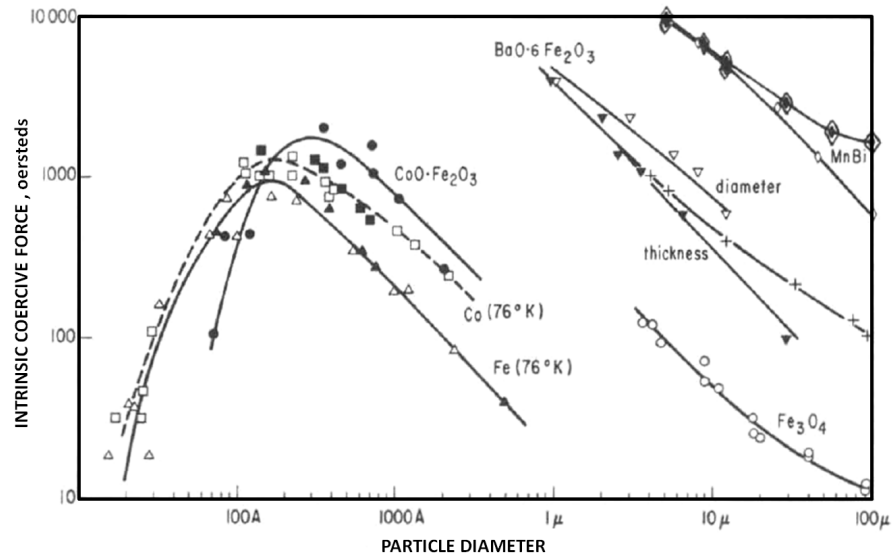


Figure 2.7: Variation of coercivity with particle size for Fe and Co [43]

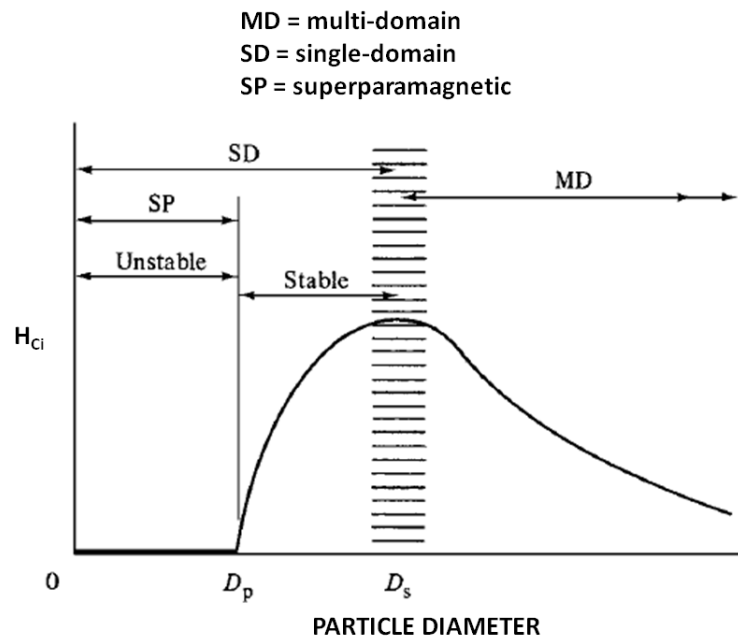


Figure 2.8: Schematic diagram of variation of the intrinsic coercivity with particle diameter [6]

In advanced thin film media the grain size is less than 10 nm and hence incoherent reversal processes do not occur. This leads to higher values of coercivity of up to 10 kOe being available even though the write field available is limited to about 10kOe. The grains in thin film media are somewhat elongated as can be seen in the cross-sectional TEM image in figure 2.9. However the elongation, which is due to the columnar structure, is along the c-axis and hence any shape anisotropy is parallel to the magnetocrystalline anisotropy which also promotes coherent rotation. The shape term is generally quite small compared to the magnetocrystalline anisotropy due to the low value of  $M_S$ . For a typical medium with  $M_S = 500$  emu/cc and the grain size and recording thickness about 8 and 12 nm respectively, the value of  $K_S$  is  $2.36 \times 10^5$  emu/cc compared to  $K_C = 8 \times 10^6$  ergs/cc and hence only coherent reversal needs to be considered.

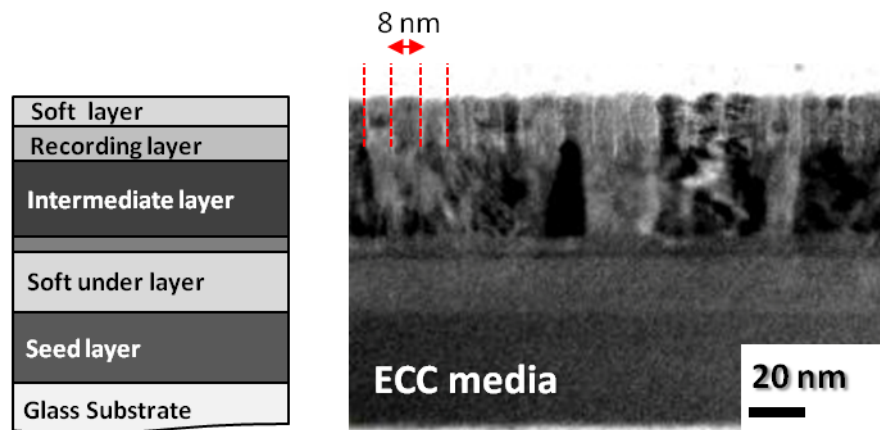


Figure 2.9: Schematic diagram of cross-section and typical in-plane TEM image for ECC media

### 2.2.2 Stoner-Wohlfarth Theory

$\text{SiO}_2$  at the grain boundaries in the medium reduces both the size of the magnetic grains and the exchange interaction between them. The small grain size ensures the film is composed of single domain particles. The model that describes the magnetisation reversal of such particles is the Stoner-Wohlfarth (SW) model [44]. SW theory [15] shows the process of magnetisation reversal of single-domain particles having a prolate spheroid shape. Figure 2.10 shows a schematic of a single particle with its easy axis, the applied field,  $H$  and the magnetisation.

From fig.2.10, an external field is applied at an angle  $\alpha$  to the easy direction which is the  $c$ -axis in hcp cobalt. The total energy,  $E_T$  of the particle can be represented by a combination of the anisotropy energy,  $E_a$  and the Zeeman energy,  $E_p$

$$E_T = E_a + E_p = K_U V \cdot \sin^2 \theta - H M_S V \cdot \cos(\alpha - \theta) \quad (2.27)$$

where  $\theta$  is the angle between the magnetisation and  $c$ -axis,  $K_U$  is the uniaxial anisotropy constant,  $V$  is the volume of particle and  $M_S$  is the saturation magnetisation.

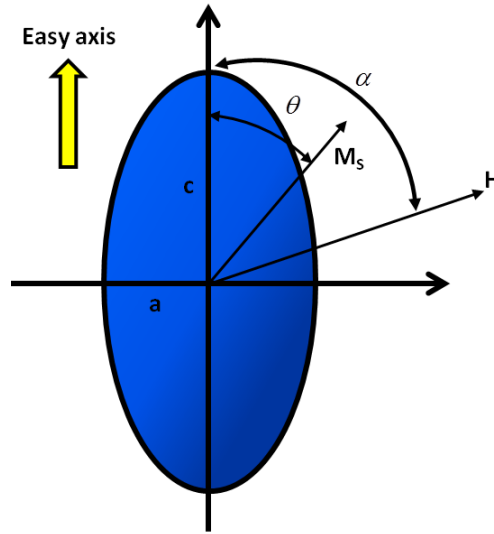


Figure 2.10: Schematic of prolate spheroid single domain particle with magnetisation and applied field

In order to determine the stability of a grain state, the total energy is minimized

$$\frac{dE_T}{d\theta} = 2K_U \cdot \sin\theta \cos\theta - H M_S \cdot \sin(\alpha - \theta) = 0 \quad (2.28)$$

and

$$\sin\theta \cos\theta = h \cdot \sin(\alpha - \theta) \quad (2.29)$$

where the magnetisation along the field direction is  $M_S \cdot \cos(\alpha - \theta)$ ,  $h = H (M_S/2K_U)$  which represents the ratio between the applied field and the anisotropy field ( $H_K = 2K_U/M_S$ ). In the case of  $\alpha = 90^\circ$ , the magnetisation along the applied field is  $M_S \cos(90^\circ - \theta)$  or  $M_S \sin\theta$ . Therefore, the normalised magnetisation  $m = M/M_S$  is

$$2K_U \frac{M}{M_S} = H M_S \quad (2.30)$$

So,

$$m = \frac{M}{M_S} = \frac{HM_S}{2K_U} \quad (2.31)$$

Therefore, if the applied field is normal to the easy axis the magnetisation is a linear function of  $H$ . In the general case, the equilibrium state and the component of the magnetisation along the applied field direction are represented by the normalised field term ( $h = H/H_K$ ) and the normalised magnetisation ( $m = M/M_S$ ) by

$$\sin\theta \cos\theta - h \cdot \sin(\alpha - \theta) = 0 \quad (2.32)$$

and

$$m = \cos(\alpha - \theta) \quad (2.33)$$

The variation of the normalised magnetisation  $m$ , as a function of applied field at any angle of  $\alpha$  can be calculated from the second derivative of  $E_T$ . A full mathematic deviation can be found in Cullity and Graham [6]. Fig.2.11 shows the hysteresis loop of a single domain particle at different angles between the applied field and the easy axis [15].

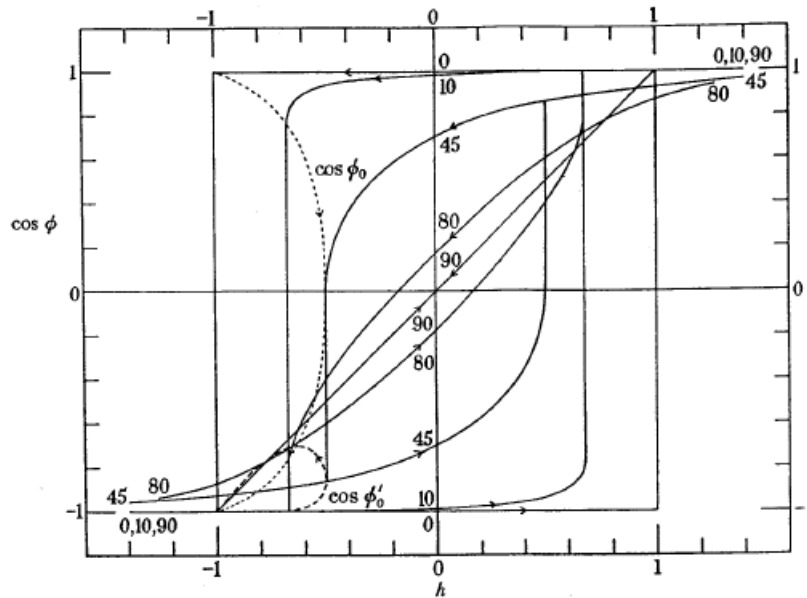


Figure 2.11: Magnetisation curves of the Stoner-Wohlfarth theory [15]

When the magnetisation is non-collinear with the applied field, it rotates easily along the field direction due to a *torque effect*. When the magnetisation is parallel to

the field, the magnetisation will not switch or flip until the field energy can overcome the energy barrier. The SW model shows that a small deviation of the easy axis from the applied field direction leads to a large reduction in  $H$  and hence the coercivity. For example, a deviation of  $10^\circ$  leads to a reduction in the switching field  $H_S$  of a single grain of 30%. For perpendicular recording media, the energy barrier which prevents magnetisation reversal is

$$\Delta E = K_U \cdot V \left(1 - \frac{H}{H_K}\right)^2 \quad (2.34)$$

where  $H$  is the applied field and  $H_K$  is the anisotropy field. The origin of the energy barrier is discussed in section 2.4.1. The competition between  $H$  and  $H_K$  leads to the switching of the magnetisation. There are several factors which dominate the energy barrier preventing magnetisation reversal such as the anisotropy constant  $K$  which can vary due to faults in the crystallinity of the grains, the distribution of grain size, intergranular magnetostatic and exchange interactions and the dispersion of the crystalline axis directions. The most significant factor affecting the switching field distribution in perpendicular media is the crystalline axis dispersion or easy axis distribution. The switching field is correctly written as

$$H_S = \frac{\alpha K}{M_S} \quad (2.35)$$

where  $\alpha$  is the alignment factor or the grain orientation factor with a value ranging from 0.96 for the random case [43] to 2 for the aligned case. The distribution of easy axis orientation is a critical factor for advanced recording media because a small angle change from the perpendicular can lead to a large change of the coercivity as described by Stoner-Wohlfarth theory.

### 2.2.3 Coherent and Incoherent Reversal Processes

When a magnetic field is applied to a magnetic material several mechanisms by which the magnetisation reverses are possible. In thin film media magnetisation reversal can occur in 3 different ways. The first is the reversal of individual grains which rotate independently, the second is the reversal of coupled grains which rotate in unison but separately in each cluster and thirdly, coupled long range grains which rotate when domain wall motion occurs.

The mechanism of magnetisation reversal of the three modes can be described by two types of spin rotation: *Coherent reversal* and *Incoherent reversal*. The first was

modelled by Stoner and Wohlfarth to describe the magnetisation reversal of uniaxial single-domain particles. This is known as the Stoner-Wohlfarth (SW) model [15] as discussed in section 2.2.2. The SW-model assumes that the atomic moments are parallel during reversal. The reversal process of a single magnetic domain must be coherently rotated from the easy direction towards the field direction as shown in fig.2.12 a). This behaviour of reversal is known as the *Stoner-Wohlfarth mode*. For the SW mode, the calculation can also predict the coercivity of single domain particles with the variation of angles between the easy axis and applied field and different axial ratio ( $c/a$ ).

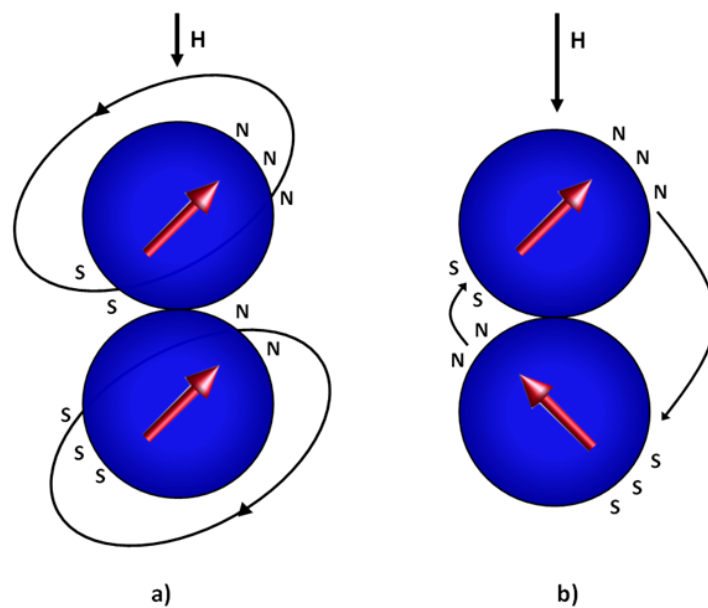


Figure 2.12: Schematic diagram of the reversal modes a) coherent reversal b) incoherent reversal [6]

The calculation of  $H_C$  is essentially a complex approach to the micro-magnetic system due to the limitations such as excluding exchange and dipolar interactions between the grains. In 1961, Luborsky [43] found that the coercivity of elongated iron particles with different axial ratios ( $c/a$ ) was less than that of the value determined by SW mode. From this discrepancy, there were several models proposed in order to describe the complicated mechanism of magnetisation reversal. The assumptions are based on the incoherent rotation, in which the magnetisation of all spins are not parallel to one another. This mechanism is shown in fig.2.12 b). For advanced recording media, the efficiency of the  $\text{SiO}_2$  at the grain boundaries provides exchange decoupling between the

grains. Hence, the Stoner-Wohlfarth model is adequate to describe the magnetisation reversal.

In real thin film media, the magnetisation reversal can be more complicated because more than one reversal mode may occur such as co-operative reversal between grains due to exchange interactions. There have been several models used to describe magnetisation reversal in real recording media. The first simulation which included the effect of magnetostatic coupling of randomly oriented grains was proposed by Hughes in 1983 [45]. In this model a hexagonal cell was used to represent a single domain particles of Co-P and Co-Ni-P for longitudinal media. The micromagnetic calculation gave predictions close to experimental results. Figure 2.13 shows a schematic illustration of this mechanism of reversal in a polycrystalline film. Zhu and Bertram [46], [47] undertook a micromagnetic study of thin metallic films which included the exchange coupling between the grains. They found that magnetostatic interactions and particularly exchange coupling dominated the magnetisation reversal which increased the squareness and reduced the coercivity of thin films.

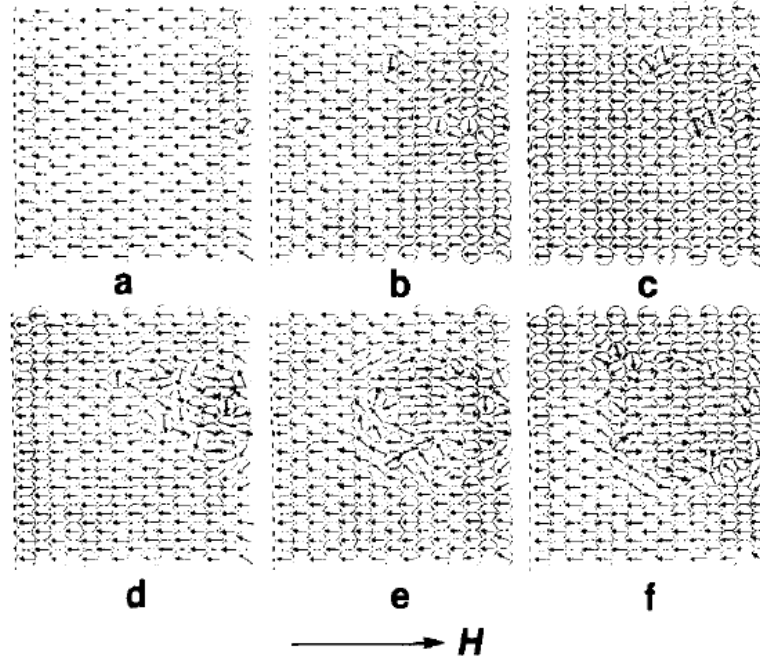


Figure 2.13: Schematic diagram of a mechanism of reversal in a polycrystalline film in LRM [45]

In the case of perpendicular recording media, there have been also several simulations proposed to understand the physics behind the mechanism of the magnetisation reversal processes. For example, the reversal process of an exchange coupled composite (ECC) media was described by Suess *et al.* [13] and Victora and Shen *et al.* [12] [48]. The simulations were based on single grains which consisted of two different magnetic regions which were magnetically soft and hard. They used the Landau-Lifshitz-Gilbert (LLG) calculation to describe the switching process including the interlayer interaction between the two regions. The magnetisation of the hard layer was reversed coherently by the reversal of the soft layer following Stoner-Wohlfarth theory [15]. From the model, ECC media have been used as an alternative perpendicular recording media to extend the recording density. For advanced perpendicular recording media, the reduced grain size and the complete grain segregation by a non-magnetic material leads to single domain behaviour. Tannous and Gieraltowski [44] gave a mathematical calculation of the SW model which was adequate to describe the magnetisation reversal.

## 2.3 Interaction Mechanisms in Thin Film Media

### 2.3.1 Exchange Interaction

The orientation of the spin in an atom of a magnetic material is caused by the *exchange interaction*. The principle of the exchange coupling of spins was first described via a quantum mechanical exchange force by Heisenberg in 1928. In a simple case of two hydrogen atoms the spins can pair at the same energy by alteration of the spin orientation due to the *exchange force*. The spin is aligned parallel or anti-parallel in order to minimise the total energy. In quantum mechanics the magnetic interactions can be classified into an electronic interaction; direct exchange, indirect exchange and super-exchange.

For advanced recording media, there are only direct and indirect (RKKY type) exchange interactions which influence the magnetic properties of the material. The direct exchange interaction is generally present via the *Coulomb interaction* among electrons with the presence of the exchange force due to the orientation of the spins. It arises when the atoms are close enough to each other so that the orbitals can overlap. This leads to ordered orientation with the spins parallel or antiparallel in order to minimise the energy.

---

This exchange energy  $E_{ex}$  can be shown in the form of a *Heisenberg Hamiltonian* [6] [49].

$$E_{ex} = H^{spin} = - \sum J_{ij} S_i \cdot S_j \quad (2.36)$$

where,  $H^{spin}$  is the Heisenberg Hamiltonian,  $J_{ij}$  is the exchange integral or the exchange coupling constant and  $S_i, S_j$  are the spin angular momenta of atoms  $i$  and  $j$  respectively. The orientation of spins is controlled via the exchange integral,  $J_{ij}$ . The stable state is at the minimum energy of the summation over all pairs of ions. In the case of a ferromagnetic material,  $J_{ij}$  is positive and the spins align parallel to each other. For this to occur from grain to grain in a granular system, the crystal planes need to align precisely parallel with the correct inter-atomic spacing. This cannot occur. Typical high resolution transmission electron microscopy (HR-TEM) images show the non collinearity of the crystal planes between grains as shown in fig.2.14.

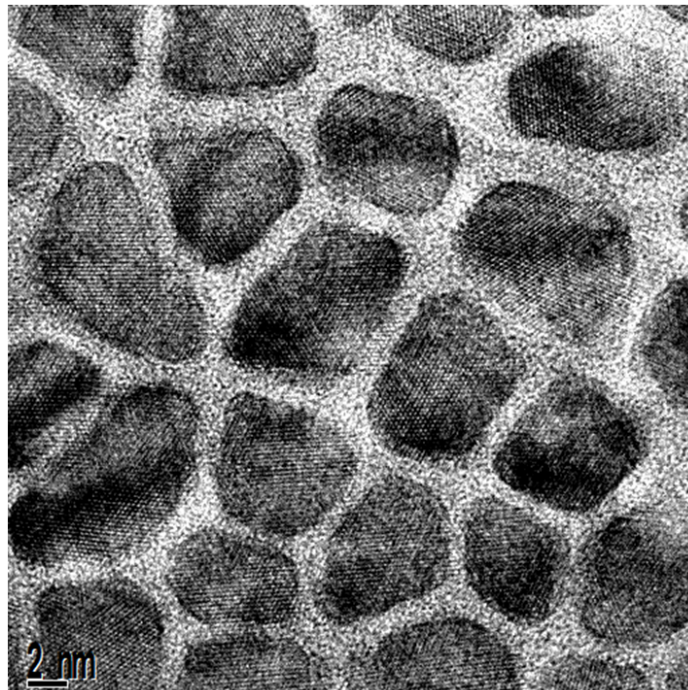


Figure 2.14: Typical high resolution transmission electron microscope of advanced recording media

The indirect exchange interaction was proposed by **Ruderman** and **Kittel** (1954), **Kasuya** (1956) and **Yosida** (1957) and is known as the **RKKY** interaction. This interaction is where the wave functions of the spins are able to interact via magnetically

---

polarised conduction electrons at long distance. There is no direct overlap between the wave function of neighbouring electrons. This model is basically described by the exchange coupling between the local magnetic moment and the conduction electrons. This leads to oscillatory coupling of the spin polarisation which causes an oscillation of the exchange integral,  $J_{ij}$  from positive to negative giving rise to ferromagnetic and antiferromagnetic states.

In thin film media, the exchange interaction between grains plays an important part in the magnetic behaviour. For longitudinal media, exchange interactions were usually investigated by measuring the difference of two remanence measurements denoted  $\Delta M$ ; A full discussion of this technique is given in section 4.2.2. Positive and negative values of  $\Delta M$  indicate that the interactions either stabilise the magnetised state leading to cooperative reversal, or tended to demagnetise the system respectively [36]. This method was commonly used for LRM [50], [51]. In perpendicular recording media the demagnetising field prevents an accurate measurement of  $\Delta M$ . In consequence all attempts to measure the indirect exchange coupling in PRM have been only partially successful.

### 2.3.2 Dipolar Interaction

Dipolar interactions originate from the demagnetising energy which is the Zeeman energy of the dipole magnetic moment interacting with others dipoles around it at long range. If two magnetic moments,  $m_1$  and  $m_2$  are separated by a distance  $r$  where the angles made by  $m_1$  and  $m_2$  with the center to center distance are  $\theta_1$  and  $\theta_2$  as shown in fig.2.15 a). The dipolar interaction energy is

$$E_d = \frac{m_1 \cdot m_2}{r^3} [\cos(\theta_1 - \theta_2) - 3 \cos \theta_1 \cos \theta_2] \quad (2.37)$$

where,  $E_d$  is the dipolar interaction energy. Equation 2.37 is valid for the case where  $r$  is much larger than the inter-polar distance,  $l$ . The energy is proportional to the magnitude of the magnetic moments and inversely proportional to the cube of the distance between them.

For  $l \simeq r$ ,  $E_d$  is not given by equation 2.37. Figure 2.15 b) shows interacting dipoles at short range. The interaction when the positive and negative magnetic charges are close becomes very strong and the dipolar interaction can be approximated as a

Coulomb interaction which represents the interaction of two electric charges as shown in fig 2.15 b) (bottom).  $E_d$  is then inversely proportional to  $r^2$

$$E_d \propto \frac{1}{r^2} \quad (2.38)$$

In perpendicular recording media dipolar interactions will strongly influence the magnetic behaviour leading to a thermal instability effect. There have been several experimental measurements and analytical models used to investigate this interaction. There have also been analytical models using atomistic calculations and micromagnetic calculations which include the dipolar energy in the system using the Landau-Lifshitz-Gilbert (LLG) equation to describe the dynamic motion of the magnetisation. However these usually use the dipole-dipole interaction inversely proportional to  $r^3$  [52], [53]. In reality, this interaction will be a complicated mixture of both effects with the  $r^2$  term dominating.

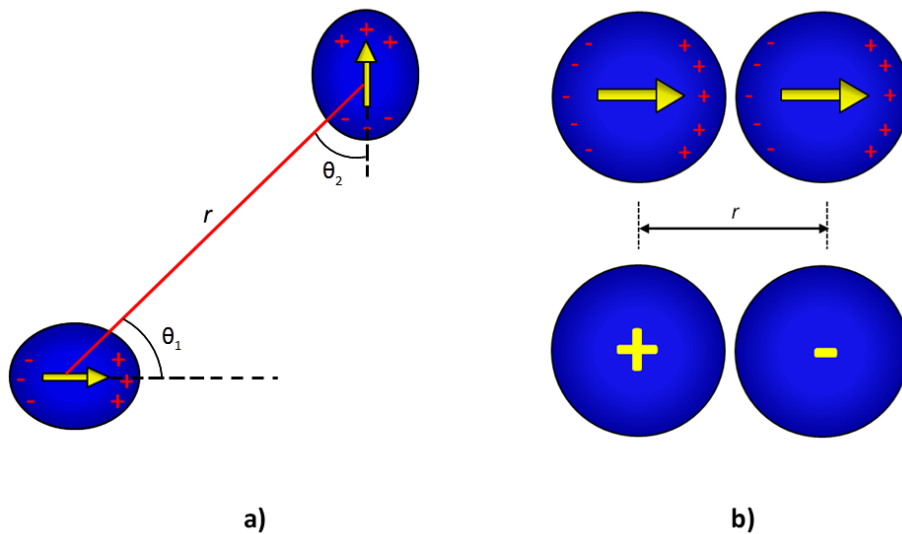


Figure 2.15: Schematic of the interacting dipoles as a) long distance and b) short distance

### 2.3.3 Multilayered Interaction

Perpendicular recording media was originally proposed in 1978 by Iwasaki and Nakamura [54]. Initially, the medium was based on single layer CoCr alloys. These materials suffered from poor surface roughness. Several Co-alloy media have since been proposed and used to improve the performance with low noise and high thermal stability. For current PRM, CoCrPt alloys are used [55]. In addition several works also proposed

novel perpendicular composite media structures using multilayer films with exchange interactions to overcome writability and thermal stability issues.

The first experimental and simulation studies were proposed by Sonobe *et al.* and Greaves *et al.* [11], [56]. The medium structure consists of Co-Pt multilayers or an amorphous CoPrTb alloy as a coupled granular/continuous (CGC) layer sitting on top of the granular medium [57] [58]. The interaction between the layers is known as interlayer exchange coupling. The multi-layer medium structure leads to 3 kinds of interactions [57] as shown in fig.2.16 a).

1) Because of the epitaxial growth of the CGC layer on the recording layer there will be direct exchange coupling between the grains in each layer.

2) Within the CGC layer the grains are coupled by excluding materials such as Cr which promote grain segregation. However this is an indirect RKKY type interaction.

3) The grains in the recording layer are exchange decoupled from each other using materials such as Cr in the alloy composition. However Cr is only partially successful as a segregation material and the latest media use SiO<sub>2</sub> segregation to achieve almost perfect decoupling. This coupling is also of the RKKY type and hence the insulating properties of SiO<sub>2</sub> are important

In addition to the coupling mechanisms described above it is also possible that individual grains in the recording layer can couple via the CGC layer. This is similar to the coupling reported in so called keepered media some years ago [59].

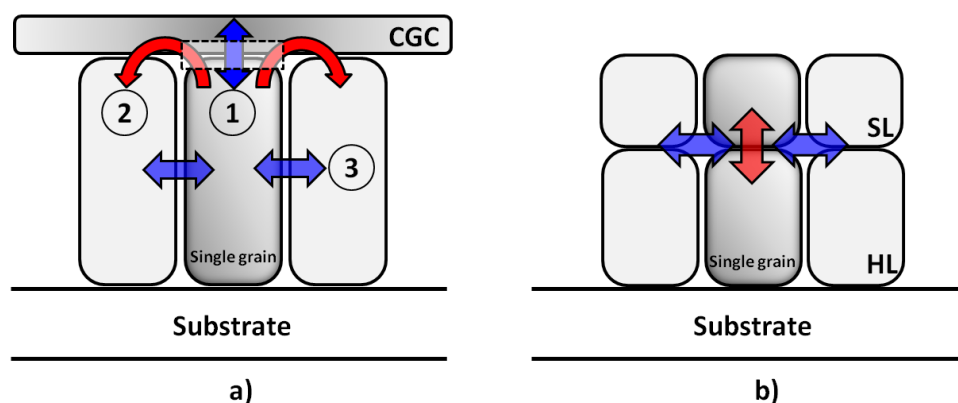


Figure 2.16: Schematic illustration of exchange multi-layer of a) CGC model and b) ECC model [57]

From the multilayer interactions the recording performance is improved by a reduction in the noise signal. High thermal stability due to the strong interlayer exchange coupling is also achieved. The granular layer pins domain wall movement [57] in the CGC layer leading to an increase in the nucleation field, a decrease in the saturation field and a loop with high squareness [56] [60]. The strong interlayer interaction increases the coercivity and the thermal stability of the media.

There are other well-known composite media structures proposed by Suess *et al.* [13] and Victora and Shen [12], [48]. They were designed to resolve the writability problem due to the high anisotropy field in the media. These new designs are known as exchange coupled composited (ECC) media based on two coupled layers of a magnetically soft and a hard material as shown schematically in fig.2.16 b). For ECC media the soft and hard grains are coupled via direct exchange due to the epitaxial growth. However in both layers materials such as Cr or SiO<sub>2</sub> are used to inhibit or prevent the RKKY type intergranular coupling. In principle the soft layer, which has a lower anisotropy field, is rotated first by the external field. This leads to a reversal of the hard layer due to the direct exchange coupling. The hard layer which has a very high anisotropy field will switch coherently with the soft layer following SW theory [61]. Therefore, multilayer interactions are significant factors to improve the performance of conventional Co-alloy perpendicular media using novel media designs [14].

## 2.4 Time-Dependence of Magnetisation

### 2.4.1 Energy Barrier

The energy barrier is the key parameter which prevents magnetisation reversal due to an external field, demagnetising field or thermal fluctuation field. The energy barrier is the difference between the maximum and minimum energy of a single domain particle reversing coherently [61]. From eq.2.27, the applied field is assumed to be along the easy axis. The total energy is then

$$E_T = V[K_U \cdot \sin^2 \theta - H \cdot M_S \cos \theta] \quad (2.39)$$

and the minimum energy is

$$E_{min} = H \cdot M_S V \quad (2.40)$$

From equation 2.39 the angle of the magnetisation where the energy is a maximum can be determined

$$\frac{dE_T}{d\theta} = 2K_U \cdot \sin\theta \cos\theta - HM_S \cdot \sin\theta = 0 \quad (2.41)$$

and

$$\cos\theta = \frac{H \cdot M_S}{2K_U} = \frac{H}{H_K} \quad (2.42)$$

where,  $H_K (= 2K_U/M_S)$  is the anisotropy field, Therefore, the maximum energy of a single domain particle can be determined by replacing the  $\cos\theta (= H/H_K)$  in equation 2.39

$$E_{max} = K_U \cdot V \left[ 1 + \left( \frac{M_S H}{2K_U} \right)^2 \right] \quad (2.43)$$

Therefore the energy barrier to magnetisation reversal is the difference between the maximum and minimum energy from equations 2.43 and 2.40

$$\Delta E = K_U \cdot V \left( 1 - \frac{M_S H}{2K_U} \right)^2 = K_U \cdot V \left( 1 - \frac{H}{H_K} \right)^2 \quad (2.44)$$

In the case of zero applied field, the energy barrier of single domain particles is proportional to the uniaxial anisotropy constant and the volume of particle. From eq.2.44, the energy barrier can be reduced by an applied field. When the external energy can overcome  $\Delta E$  the magnetisation will be rotated along the field direction. Figure 2.17 shows a schematic of the reversal process of a single columnar grain. The stable states I and II are separated by the energy barriers  $\Delta E_1$  and  $\Delta E_2$  respectively. Therefore, the switching process of the grain where the magnetisation is aligned parallel to the easy anisotropy axis from state I to II or II to I occurs when the external field can overcome  $\Delta E$  [62].

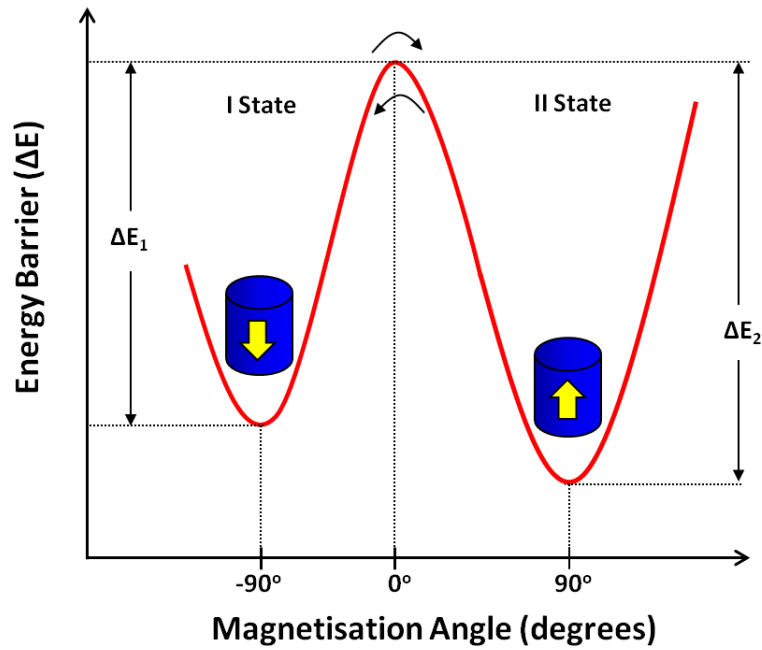


Figure 2.17: Schematic of the reversal process in the presence of an energy barrier

In reality, the energy barrier in recording media does not have a single value because of several intrinsic factors of the physical structure and the orientation of each grain but also dipole-dipole and exchange interactions. The intrinsic energy barrier can be written as

$$\Delta E = K_U \cdot V \left( 1 - \frac{M_S H}{\alpha K} \right)^2 \quad (2.45)$$

Equation 2.45 leads to the switching field distribution (SFD) which is the most important parameter in PRM. The SFD originates from the the distribution of grain size, the distribution of composition ( $K$  and  $M_S$ ), and the effects of crystalline axis dispersion ( $\alpha$ ) leading to a distribution of intrinsic switching fields  $H_K = \alpha K / M_S$  where  $\alpha$  is the alignment factor. The dipole-dipole and exchange interaction cannot be described via analytic functions and their effects can only be assessed by computer simulation.

### 2.4.2 Thermal Activation

Thermal activation is one of the media-trilemma problems for recording media. From equation 2.45 the energy barrier which prevents magnetisation reversal is proportional to the anisotropy constant and the volume of a single particle. If the volume is reduced

in order to increase the areal density, the energy barrier may be too small and can be overcome by the thermal energy.

In 1949, Néel [63] showed that the magnetisation could be spontaneously reversed for aligned single domain particles from one easy direction to the other by the effect of thermal energy via a fictitious field known as the fluctuation field ( $H_f$ ), without an external field. Fig.2.18 shows a schematic diagram of the thermal activation of a single grain. The single grain is magnetised by an applied field and the field is removed after saturation ( $t_{start} = 0$ ). Subsequently, thermal energy will cause the magnetisation to fluctuate until it can overcome the energy barrier ( $KV$ ). This phenomenon is important as it can lead to data being lost in recording technology.

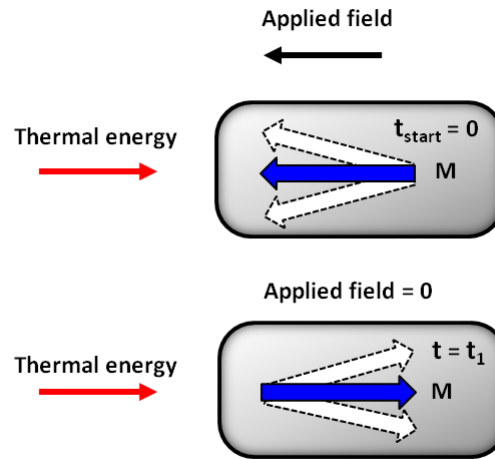


Figure 2.18: Schematic of thermal activation in a single grain

The rate of decrease of magnetisation of uniaxial particles is described by the Néel-Arrhenius law discussed in section 2.1.3. [63].

$$\tau^{-1} = f_o \cdot \exp(-K_U V / k_B T) \quad (2.46)$$

The relaxation time is very sensitive to the volume of the particle. In the case of Cobalt, if the diameter changes from 6.8 nm to 9 nm, the relaxation time will increase from 0.1 sec to 100 years [6]. If the moment relaxes in a time shorter than the measurement time the behaviour is described as *superparamagnetic*. If the remanence is

measured at  $t = 100$  seconds, the criterion can be expressed as

$$\ln\left(\frac{10^{-2}}{10^9}\right) = -\frac{K_U V}{k_B T} \quad (2.47)$$

so,

$$K_U V = 25k_B T \quad (2.48)$$

In the case of  $\Delta E \geq 25k_B T$  thermal activation is unlikely to occur during the measurement. This gives the critical size for superparamagnetic behaviour. In PRM, if an applied field is increased until the energy barrier is reduced to  $25 k_B T$  the particle will switch according to

$$H_C = H_K \left[ 1 - \left( \frac{25k_B T}{K_U V} \right)^{1/2} \right] \quad (2.49)$$

In order to stabilise data storage against thermal energy, the energy barrier must be optimised in terms of the anisotropy constant and the grain volume. In media, the magnetisation of a bit must be stable for 10 years, Therefore,  $\Delta E$  is [5].

$$\ln\left[\frac{10^{-2}}{(3.15 \times 10^8) 10^9}\right] = -\frac{K_U V}{k_B T} \quad (2.50)$$

or,

$$K_U V \sim 40k_B T \quad (2.51)$$

Thermal stability is essential as the grain size is reduced to achieve high density. Thermal activation can be studied via time dependence measurements known as magnetic viscosity.

### 2.4.3 Magnetic Viscosity

Néel [63] showed the effect of thermal energy on the magnetisation of single domain particles can lead to spontaneous reversal via a fictitious field,  $H_f$ . The behaviour of a single particle is an exponential time decay given by equation 2.46. Street and Woolley [64] were the first experimental group to find that the behaviour of the magnetisation disagreed with the exponential time decay. They described the phenomenon as *magnetic viscosity* [64]. The time dependence of the magnetisation can be shown in terms of two components under a constant steady reverse field after saturation.

$$M(t) = M_{irr}(H, t) + M_{rev}(H) \quad (2.52)$$

where,  $M(t)$  is the time dependent magnetisation,  $M_{rev}(H)$  is the reversible magnetisation which is constant in a steady reverse field, and  $M_{irr}(H,t)$  is the irreversible magnetisation where thermal energy can overcome the energy barrier in a field  $H$  and a time  $t$ . Therefore the time dependence of the magnetisation is only due to the  $M_{irr}$  component. The behaviour was observed to follow logarithmic time decay

$$M_{irr}(H, t) = M_{irr}(H, t = 0) \mp S(H) \ln(t) \quad (2.53)$$

The sign,  $\mp$  represents the rate of change of magnetisation which can decrease or increase with  $t$  depending on the point on the hysteresis loop, due to  $H$ .  $S(H)$  is the coefficient of magnetic viscosity or the time dependence coefficient which is given by the slope of the magnetisation versus  $\ln(t)$  when a wide distribution of energy barriers is present [65], [66]

$$S(H) = -\frac{dM(H)}{d\ln(t)} \quad (2.54)$$

The origin of the time dependence is also related to the value of the energy barrier distribution at the field  $H$ ,  $f(\Delta E(H))$ . Therefore, the coefficient of magnetic viscosity can be represented in terms of  $\Delta E(H)$  [67]

$$S(H) = 2M_S k_B T \cdot f[\Delta E(H)]_{\Delta E_C} \quad (2.55)$$

where,  $\Delta E_C$  is the activation energy where the magnetisation is being reversed.

Several experimental and theoretical groups found that the time dependence of magnetisation was non-linear with  $\ln t$  when the dispersion of energy barriers was narrow. Aharoni [68] determined an analytical form of the magnetisation decay using a gamma distribution. The results predicted that the magnetisation decay with  $\ln t$  was concave downwards which was consistent with some experimental results for spin glasses studied by Chamberlin *et al.* [69]. Yeung *et al.* also reported the magnetisation decay of PtMn alloys as being concave downwards and concave upwards when the temperature was below and above the spin-glass temperature respectively [70].

The non-linear behaviour of the time dependence of magnetisation with  $\ln t$  was finally determined as being due to the distribution of energy barriers by El-Hilo *et al.* in 1992 [71]. They found that the variation of the magnetisation with  $\ln t$  was concave downwards and concave upwards only in the case of a narrow  $f(\Delta E)$ . Figure 2.19 a) shows a narrow dispersion of energy barriers which is divided into 3 regions; The first

where  $f(\Delta E)$  is increasing steeply, the second where  $f(\Delta E)$  peaks, and the third where  $f(\Delta E)$  is decreasing sharply. The concave downwards variation derives from the first region where, as time passes, regions of the distribution with larger values of  $f(\Delta E)$  are activated over time. Then from equation 2.55 the value of  $S(H)$  progressively increases. Similarly, the third region with decreasing  $f(\Delta E)$  leads to the curvature being concave upwards as  $f(\Delta E)$  decreases. In the second region where the peak of the energy barrier distribution occurs, the time dependence follows an  $S$  shape due to the combination of the two types of variation of  $f(\Delta E)$  on either side of the peak. Fig.2.19 b) shows the calculated variation of three different curvatures of the time dependence of magnetisation with  $\ln t$  for a  $f(\Delta E)$  with a standard deviation of 0.1 [71].

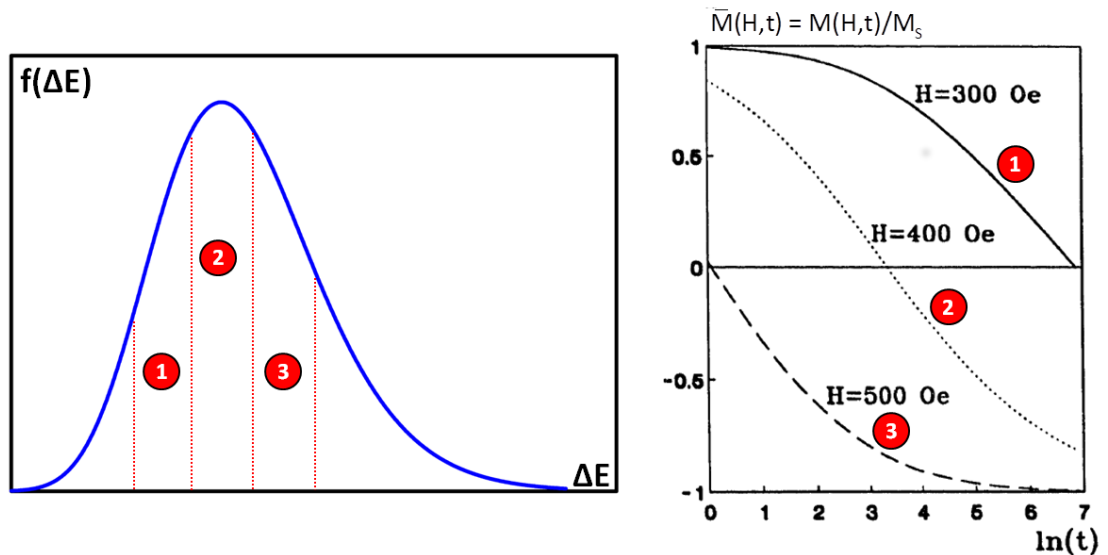


Figure 2.19: Schematic of a) a narrow distribution of energy barriers and b) the calculated variation of magnetisation decay with  $\ln t$  in different regions of  $f(\Delta E)$  [72]

When the distribution of energy barrier is narrow, non-linear  $\ln t$  time dependence occurs and equation 2.53 cannot be used. For PRM the presence of  $\text{SiO}_2$  leads to small grains and a narrow grain size distribution which gives rise to a narrow  $f(\Delta E)$ . El-Hilo [72] showed the more general form for the time variation of magnetisation as

$$M(t) = M_o \int_0^{\infty} \exp\left(-\frac{t}{\tau}\right) f(\Delta E) d(\Delta E) \quad (2.56)$$

where,  $\tau$  is the relaxation time and  $f(\Delta E)$  is the energy barrier distribution. The blocked particles which can be activated by the field and the fraction which cannot overcome

the energy barrier are taken into account in a complex calculation [71], [72]. The rate of change of the magnetisation with  $\ln t$  can also be expressed as a power series expansion of magnetic viscosity coefficients

$$\frac{\Delta M}{\Delta \ln(t)} = \sum_{n=0} S_n \ln \left( \frac{t}{t_o} \right)^n = S_o + S_1 \ln \left( \frac{t}{t_o} \right) + S_2 \ln \left( \frac{t}{t_o} \right)^2 + \dots \quad (2.57)$$

where  $S_1$  and  $S_2$  are the non-linear time dependence coefficients,  $t_o$  and  $t$  are the times at the beginning and end of the measurement respectively. Equation 2.57 is the general form for the behaviour of the time dependence of magnetisation including the curvature of the magnetisation with  $\ln t$  via the second and third terms. For a wide distribution the third and higher order terms are zero giving linearity with  $\ln t$ .

#### 2.4.4 The Fluctuation Field and Activation Volumes

The fluctuation field  $H_f$  depends on the thermal energy and was written by Néel as [73]

$$H_f \propto k_B T \quad (2.58)$$

and

$$H_f = \frac{k_B T}{Q} \quad (2.59)$$

where,  $H_f$  represents the fluctuation field,  $k_B$  is Boltzmann's constant and  $T$  is the temperature. In 1984 Wohlfarth, arguing on dimensional grounds, pointed out that the denominator in equation 2.59 must represent a magnetic moment and rewrote equation 2.59 as [61]

$$H_f = \frac{k_B T}{V_{act} \cdot M_S} \quad (2.60)$$

where,  $M_S$  is the saturation magnetisation of the material and  $V_{act}$  is the activation volume.  $V_{act}$  represents that volume of a material that reverses coherently in a single step and gives the *smallest unit* that can be reversed.

Gaunt [67] showed theoretically that for a single domain particle reversing via a coherent mechanism  $V_{act}$  was equal to the grain volume. This was subsequently verified experimentally [74]. It has also been shown that for elongated particles reversing incoherently via the fanning mechanism that  $V_{act} = V/n$  where  $n$  is the axial ratio of the grains. This result is a validation of the chain of spheres model of Jacobs and Bean [75]. For coupled granular ferromagnetic materials  $V_{act}$  has also been shown to be indicative

---

of the degree of intergranular exchange coupling in thin films where co-operative reversal occurs leading to  $V_{act} > V_{TEM}$ , where  $V_{TEM}$  is the physical single grain volume.

In the case of thin film disc recording media,  $V_{act}$  gives the minimum volume required to store a bit of data. No bit can be smaller than  $V_{act}$  as it represents the smallest entity that can reverse. It is also useful for the study of the reversal processes that occur in the complex multilayer stacks used to form thin film media.

There have been a number of methods used to determine the fluctuation field [76], [77]. Néel [73] showed that  $H_f$  could be determined from measurements of the time dependence coefficient  $S(H)$  and the irreversible susceptibility  $\chi_{irr}(H)$  such that

$$H_f = \frac{S(H)}{\chi_{irr}} \quad (2.61)$$

From equations 2.60 and 2.61 the activation volume is

$$V_{act} = \frac{k_B T \cdot \chi_{irr}(H)}{M_S \cdot S(H)} \quad (2.62)$$

Here,  $\chi_{irr}(H)$  is usually determined as the differential of the isothermal remanence curve (IRM curve) or the dc demagnetisation remanence curve (DCD curve), fully described in section 4.2.2.  $S(H)$  is the slope of a measurement of the time dependence of magnetisation when it follows a  $\ln(t)$  variation. Equation 2.62 cannot be used for systems with a narrow  $f(\Delta E)$ . For systems with perpendicular anisotropy the presence of the large demagnetising field means that  $\chi_{irr}(H)$  cannot be measured accurately as well.

For system with a narrow distribution of energy barriers Estrin *et al.* [78] proposed an *equation of state model* or *constitutive relation* to investigate the fluctuation field. Using the relationship between the magnetic field, the irreversible magnetisation, ( $M_{irr}$ ) and the rate of change of the irreversible magnetisation ( $\dot{M}_{irr}$ ), the constitutive relation becomes

$$dH_i = \left( \frac{1}{\chi_{irr}^i} \right) dM_{irr} + H_f d(\ln \dot{M}_{irr}) \quad (2.63)$$

where,  $H_i$  is the internal field corrected for the demagnetisation factor,  $\chi_{irr}^i$  is the irreversible magnetic susceptibility, and  $d(\ln \dot{M}_{irr})$  is the rate of change of the irreversible magnetisation with time for a change of internal field ( $\dot{M}_1 \rightarrow \dot{M}_2$ ,  $H_1 \rightarrow H_2$ ) in terms of a fluctuation field,  $H_f$ . The fluctuation field at a constant irreversible magnetisation is

$$H_f = \frac{H_2 - H_1}{\ln(\dot{M}_{irr2}/\dot{M}_{irr1})} \Big|_{M_{irr}} \quad (2.64)$$

The fluctuation field can be then determined directly from a measurement of the change of irreversible magnetisation with time. At constant irreversible magnetisation the rate of change of the irreversible magnetisation with time for different values of the internal field can be measured from the gradient of the curves. The limitation of this method is the intrinsic difficulty of keeping  $M_{irr}$  constant at the different internal fields. This leads to a significant error in the calculation of  $H_f$  [79].

In 1997, Lyberatos *et al.* [80] proposed a technique which can reduce the error in the measurement of  $\dot{M}_{irr}$  at small internal fields. The change of the irreversible magnetisation can be determined from the differential of the equation of state or constitutive equation in eq.2.63. It is based on the relationship between magnetic viscosity and irreversible susceptibility

$$dM_{irr} = S \cdot d \ln(t) + \chi_{irr} dH \quad (2.65)$$

Moreover,  $S(H)$  and  $\chi_{irr}$  is

$$S(H, t) = \left. \frac{\partial M_{irr}}{\partial \ln(t)} \right|_H \quad (2.66)$$

and

$$\chi_{irr}(H, t) = \left. \frac{\partial M_{irr}}{\partial H} \right|_t \quad (2.67)$$

Equations 2.66 and 2.67 are substituted into eq. 2.65 and  $H_f$  becomes

$$H_f = \left. \frac{\Delta H}{\ln(t_2/t_1)} \right|_{M_{irr}} \quad (2.68)$$

This expression defines a waiting time experiment where  $H_f$  is determined from the values of  $t_1$  and  $t_2$  which are the times taken for the magnetisation to fall to a constant value of  $M_{irr}$  in the presence of applied fields  $H_1$  and  $H_2$  separated by  $\Delta H$ . For PRM the chosen value of  $M$  is generally  $M = 0$  so that  $H_f$  is determined at the coercivity. This also has the advantage that the demagnetising field  $H_D$  is zero.  $V_{act}$  is then given by

$$V_{act} = \frac{k_B T}{M_S H_f} \quad (2.69)$$

However equation 2.69 still suffers from the difficulty that  $H_f$  is determined at constant  $M_{irr}$ . For PRM it is approximately true that  $M_{total} = M_{irr}$  at  $H = 0$  but not at other field values and in particular at the coercivity. El-Hilo *et al.* reformulated equation 2.65 and showed its equivalence to the original formulation of Néel [73] and the work of Estrin *et al.* [78]. Also for the case of small  $\Delta H$  (i.e.  $\Delta H \simeq \delta H$ ) the requirement

of  $M_{irr}$  being constant is achieved within the normal range of error on the measurements themselves. Hence equation 2.68 gives an accurate and accessible method to obtain  $H_f$  and therefore  $V_{act}$  via equation 2.69

---

## CHAPTER III

### Advanced Recording Media

Magnetic recording was invented by Valdemar Poulsen in 1898 [16]. The device known as the *Telegraphone* was a magnetic wire system. It recorded a signal under an electromagnet on a steel wire wound helically on a cylinder. The basic concept of magnetic recording relies on two main parts; the capability of the magnetisation to be rotated by the field and for it to provide a signal to be read. It leads to the procedure of writing and reading information in hard disk drive (HDD) technology.

In 1956, the first commercial computer to use a hard disk drive to store information was released when IBM launched the *Random Access Method of Accounting and Control* (RAMAC) called the IBM305 RAMAC [81]. In the initial hard drives the capacity was 5 megabytes and RAMAC used 50 magnetic disks with a diameter of 24 inches and wet coated  $\gamma$ -Fe<sub>2</sub>O<sub>3</sub>. The areal density was 2 kbits/in<sup>2</sup>.

Figure 3.1 shows a typical hard disk drive and schematic diagrams of the write/read head for LRM and PRM technology and a conventional recording medium. In order to achieve a high areal density three key components are critical i.e. the read head, which converts the magnetic signal from the medium into an electrical signal, the write head, which provides the local magnetic field to write information and the medium to store information.

The development of these components has been designed to overcome the limitations of thermal loss of data. Read/write heads have evolved from the original magneto-resistance (MR) head [82] via giant magneto-resistance (GMR) with current in-plane, (CIP), tunnelling magneto-resistance (TMR) to GMR with current perpendicular to plane (CPP). The advances have been introduced following the discovery of GMR by Grünberg *et. al.* [1] and Fert *et. al.* [2]. The paradigm shift of recording from longitudinal to perpendicular [54], has resulted in areal density growth from 2 kbits/in<sup>2</sup> up to 1 Tbit/in<sup>2</sup> [83]. This is an increase of a factor of 500 million since the RAMAC was introduced. Therefore, it is important to understand the fundamental physics underpinning recording technology. The development of perpendicular recording is the main factor

---

allowing the areal density to increase to 1 Tbit/in<sup>2</sup> announced by Seagate in 2012 [83].

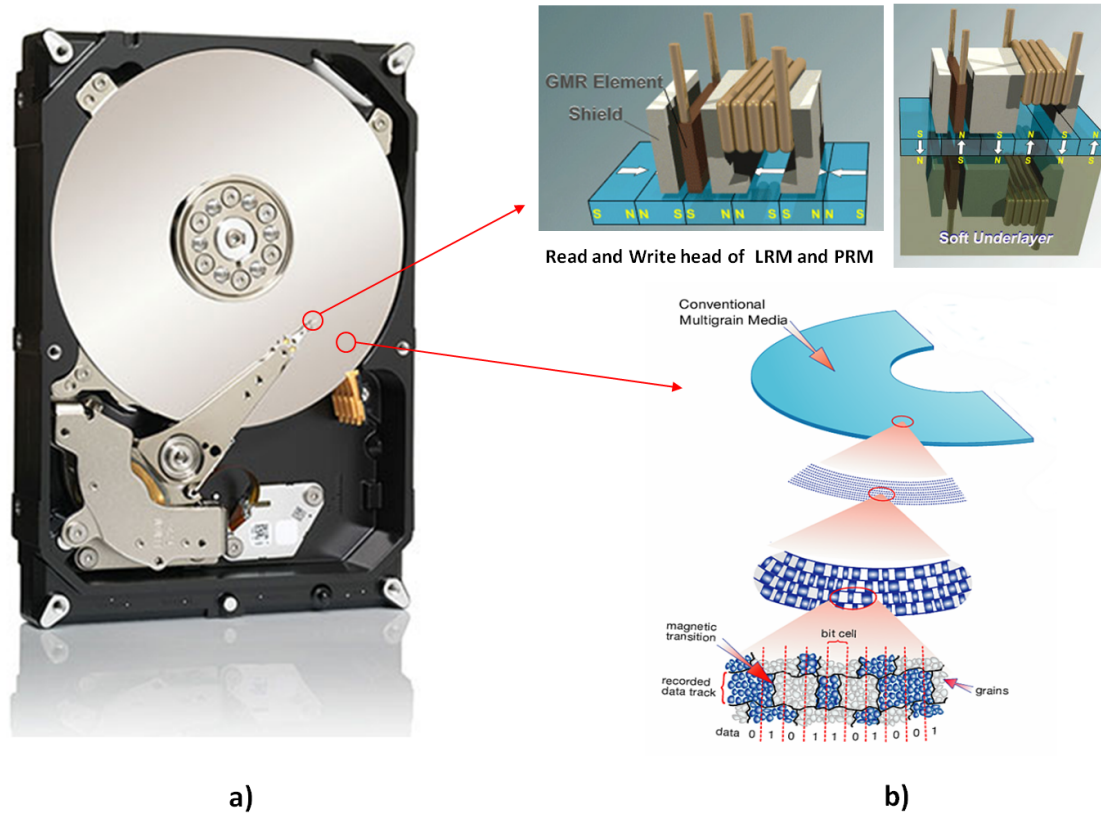


Figure 3.1: a) Image of a hard disk drive [84] and b) schematics of the read and write heads for LRM and PRM and a conventional recording media [85]

## 3.1 History of Recording Media

### 3.1.1 Transition to Perpendicular Recording Media

When IBM introduced RAMAC as the first commercial computer, all magnetic recording devices used longitudinal recording technology to store information [86]. In the initial life of HDD the data was stored as a magnetisation pattern in which the magnetisation prefers to lie in the plane of the recording medium. The storage process occurs by the write head providing a fringing field from its poles. When the write head moves along the medium the direction of magnetisation is changed. The data stored in the recording medium is read back by the read head which converts the stray field from the medium

into a voltage as shown in fig.3.1.

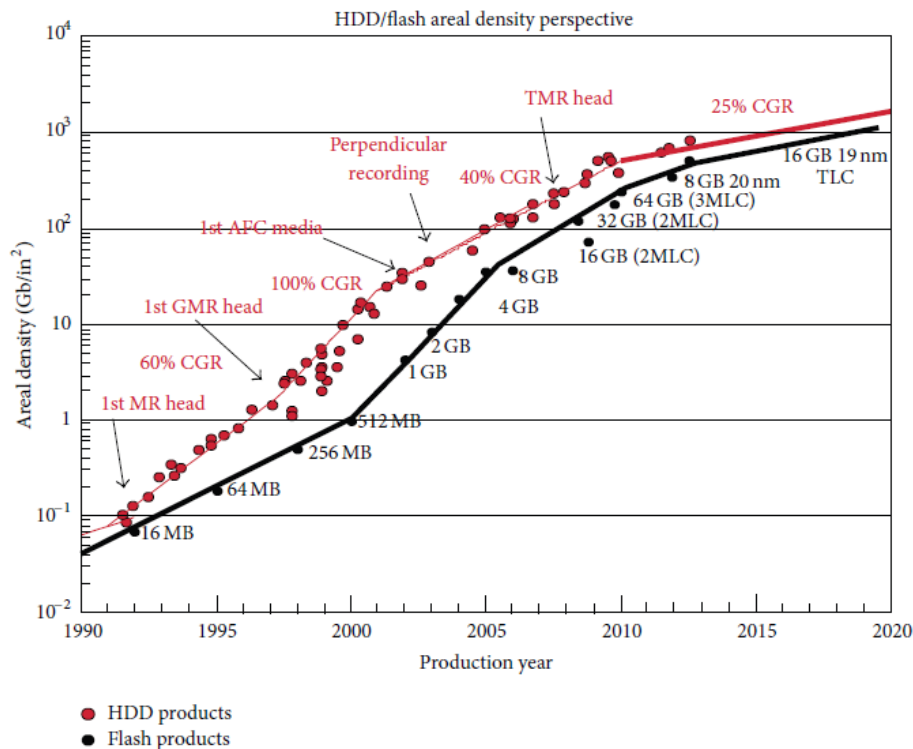


Figure 3.2: Schematic diagram of the areal density evolution for HDD and flash memory products [87]

In order to control the orientation of the easy axes in-plane, the most important layer of LRM is an underlayer or intermediate layer i.e. Cr or Cr-alloy [88] [89] which is deposited on top of the substrate which is either an Al-Mg alloy with Ni-P or glass, by dc magnetron sputtering. The seed provides (200) in-plane orientation of the hexagonal Co-alloy which keeps the  $c$ -axis of the Co alloy parallel to the surface with (110) texture. The areal density growth rate of LRM was mainly attributed to the development of the read head. Fig.3.2 shows a schematic diagram of the areal density evolution for HDD products through LRM to PRM from 1990 to 2020. In the first generation of recording media the compound growth rate (CGR) in areal density was 25%/annum with a thin-film inductive read head. In 1991, CGR dramatically increased reaching 60% to 100% following the introduction of the first magneto-resistive (MR) and subsequently GMR head [1], [2]. The GMR effect is based on spin-dependent scattering leading to an increased read-back signal responding to the step-like change in the magnetisation of the

recording medium. This growth-rate is higher than the historical Moore's law which is equivalent to  $\sim 40\%$ /annum [90].

In the later lifetime of LRM, CGR was reduced from 100%/annum to 20-30%/annum in late 2001 [87]. The main factors causing this reduction were firstly, the thermal stability of the data due to the reduction of the grain size. Secondly, when the bit length is reduced, the demagnetisation effect will decrease the energy barrier. The competition between the  $H_D$  and the energy barrier is

$$\Delta E = K_U \cdot V \left(1 - \frac{H_D}{H_K}\right)^2 \quad (3.1)$$

where

$$H_K = \frac{2K_U}{M_S} \quad (3.2)$$

Therefore, the reduction of the grain size which is required to increase the areal density is limited due to the presence of the large demagnetising field. In 2001 alternative longitudinal media were developed to extend the increase in areal density by the reduction of  $M_R \cdot \delta$  as in equation 2.10 where,  $M_R$  and  $\delta$  are the remanent magnetisation and the thickness of the medium respectively. These were known as *antiferromagnetically coupled media* (AFC) or synthetic anti-ferromagnetic media [91], [92]. AFC media consists of a thin Ru layer sandwiched between two ferromagnetic layers which are antiferromagnetically coupled to each other [93]. The ferromagnetic layers act as the recording layer and consists of a thicker layer and a stabilizing layer. From this media design shown schematically in figure 3.3 a reduction of  $M_R \cdot \delta$  was achieved due to the partial cancellation of  $M_R$  between the two ferromagnetic layers. If the interface coupling energy is greater than the anisotropy of the stabilizing layer, it leads to the switching of the stabilizing layer [92] [94]. Despite the improvements of longitudinal recording technology thermal stability and the large  $H_D$  were still limiting issues for HDD technology. Therefore, perpendicular technology has become the current magnetic storage technology in order to overcome these limitations.

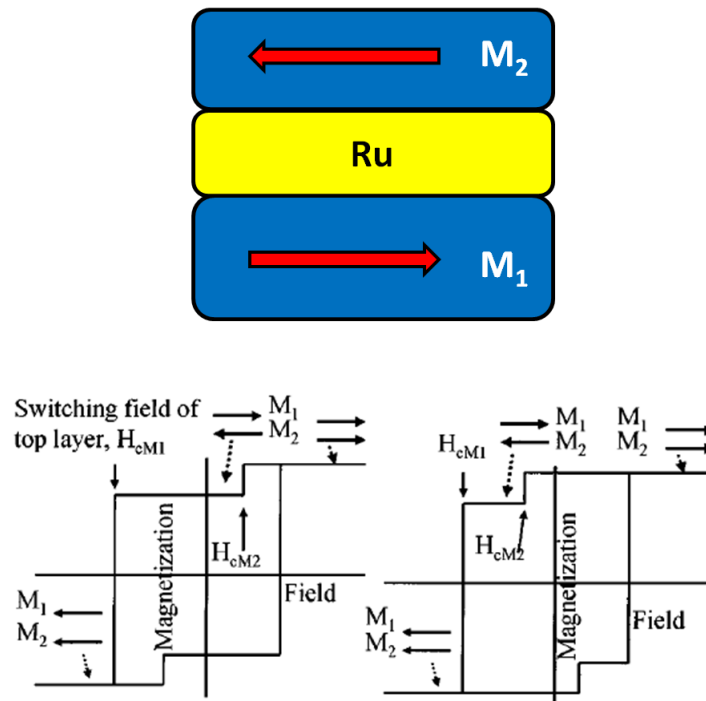


Figure 3.3: Schematic diagram of antiferromagnetically coupled film [92]

### 3.1.2 Perpendicular Recording

#### i) Basic Principles

In order to overcome the limitations of LRM, Iwasaki and Nakamura [54], [95] introduced perpendicular recording media in 1978 leading to the transition from LRM to PRM technology. The crucial concept of PRM is the change of the orientation of bits written on the medium to perpendicular to the surface. The advantage of PRM is the reduction of the demagnetising field to achieve high areal density. The demagnetising field from neighbouring bits is reduced due to the flux closure between neighbouring bits of opposite polarity. A second significant difference is the writing process. For PRM technology the fringing field of longitudinal recording is replaced by a single pole head which is made from CoFe with a high magnetisation. The image pole is provided by a soft underlayer (SUL) used to create a magnetic mirror. If the writing head represents a north pole the SUL will act as a south pole. The magnetic field in this configuration is much higher than the fringing field used in LRM. Hence the medium can have high anisotropy for thermal stability.

Figure 3.4 shows a schematic diagram of the perpendicular recording process. There are three main components in the system; the write head, read head and the recording medium. The basic principle for the production of a field in the write head is based on magnetic induction. The magnetic field is generated when a current passes through the coil wound on the CoFe pole piece. The magnetic flux from the single pole head is focused through the medium by the SUL. The gap field from the single pole and SUL can produce a writing field of up to 10 kOe with the saturation magnetisation of CoFe (2.4 Tesla) [40]. The maximum writing field can be up to 10 kOe while the fringing field in LRM is about 5-6 kOe (private communication, M. Gubbins from Seagate).

The read head has an identical structure to that used in longitudinal recording. A tunnelling magnetoresistance (TMR) sensor is used which has a high permeability and is surrounded by two soft magnetic shields. A second CoFe layer is used as a pinned or reference layer which is deposited on an antiferromagnetic layer in order to pin the magnetisation. The other ferromagnetic layer acts as a free layer which can change the direction of its magnetisation depending on the stray field from the medium. When the head flies along the medium the stray field emanating from the transitions penetrates the TMR sensor. The orientation of magnetisation in the free layer rotates giving a change in the electrical resistance of the device. Fig.3.4 illustrates the perpendicular recording process.

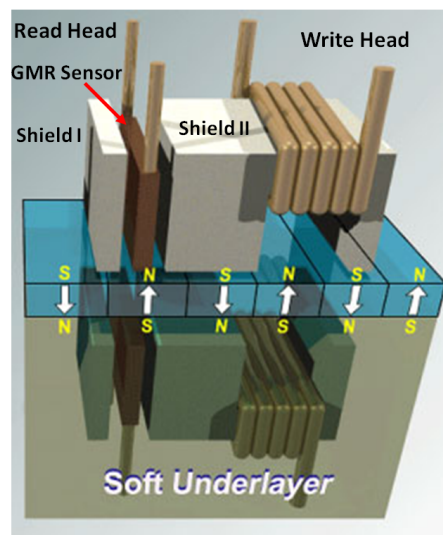


Figure 3.4: Schematic diagram of PRM with the read/write head [85]

## ii) Perpendicular Media Design

Perpendicular media design is based on double-layers used as a storage layer and a soft underlayer (SUL) [54], [95]. The structure of practical PRM has a range of functional layers which are tailored for specific functions. Fig.3.5 a) shows a schematic diagram of a whole structure compared to a cross-section TEM image of an advanced PRM medium. The substrate is usually a hard material, either an Al-Mg alloy coated with Ni-P to provide a smooth, hard surface or a glass ceramic substrate. An adhesion or interface layer made of Ta or a Ti alloy [96] is grown on top of the substrate with a thickness of 25-30 nm. This layer is used to improve the adhesion of all subsequent layers to the substrate. The soft underlayer is deposited on top of the adhesion layer. The SUL can generate noise in the medium [97] which decreases the signal to noise ratio of the medium. This issue of noise from SUL is resolved by pinning the magnetisation orientation along the surface [98] using a hard magnetic material or an antiferromagnetic pinning layer to fix the orientation of the SUL.

The intermediate or exchange break layer is deposited on top of the SUL with a thickness of  $\sim 25$  to 35 nm. The function of this layer is to prevent intergranular exchange coupling in the storage layer via the SUL and to improve the perpendicular  $c$ -axis growth of the recording layer. In order to grow the Co-alloy perpendicular to the film surface the intermediate layer has to have an fcc (111) or hcp (0002) texture. A thin seed layer may also be deposited under the intermediate layer in order to enhance the preferred growth texture. In the case of CoCrPt alloys Ru is used as the intermediate layer. Choe *et al.* [99] and Park *et al.* [100] showed a  $c$ -axis orientation dispersion  $\Delta\theta_{50}$  of  $3^\circ$  to  $4.5^\circ$  using X-ray diffraction rocking curves indicating the success of the preferred growth texture process.

---

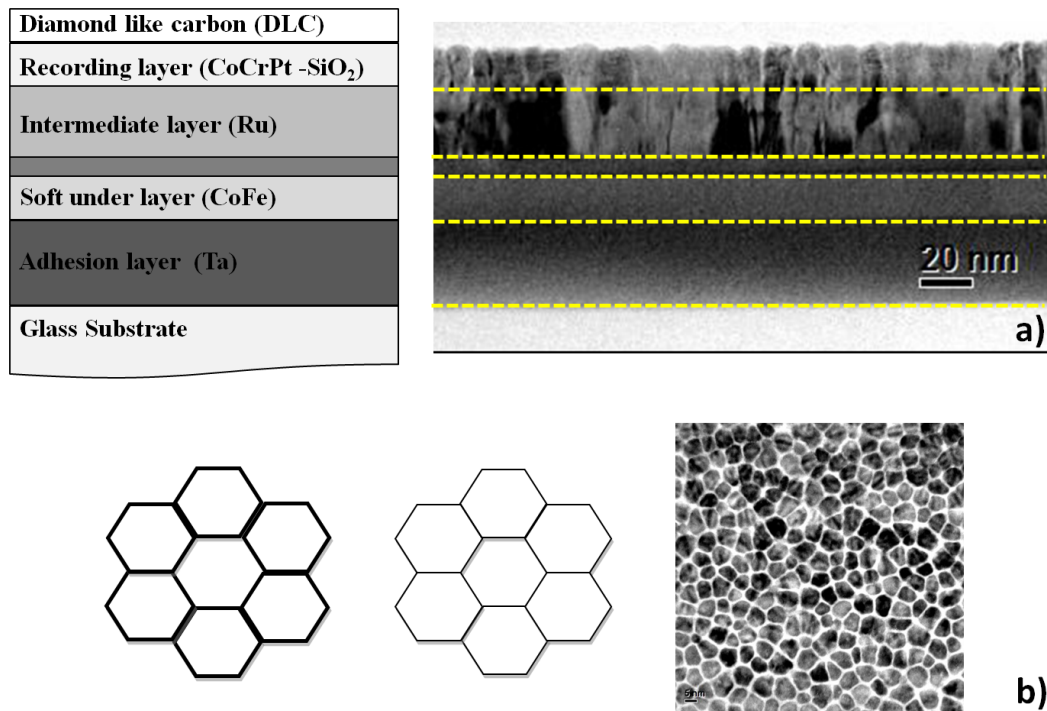


Figure 3.5: a) Schematic diagram of a typical layer structure and a cross-sectional image of a perpendicular recording medium b) Schematic diagram of the magnetic grains with different grain boundary widths compared to an in-plane TEM image.

The storage layer is the most significant layer in HDD. The composition of the layer has been investigated to give both thermal stability and high areal density. Co-Cr perpendicular films were first introduced as storage layer due to the presence of a large uniaxial anisotropy normal to the surface by Iwasaki *et al.* [4]. Cr was used to reduce the grain size and segregate the grains but it led to a decrease of the anisotropy. Optimised CoCr alloys with an additive element such as Ta, Pt, Nb [17], [18], [101] were developed to improve the performance of PRM such as a small grain size, narrow grain size distribution, narrow  $c$ -axis dispersion and exchange decoupling. CoCrPt co-sputtered with SiO<sub>2</sub> is currently used as perpendicular recording media. The function of the SiO<sub>2</sub> is to reduce the grain size and exchange decouple the grains as it is an insulator. Pt increases the anisotropy constant by stretching the  $c$ -axis of the Co alloy. Fig.3.5 b) shows a schematic of the structure with different grain boundary widths due to the effect of the SiO<sub>2</sub> content.

## 3.2 Alternative Perpendicular Recording Media

### 3.2.1 Coupled Granular Continuous Recording Media (CGC)

Conventional perpendicular recording media were introduced in order to overcome the strong demagnetising field. The areal density was increased beyond 300 Gbits/in<sup>2</sup> by reducing the grain size and increasing the magnetic anisotropy constant. PRM faced several problems such as the deviation of the easy axis orientation from perpendicular, the distribution of the anisotropy leading to a large transition width ( $a_o$ ), thermal stability and the signal to noise ratio (SNR).

However, the main problem is the degree of intergranular exchange coupling. This factor can improve the thermal stability via an increase in the activation volume of the medium but an excess of coupling leads to a deterioration of the SNR which is proportional to the number of grains in a bit. Therefore intergranular exchange coupling has to be optimised considering the thermal stability and SNR. Alternative perpendicular recording media were therefore proposed to further increase the areal density.

The first alternative PRM proposed by Sonobe *et al.* [11] was a combination of a perpendicular continuous layer and a small grain layer. It is known as **coupled granular continuous (CGC)** perpendicular recording media and can control intergranular exchange coupling. The design features of a CGC structure has a significant advantage by creating a strong pinning between the two layers as shown in fig.3.6 (top). Two types of continuous layers, which have less magnetic isolation, have been used [57]: The first was a multi-continuous layer of  $(\text{Co/Pd or Pt})_n$  and the other was a single thin layer called a *capped media or stacked media* which used CoCrPtB [102] as shown in fig.3.6 (bottom).

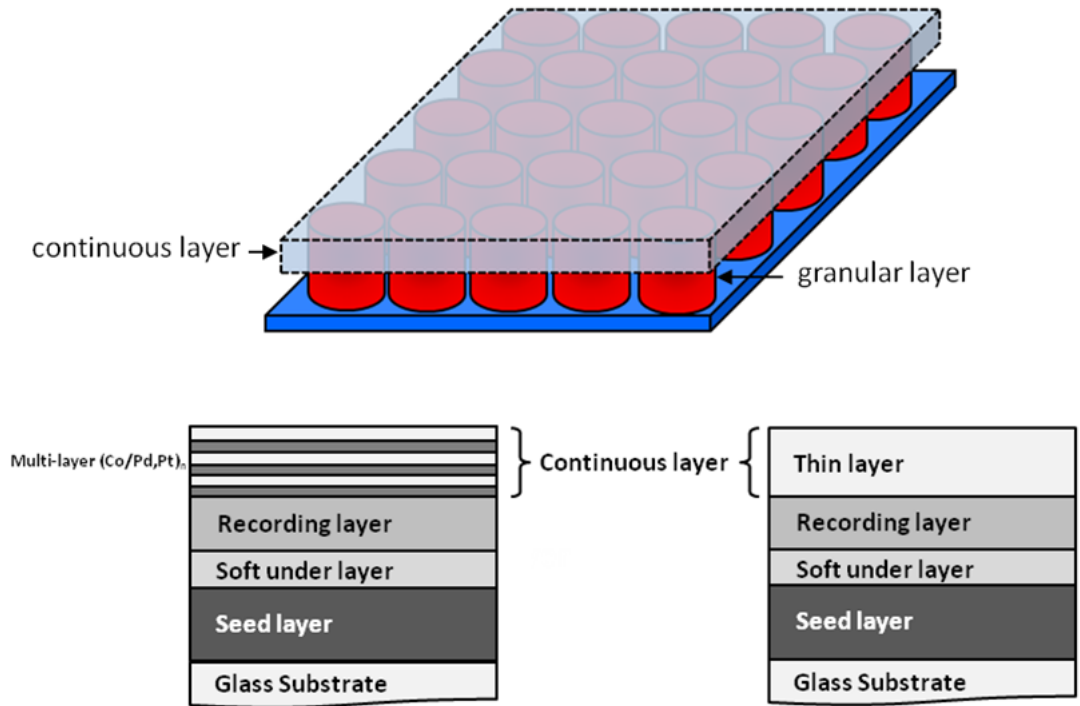


Figure 3.6: Schematic diagram of CGC media with a multi-layer and a thin continuous layer

The features of the CGC structure are designed to enhance the performance of the medium for high thermal stability and SNR. The granular layer has small grains which are well segregated to support a high areal density. They act as dense pinning centres for the domain walls that form in the continuous layer. Magnetisation reversal in the granular and recording layers cannot occur without domain wall nucleation in the continuous layer. Therefore the thermal stability of CGC media is greater than that in conventional PRM with decoupling between the grains. The interfacial exchange energy,  $E_{ex}$  for one cylindrical structure is [57]

$$E_{ex} = \frac{\pi D^2 A}{a} = \frac{M_S H_{ex} v}{2} \quad (3.3)$$

where,  $D$  is the grain diameter,  $A$  is the exchange stiffness,  $a$  is a lattice constant,  $H_{ex}$  is the exchange field and  $v$  is the grain volume. From eq.3.3 the exchange field can be rewritten as

$$H_{ex} = \frac{8\pi A}{a\delta M_S} \quad (3.4)$$

where  $\delta$  is the thickness of the granular layer. Sonobe *et al.* [57] calculated the value

of  $K_U V/k_B T$  as a function of the interlayer exchange interaction represented by the exchange field and for different values of the anisotropy constant. They found that when the value of  $K_U$  of the granular layer increases the required exchange field decreases as shown in fig.3.7. As a result a granular layer with  $K_U \sim 5 \times 10^6$  ergs/cc can be stable  $K_U V/k_B T \sim 60$  with a low exchange field of only 4 kOe. This shows that CGC media can reduce the switching field ( $H_S$ ), which is limited by the write field in conventional PRM, due to the continuous layer. It also improves the performance of recording media by reducing the transition width via the increase of the coercivity. It should be noted that  $a_o$  is simply expressed as

$$a_o = \frac{M_R \delta}{H_C} \quad (3.5)$$

where  $\delta$  is the thickness of medium. Several experiments have shown that the optimal thickness of a Co/Pd multi-layer can improve the performance of recording media by increasing the negative nucleation field ( $H_n$ ) and the squareness while decreasing the coercivity [60] [103] [104]. Tham *et al.* [105] also showed that CGC media can significantly improve SNR by depositing a Co/Pd multilayer onto a CoCrPt-SiO<sub>2</sub> storage layer via a domain-wall pinning effect and transition smoothing [106]. This is due to the interlayer exchange coupling between the two layers. Therefore CGC media is a suitable alternative PRM candidate for high areal density.

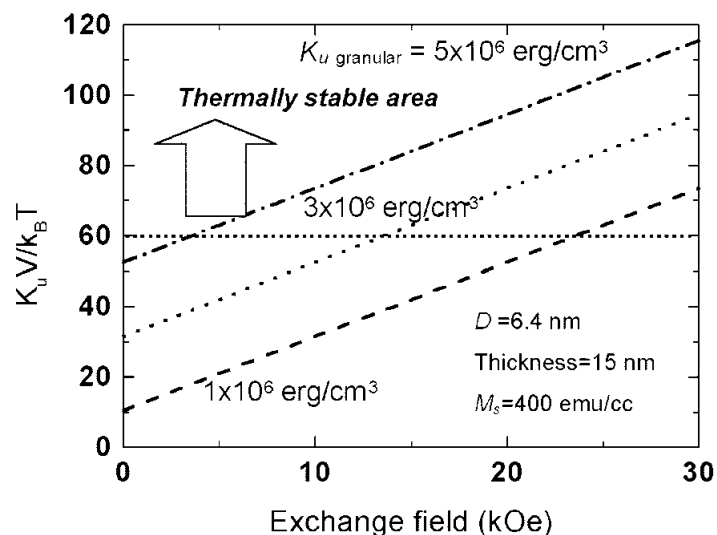


Figure 3.7: Dependence of  $K_U V/k_B T$  as a function of the interlayer exchange field for a CGC structure with various values of  $K_U$  [57]

### 3.2.2 Exchange Coupled Composite Media (ECC)

Conventional and CGC media achieved an areal density of 300-400 Gbits/in<sup>2</sup> by reducing the grain volume and increasing the anisotropy of the medium. However the switching field of the medium becomes very high and is difficult to switch. To address this problem there are two possibilities: the field from the write head can be increased or the switching field of medium can be reduced. The limitation of writability is due to the saturation magnetisation of the head material. The material used is Co<sub>40</sub>Fe<sub>60</sub> which has the highest  $M_S$  of any known material of 2.4 Tesla. Therefore the only strategy available to improve writability is a reduction in the switching field.

In 2003, Zou *et al.* [107] introduced a new design of perpendicular recording media known as *tilted media*. Tilted media were designed to have the easy axis orientation of the medium rotated at about 45° from the perpendicular. At this angle the switching field is reduced to 0.5 $H_K$  [15]. Figure 3.8 shows a comparison of the geometry of tilted and conventional PRM. Of course the intrinsic energy barrier of the grains is unaltered so that the thermal stability of the stored data is not affected.

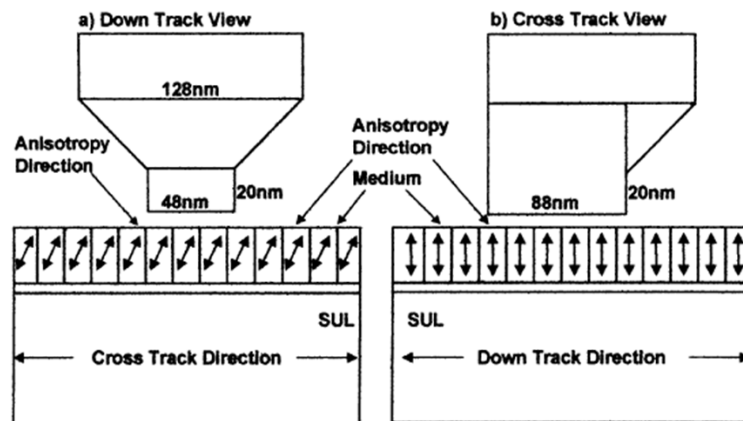


Figure 3.8: Schematic diagram of the geometry of tilted and conventional PRM [108]

The thermal stability of the medium can be represented by the ratio of the energy barrier  $\Delta E$  to the switching field,  $H_S$

$$\xi = \frac{2\Delta E}{H_S \cdot M_S \cdot V} \quad (3.6)$$

For tilted media the ratio  $\xi$  can be increased by a factor of 2 which doubles the thermal stability. Therefore a high anisotropy material can be used which allows a grain

size reduction. The difficulty with tilted media is the fabrication of a film with tilted easy axes [109]. Hence other media designs were proposed.

The other well-known alternative recording media are exchange coupled composite (ECC) media proposed by Suess *et al.* [13] and Victora and Shen [12] [48] in 2005. ECC media consists of two coupled layers of a magnetically soft and a hard material. The hard layer acts as the storage layer and has a high anisotropy to enhance the thermal stability for small grain sizes. The soft layer is used as the switching layer. The reversal process occurs when the soft layer is reversed by the applied field. This leads to reversal of the hard layer due to the exchange coupling between the two layers. The hard layer will reverse coherently with the soft layer following Stoner-Wohlfarth theory [15]. The switching mechanism of ECC media is shown in fig.3.9.

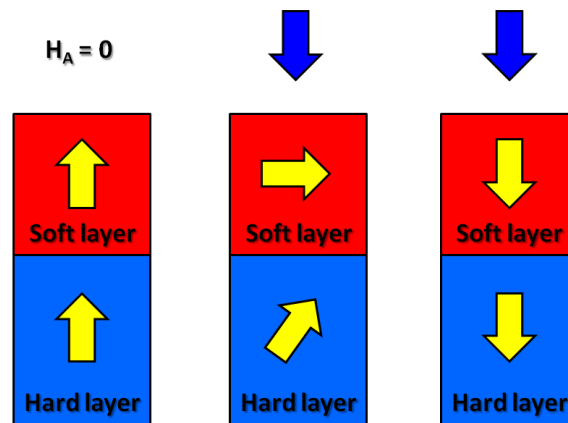


Figure 3.9: Schematic diagram of the switching process of ECC media [12]

The performance of ECC media can be examined via the ratio of the energy barrier and the switching field  $\xi$  given in equation 3.6. Victora and Shen [12] simulated and optimised the factors controlling the performance of ECC media using the Landau-Lifshitz-Gilbert (LLG) equation. The highest value of  $\xi$  obtainable is close to 2. In 2005, Wang *et al.* [110] produced the first experimental work on ECC media with a  $(\text{Co-PdSiO})_n$  hard layer and FeSiO as the soft layer. The writing efficiency and thermal stability were dramatically improved compared with conventional PRM. Therefore, ECC media has been adopted for the next generation of PRM due to its ease of fabrication compared to tilted media.

### 3.2.3 ECC and CGC Media

A new composite media design was introduced by Nolan *et al.* [14] in 2011. The new media combines the ECC and CGC structures where the ECC structure has a high degree of SiO<sub>2</sub> segregation to provide almost perfect intergranular exchange decoupling. The continuous layer grown on top is very thin and the grains have high exchange coupling forming an *ECC/CGC* medium. To achieve high performance from the new media the complex interactions and other parameters must be controlled and optimised. The variables include the lateral exchange coupling ( $H_{ex}$ ), the crystalline anisotropy  $H_K$  and the interlayer exchange coupling ( $J$ ). These parameters were taken into account in the simulations using the Landau-Lifshitz-Gilbert (LLG) equation.

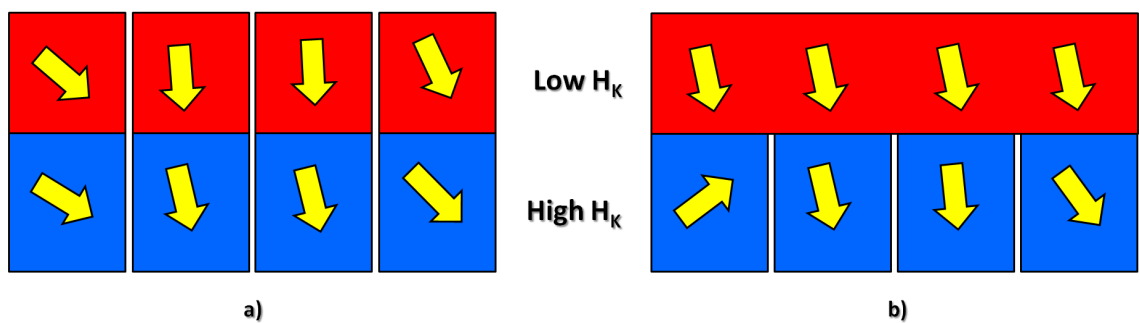


Figure 3.10: Schematic diagram of spin moments in a) ECC media and b) ECC/CGC media [14]

From the optimisation of the parameters, ECC/CGC media can produce a reduction in the coercivity. It also decreases the switching field distribution as is evident from the hysteresis loop shearing. Figures 3.10 a) and b) show a schematic diagram of the mechanism of the layer moments in ECC media and ECC/CGC media respectively. The ECC structure reduces the overall coercivity of the film because the moments of grains in the soft layer provide a torque to help switch the grains in the recording layer. The disadvantage of this structure is that it can lead to a reduction of the loop squareness and a broadening of the SFD if the grains are well exchange decoupled. This places an increased requirement on the uniformity of the grain size and the value of the anisotropy constant. It also makes a requirement that the grain orientation must be highly perpendicular to avoid a wide switching field distribution which will broaden

written transitions.

The CGC layer on top of the ECC structure acts as a *head-on* magnetisation [14] due to the strong coupling shown in fig.3.10 b). When a torque from the CGC layer passes through the hard layer the magnetisation of both layers rotates in unison. From calculations of the M-H loops of ECC and ECC/CGC media using the LLG equation [14], the coercivity can be reduced by about 15% and the SFD is also improved and the slope at the coercivity is increased compared with the ECC sample. Therefore the thermal stability and the squareness can be improved for the new composite media design.

### 3.3 Future Recording Media

#### 3.3.1 Bit Patterned Media

For conventional PRM it is predicted that the maximum areal density will be limited to about 1 Tbit/in<sup>2</sup> [87]. In order to achieve densities greater than this, new media architectures are required such as bit patterned media (BPM), heat assisted magnetic recording (HAMR) media, or microwave assisted magnetic recording (MAMR) media.

A patterned recording medium is one of the new media designs used to extend the limitation of thermal loss using nanofabrication. The fabrication is based on a lithographic process. Patterned media can be divided into three categories depending on the geometry of medium such as *patterned servo marks*, *discrete track media* (DTM) and *bit patterned media* (BPM) [9]. Patterned servo was the first generation of patterned recording media. It provided distinct data tracks in order to support the writing process from the head. The disadvantage of this type of media is the time consuming and expensive fabrication process. DTM and BPM are suitable for future HDD storage. DTM is based on continuous granular films which are lithographically patterned into tracks with a non-magnetic material or a gap as segregation [10]. DTM can easily achieve a density of up to a few Tbits/in<sup>2</sup> but not more than 10 Tbits/in<sup>2</sup> [111]. BPM can possibly provide an areal density of up to 10 Tbits/in<sup>2</sup> due to the dot size which gives a single domain state.

The magnetic medium is patterned into discrete magnetic islands or dots separated by a nonmagnetic material or empty gaps [10]. Each dot is a single domain state in which one bit can store information as either *spin up* (1) or *spin down* (0) shown schematically

in figure 3.11 a). If the typical bit pitch is patterned down to  $25 \times 25 \text{ nm}^2$ ,  $11 \times 11 \text{ nm}^2$  and  $7.9 \times 7.9 \text{ nm}^2$ , the density of BPM can be increased to 1, 5 and 10 Tbits/in<sup>2</sup> respectively.

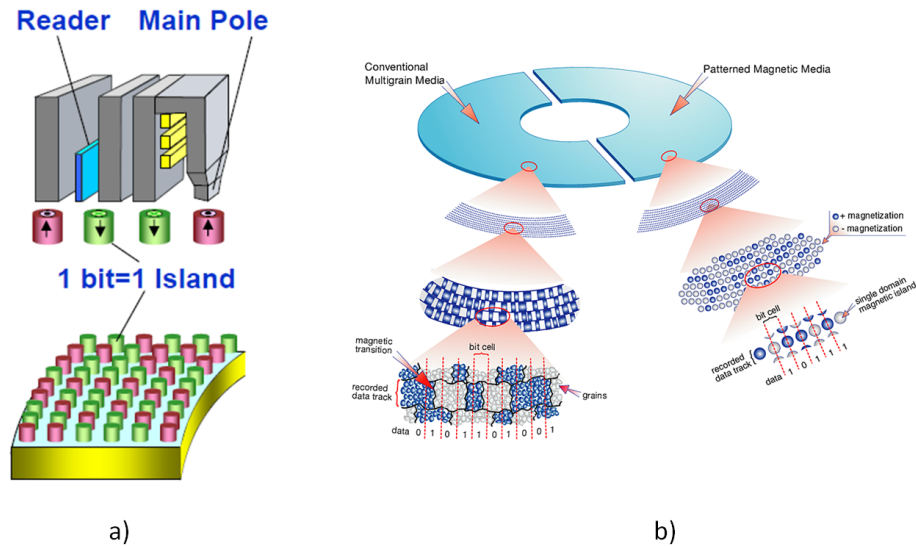


Figure 3.11: Schematic diagram of a) bit patterned media with nano-islands and b) comparison of media structure between conventional PRM and BPM [7].

BPM can in principle increase the areal density beyond 1 Tbit/in<sup>2</sup> but it faces several problems particularly the variation in the magnetic properties. Kamata *et al.* [111] reported a distribution of the coercivity of a CoCrPt bit patterned medium from 0.5 to 6 kOe. Moreover the distribution of easy axis orientation was also about  $15^\circ$  from dot by dot measured using X-ray rocking curves. A correlation between the bit size and  $H_C$  did not occur because the distribution of bit sizes was less than 0.5% [112]. Therefore one of the main reasons leading to the variation of the coercivity and wide distribution is the strong long-range magnetic dipole interaction between the bits [113].

The signal to noise ratio (SNR) in BPM is also a problem. SNR will increase when the number of grains in a single bit is increased by reducing the grain size. A single bit of conventional PRM is formed by 10 to 20 grains. The noise is reduced by averaging over the grains across the transition width. In the case of BPM the number of grains forming a transition is one. A comparison of a bit for conventional media and BPM is shown in fig.3.11 b). Therefore the noise source in BPM comes from the writing process and the shape of the pillar. In BPM write synchronization is required with the individual bit under the write head [10]. The strong head field gradient can reverse neighboring bits

leading to write errors. The critical problem for BPM technology is the time consuming fabrication and mass-production process.

### 3.3.2 Heat Assisted Magnetic Recording (HAMR)

Heat-assisted magnetic recording (HAMR) media [8] is a new technology proposed in 2006 to overcome the limitation of the trilemma effect in conventional recording media and extend areal densities beyond 10 Tbits/in<sup>2</sup>. The key factor to achieve a high density is the reduction of medium grain size to about 3-5 nm for FePt media [114], [115] with a narrow grain size distribution. The anisotropy constant of the media must be increased in order to maintain thermal stability. The write field in conventional PRM is limited but in HAMR it is overcome by the addition of thermal energy.

The fundamental write process of HAMR uses the extra thermal energy to heat small spots on the medium to change their magnetic properties. When a ferromagnetic material is heated close to its Curie temperature  $T_C$ , the intrinsic properties  $M_S$ ,  $K_U$  and  $H_C$  will drop to zero. Figure 3.12 a) shows the HAMR write process with the coercivity dependence on temperature [8]. The coercivity of the medium at room temperature is very high due to the high value of  $K_U$ . As the medium is heated the coercivity becomes lower than the write field of the head. This allows the magnetisation to reverse along the direction of the head field. The temperature is rapidly cooled back to the storage region where the coercivity is again very large.

Figure 3.12 b) shows the components of a HAMR system consisting of the heat source, write/read head and the medium. The heat source is a laser diode which can provide heat up to about 750 K for an FePt medium [116]. A near field optical transducer is used to produce a small laser spot on the nanoscale. For HAMR media a composite structure is required with a small grain size and the highest magnetocrystalline anisotropy possible. Due to the heating effect,  $\text{SmCo}_5$ ,  $\text{Nd}_2\text{Fe}_{14}\text{B}$  and FePt which have uniaxial anisotropy constants of about  $20 \times 10^7$ ,  $4.6 \times 10^7$  and  $7 \times 10^7$  ergs/cc respectively are potential materials providing coercivities of up to 5 Tesla [8], [114]. FePt has been extensively studied for HAMR media due to the extremely small grain size of about 3 nm that can be produced [117], [118]. However, FePt must be annealed at very high temperatures above 600 C° in order to produce the high anisotropy  $L1_0$  structure. This is not favourable for a fabrication process. There are several reports of attempts to reduce the annealing temperature by doping with Ag, Cu and C or using NiTa seed

layers [114].

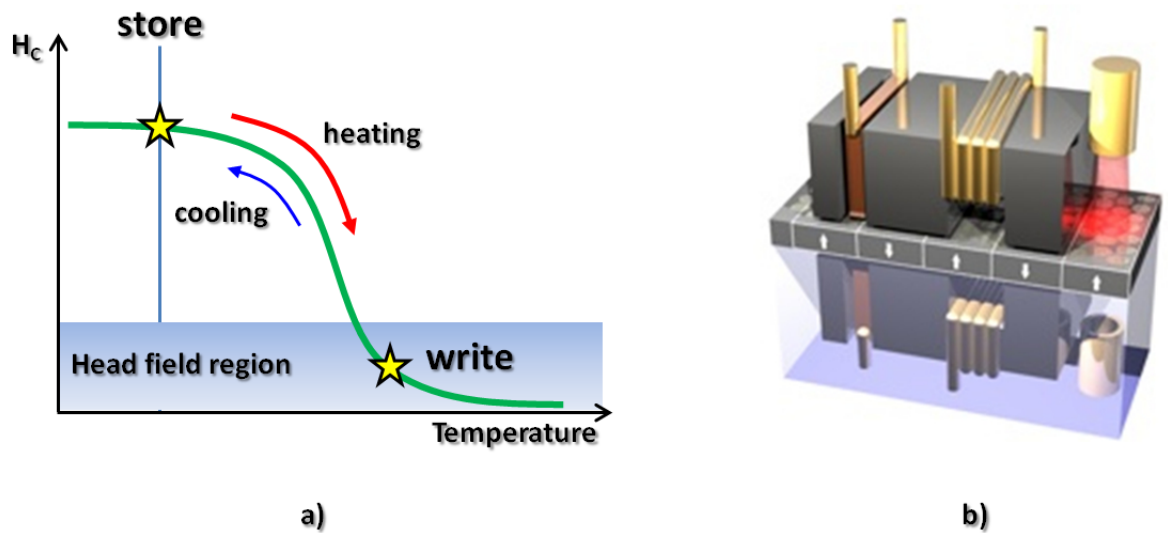


Figure 3.12: Schematic diagram of a) the HAMR write process with the relationship between  $H_C$  and  $T$  [8] and b) a HAMR system with laser, write/read head and medium [119].

Seagate recently achieved a 1 Tbit/in<sup>2</sup> HAMR demonstration [120], [121]. This technology is still limited due to the thermal effect from the writing process inducing a high bit error rate (BER) [42]. This is due to the randomisation of the magnetisation at the writing temperature. The switching field distribution and thermal spot size [120] are also limiting factors. When the medium is heated to around the Curie temperature the ratio between the applied field and the switching field will be infinite due to the reduction of the anisotropy constant to zero which causes the variation of the switching field. Therefore HAMR is a desirable technology to extend the areal density beyond 5 Tbits/in<sup>2</sup> [120] but much more development is required.

### 3.3.3 Microwave Assisted Magnetic Recording (MAMR)

Another strategy for high density recording is *microwave assisted magnetic recording* (MAMR) recently proposed by Zhu and co-workers [122]. The key idea in MAMR is an additional microwave generator in the write head to help the writability. The write head can reverse the magnetisation even though its field may be lower than the coercivity.

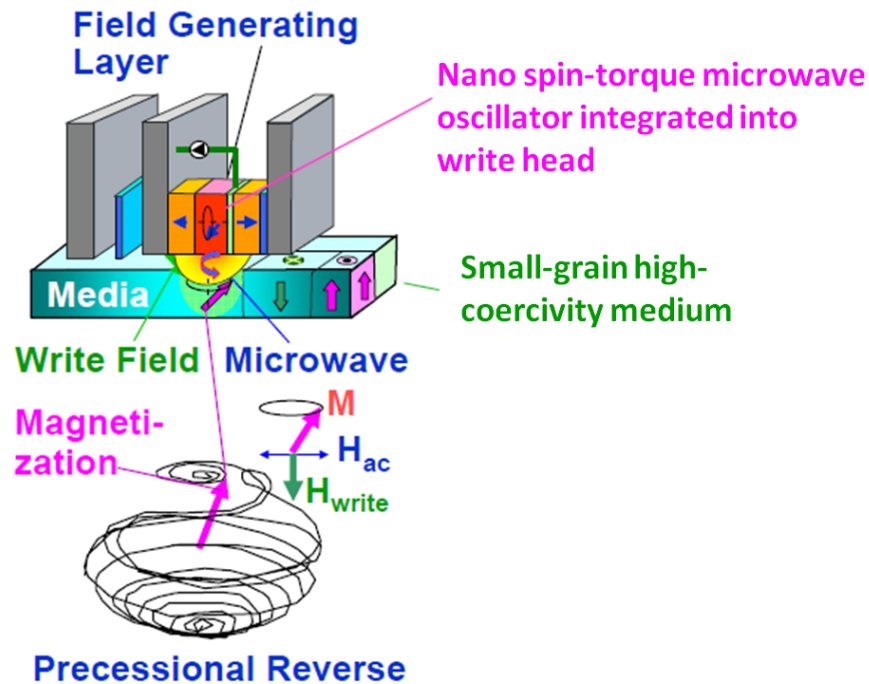


Figure 3.13: Schematic diagram of microwave assisted magnetic recording [123].

The physics behind MAMR is the use of a microwave alternating field,  $H_{ac}$ . Figure 3.13 shows a schematic diagram of the MAMR system [123]. The magnetisation is stored in a medium with a very small grain size and strong anisotropy similar to a HAMR medium. In order to write the data the write field which is lower than  $H_S$ , is applied along the easy direction. At the same time  $H_{ac}$  is applied along an orthogonal direction in order to initiate a precessional motion of the magnetisation. The switching field is possibly reduced by a factor of 3 or 4 [123]. It depends on the magnitude of  $H_{ac}$  which is a few kOe at a frequency of a few tens of GHz [124]. As shown in fig.3.13(bottom), the magnetisation initially absorbs the microwave energy and starts a precessional motion around the easy axis due to the torque from the ac field. The precession will increase when the ac frequency matches the resonant frequency of the moment of the grain [122]. This leads to the reversal of the magnetisation. MAMR in theory can achieve an areal density of a few Tbits/in<sup>2</sup> but not greater than 10 Tbits/in<sup>2</sup>. MAMR may possibly be applicable beyond 10 Tbits/in<sup>2</sup> using a combination with BMP technology. However, HAMR/BPM recording may achieve similar values.

---

## CHAPTER IV

### Experimental Techniques

#### 4.1 Magnetic Characterisations

Magnetic characterisation is the most important measurement used to improve the performance of advanced recording media. A magnetic thin film can be characterised not only in term of the basic properties, i.e. the values of the saturation magnetisation ( $M_S$ ), coercivity ( $H_C$ ) and remanent magnetisation ( $M_R$ ) which are derived from the magnetisation curve, but also their variation with temperature, the angle of the field to the easy axis and their time dependence. This has led to the proposal of alternative technologies for perpendicular recording media.

There are several techniques used to study magnetisation reversal in thin films. These can be separated into three categories: the first category are methods that are based on force techniques e.g. the alternating gradient force magnetometer (AGFM) and Magnetic Force Microscopy (MFM). In the second category are measurements based on induction by a changing flux e.g. SQUID magnetometers, BH hysteresis loop tracers, AC susceptibility and the vibrating sample magnetometer (VSM). The third group is based on measuring changes in material properties such as the Hall effect magnetometer and magneto-optic methods.

In this section the background, principles and functionality of magnetic characterisation techniques such as the VSM, magneto-optic Kerr effect (MOKE) and angular dependent MOKE techniques, which are those that have been used this study, are described in detail.

##### 4.1.1 The Vibrating Sample Magnetometer

The most common magnetic characterisation technique is the vibrating sample magnetometer (VSM) which was originally developed by Foner in 1950 [125]. The VSM has become the most common instrument for the measurement of the magnetic properties

---

of a wide range of materials. Figure 4.1 shows a schematic diagram of a VSM consisting of a vibration unit, pick-up coils, electromagnet, reference magnet, a Hall probe, lock-in amplifier and computer controller.

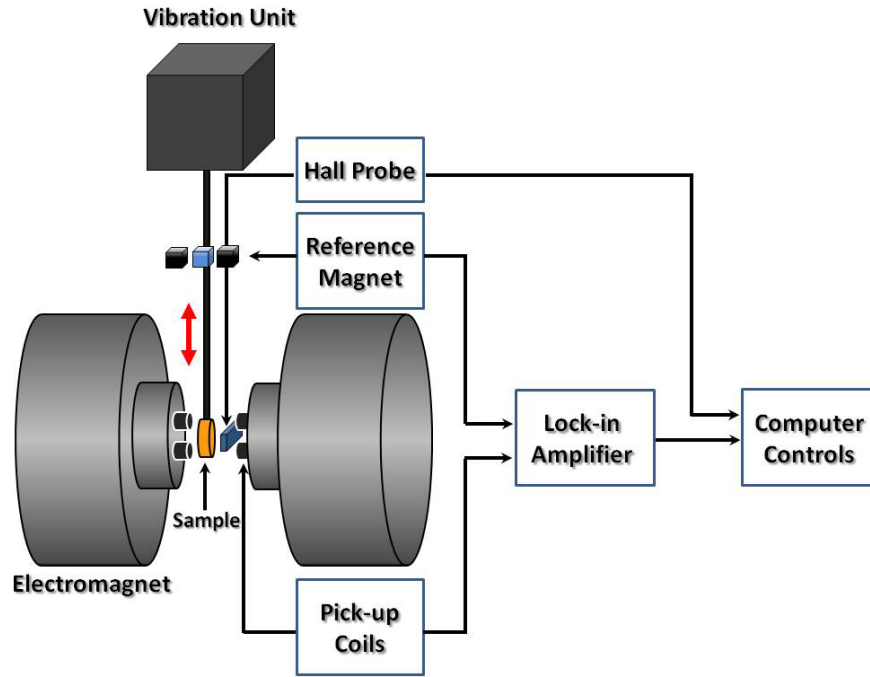


Figure 4.1: Schematic diagram of the vibrating sample magnetometer

This magnetometer is based on the principle of Faraday's law. The electromagnetic induction is shown in equation 4.1.

$$\epsilon = -N \frac{d\phi_m}{dt}, \quad (4.1)$$

where  $\epsilon$  is the induced voltage,  $\phi_m$  is the magnetic flux from the sample into the coils and  $N$  is the number of turns in the coils. The functionality of the VSM is based on the measurement of the magnetic flux changing while the sample is vibrated within a uniform magnetic field,  $H$  generated by an electromagnet. The total magnetic flux across the sample is created by the magnetic field,  $H$  and the magnetisation ( $M$ ) of the sample as shown in eq. 4.2.

$$\phi_m = B_m \cdot A = (H + M) \cdot A, \quad (4.2)$$

where  $B_m$  is the magnetic flux density in the magnetic material. As the sample is moved away from the coil by the vibrator it induces an electromotive force (*e.m.f.*) according to

Faraday's law whose magnitude is proportional to the magnetic moment of the sample

$$\int \epsilon \cdot dt = -NA \cdot M \quad (4.3)$$

The induced ac voltage is fed into a lock-in amplifier whose output is a dc signal with a magnitude proportional to the moment of the sample.

In order to obtain an accurate value of the moment of the sample a calibration is required. Pd is commonly used as a standard calibration due to its linear and large magnetic susceptibility [126]. An ADE Model 10 vibrating sample magnetometer with an applied field of up to 3.1 Tesla and a noise base of  $10^{-6}$  emu was used in this project. The hysteresis loop for each sample was measured using square samples of 5 mm<sup>2</sup> and thickness 15 nm.

The magnetic moment from the VSM is obtained after correction for the moment from the sample rod and holder by subtracting the gradient from data at high field where the film is assumed to be saturated. The typical magnetic moment obtained is about  $2.5 \times 10^{-5}$  emu.

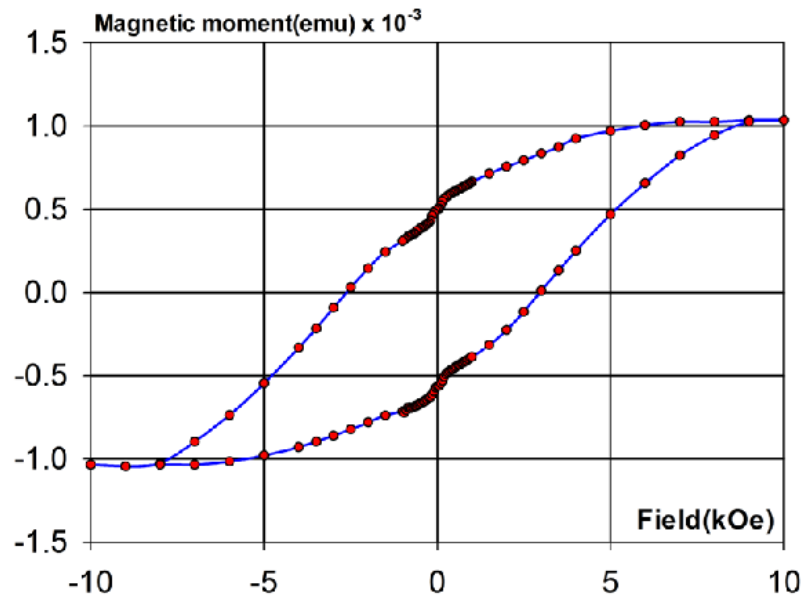


Figure 4.2: The magnetisation curve for an ECC/CGC thin film

Perpendicular media have a complex structure with a soft under layer (SUL) and storage multi-layer as shown schematically in fig.4.33 in section 4.3.4 The magnetic moment from each layer can be distinguished by a different state of magnetisation reversal

which is seen in the magnetisation curve. A typical magnetisation curve of an ECC/CGC sample is shown in fig.4.2 with three regions of magnetisation reversal. The details of the results from VSM measurements will be described in section 5.2.

#### 4.1.2 Magneto-Optical Kerr Effect(MOKE)

The magneto-optic Kerr effect (MOKE) is one of the magnetic characterisation techniques widely applied for the measurement of magnetic thin films due to the inexpensive apparatus, experimental simplicity and its sensitivity. The MOKE can be in one of three geometries; polar, longitudinal, and transverse, depending on the direction of the plane of polarisation of the incident light.

For advanced perpendicular recording media polar MOKE is mainly used to characterise the magnetisation reversal [28, 127–130]. MOKE is the study of the rotation of the reflected polarized light from a magnetised material. The polarized light is rotated away from the plane of the incident polarisation leading to elliptic polarisation. The degree of rotation is directly proportional to the magnetisation ( $M$ ) of the material. Therefore, magnetisation curves or hysteresis loops can be measured as a function of the applied field. Fig.4.3 shows a schematic of the principle of MOKE where the electric field vector of the incident laser light is rotated after reflection from a magnetised sample.

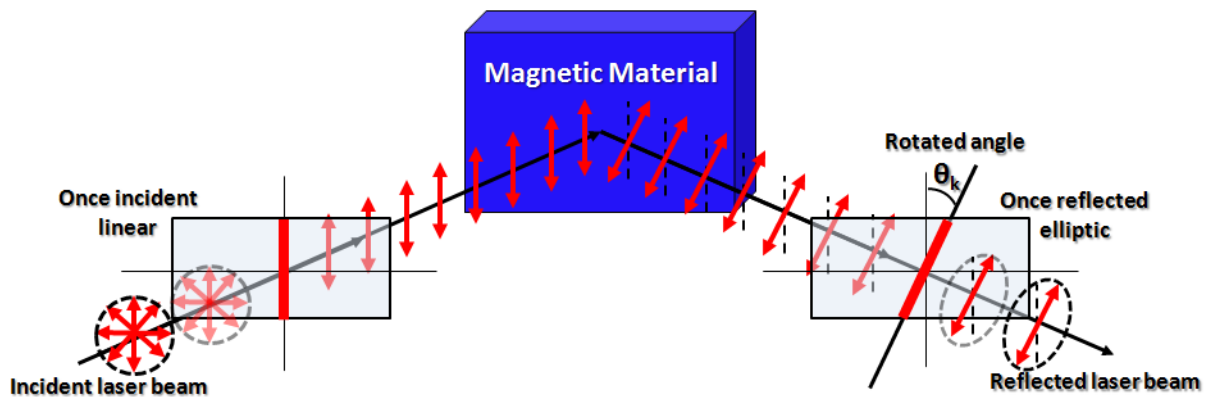


Figure 4.3: Schematic of MOKE effect

The Kerr effect was discovered by John Kerr in 1877 [131] [132]. This fundamental principle was originally developed by Faraday who discovered the magneto-optic effect from the relation between light and electricity [133] [134]. Kerr's experiment was based on the observation of the polarization of incident light reflected from a horseshoe electromagnet [131] [132].

MOKE can be described by either microscopic quantum theory or macroscopic dielectric theory. A full description and derivation of both microscopic and macroscopic theory can be found in articles by Qiu *et.al* and Weinberger [135] [136]. For the microscopic description of the magneto-optic effect, the classical motion of electrons in a medium interacting with the electric field of a light wave is considered. Circularly polarised light interacts with the external magnetic field via the electrical field of the light which generates motion of the electrons. The left and right circularly polarized electric field moves the charged particles into left and right circular motion respectively. The additional Lorentz force acting on each electron causes a circular motion of electrons. One of the motions will be slower than the other leading to a difference between the radius of motion for left and right polarised electrons. This motion will change the dynamics of the interaction for the circularly polarised light. For linearly polarized light, the field causes a rotation of the incident polarisation. For a ferromagnetic medium a strong magneto-optic effect will be observed due to the exchange interaction between the electrons. The effective field arises due to the spin-orbit interaction. A full derivation and calculation of the magneto-optic effect in a ferromagnet is given by Argyres [137].

The macroscopic theory is based on an analysis of the dielectric properties of a medium. Linearly polarised light can be described as a superposition of two circularly polarized components. When the circularly polarized light propagates into a magnetised medium there are two mechanisms which describe the magneto-optic effect. Firstly, the rotation of the plane of polarisation, i.e. the Kerr rotation,  $\theta_K$  occurs due to the different propagation velocities of left-right circularly polarised light leading to a phase shift as described in the classical motion of electron. Secondly, the elliptic angle  $\epsilon_K$  varies due to the different absorption rates of the medium affecting the left-right circularly polarisation. The Kerr rotation and ellipticity can be determined from the the antisymmetric off-diagonal element in the dielectric tensor of the medium [135].  $\theta_K$  and  $\epsilon_K$  give the real and imaginary parts of the solution.

#### 4.1.2.1 Geometry of the MOKE Experiment

The geometry of MOKE experiments is very important for magnetic measurements of recording media. However all advanced recording media have strong perpendicular anisotropy so only the polar configuration needs to be considered. The configurations between the direction of the plane incidence beam and the magnetisation orientation in a medium with respect to the magnetic field provide the geometry of the polar MOKE measurement. Fig.4.4 shows a schematic diagram of the polar mode. For polar MOKE the magnetisation is parallel to the plane of the incident beam and normal to the film surface as shown in fig.4.4.

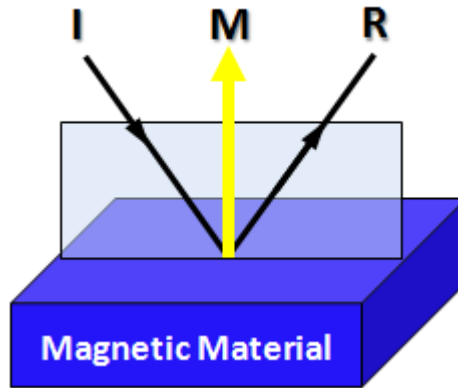


Figure 4.4: Schematic diagram of polar MOKE

In this work, composite perpendicular recording media with perpendicular anisotropy were studied. All recording layers are based on CoCrPt alloys deposited on 2.5" glass discs. A soft magnetic underlayer (SUL) is required to enable the writing of data. Due to the perpendicular anisotropy and the presence of the SUL, the magnetic characterisation can not be obtained by conventional magnetometry due to the large signal from the SUL which is 3 times larger than that from the recording layer. Hence polar MOKE was employed for the characterisation of all media [28]. MOKE will detect the change in polarisation only in the surface of the film as far as the skin depth  $\delta$  in the material. The skin depth is that to which the electromagnetic wave penetrates the material before falling to  $1/e$  ( $\sim 37\%$ ) of its initial value and is inversely proportional to the square root of the the frequency of the light and the conductivity of the material.

$$\delta = \sqrt{\frac{2}{\omega\mu \cdot \sigma}} \quad (4.4)$$

where,  $\sigma$  is conductivity of the the material,  $\omega$  is angular frequency and  $\mu$  is a magnetic permeability of the material. For most metals, HeNe laser light can penetrate between 10 and 20 nm [135]. This is approximately the thickness of the recording layer, which is between 12 and 16 nm for all samples. The MOKE signal from multilayered structures can be treated as an equivalent single magnetic layer as shown by Atkinson [138].

Fig.4.5 shows a comparison of the magnetisation curves of the same ECC/CGC medium using a VSM and polar MOKE. The results for the MOKE technique show the correct hysteresis loop from the actual recording layer whereas the VSM result shows the magnetisation of the recording layer and the SUL. The VSM result shows a significant reduction in the coercivity  $H_C$  and the squareness  $M_R/M_S$ . Therefore polar MOKE is the only suitable method for the characterisation of advanced perpendicular recording media [28].

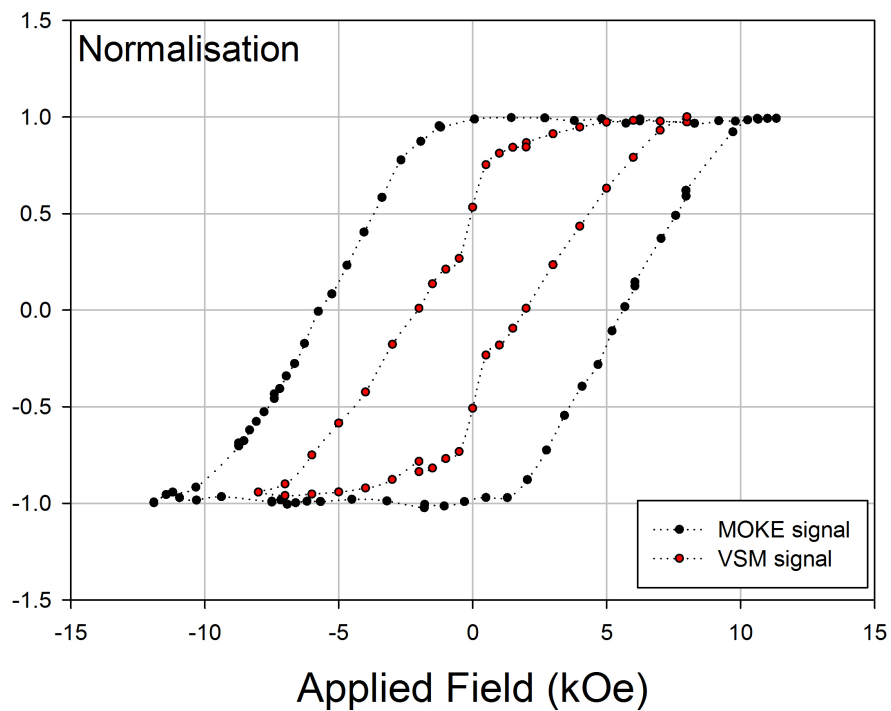


Figure 4.5: Hysteresis loop for ECC/CGC media from MOKE (black dots) and VSM (red dots)

The magnetic characterisation of all samples studied in this work has been undertaken using a polar MOKE originally built by Dutson [139]. Fig.4.6 shows a schematic diagram of the MOKE used. A Melles Griot stabilized HeNe laser (model 05-STP-901) was used due to the reduction of the drift and noise from the laser signal. This HeNe laser has a wavelength of 632.8 nm and a stability of  $< 0.04\%$  over 600 seconds which is suitable for the measurement of remanence curves and time dependence described in section 4.2.2 and 4.2.4. The laser beam passes through a Glan-Thompson polariser (GTH10M-A with 350-750 nm). The p-polarised ray is totally refracted and only the s-polarized ray will be transmitted through the non-polarising dielectric cube beam splitter. This reduces the incident intensity of the laser by 50 %. This improves the stability of the laser without changing the polarisation. For polar MOKE measurements the beam must pass through a hole in one pole-piece of the magnet. The sample is located between the magnet pole-pieces which can produce a maximum applied field of 12 kOe. The beam is reflected back through the hole to the analyser and photodiode detector. The signal from the detector is fed to a data acquisition (DAQ) system written using National Instruments LabView<sup>TM</sup> Virtual Instrument software to obtain the Kerr rotation amplitude (V).

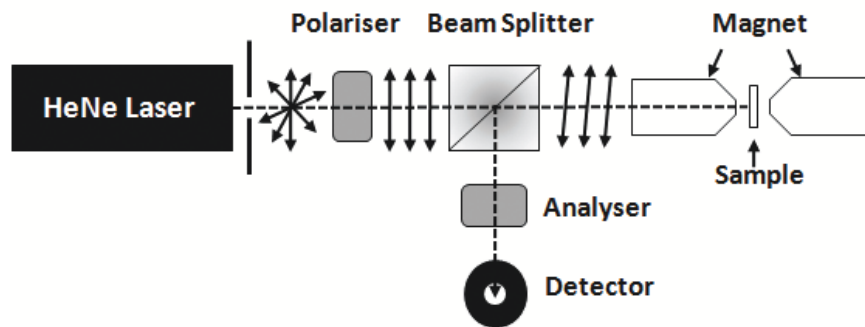


Figure 4.6: Schematic of the MOKE setup

Figure 4.7 shows a photograph of the polar MOKE system used to measure the magnetisation curve and time dependence in this work. The HeNe laser is located on the left hand side due to space limitation. The laser first passes through an aperture to remove stray light from the laser. A mirror is used to deflect the laser through  $90^\circ$ . The laser passes through a Glan-Thompson polariser and the beam splitter to polarise the s-plane rays and improve the stability of the laser. The Bell-Gauss meter (model 5080) is located between the pole-pieces to measure the applied field during measurements.

Finally, the reflected beam from the sample is returned back through the analyser to the photodiode detector. The device is located in a dark room to avoid stray light affecting the measurements.

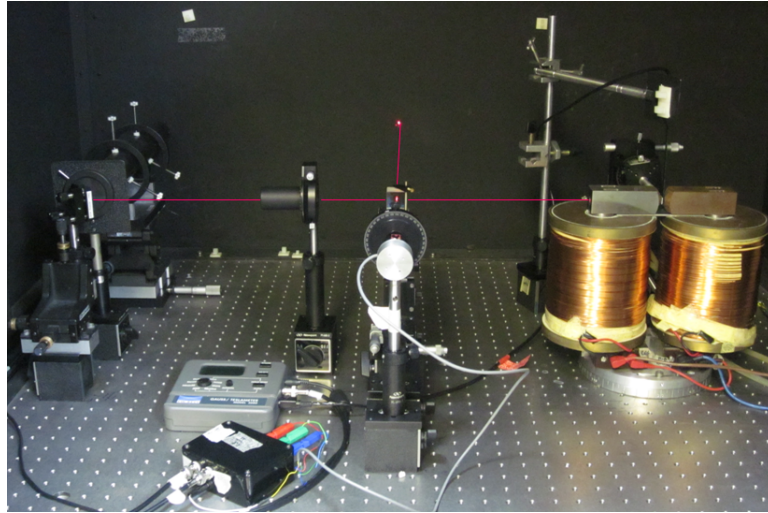


Figure 4.7: The polar magneto-optic Kerr effect magnetometer

### 4.1.3 Angular Dependent MOKE

New composite perpendicular recording media such as granular media and exchange coupled composite (ECC) media are designed in order to provide high thermal stability and small grain size. Therefore, the mechanism of their magnetisation reversal is required. In order to gain a deeper understanding of the magnetisation reversal mechanisms, one of the important measurements is the angular dependent behaviour. These have been studied theoretically and experimentally to investigate the distribution of easy axis orientation of the thin films [140–147]. This is one of the crucial factors dominating the switching field distribution.

Measurements of magnetisation curves with different angles ( $\theta$ ) between the applied field and the film normal surface is required. Simple polar MOKE is not suitable for the angular dependent measurement because the magnetic pole and sample holder are fixed. In order to achieve the angular dependent measurement, two critical factors need to be considered: firstly, the sample must be normal to the plane of the incident laser. Secondly, a variation of the angle between the applied field and the film plane is required.

An angular dependent polar-MOKE system was proposed by Hasegawa *et.al* [148] to determine  $H_{cr}$  as a function of angle. Figure 4.8 shows a schematic diagram of the optics of the system [148]. The principle of angular dependent MOKE is similar to the simple polar MOKE using a polariser and analyser to detect the Kerr rotation signal. The key component of this system is the rotation stage. This uses a fibre optic mounted on the rotation stage so the laser beam is always at  $90^\circ$  to the sample as shown in fig.4.9. The inset shows an enlarged view of the reflected light on the sample. Therefore, the Kerr signal component of magnetisation of the media is independent of the angle  $\theta$ .

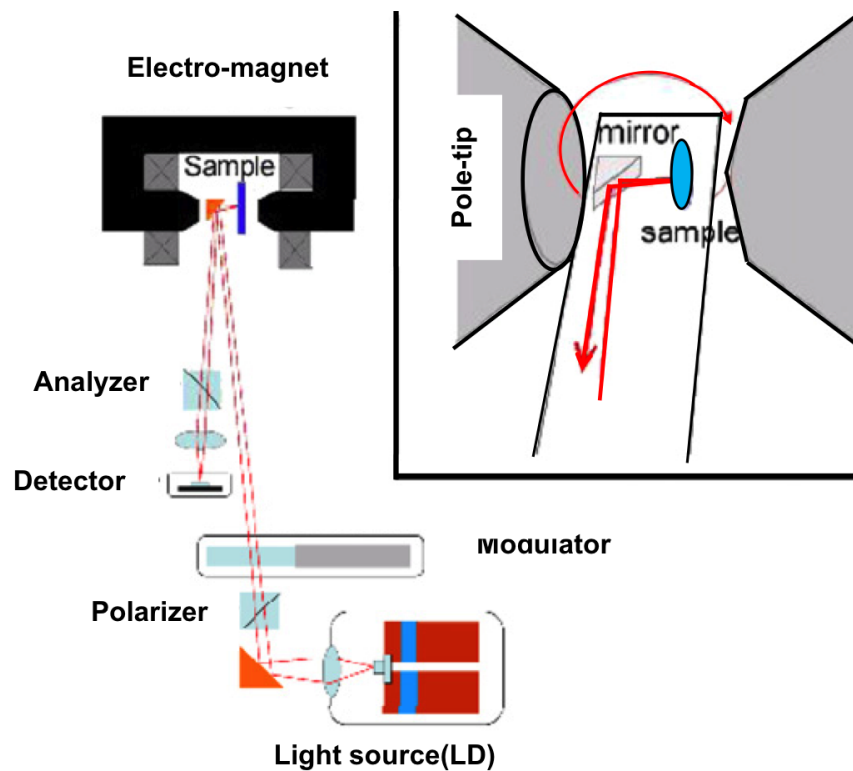


Figure 4.8: Schematic diagram of the MOKE system [148]

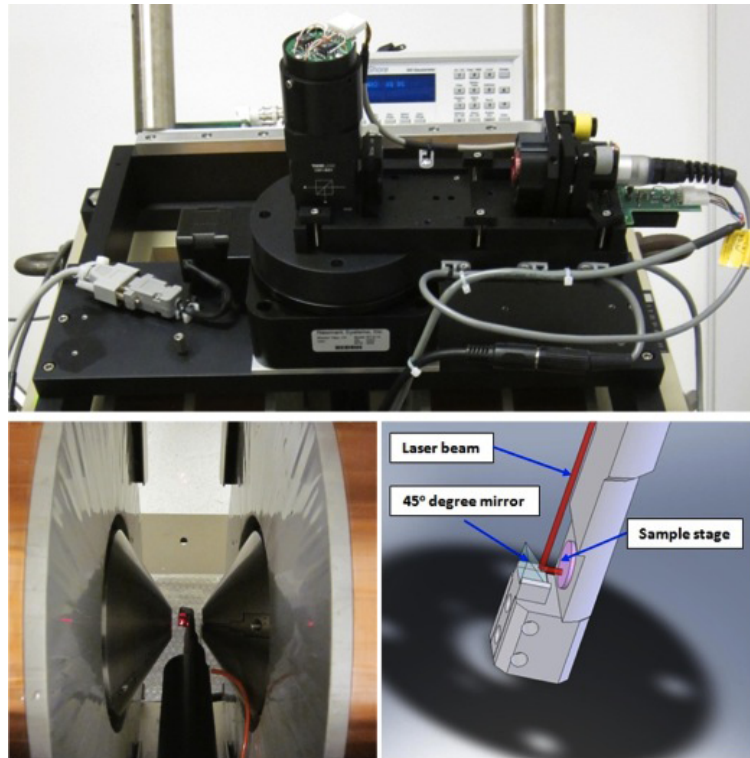


Figure 4.9: The rotation system with sample holder

In this work the angular dependent MOKE measurements were made at Seagate Media Research in Fremont California. Fig.4.10 shows a schematic diagram of the angular dependent MOKE instrument. In principle, the laser is linearly polarised and focussed onto the sample after passing through the polariser with a spot size of approximately 2 mm. The detector obtains the Kerr rotation signal from the reflected beam from the mirror on the sample holder. The measurements were made at room temperature with a maximum applied field of 30 kOe. The magnetisation curve and the dc demagnetisation (DCD) curve were measured. The sample was saturated with  $H_{sat} = \pm 15$  kOe and a field step of 50 Oe was used for the hysteresis loops. In the case of the DCD curve the data was obtained using  $H_{sat} = 15$  kOe with reverse field steps of 500 Oe. The measurements were repeated varying the angle,  $\theta$  from  $0^\circ$  to  $10^\circ$  in  $1^\circ$  steps. The results were normalized to the maximum signal amplitude which is proportional to the saturation magnetisation giving curves in term of  $M/M_S$ .

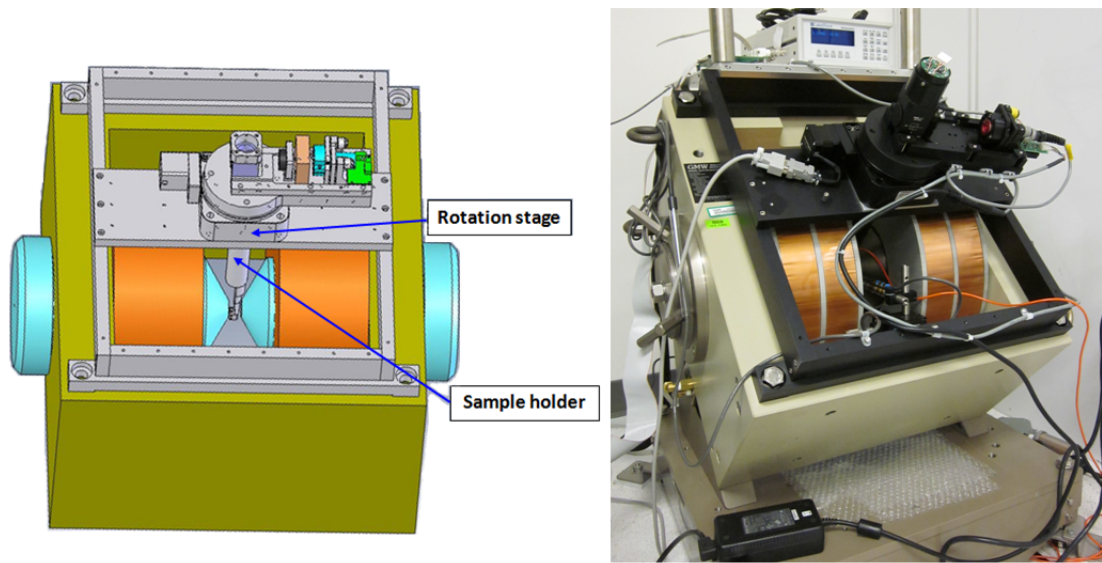


Figure 4.10: Schematic of angular dependent MOKE at Seagate Media Research in Fremont CA

## 4.2 Magnetic Measurements

### 4.2.1 Magnetisation Curve

The hysteresis loop provides the primary magnetic quantities as shown in fig.4.11. The field is applied perpendicular to the plane of the film determined by finding the maximum remanence. The primary magnetic parameters are determined i.e. the saturation magnetisation  $M_S$ , the remanent magnetisation  $M_R$ , the coercivity  $H_C$ , the loop squareness  $S_q = M_R/M_S$  and the nucleation field  $H_n$ .  $H_n$  is the negative field at which the magnetisation starts to reverse [149] [150]. Generally the loop is plotted with the magnetisation normalised to  $M_S$ . Fig.4.11 shows a typical magnetisation curve for an ECC/CGC media with all the key magnetic parameters.

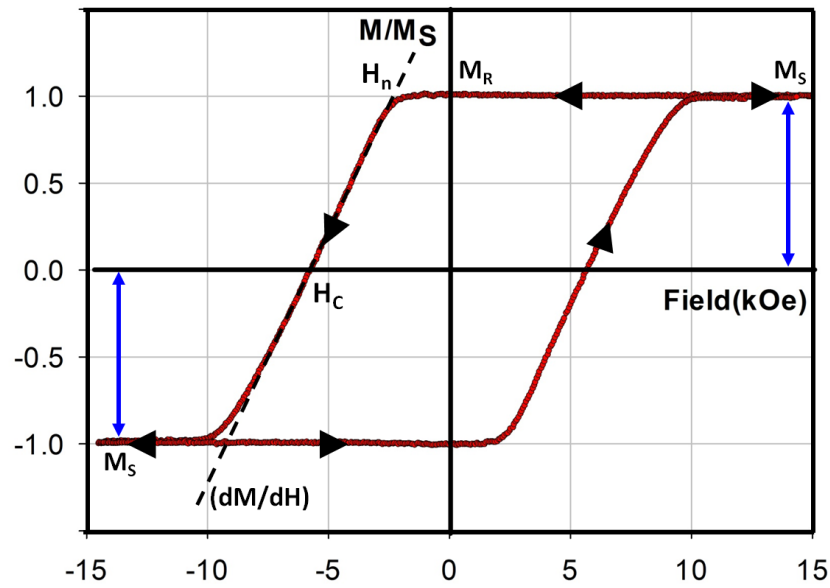


Figure 4.11: Schematic diagram of hysteresis loop from the MOKE magnetometer for an ECC/CGC medium

In perpendicular recording media the presence of the large demagnetising field (section 2.1.2)  $H_D = -4\pi \cdot M_S$  affects the measurements. There have been a number of attempts both theoretical and experimental, to correct for  $H_D$  in perpendicular recording media [27–29,31]. However,  $H_D$  cannot be determined correctly due to its non-uniformity near the film surface as shown in fig.4.12. In particular the demagnetising field affects measurements of remanence which prevents the use of most techniques commonly used to determine the distribution of easy axis orientation in the films. These techniques were developed for materials with in-plane anisotropy and whilst a correction for  $H_D$  can be applied the accuracy of the correction usually makes the measurement of little use [147]. In this work, we have used a new technique to study the effective easy axis distribution by measuring the variation of coercivity with angle. This has the advantage that at the coercivity there is no effect from the global  $H_D$  since  $M = 0$ . Therefore, correction for  $H_D$  is not required.

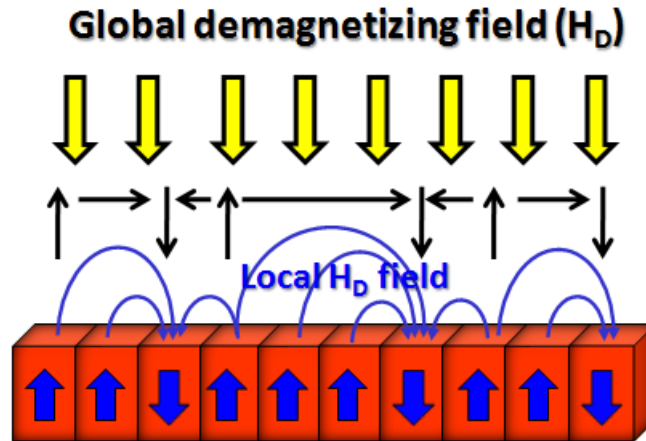


Figure 4.12: Schematic diagram of the demagnetising field in PRM

### 4.2.2 Remanence Curves

The total magnetisation consists of reversible and irreversible components. Further useful characterisation can be determined from *remanence curves* which measure only the irreversible magnetisation. The remanence  $M_R$  is the sum of the moments whose energy barrier  $\Delta E$  has been overcome after the medium is magnetised and the field removed. The fraction of the remanent magnetisation of the sample is the integral over the energy barrier distribution  $f(\Delta E)$  as shown in equation 4.5. At the coercivity, the magnetisation is zero due to the balance of the summation of the irreversible and reversible parts of the magnetisation that has switched which is equal to the irreversible part which has not switched. This is shown in equation 4.6 and diagrammatically in figure 4.13.

$$M_R/M_S = \int_{\Delta E_C}^{\infty} f(\Delta E) d\Delta E \quad (4.5)$$

where,  $\Delta E$  is the energy barrier,  $\Delta E_C$  is the energy barrier crossed at the field applied and  $f(\Delta E)$  is the energy barrier distribution.

$$\int_0^{\Delta E_C} g(H) \cdot f(\Delta E) d\Delta E + \int_{\Delta E_C}^{\Delta E(H_C)} f(\Delta E) d\Delta E = \int_{\Delta E(H_C)}^{\infty} f(\Delta E) d\Delta E \quad (4.6)$$

where,  $g(H)$  is a function which represents the reversible behaviour and  $\Delta E(H_C)$  is the energy barrier at the coercivity.

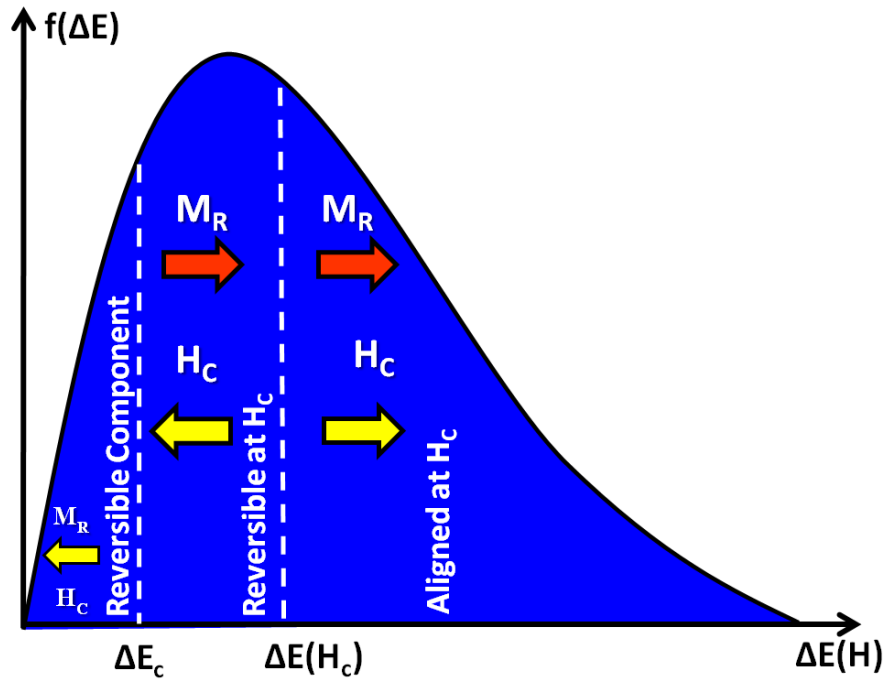


Figure 4.13: Schematic of the energy barrier distribution at  $H_C$

Remanence curves have been used to characterise recording media [36, 151, 152] via the remanent coercivity,  $H_{cr}$  which is the applied field giving zero irreversible magnetisation. They have also been used to give the switching field distribution (SFD) and the irreversible susceptibility  $\chi_{irr}$  [36]. The degree of intergranular exchange interaction can also be obtained from  $\Delta M$  measurements [50].

$$\Delta M(H) = M_D(H) - [1 - 2M_R(H)] \quad (4.7)$$

where,  $M_D(H)$  and  $M_R(H)$  are the remanent magnetisation values measured from the dc demagnetisation remanence (DCD) and the isothermal remanent magnetisation (IRM) curves respectively at an applied field,  $H$ .

Remanence curves can be measured by two techniques; the dc demagnetisation remanence curve and the isothermal remanent magnetisation curve. The DCD curve is measured from the saturation state. A small negative field is applied and removed and the remanence ( $M_R$ ) recorded. The process is repeated with higher negative fields. The remanence is plotted as a function of the negative field as shown in fig.4.14 to obtain the DCD curve.

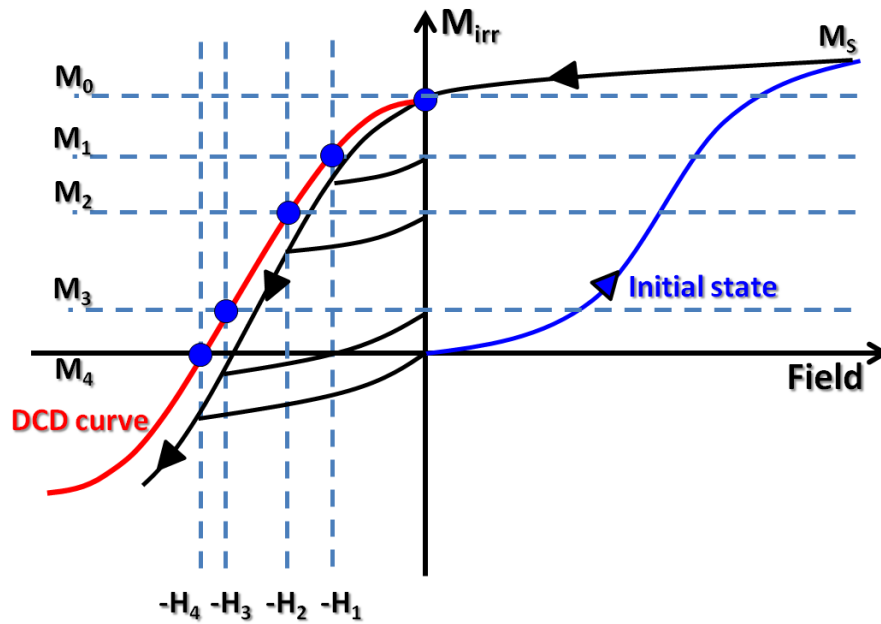


Figure 4.14: Schematic of the DCD curve

For the IRM curve as shown in fig.4.15, the process is similar but the remanence is measured from a demagnetised state applying positive fields. The sample is first fully demagnetised. A small positive field is applied and  $M_R$  measured. The process is repeated with higher fields until the remanence is saturated.

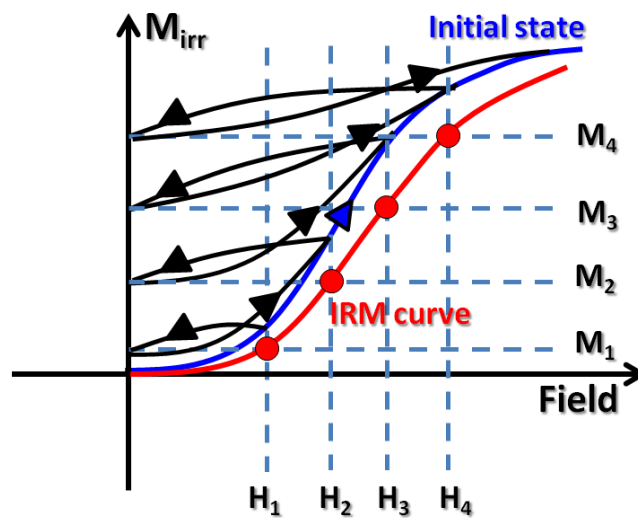


Figure 4.15: Schematic of the IRM curve

In this work the DCD curve was used to study the easy axis distribution by measuring the remanent coercivity  $H_{cr}$ .  $H_{cr}$  can be determined from the median switching field by differentiating a remanence curve [36] [151]. However, the effects of the large demagnetising field in perpendicular recording media cannot be corrected for due to the global demagnetising field and local demagnetising fields along the surface as shown in fig.4.12. There have been a number of attempts to correct for  $H_D$  on the IRM and DCD curves [27, 29, 31]. Unfortunately, the demagnetising field cannot be determined correctly. Therefore,  $H_{cr}$  cannot be determined from the differential of a remanence curve. In this work,  $H_{cr}$  is taken as the point at which  $M_R = 0$ . The effect of the global  $H_D$  is corrected for [28]

$$H_{cr} = -[H_A(M = 0) + 4\pi \cdot M_S] \quad (4.8)$$

where,  $H_A(M = 0)$  is the negative applied field. Angular dependent MOKE (section 4.1.3) was used to measure the DCD curves for all samples. The samples were saturated with an applied field of 15kOe. Subsequently, a reverse field is applied and removed for a remanence measurement at zero field. The measurements were repeated using 500Oe field steps. The results were normalised to the maximum signal amplitude which is proportional to the saturation magnetisation. Fig.4.16 shows a typical DCD curve measured using angular dependent MOKE for an ECC/CGC sample.

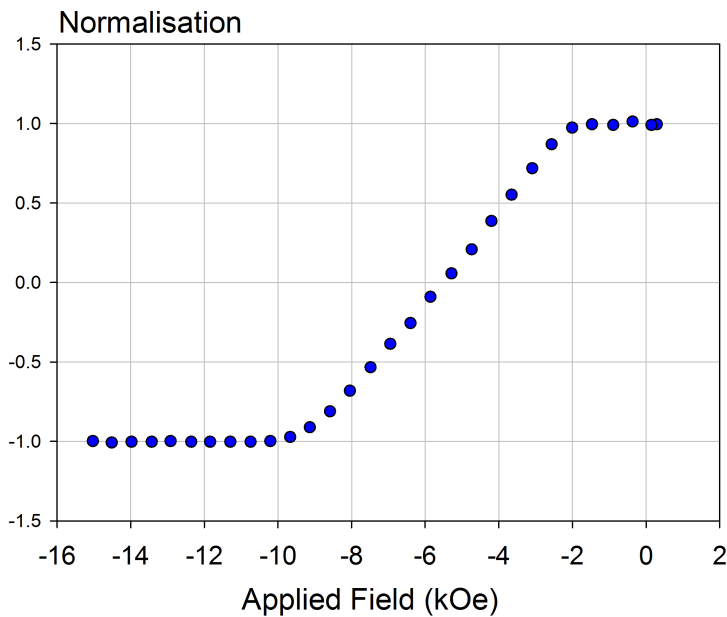


Figure 4.16: Typical DCD curve for an ECC/CGC sample

### 4.2.3 Angular Measurements

In this work, we have utilised a new technique to determine the effective easy axis distribution of perpendicular recording media which is the major factor affecting the switching field distribution (SFD) within the media. The SFD originates from several factors such as the distribution of the grain size, the distribution of composition (the anisotropy constant  $K$  and  $M_S$ ), intergranular magnetostatic and exchange interactions and the effects of crystalline axis dispersion. These effects can lead to a distribution of the intrinsic switching field

$$H_K = \frac{\alpha K}{M_S} \quad (4.9)$$

where  $\alpha$  is a factor describing the orientation of the grains and  $K$  is the anisotropy constant. The distribution of easy axis orientation is the crucial factor for the SFD as a small deviation from the perpendicular orientation leads to a large change in the switching field as discussed in section 2.2.2. The magnetisation reversal of each single domain grain can be described by Stoner-Wohlfarth theory [15] due to the small grain size and the effect of  $\text{SiO}_2$  which leads to exchange decoupling.

There have been a number of attempts to measure of the effective distribution of easy axes by measuring the crystalline *c-axis* dispersion characterised by the full-width half maximum (FWHM) of X-ray rocking curves [145], [147]. Magnetic measurements have also been used [143,144,146]. However magnetostatic and exchange interactions are not evident in X-ray measurements, and therefore, magnetic measurements are preferred. The variation of coercivity  $H_C$  with angle can give the magnetic orientation according to Stoner-Wohlfarth theory [15]. Due to the complex structure of particularly ECC/CGC media there are two peaks in the energy barrier distribution as shown schematically in figures 4.17 a) and 4.17 b) compared to a normal granular or ECC medium.

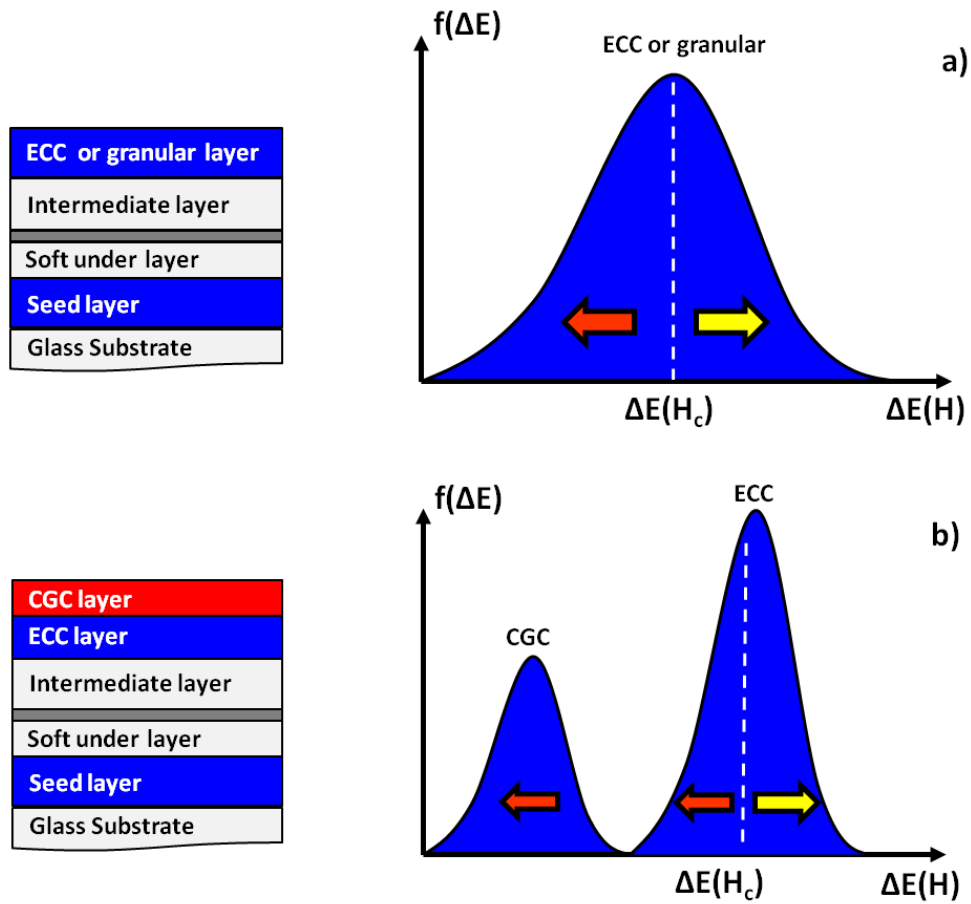


Figure 4.17: Schematic of the distribution of the energy barriers a) a normal granular or ECC medium and b) an ECC/CGC medium

#### 4.2.4 Time Dependence Measurements

As discussed in section 2.4 a time dependence measurements have been used to measure the magnetisation decay in order to determine the fluctuation field. The sample was first saturated in a field of 12 kOe. A constant reverse field,  $H_{rev}$  within the switching region, was then applied. The decay of the magnetisation was measured for 600 seconds. The process was repeated for a range of reverse fields, i.e.

$$H_{rev}^n = H_{rev} + n \cdot \Delta H \quad (4.10)$$

where,  $H_{rev}^n$  is the new reverse field,  $n$  is the number of steps and  $\Delta H$  the field step. Due to the period of time dependence measurements, the intensity of the laser may drift even using the highly stabilised HeNe laser used in this work. Therefore, the hysteresis

loop was measured before each run in order to normalise the Kerr rotation amplitude (V) for each step.

The range of fields  $H_{rev}$  must cover the switching field distribution. Therefore, the time-dependence measurement was designed to measure groups of closely-spaced measurements ( $\Delta H = 80$  Oe) divided by a larger field step ( $H_{rev} = 600$  Oe). Figure 4.18 shows a typical group of time dependence measurements. Due to the presence of a large demagnetising field in PRM, the fluctuation field is determined at zero magnetisation i.e. the coercivity ( $H_C$ ). The calculation of  $H_f$  and  $V_{act}$  will be described in section 4.2.5.

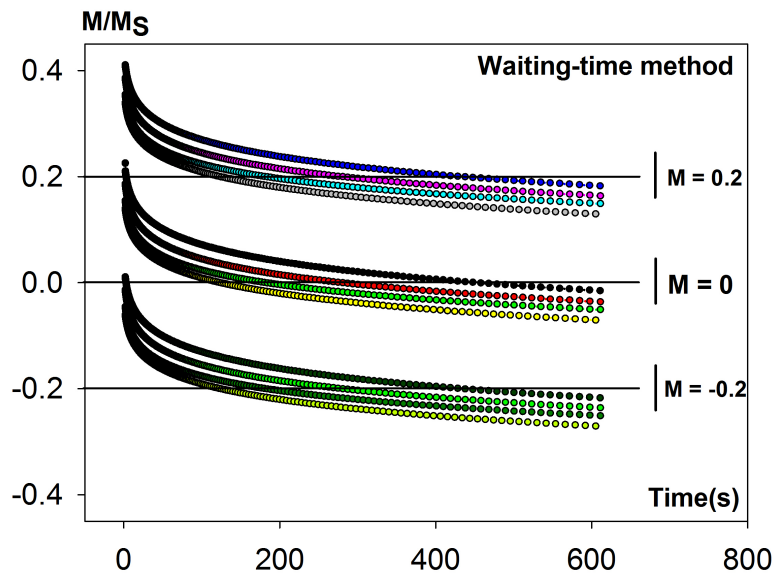


Figure 4.18: Schematic of a group of time dependence magnetisation decay measurements for the waiting time method

#### 4.2.5 Determination of Fluctuation Field and Activation Volume

As discussed in section 2.4.4, non-linear time dependence can be described by the equation of state formalism of El-Hilo *et al.* [77] which gives  $H_f$  as

$$H_f = \frac{\Delta H}{\ln(t_2/t_1)} \Big|_{M_{irr}} \quad (4.11)$$

The fluctuation field can be directly measured from two different applied field values and the time to reach the same constant level of irreversible magnetisation. In order to obtain an accurate value for  $H_f$ , the fluctuation field was determined from a graph of applied field versus  $\ln(t)$  for a number of intercepts at the same magnetisation.

Several intercepts are required at the same constant magnetisation with different reverse fields. The small field and the large field steps are carefully selected to cover the switching field region. Fig.4.19 a) and b) show the magnetisation decay as a function of the reverse field with  $\ln(t)$  and the variation of the reverse field and  $\ln(t)$  at zero magnetisation ( $M = 0$ ) respectively.

$H_f$  is inversely proportional to the activation volume as shown in equation 4.12. Hence,  $V_{act}$  can be rewritten as .

$$V_{act} = \frac{k_B T}{H_f M_S} \quad (4.12)$$

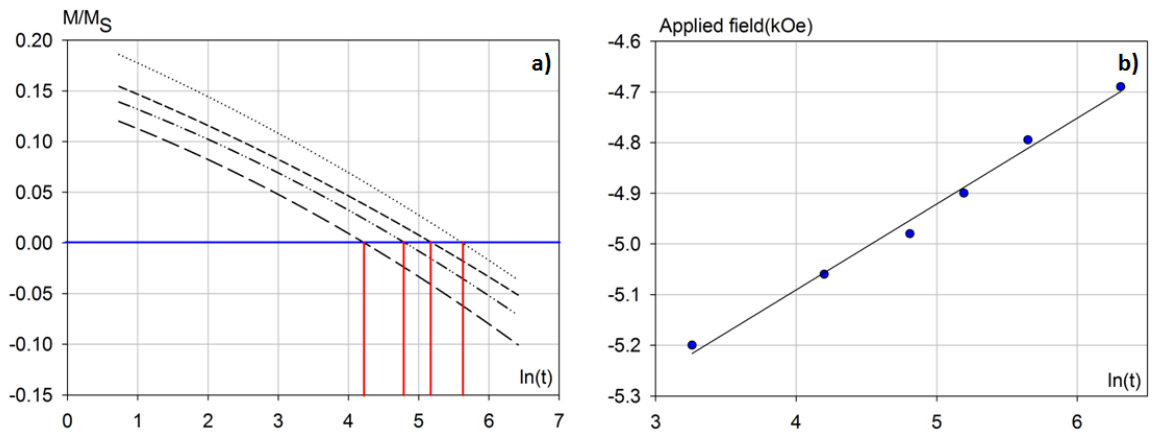


Figure 4.19: Schematic of a) the magnetisation decay with  $\ln(t)$  and b) the variation of reverse field versus  $\ln(t)$

In order to calculate  $V_{act}$ , the temperature and the saturation magnetisation must be known. The saturation magnetisation is the bulk saturation magnetisation. Due to the SUL, the saturation magnetisation is difficult to obtain accurately. The magnetisation is made up of contributions from the recording layer and the SUL which can be observed from the hysteresis loop. The signal from the SUL is not large enough to swamp the signal from the recording layer. Figure 4.20 a) and b) shows a schematic of the magnetisation reversal with the 4 different states and a typical magnetisation curve respectively.

The 4 different states of the magnetisation behaviour are shown at  $H_A \gg +$  (the positive saturation field),  $H_A \gg 0$ ,  $H_A \ll 0$  and  $H_A \ll -$  (the negative saturation field). The magnetisation from the hysteresis loop results from the moment from both

layers. The recording layer and SUL are both saturated at high applied fields (state **I**). After removing the field the SUL will reverse due to the high magnetisation and low coercivity (state **II**). The magnetisation of SUL will switch when a negative field is applied (state **III**). Eventually, the magnetisation of the recording layer is saturated (state **IV**).

The moment of the recording layer is measured at state **III** in order to determine  $M_S$ . The thickness of the films was measured from cross-section TEM images.  $V_{act}$  is then determined from eq. 4.12.

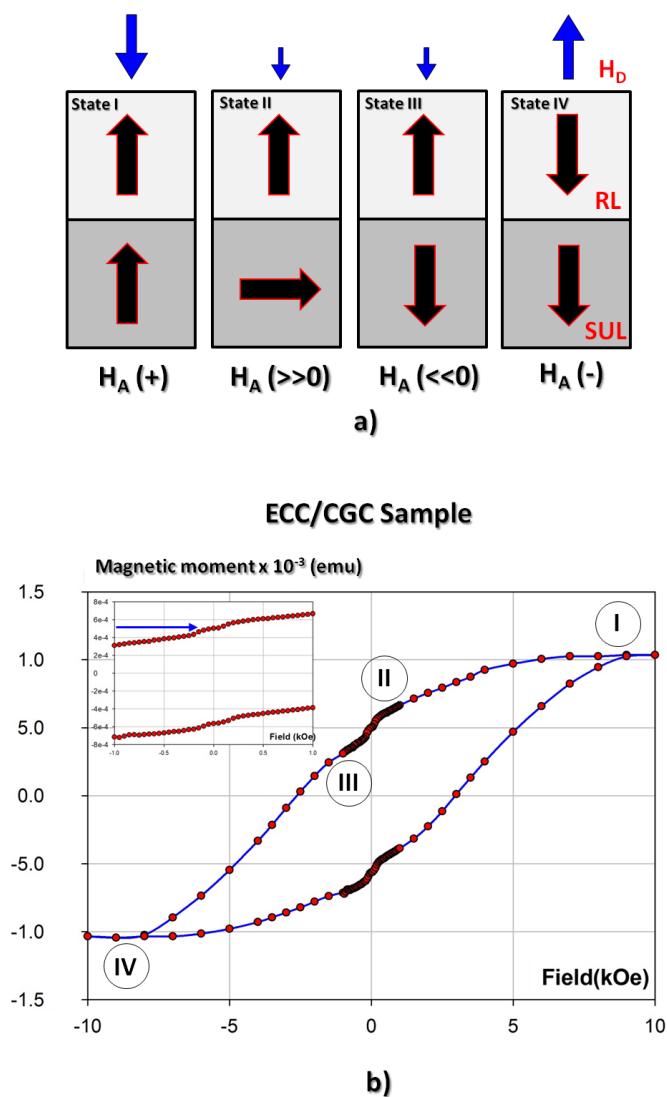


Figure 4.20: a) Schematic of the magnetisation reversal in different applied fields and b) magnetisation curve measured using the VSM for the ECC/CGC sample

## 4.3 Physical Structure Characterisation

### 4.3.1 X-Ray Rocking Curves

X-ray diffraction (XRD) is one of the most powerful techniques for providing the crystalline structure, crystallinity and the distribution of preferred orientation for thin films. The technique is based on Bragg's law describing the relationship between the diffraction of X-rays and the lattice spacing of the atomic planes. The X-ray beam is incident on the sample and scattered by lattice planes separated by  $d_{hkl}$  [153]

$$2d_{hkl} \sin \theta_{hkl} = n\lambda \quad (4.13)$$

where  $d_{hkl}$  is the lattice spacing or interplanar spacing,  $\theta_{hkl}$  is the Bragg angle which is the angle between the incident beam and the crystal planes and  $\lambda$  is the wavelength of the X-rays. The planes ( $hkl$ ) and directions  $[hkl]$  in the crystal are determined from the relationship between the lattice constant of the film,  $a_o$  and  $d_{hkl}$  is given by

$$d_{hkl} = \sqrt{\frac{a_o^2}{h^2 + k^2 + l^2}} \quad (4.14)$$

There are various diffraction methods used to study the structure of thin films such as out-of-plane measurements, in-plane measurements, small angle scattering and rocking curve measurements [154]. The crystalline structure and the preferred orientation distribution in thin films are usually investigated by conventional  $\theta/2\theta$  and X-ray rocking curve measurements.

Figure 4.21 a) shows a schematic diagram of a geometry of the conventional  $\theta/2\theta$  measurement. This technique is based on the measurement of the diffracted X-rays from the crystal lattice planes which are parallel to the sample surface and is known as *the symmetrical reflection measurement*. The X-rays coming from the source are fixed at an angle  $\theta$  which is the angle between the incident beam and the surface plane. The detector which is located at an angle  $2\theta$ , is moved around with the sample in order to obtain the intensity. For a strongly preferred orientation of a crystalline plane which is parallel to the film surface, the highest intensity of the diffraction peak is obtained according to Bragg's law. For  $c$ -axis perpendicular Co-alloys the peak is located at  $2\theta = 44^\circ$  at wavelength,  $\lambda = 1.54\text{\AA}$  corresponding to (0002) texture.

In order to determine the  $c$ -axes dispersion, rocking curve measurements are used. The orientation dispersion is obtained by rocking the sample at the peak of the preferred texture while the detector is kept at a fixed angle of  $2\theta$  to record the diffraction intensity. Fig.4.21 b) shows typical results for an X-ray rocking curve for a (0002) oriented cobalt based recording layer [147]. The degree of dispersion is estimated from the full width at half maximum (FWHM) denoted  $\Delta\theta_{50}$  as shown in fig.4.21 b).

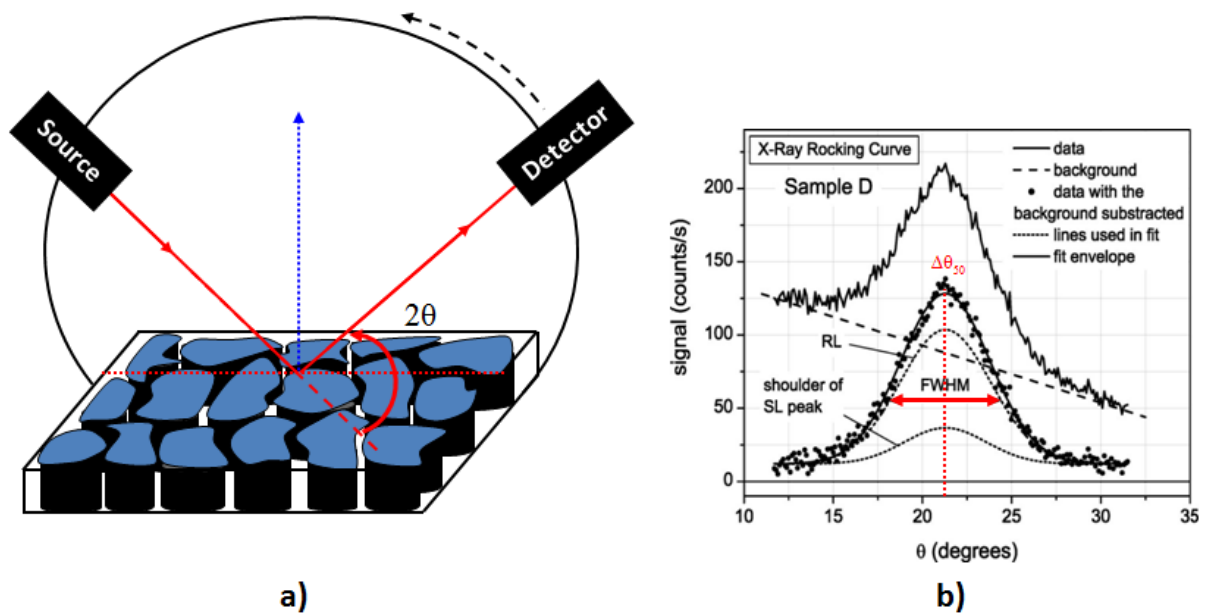


Figure 4.21: a) Geometry of a  $\theta$ - $2\theta$  angle measurement. b) Typical X-ray rocking curve of a (0002) recording layer peak [147]

Fig.4.22 shows a cross-section TEM image and the uniform atomic structure of the medium particularly at the interface between the intermediate layer and the recording layer. It is clear that if the  $c$ -axis orientation of some grains are not correctly aligned it leads to a large orientation dispersion with a high value of  $\Delta\theta_{50}$  as shown in 4.22. In this work X-ray rocking curve measurements were obtained from Seagate Media Research at CA. These are used to compare the  $c$ -axis distributions with magnetic measurements

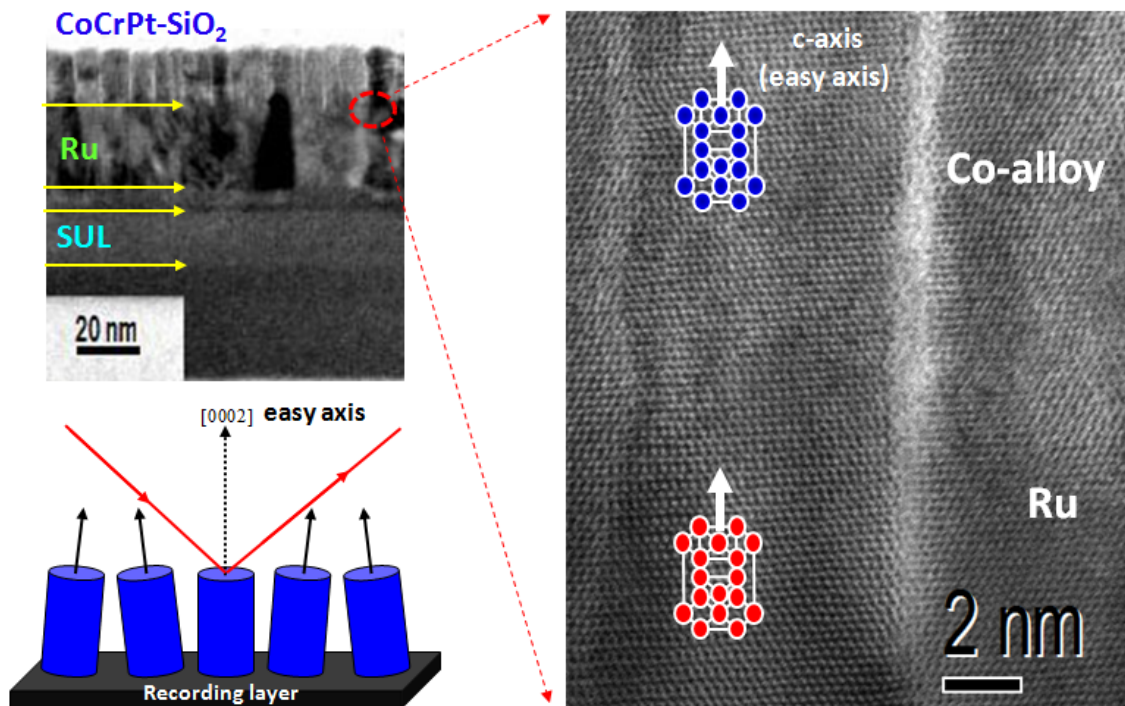


Figure 4.22: Cross-section HR-TEM image showing the interface structure between a Co-alloy and Ru intermediate layer and a schematic of the medium structure.

### 4.3.2 Transmission Electron Microscopy (TEM)

In order to study the physical structure of perpendicular recording media transmission electron microscopy (TEM) is one of the most powerful techniques. TEM can obtain not only atomic scale images but also elemental analysis. The image from TEM occurs when a beam of electrons passes through a thin specimen. The interactions between the electrons and the atoms in a specimen leads to significant phenomena e.g. elastic scattering, inelastic scattering, secondary electron and X-ray emission. The image is created from the different contrasts of the electron scattering phenomena.

The resolution of a TEM is described by equation 4.15 [155]. In order to obtain the highest resolution, it is necessary to reduce the wavelength of the electrons ( $\lambda$ ) and increase the refractive index of the viewing medium ( $\mu$ ).  $\theta$  is the semi-angle of the magnifying lens.

$$\delta = \frac{0.61\lambda}{\mu \cdot \sin \theta} \quad (4.15)$$

The wavelength of green light in the middle of the visible spectrum, is about 500 nm. The resolution of a visible light microscope is therefore approximately 300 nm from eq.4.15. The resolution of TEM is very small due to the electron wavelength  $\sim 5$  pm at 100 keV. Consequently, it provides a resolution 10,000 greater than that of an optical microscope. This is low enough to resolve at the atomic scale.

Figure 4.23 shows a schematic of a conventional TEM (left). A JEOL JEM-2011 TEM was used in this work. At the top of the column a LaB<sub>6</sub> filament in the form of a  $1\mu\text{m}$  tip emits an electron beam after it is heated to overcome the work function ( $\phi$ ). The electrons are accelerated to up to 200 keV to produce a monochromatic electron beam in an ultra high vacuum of  $10^{-10}$  mbar. The electrons travel through a hole in the anode and a condenser lens consisting of electromagnetic field coils. The condenser lens is responsible for control of the spot size. The spot size can be controlled by varying the current through the coils.

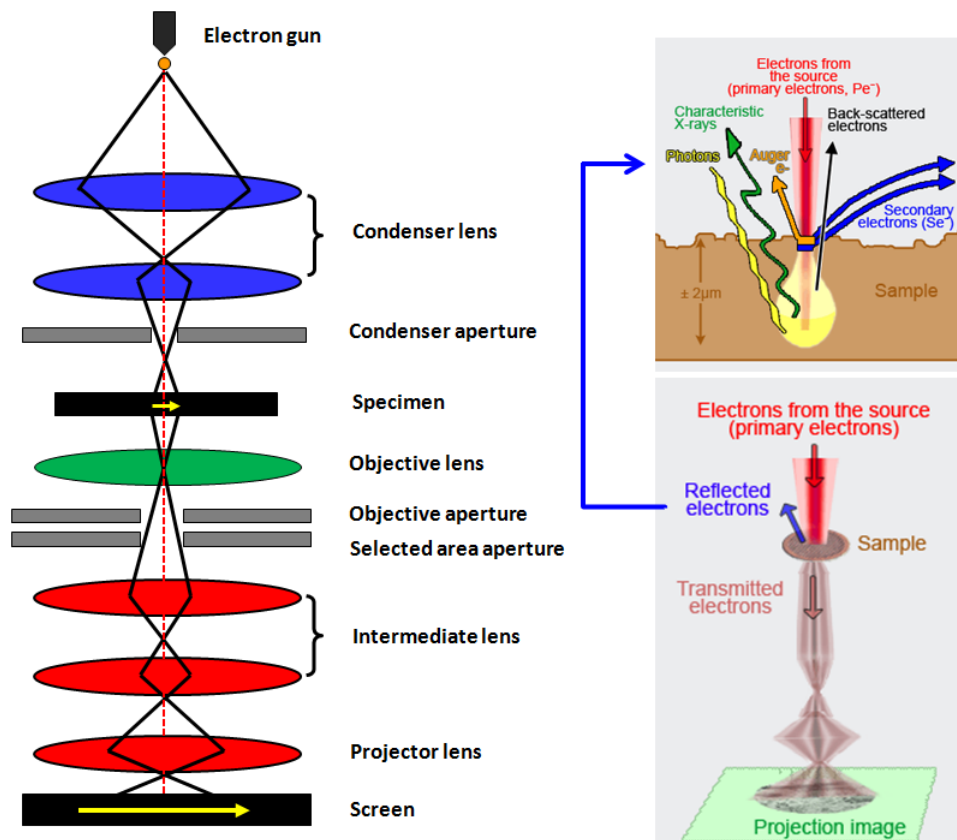


Figure 4.23: Schematic of a conventional transmission electron microscopy (left) and the process of an e-beam interaction with the sample surface (right) [156]

The specimen is located under the condenser aperture. Transmitted electrons travel down through an objective lens in order to create the first intermediate image. There are three or four lenses sitting below the first intermediate image. They enable two imaging modes namely the physical structure and the diffraction modes which show the crystal structure by magnifying or demagnifying the intermediate lens as shown in fig.4.24. Finally, the image is focussed onto a charge-coupled device (CCD) camera by the projector lens.

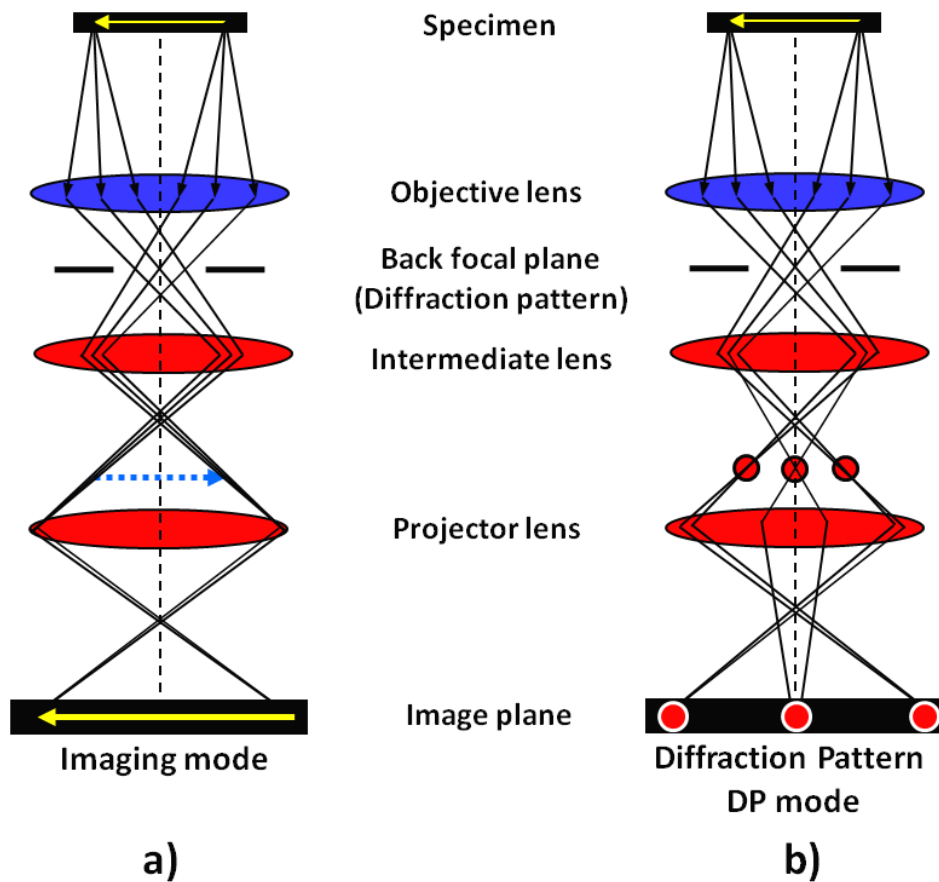


Figure 4.24: a) A comparison of TEM configurations in imaging mode and b) diffraction pattern mode

The most common TEM mode is bright field (BF) mode. It is obtained by inserting an aperture into the back focal plane of the objective lens in order to allow only the main beam to pass. The diffracted beams are blocked by the aperture. Therefore image contrast is improved but the quality of the image is reduced due to loss of the diffracted electrons.

In the case of dark field (DF) images, the operation is almost the same as the BF mode. The aperture is used to block the main beam while one diffracted beam is allowed to pass. The diffraction pattern of a particular part of the image can then be observed by inserting the selected area diffraction (SAD) aperture at the first intermediate image. From the particular diffraction image, the crystal structure of the sample can be obtained.

In this work the BF imaging mode has been used to observe the physical structure to measure the mean grain diameter and the grain size distribution (section 4.3.5). The physical cross-section grain structure was observed with High Resolution Transmission Electron Microscopy (HRTEM) to study the effect of the SiO<sub>2</sub> at the grain boundaries. HRTEM is an imaging mode using a large objective aperture to allow the main beam and also the scattered electrons to pass. The atomic image is created by the interference of the main beam with the diffracted beams.

### 4.3.3 Scanning Transmission Electron Microscopy (STEM)

Scanning transmission electron microscopy (STEM) is a useful technique for the characterisation of recording media providing information for qualitative and quantitative elemental analysis, surface topology composition, and X-ray analysis such as energy dispersive X-ray (EDX) mapping. This technique combines the principles of transmission electron microscopy (TEM) and scanning electron microscopy (SEM). The key advantage of the STEM is the fine beam of electrons that can be raster-scanned across the surface of a specimen by controlling two pairs of scanning coils. It is not available in conventional TEM. The signals from the interaction between the electron beam and the bulk of the specimen give a number of different effects including back-scattered electrons, characteristic X-ray and secondary electrons as shown in fig.4.23. These are collected by the signal detector mounted near the specimen. In addition, the transmitted electrons pass through to the screen and are collected by several detectors in order to form an image mode. A schematic of a STEM is shown in fig.4.25.

---

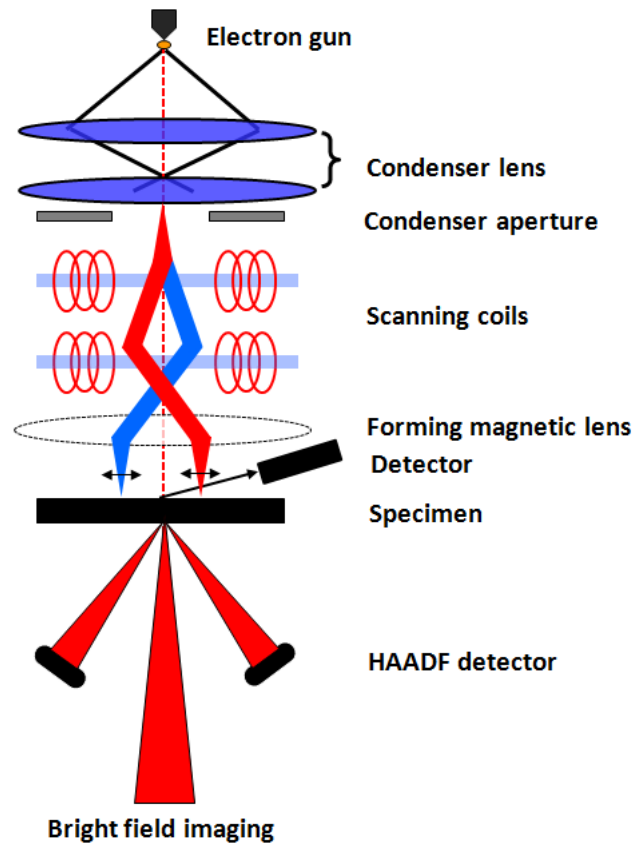


Figure 4.25: Schematic of a STEM with two pairs of scanning coils

In order to achieve high resolution and other strong signals with STEM a very fine electron beam is required. A field emission electron gun (FEG) is used to generate electron beams which carry a current density of up to  $10^{10}$  A/m<sup>2</sup> in a beam of diameter 0.2 nm in an ultra high vacuum (UHV) of  $10^{-11}$  mbar [155] [157]. Therefore higher signal levels and better spatial resolution are available only in an STEM. The specimen therefore needs to be particularly thin to allow electron transparency. When a convergent electron beam is scanned across a region highly localized signals from the specimen are simultaneously collected by a range of detectors including a reflected electron detector, an annular dark field (ADF) detector, bright field detector, high-angle ADF (HAADF) detector and secondary electron detector. These provide the different imaging modes and qualitative and quantitative elemental analysis.

In this work a JEOL-JEM-2200FS double Cs-corrected scanning transmission electron microscope (STEM) was used to determine the composition of recording media using energy dispersive X-ray (EDX) mapping and a line-scanning technique. The technique is based on the measurement of characteristic X-rays of the atom. There are two kinds of analysis; *qualitative analysis* which is the measurement of the energy of each characteristic X-ray that is emitted in order to determine the composition of the specimen and *quantitative analysis* which is the measurement of the intensity distribution of the X-rays in order to determine the percentage of each element present. In the line-scanning method an electron beam is scanned along the chosen line. The composition can be obtained from the instantaneous collection of X-ray signals along the line. EDX mapping is similar to the line-scanning method extended to two-dimensional scanning of the region of interest. The composition is presented via a dot array giving a qualitative measurement of the X-ray signal.

Figure 4.26 shows an analysis of the composition of an ECC recording medium using line-scanning and EDX mapping techniques. For line scanning imaging (top), the fine beam of electrons is moved across the cross-sectional surface from the substrate (bottom) to the recording layer (top). As a result the composition signal of the recording layer is very low comparing to other layers due to the low thickness ( $\sim 10$  nm). The composition signal for each layer is not of high enough resolution to separate the layers due to beam damage, contamination and signal drift. In particular the grain boundary region of the recording layer gives very low compositional signals. Therefore, these techniques could not be used for atomic interfacial analysis.

Qualitative atomic resolution analysis can be also provided by *Z-contrast imaging* known as high-angle annular dark field (HAADF) imaging. In principle when the convergent electron beam penetrates the electron cloud of an atom in a specimen, the strong Coulomb interaction leads to high-angle Rutherford-scattered electrons according to the atomic number ( $Z$ ) of the elements in the specimen. HAADF detectors collect electrons that are scattered to high angles as shown in fig. 4.25. The contrast of HAADF images is proportional to  $Z^2$ . Heavy atoms with high atomic number will then appear with the brighter contrast.

---

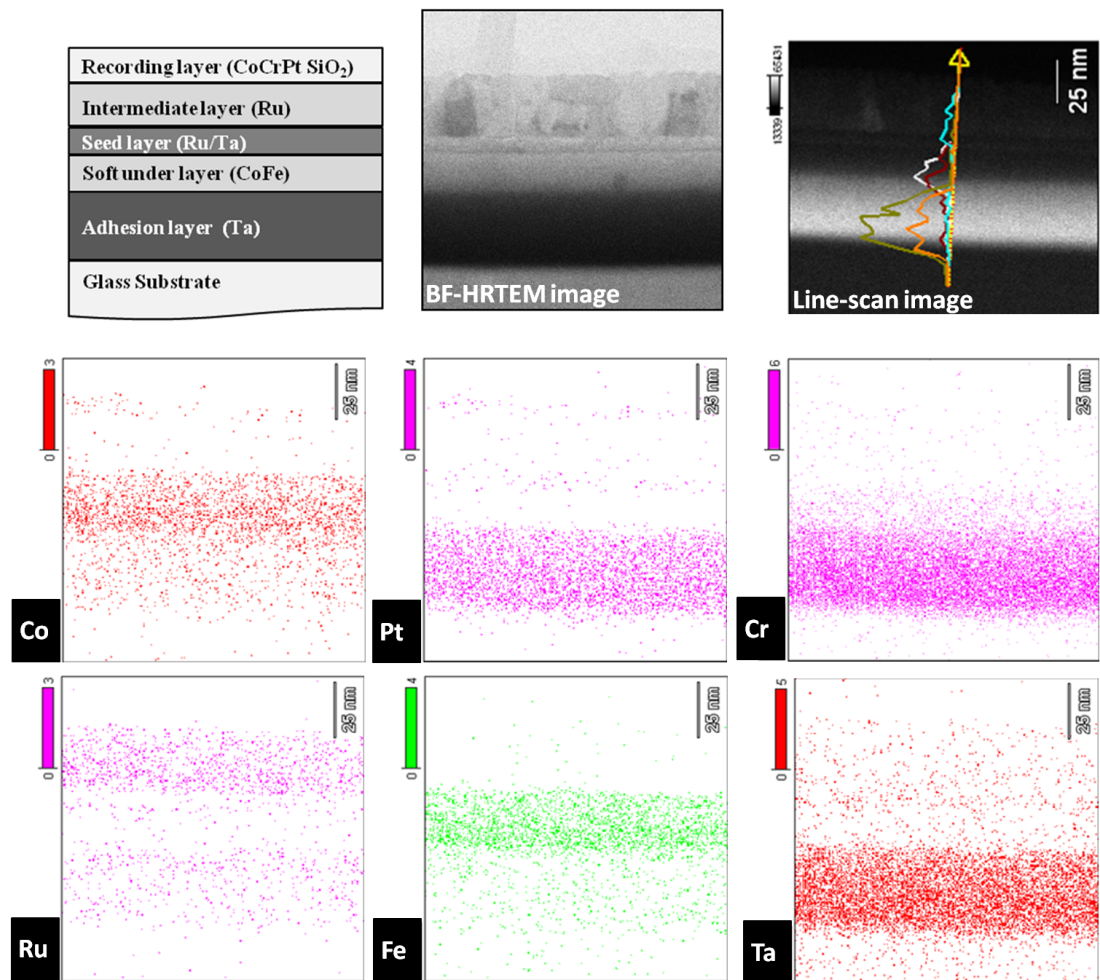


Figure 4.26: Typical cross-section STEM image with a line scan image and EDX mapping for a range of elements in the film (courtesy of Dr. L. Lari).

In this work, the effect of SiO<sub>2</sub> at the grain boundaries between CoCrPt grains has been studied. Figure 4.27 shows a comparison of a typical cross-sectional image of the BF-HRTEM and HAADF-STEM images. The CoCrPt grain has atoms with higher atomic numbers compared to SiO<sub>2</sub> and appears as bright dots whereas the SiO<sub>2</sub> appears as dark areas.

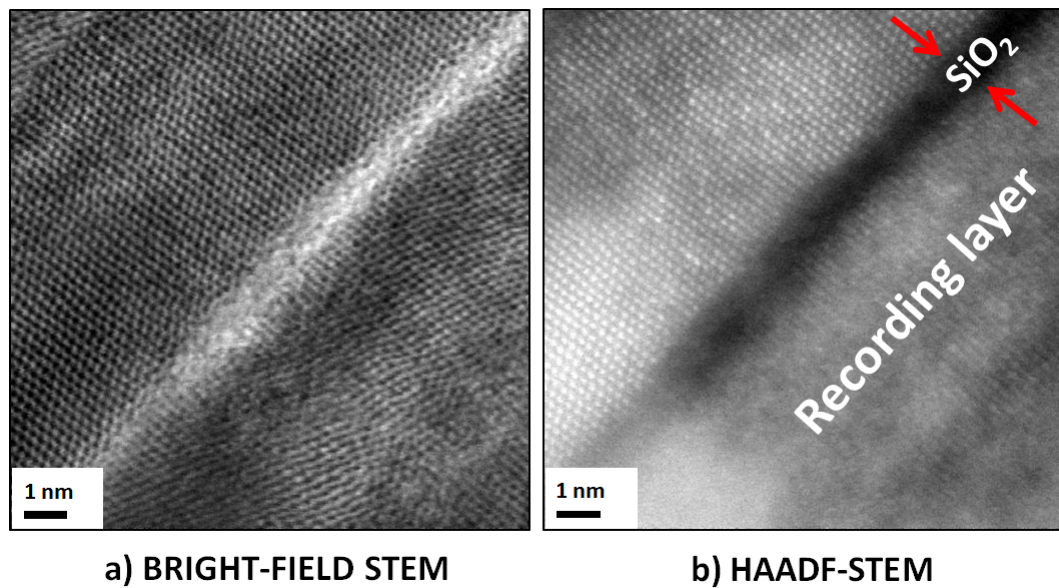


Figure 4.27: a) Typical BF-HRTEM cross-sectional image and b) High angle annular dark field (HAADF)-STEM (courtesy of Dr. L. Lari)

#### 4.3.4 In-plane and Cross-section Sample Preparation

In order to study the microstructure of recording media, the preparation of in-plane and cross-section samples is required. The most successful samples were prepared using the conventional technique [158] using silicon carbide for grinding and  $\text{Ar}^+$  milling (Precision Ion Polishing System, PIPS) to produce electron transparent samples. The sample preparation procedure is separated into 2 methods for in-plane TEM specimens and cross-section TEM specimens.

##### 4.3.4.1 In-plane Sample Preparation

The sample was first cut into a 2.5 x 2.5 mm piece. After cleaning the sample with acetone and ethanol, the film side is affixed to a TEM grid with epoxy resin. The sample is annealed on a hot plate at 120°C for 30 minutes in order to set the epoxy. The thickness of the sample is measured using a micrometer gauge. The sample is then mechanically ground from the substrate side with silicon carbide paper using a polishing machine down to  $\sim 150 \mu\text{m}$ . Then, silicon carbide paper is replaced by diamond paper. The grinding process is repeated with 9  $\mu\text{m}$  diamond paper until the thickness  $\sim 100 \mu\text{m}$ , 3  $\mu\text{m}$  diamond paper until the thickness  $\sim 50 \mu\text{m}$ , and 1  $\mu\text{m}$  diamond paper until

the final thickness was  $\sim 30 \mu\text{m}$ . The sample is polished on the dimple-grinder with  $0.05 \mu\text{m}$  alumina balls to produce a smooth surface. The sample is further back-thinned using a Gatan 691 precision ion polishing system (PIPS) with  $\text{Ar}^+$  ions with an energy of  $3.5 \text{ keV}$ , milling from above at an angle at  $6$  degrees. Beam modulation is used to control heating and prevent damage to the film. The thin area which is in center of the sample, is thinned further until a small hole appears. A schematic diagram of the sample structure is shown in figure 4.28.

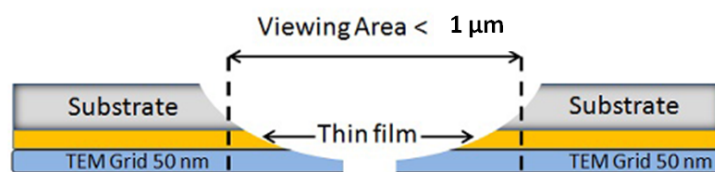


Figure 4.28: Schematic of the sample structure for in-plane imaging

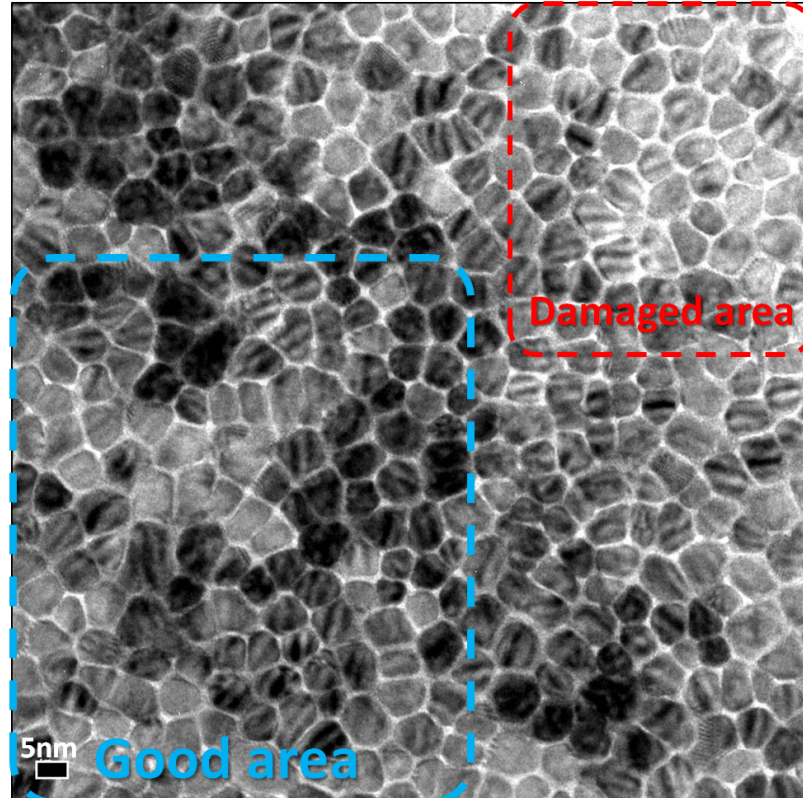


Figure 4.29: Typical in-plane TEM image with damaged and undamaged regions

The thinned area is less than  $1\ \mu\text{m}$  across as shown in figure 4.28. The preparation procedure can damage the grains of recording media due to heating and contamination by the grinding materials so the selecting of the area for imaging is crucial. Fig.4.29 shows a bright field in-plane image of ECC media with a high oxide level. This image shows undamaged grains in the region within the blue dotted line and damaged grains in the area contained by red dotted line. It can be seen that in the thin area there are abnormally loose packed grains with distorted shape due to excess ion-milling. The area selected to perform the grain size analysis is imaged carefully.

#### 4.3.4.2 Cross-sectional Sample Preparation

For cross-sectional TEM samples the preparation procedure is similar to that for in-plane sample preparation. However it is more complicated and time-consuming. The sample is cut into a square of  $2.5\ \text{mm}^2$ . Two sample pieces are glued together face to face on the film side. The specimens are sandwiched between blank Si substrates with epoxy resin as shown in figure 4.30. The Si substrates are used to monitor the specimen thickness. When the sample is ground down to  $20\text{-}30\ \mu\text{m}$  at the final step of preparation. A clamp is used to fix the specimen and placed on a hot plate to set the glue as shown in figure 4.30.

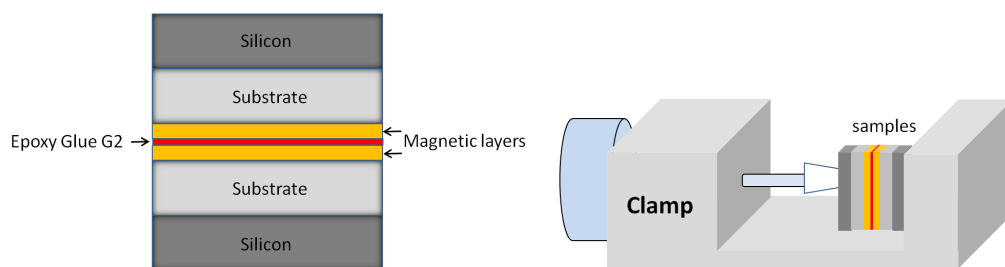


Figure 4.30: Schematic of cross-section TEM sample preparation

One side of the specimen is thinned using silicon carbide paper and  $1\ \mu\text{m}$  diamond paper to polish the samples and create a smooth surface. Then a sponge polish was used to obtain the final state on the dimple-grinder with  $0.05\ \mu\text{m}$  alumina balls to produce smooth surfaces before sticking to a TEM grid. The specimen is then flipped over and thinned down with silicon carbide paper and diamond paper as for the in-plane samples.

When the specimen is less than  $80\ \mu\text{m}$  thick, it is checked by shining light through it from the bottom. Whenever orange light is transmitted the sample thickness is approximately  $20\text{--}30\ \mu\text{m}$ . The sample thickness is the most important step for cross-section preparation. Again a sponge polishing is used for final stage of preparation. A schematic diagram of the first and final state of the TEM grid is shown in figure 4.31.

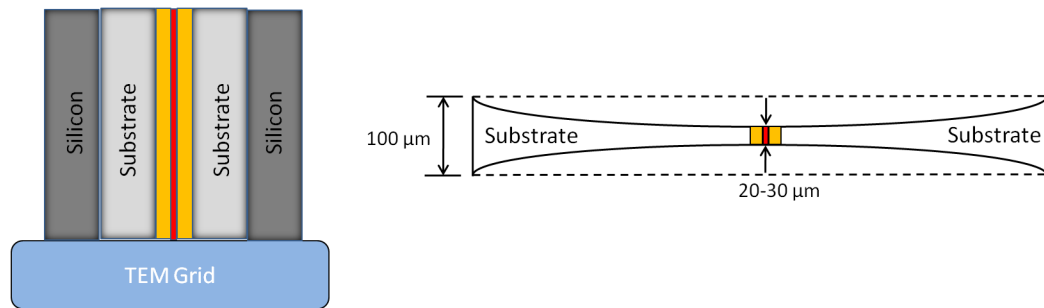


Figure 4.31: Schematic of the complete dimple specimen

The specimen is then ion-milled from both sides with an energy of  $3.0\text{--}3.5\ \text{keV}$  which is suitable for glass substrates. Each electron gun is set with top and bottom angles of  $5\text{--}6$  degrees. Beam modulation and low energy are used to limit heating and sample damage. A schematic diagram of a cross-section sample showing the milling angle is shown in figure 4.32. The specimen was finally cleaned using ion-milling with a high angle of top and bottom electron guns at a low energy of  $0.5\ \text{keV}$  in order to avoid contamination.

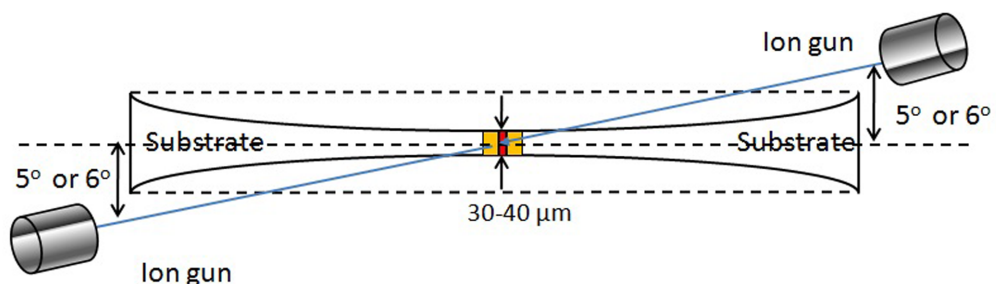


Figure 4.32: Schematic of a dimple sample with the milling angle

Figure 4.33 shows a bright field cross-section TEM image and a schematic diagram of the sample. The image clearly shows the recording layer of CoCrPt grains separated by silica at the grain boundaries. This image again shows damaged and undamaged areas due to the ion-milling process.

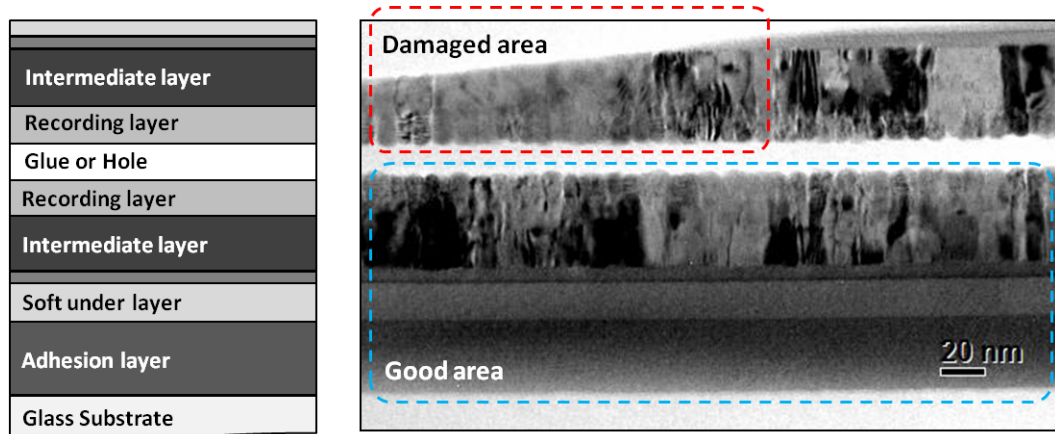


Figure 4.33: Schematic of perpendicular recording media cross-section TEM image

#### 4.3.5 Grain Size Analysis

The most important factor in the advance of perpendicular media is the reduction of the grain size which is currently smaller than 7 nm [143] [159]. The recording layer grains grow in a columnar stack on top of the grains in the seed and intermediate layers. Hence a small grain size in these layers can determine the grain size of the upper layer.

In order to investigate the grain size distribution, in-plane TEM samples must be prepared as discussed in section 4.3.4. Bright field transmission electron microscopy has been used to obtain images of the grains. Typical images of ECC/CGC, ECC and granular media studied in this work are shown in fig.4.34.

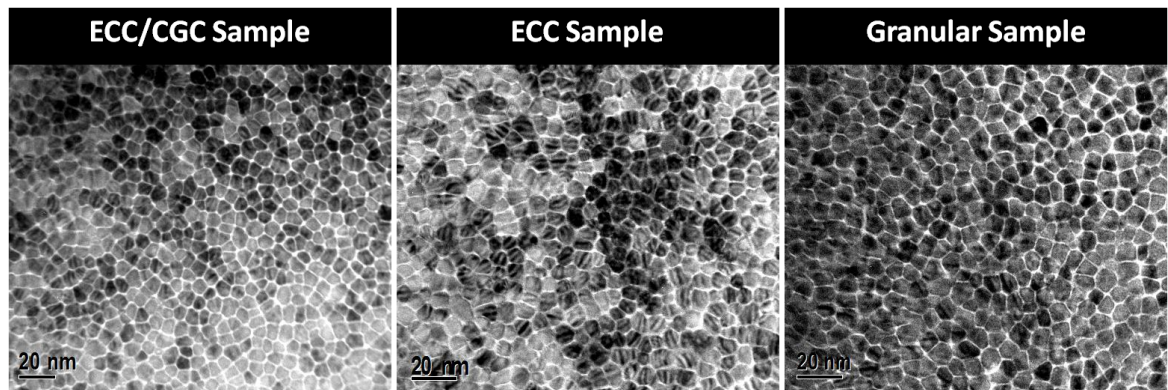


Figure 4.34: Typical in-plane TEM images for ECC/CGC, ECC and granular samples

The magnetic grains are composed of a CoCrPt alloy with heavy atoms which give greater scattering of the electrons than the SiO<sub>2</sub>. Hence, the dark areas indicate the magnetic grains and lighter areas are the SiO<sub>2</sub> as shown in figure 4.34. Therefore, the dark regions are measured for grain size analysis.

A Zeiss particle size analyser was used to measure the distribution of grain sizes in the recording media. Photographs of the grains were taken from different areas of the sample in order to obtain sufficient grains for measurement. The particle size analyser has a circular beam of light whose spot size can be adjusted to the grain size. In practice the grains are not perfectly circular. Hence the area of the circular beam is adjusted to be equal to the area of the grain in order to obtain the grain diameter. The grain is counted using a bar with a sharp pin at the end which punches the photograph to mark the measured particles. The iris size and number of grains are logged using LabView software. Finally the grain size distribution of the sample is created by plotting the number of grains and size of the bin which is converted to the actual scale from the TEM image.

The fundamental process of grain growth is described in terms of nucleation, growth, coalescence and grain boundary motion leading to the grain size distribution [160] [161]. The size distribution of thin films is found consistently to follow a log-normal distribution [162] [163]. The log-normal distribution is a probability function of a random variable in which the natural logarithm follows a normal or Gaussian form. The distribution for a linear interval is

$$f(D)dD = \frac{1}{\sqrt{2\pi}\sigma_{\ln D}D} \exp\left\{-\frac{[(\ln D) - \mu]^2}{2\sigma_{\ln D}^2}\right\} dD \quad (4.16)$$

where,  $D$  is the magnetic grain diameter,  $\sigma_{\ln D}$  is the standard deviation of  $\ln D$  and  $\mu$  is the mean of  $\ln D$  ( $\mu = \sum_i \frac{N_i \ln(D_i)}{N_i}$ ,  $N$  is the number of the grains measured). The distribution is normalised by a factor  $\frac{1}{\sqrt{2\pi}\sigma_{\ln D}D}$  so that

$$\int_0^{\infty} f(D)dD = 1 \quad (4.17)$$

The median diameter  $\bar{D}_m$  and the standard deviation of  $\ln D$  are determined from

$$\bar{D}_m = e^{\mu} \quad (4.18)$$

and

$$\sigma_{\ln D} = \left[ \frac{1}{\sum N} \sum N \cdot (\ln D)^2 - \left( \frac{1}{\sum N} \sum N \cdot \ln D \right)^2 \right]^{1/2} \quad (4.19)$$

For the log-normal distribution of  $D$ , the grain volume  $V$  follows the same distribution with  $\sigma_{\ln V} = 3\sigma_{\ln D}$  which is valid for spherical particles. In the case of recording media grains, the median grain volume,  $V$  is  $\frac{\pi D^2}{4} \cdot t$  where  $t$  is the thickness of the storage layer. Hence  $\sigma_{\ln V} = 2\sigma_{\ln D}$

In this work, the number of grains measured was at least 500 for each sample. A typical example of the data is shown in figure 4.35 for an ECC sample. The effect of  $\text{SiO}_2$  at the grain boundaries leads to a different distribution of the center to center distance of the grains. Figure 4.36 shows a typical image with the center to center distances marked.

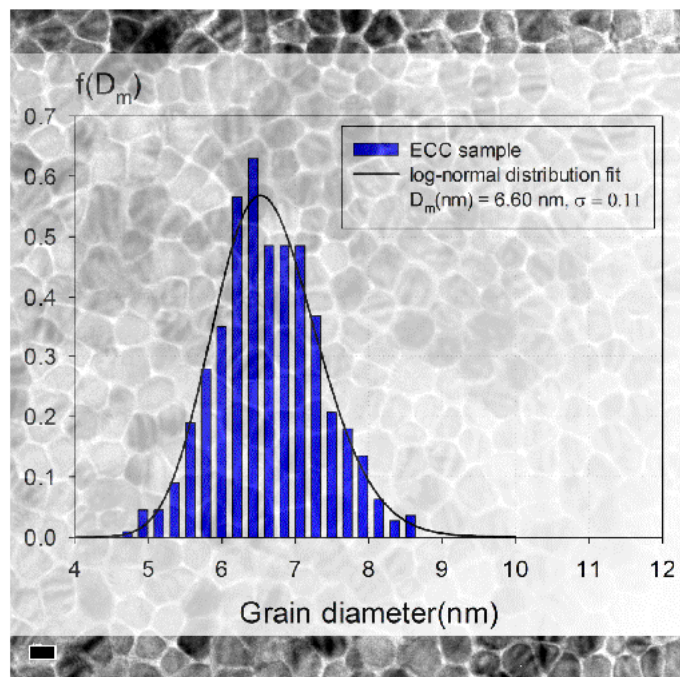


Figure 4.35: Typical in-plane TEM image of ECC media and the measured log-normal distribution.

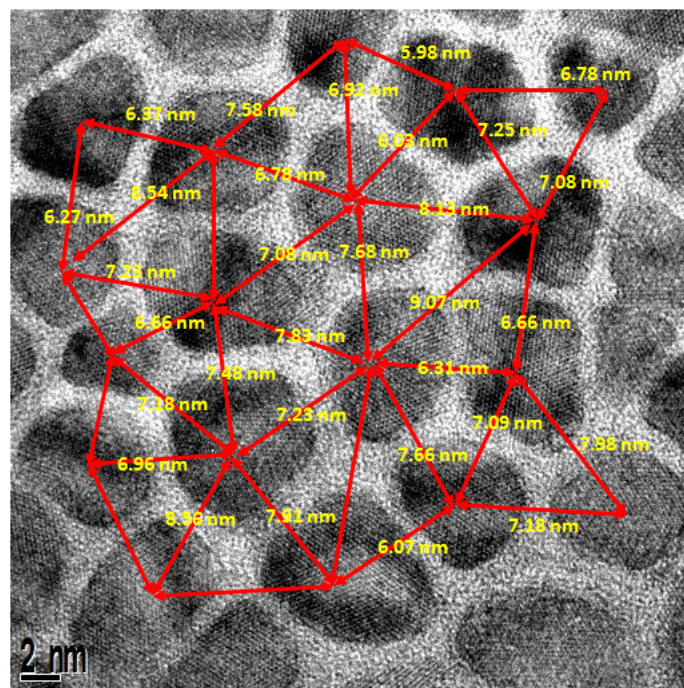


Figure 4.36: Typical HRTEM image of ECC sample with center to center distances marked

## 4.4 Simulation of Easy Axis Distribution

The traditional remanence method [145] [146] [147] to determine the distribution of easy axes cannot be used for perpendicular media due to the large demagnetising field [28]. Also this measurement is difficult to interpret due to the small change in the squareness ( $M_R/M_S$ ) with angle ( $< 5\%$  in  $10^\circ$ ). A new technique has been developed to extract the distribution from the variation of coercivity with angle. The detail of the experimental technique has been described in section 4.2.3. In order to investigate the distribution of easy axis orientation of the grains a computational method was required to compare with the experimental results.

### 4.4.1 Stoner-Wohlfarth Simulation

In order to determine the easy axis distribution the variation of the coercivity is calculated with a Gaussian distribution of easy axes orientation with a standard deviation  $\sigma_\phi$ . The calculation is essentially a complex, large-scale integral due to the rotation of the field and the easy axis orientations. When the sample is rotated a previously aligned grain moves out of alignment with the applied field and a previously misaligned grain may become aligned. Following standard thermal activation theory for a single grain aligned with the applied field, the coercivity is [15]

$$H_C = \alpha H_K \left[ 1 - \left( \frac{25k_B T}{KV} \right)^{1/2} \right] \quad (4.20)$$

where,  $H_K = 2K/M_S$  is the anisotropy field,  $K$  is the anisotropy constant,  $V$  is the grain volume,  $T$  is the temperature and  $\alpha$  is the orientation factor for that grain. Equation 4.20 shows that the value of  $H_C$  is strongly dependent on the parameters  $K$  and  $V$ . However, the term inside the brackets is independent of easy axis the orientation. For the aligned case the pre-factor is equal to  $H_K$  and for any angle it can be determined using Stoner-Wohlfarth theory.

For each sample all parameters in eq.4.20 are assumed constant with angle other than the term  $\alpha$ , Exchange and dipolar interactions were not included in the calculations. The calculations were based on 20,000 grains with a Gaussian distribution of easy axes orientations  $f(\phi)$ , with a standard deviation  $\sigma_\phi$ . Figure 4.37 shows a typical schematic diagram of the model

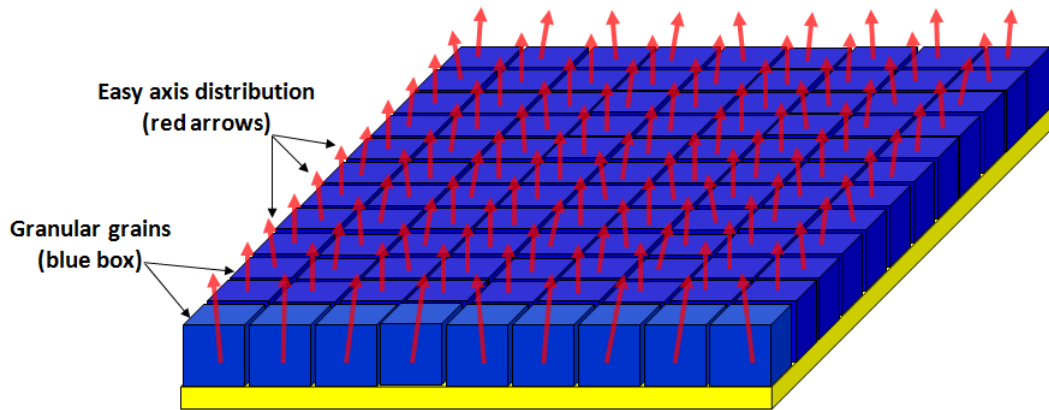


Figure 4.37: Schematic of a film whose grains have an easy axis distribution

The variation of  $H_C(\theta)$  is calculated varying the standard deviation from  $0^\circ$  to  $10^\circ$  with a step size of  $0.5^\circ$ . The normalised coercivity at an angle  $\theta$  from  $-10^\circ$  to  $10^\circ$  in  $1^\circ$  steps is then evaluated from the average value of the normalised coercivity [ $h = H_C(\theta)/H_C(0)$ ] for all easy axis orientations. The normalised coercivity,  $h$  at any angle is then given by

$$h = -\frac{(1 - t^2 + t^4)^{1/2}}{(1 + t^2)} \quad (4.21)$$

where  $\theta$  is the angle between the applied field and the normal to the film plane,  $t$  is  $\tan(\theta')^{1/3}$  and  $\theta'$  is the angle between the applied field and the easy axis direction. Figure 4.38 shows a schematic of the easy axis distribution and the applied field direction relative to the thin film surface.

From the Stoner-Wohlfarth simulation the variation of the normalised coercivity for the different values of standard deviation is shown in figure 4.39. In the case of  $\sigma_\phi = 0$  the easy axis distribution is that for the perfectly aligned case. When the standard deviation is increased the variation broadens. The predicted reduction of  $H_C$  of 30 % for a rotation of  $10^\circ$  is not observed except for the aligned case because as an originally aligned grain rotates out of the field direction other previously misaligned grains come into alignment. The actual effective easy axis distribution has to be obtained by fitting the experimental results to the S-W calculation.

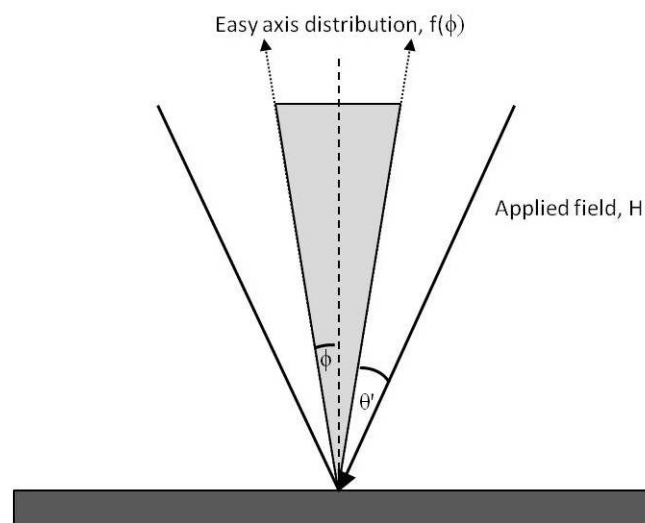
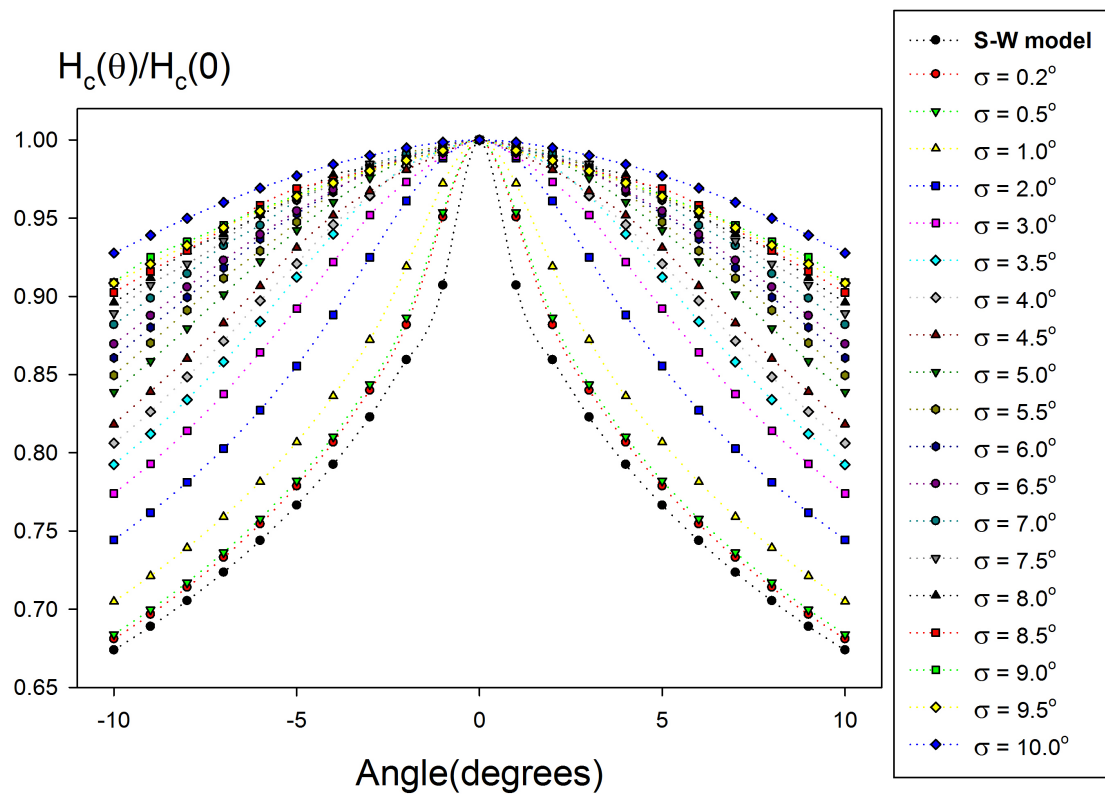


Figure 4.38: Schematic of the easy axis distribution and the applied field

Figure 4.39: The S-W calculation of the variation of  $H_C(\theta)/H_C(0)$  for  $\sigma_\phi = 0$  to 10 degrees

## Notes on units and errors

There are two widely used unit systems in magnetism: the first is the **System International (SI)** unit and the second is the **Gaussian cgs** system. (**SI**) units are the current standard system with the base units of **m, kg, s**, etc. However, the SI system is not favoured in the field of magnetism. The standard system used in magnetic equipment and the magnetic recording industry is the **Gaussian cgs** unit system. These units are also accepted widely in the applied magnetism community. Therefore, the **Gaussian cgs** units has been used for all equations, experimental results and calculations in this thesis. Details of the unit system can be found in Cullity and Graham [6] and O'Handley [22].

The errors on the experimental and numerical results in graphs and tables in this thesis have been calculated based on standard Gaussian error techniques.

---

## CHAPTER V

### Experimental Results

The fundamental magnetic properties of advanced perpendicular recording media have been characterised. The results have also been compared with conventional media in order to study the advantages and disadvantages of media structure. In particular the characterisation of the easy axis distribution using magnetic measurements in perpendicular media has been developed. The physical structure has been investigated and analysed to observe the complex structure of the films and in particular the influence of  $\text{SiO}_2$  at the grain boundaries.

#### 5.1 Structure of Advanced Recording Media

New composite recording media are designed in order to improve the thermal stability, narrow the distribution of easy axis orientation and use  $\text{SiO}_2$  segregation to control the exchange coupling between the grains. Three sets of perpendicular media designs have been studied: the first is a single layer, granular medium which is a conventional PRM. The second is an exchange coupled composite (ECC) medium [12,48] consisting of hard and soft grains with  $\text{SiO}_2$  segregation. The third is an alternative PRM which combines ECC and a coupled granular continuous (CGC) layer [11,14]. This is an ECC structure with a continuous layer on top in which the grains are not segregated with  $\text{SiO}_2$  giving strong intergranular coupling. All samples were supplied by Seagate Media Research of Fremont California using a commercial disk production machine.

Figure 5.1 shows a schematic of the layer structures with a typical cross-section TEM images for each sample. The various layers for each type of medium are similar to each other excluding the storage layer. The substrates were made from a glass ceramic. The adhesion layer is grown on top of the substrate to prevent flaking of the films. The exact composition of the adhesion layer is not known but it is probably a Ta alloy. The next layer is the soft underlayer (SUL). It acts as a magnetic mirror for the single pole write head and also conducts the flux from write head back to the pole. The intermedi-

---

ate/exchange break layers are deposited on top of the SUL. This layer provides exchange decoupling between the SUL and the storage layer. It also acts as a seed layer having in-plane fcc (111) texture to improve the perpendicular orientation of the storage layer. Generally, Ru is used with a thickness of about 25-35 nm.

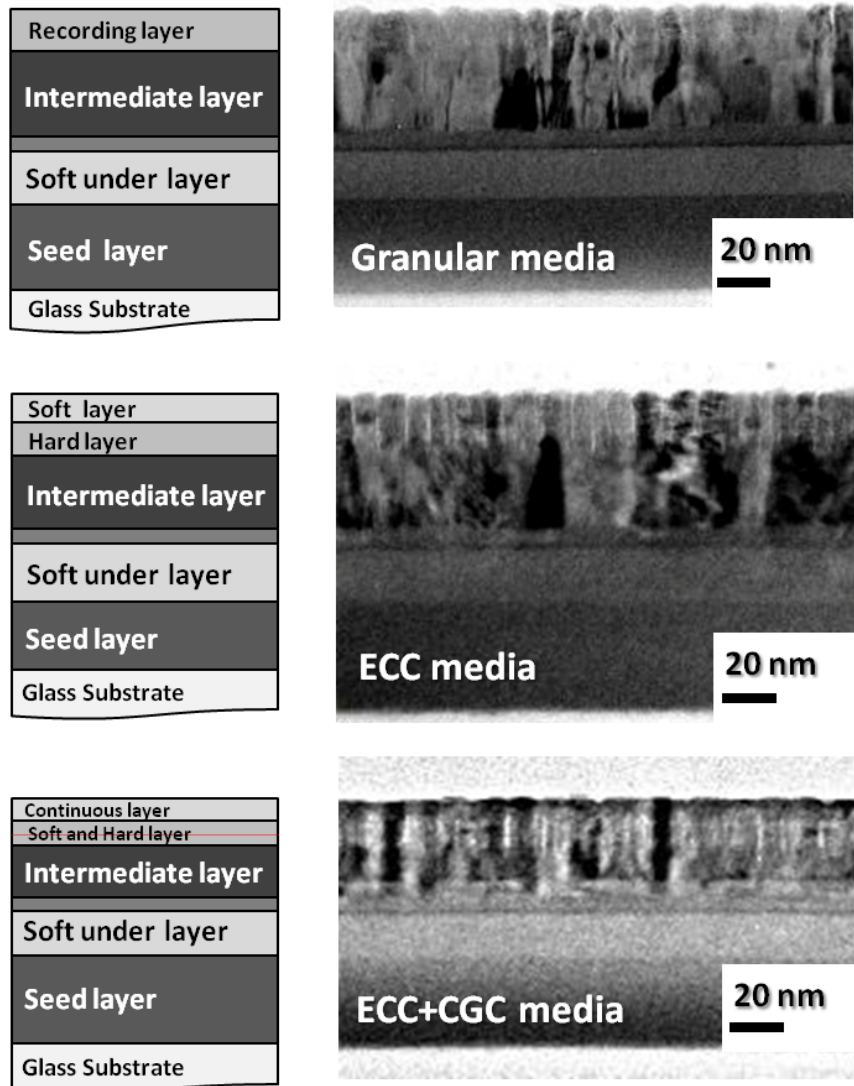


Figure 5.1: Schematic of the structures and typical cross-section TEM images for the three types of media.

The storage layer for all samples was based on a CoCrPt alloy with different levels of silica. On top of the films, a thin diamond-like carbon (DLC) overcoat and lubricant were deposited for tribological reasons.

## Granular Media

Two set of granular media were produced to study the effect of SiO<sub>2</sub> segregation and the effect of easy axis orientation. The two groups provide a good *c*-axis orientation (**GO**) or a poorer orientation (**GPO**) based on the measurement of crystal orientation dispersion  $\Delta\theta_{50}$ . Samples with three different oxide levels denoted high (**h**), medium (**m**), and low (**l**) have been also provided for each group. The structures and the thickness of the recording layer ( $t_g$ ) were exactly the same for all samples. Table 5.1 shows details of the structures and the dispersion of easy axis distribution determined from X-ray rocking curves via the full width half maximum FWHM denoted  $\Delta\theta_{50}$ .

There is no relative error for the measurements of  $\Delta\theta_{50}$  because this data was supplied by Seagate. As discussed in section 4.3.1 the values of  $\Delta\theta_{50}$  give the angular dispersion in the grain orientation of the (0002) of the recording layer which is commonly identified as the easy axis distribution in thin films. From Table 5.1, the values of  $\Delta\theta_{50}$  for the good orientation **GO** with different levels of SiO<sub>2</sub> are about 3.33° to 3.39°. The magnitude of  $\Delta\theta_{50}$  for **GPO** films was about 15% higher than the **GO** films. There was no correlation between the oxide content and the value of  $\Delta\theta_{50}$ . For the storage layer thickness ( $t_g$ ), cross-section TEM samples were prepared to observe the exact thickness. In the case of low magnification resolution, it is clear that the boundary between the recording layer and the intermediate layer (Ru) is difficult to discern as shown in fig.5.1(top). High-resolution (HR)-TEM images were used to measure the thickness at a magnification of about 500k times. The recording layer thickness can be seen clearly via the different texture between the intermediate layer and the CoCrPt alloy as shown in fig.2.2. However, the relative error was still found to be about 5% using DigitalMicrograph software.

Table 5.1: Summary of granular sample parameters.

Samples	Oxide level	$t_g$ (nm) $\pm$ 5%	$\Delta\theta_{50}$ (°)
GO <sub>h</sub>	high	11	3.39
GO <sub>m</sub>	medium	11	3.36
GO <sub>l</sub>	low	11	3.33
GPO <sub>h</sub>	high	11	3.90
GPO <sub>m</sub>	medium	11	3.80
GPO <sub>l</sub>	low	11	3.92

## ECC Media

For the ECC media studied [12], [13], the recording layer consists of a hard layer based on a decoupled hard CoCrPt alloy with SiO<sub>2</sub> segregation and another segregated Co alloy as a switching layer. Exact compositions are not known for commercial reasons. The thickness of the hard layer, ( $t_g$ ) and the soft layer ( $t_s$ ) for all samples was fixed as shown in table 5.2 in order to study the effect of oxide segregation and the dispersion of easy axis orientation. Similarly **EO** and **EPO** refer to ECC samples with good orientation and poorer orientation respectively based on X-ray rocking curve data again supplied by Seagate.

From Table 5.2, the angular dispersion of the crystal orientation for **EO** gave values from 3.31° to 3.37° which was about 15% narrower than **EPO** films. Again, there was no evidence of a relationship between the dispersion of the crystal orientation and the effect of different oxide levels from the X-ray rocking curve measurements. The data for the thickness and  $\Delta\theta_{50}$  were supplied by Seagate and no relative error is known. The thickness of the soft ( $t_s$ ) and hard layers ( $t_g$ ) were examined using cross-section TEM images. It is difficult to measure the exact thickness for each layer from the bright field (BF) HR-TEM images due to the presence of the uniform texture of both layers. The high angle annular dark-field (HAADF) technique discussed in section 4.3.3, was used to investigate the thickness. The contrast of HAADF images which is proportional to  $Z^2$ , allows the thicknesses of both layers to be obtained due to the different contrast of the layers.

Table 5.2: Summary of ECC sample parameters.

Samples	Oxide level	$t_g$ (nm)	$t_s$ (nm)	$\Delta\theta_{50}(^\circ)$
		$\pm 5\%$	$\pm 5\%$	
EO <sub>h</sub>	high	9	5	3.31
EO <sub>m</sub>	medium	9	5	3.37
EO <sub>l</sub>	low	9	5	3.31
EPO <sub>h</sub>	high	9	5	3.97
EPO <sub>m</sub>	medium	9	5	3.83
EPO <sub>l</sub>	low	9	5	3.85

## ECC/CGC Media

For the ECC/CGC media [14], the storage layer was similar to the ECC media

studied but with a CGC layer deposited on top in which the grains are not segregated with SiO<sub>2</sub>. The samples were separated into 2 groups to allow the study of the easy axis distribution. The thickness of the granular layer, ( $t_g$ ) was fixed for all samples. The thicknesses of the soft layer with decoupled grains, ( $t_s$ ) and the continuous layer with coupled grains, ( $t_c$ ) were varied in order to study the effect of the lateral exchange coupling ( $H_{ex}$ ) and the interlayer exchange coupling ( $J$ ). A summary of ECC/CGC structures is shown in Table 5.3. **ECO** and **ECPO** refer to the ECC/CGC samples with good orientation and poorer orientation of the easy axes respectively. All samples are based on a CoCrPt alloy with a high level of silica.

Again the thickness for each layer and  $\Delta\theta_{50}$  were provided by Seagate as shown in Table 5.3. The crystal orientation for the **ECO** group which has an identical thickness to that of the **ECPO** group, and showed a dispersion  $\Delta\theta_{50}$  about 13% narrower for all cases. It is not clear from the X-ray rocking curve measurements if the thicknesses  $t_s$  and  $t_c$  affect the dispersion of the easy axis orientation due to the presence of the similar values of  $\Delta\theta_{50}$  for the ECO and ECPO groups.

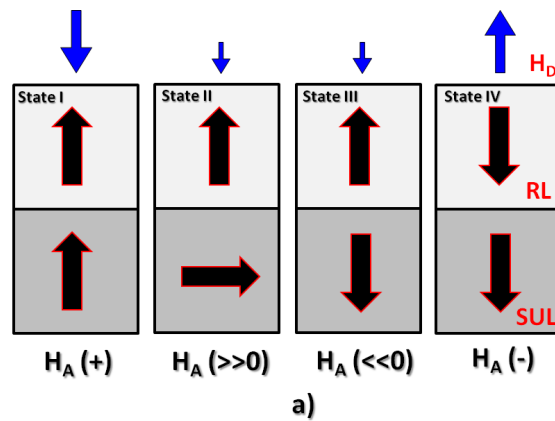
Cross-section TEM images were again obtained to measure the thickness of each layer. The exact thickness is difficult to measure due to the complex structure. The CGC layer on top of the ECC layer was easy to measure from the cross-section image as shown in fig.5.1 due to the presence of the continuous film without SiO<sub>2</sub> segregation. The ECC layers show well segregated columnar grains. However, the thickness of both layers was difficult to measure from the TEM analysis. Therefore, the values of  $t_g$  and  $t_s$  shown in Table 5.3 were provided by Seagate.

Table 5.3: Summary of ECC/CGC sample parameters.

Samples	Oxide level	$t_g$ (nm)	$t_s$ (nm)	$t_c$ (nm)	$\Delta\theta_{50}(^\circ)$
ECO1 <sub>h</sub>	high	9	3	5	3.26
ECO2 <sub>h</sub>	high	9	2	7	3.34
ECO3 <sub>h</sub>	high	9	4	3	3.33
ECPO1 <sub>h</sub>	high	9	3	5	3.71
ECPO2 <sub>h</sub>	high	9	2	7	3.87
ECPO3 <sub>h</sub>	high	9	4	3	3.83

## 5.2 Magnetic Properties of Thin Film Media

The main purpose of the first part of this study was to measure the distribution of easy axis orientation using magnetic measurements. The coercivity technique originally described by Carter *et al.* was used in this work [144]. This technique does not require a correction of demagnetising field,  $H_D$  because  $M = 0$ . The effect of the degree of grain segregation has been also studied via varying the level of  $\text{SiO}_2$ . The basic properties of all samples have been determined in order to compare the advantages and disadvantages of each media design.



ECC/CGC Sample

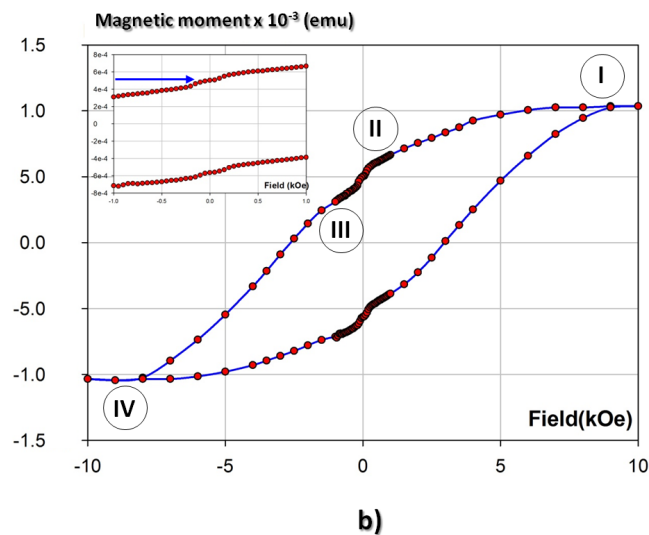


Figure 5.2: a) Schematic of the magnetisation reversal in different applied fields and b) the magnetisation curve measured using a VSM for sample  $\text{ECO1}_h$

A polar magneto-optic Kerr effect (MOKE) magnetometer was used. The measurements were made at room temperature using a maximum applied field of 12 kOe. Hysteresis loops were measured and normalised to the maximum Kerr value giving the loop in terms of  $M/M_S$ . Several parameters can be obtained directly from the magnetisation curve such as  $H_n$ ,  $H_C$ , the loop squareness  $M_R/M_S$ , and the slope of the magnetisation curve at  $H_C$  which gives a rough measure of the intergranular exchange coupling. The one parameter which cannot be obtained directly from MOKE is the saturation magnetisation. The magnetic moment of the film can be measured using a VSM. Figure 5.2 shows a schematic of the magnetisation reversal of the 4 different states and a hysteresis loop of sample ECO1<sub>h</sub> from a VSM measurement. The determination of the saturation moment from the recording layer is fully described in section 4.2.5.

### 5.2.1 Granular Media with Different Oxide Levels

Two sets of normalised magnetisation curves for samples with good and poor easy axis distributions with three different level of silica oxides are shown in figure 5.3 a) and b) respectively. The structure of all samples is the same. It is clear that the dispersion of easy axis orientation and the level of SiO<sub>2</sub> have a significant effect on the magnetic properties especially  $H_C$ ,  $M_R/M_S$  and the slope of the curve at  $H_C$ . A summary of the parameters is shown in Table 5.4.

The effect of orientation is clear from the curves in figure 5.3 and the data in Table 5.4. The coercivity, in particular for the samples with low levels of SiO<sub>2</sub> (GO<sub>l</sub> and GPO<sub>l</sub>), is reduced by about ~35% for identical structures. The value of the loop squareness ( $M_R/M_S$ ) of all samples with good orientation is almost equal to 1 whereas it drops by 10 to 15 % for the PO group. This shows that the effect of the easy axis distribution dominates  $H_C$  and the loop squareness due to the torque from the applied field reducing the energy barrier of the grains.

The level of SiO<sub>2</sub> segregation also affects the coercivity  $H_C$  and the slope of the magnetisation curve at  $H_C$ . For the samples with a high level of SiO<sub>2</sub>, the coercivity is 7.51 kOe and 6.50 kOe for the **O** and **PO** groups respectively which is ~50% higher than the values for the samples with low levels of SiO<sub>2</sub>. Increasing the level of SiO<sub>2</sub> also reduces the median grain size due to the silica restricting the grain growth. From the simple theory of non-interacting single domain particles this would be expected to reduce the coercivity following equation 5.1 [15]. However the effect of the grain

segregation eliminates the intergranular exchange coupling. This prevents co-operative reversal where the grain with the smallest energy barrier reverses and those with larger energy barriers are then switched by the exchange field from the first grain. The silica also makes the grain size more uniform eliminating small grains which can initiate co-operative reversal in this so called *weak link* mechanism.

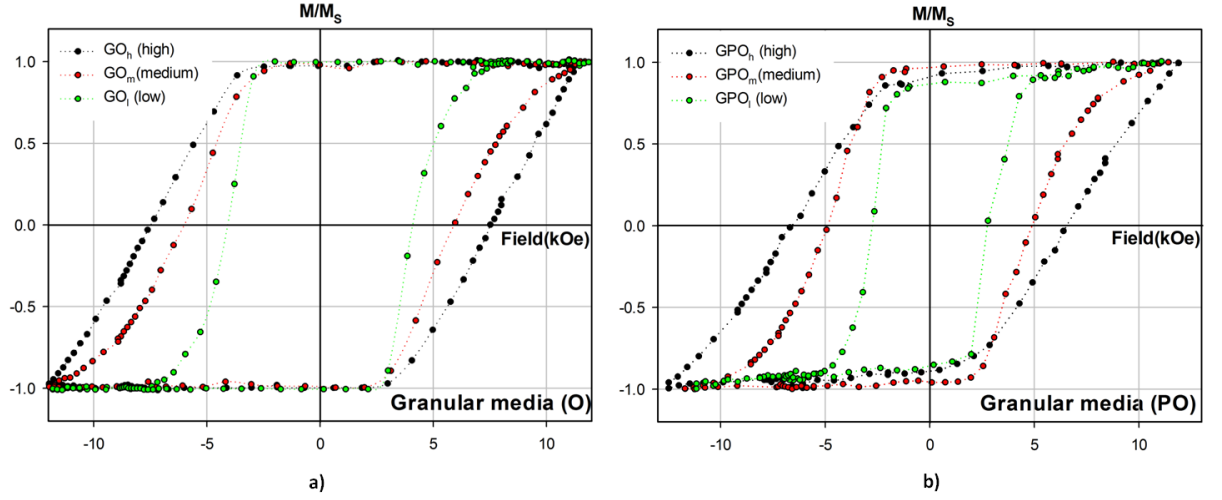


Figure 5.3: Magnetisation curves  $M(H)$  of the granular samples a) good easy axis orientation and b) poor easy axis orientation.

Table 5.4: Summary of the magnetic properties of granular samples.

Samples	$H_C$ (kOe)	$H_n$ (kOe)	$M_R/M_S$	$M_S$	slope $_{H_C} \times 10^{-4}$
	$\pm 1\%$	$\pm 1\%$			
$GO_h$	7.51	2.48	0.95	530	2.35
$GO_m$	5.96	2.22	0.98	530	3.06
$GO_l$	4.10	2.13	0.99	540	6.77
$GPO_h$	6.50	1.99	0.90	530	2.02
$GPO_m$	4.87	1.75	0.96	520	3.67
$GPO_l$	2.74	0.96	0.86	545	8.55

The films are also deposited on heated substrates. This is done to improve the segregation and crystallinity of the  $SiO_2$ . However it will also improve the crystallisation of the CoPtCr alloys which will increase the value of the anisotropy constant ( $K$ ) and improve its uniformity. The use of the Ru decoupling layer will aid this effect. Both

these effects will result in a narrow SFD. Therefore the energy barrier distribution has been minimised. This is obvious from fig.5.3 where the slope of the curve at  $H_C$  decreases when the level of  $\text{SiO}_2$  is increased.

$$H_C = \alpha H_K \left[ 1 - \left( \frac{25k_B T}{K_U V} \right)^2 \right] \quad (5.1)$$

In equation 5.1 the orientation factor,  $\alpha$  represents the angular effect of the Co-alloy  $c$ -axis orientation of a given grain. Given that the grain volume and the anisotropy constant have now been made highly uniform and the intergranular exchange coupling essentially eliminated, this makes the orientation factor critical in controlling the barrier and hence the SFD.

Whilst the  $c$ -axis orientation can be determined from the X-ray rocking curves, this is an indirect measurement of the magnetic easy axis distribution. As discussed in section 4.3.1 it is also a relatively insensitive measurement. Hence the distribution of magnetic easy axes is the most appropriate measurement of  $\alpha$ .

### 5.2.2 ECC Media with Different Oxide Levels

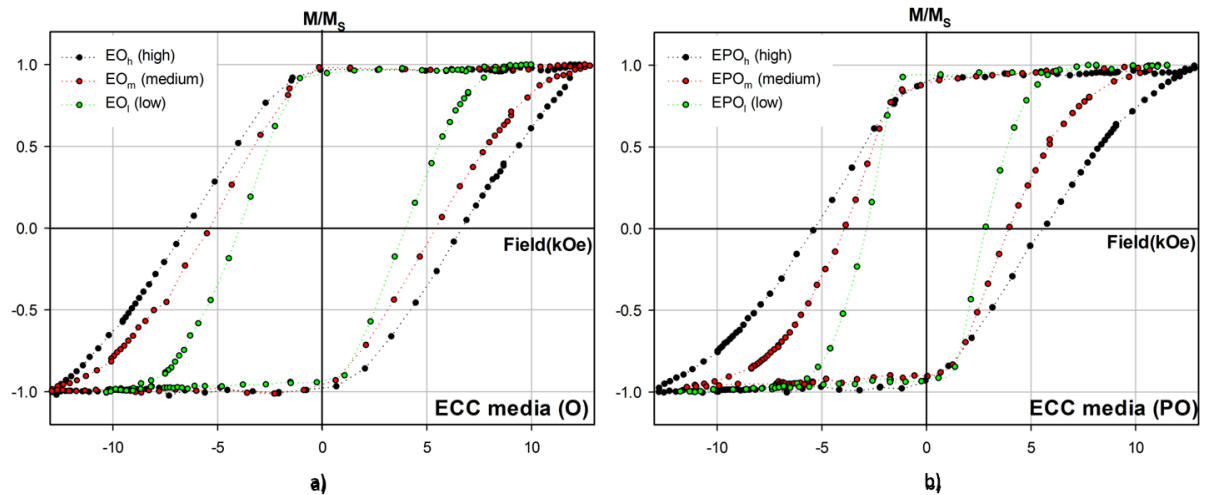


Figure 5.4: Magnetisation curves of ECC samples a) good easy axis orientation and b) poor easy axis orientation

Table 5.5: Summary of the magnetic properties of ECC samples.

Samples	$H_C$ (kOe) $\pm 1\%$	$H_n$ (kOe) $\pm 1\%$	$M_R/M_S$	$M_S$ (emu/cc)	slope $ _{H_C} \times 10^{-4}$ (Oe $^{-1}$ ) $\pm 1\%$
EO $_h$	6.75	1.42	0.97	480	1.95
EO $_m$	5.41	1.04	0.98	450	2.27
EO $_l$	3.97	1.03	0.95	450	3.00
EPO $_h$	5.46	0.99	0.90	470	1.81
EPO $_m$	3.93	0.66	0.89	460	2.97
EPO $_l$	2.98	0.60	0.93	460	5.74

The normalised magnetisation curves of the ECC samples for **EO** and **EPO** are shown in figure 5.4 a) and b) respectively. A summary of the magnetic properties is given in Table 5.5. The effect of the orientation and SiO<sub>2</sub> segregation causes the magnetic properties to vary in a systematic manner which are similar in many respects to the granular samples. Interestingly, the value of coercivity for all ECC samples is lower than that for the granular media set due to the presence of the soft layer. It is well established that exchange coupling between two layers leads to co-operative reversal within each grain where the low anisotropy layer switches and the layer with higher anisotropy reverses in a single event [164]. The thermal stability and writing capability are also improved by the ECC design. The effect of the dispersion of the crystal orientation also affects the magnetic properties of the ECC media. In the case of identical structures with high, medium and low oxide levels,  $H_C$  for samples with poor orientation was reduced by about 25% to 30% due to the wide distribution. The loop squareness of EO samples is almost equal to 1 whilst it is reduced to about 0.9 for the PO group. It is obvious that the dispersion of the easy axis orientation is the significant factor affecting the magnetic properties of the recording media.

Moreover, the effect of oxide levels and the presence of the soft layer causes a shearing of the hysteresis loop and lowers the nucleation field which can be seen via a reduction of the slope of loop at  $H_C$  [14]. In a micromagnetic study by Nolan *et al.* [14], increasing the soft layer thickness can reduce the crystal anisotropy field ( $H_K$ ) of the hard layer leading to a reduction of  $H_C$  and  $H_n$  due to the strong interlayer exchange coupling ( $J_{ex}$ ) which is dominant. However increasing the thickness of the ECC layer does not cause a shearing of the hysteresis loop because the mechanism of magnetisation

reversal of ECC media does not change the lateral exchange coupling ( $H_{ex}$ ) between the grains. Therefore, the main factor controlling the shearing of the loops comes from the effect of  $\text{SiO}_2$  at the grain boundaries controlling  $H_{ex}$ . From Table 5.5, the values of the slope at  $H_C$  for  $\text{EO}_l$  and  $\text{EPO}_l$  at a low level of oxide are  $3.00 \times 10^{-4}$  and  $5.74 \times 10^{-4}$  respectively which is 50% steeper than that for the samples with a high level of  $\text{SiO}_2$ . Deakin *et al.* [30] found that the introduction of oxide in ECC media can reduce not only the in-plane exchange coupling but also the interlayer exchange coupling. Therefore, the magnetisation reversal of the samples with the low oxide levels shows co-operative reversal of the small grains with low energy barriers switching the grains with higher energy barriers.

### 5.2.3 ECC/CGC Media with Different Thicknesses

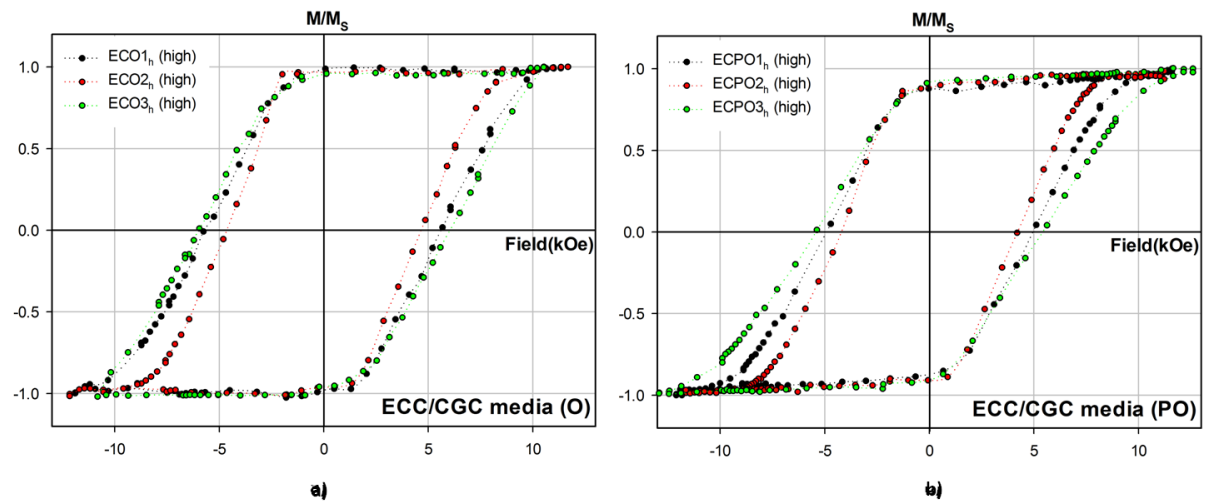


Figure 5.5: Magnetisation curves of ECC/CGC samples a) good easy axis orientation and b) poorer easy axis orientation

Figure 5.5 a) and b) shows two groups of hysteresis loops for the ECC/CGC samples with good and poorer axis orientation respectively. It should be noted that all samples are fabricated with a high level of  $\text{SiO}_2$ . The summary of the magnetic properties for all samples is given in Table 5.6. The magnetic properties of the ECC sample with a high oxide level for **O** and **PO** is also presented in Table 5.6 in order to compare the properties with these of the ECC/CGC samples. The effect of the easy axis orientation is clear from the loop squareness.  $M_R/M_S$  and the nucleation field of the good orientation

Table 5.6: Summary of the magnetic properties of ECC/CGC samples.

Samples	$H_C$ (kOe) $\pm 1 \%$	$H_n$ (kOe) $\pm 1 \%$	$M_R/M_S$	$M_S$ (emu/cc)	slope $_{H_C} \times 10^{-4}$ (Oe $^{-1}$ ) $\pm 1 \%$
ECO1 $_h$	5.60	1.12	0.99	455	2.49
ECO2 $_h$	4.64	1.38	0.97	455	3.17
ECO3 $_h$	6.03	1.04	0.95	480	2.40
ECPO1 $_h$	4.94	0.94	0.86	455	2.43
ECPO2 $_h$	4.20	0.95	0.88	450	2.85
ECPO3 $_h$	5.42	0.66	0.91	480	1.94
EO $_h$ *	6.75	1.42	0.97	480	1.95
EPO $_h$ *	5.46	0.99	0.90	470	1.81

samples are almost 1 and 1.4 kOe respectively while the **PO** group shows a reduction of  $M_R/M_S$  and  $H_n$  of about 10% and 30% respectively for all samples.

The thickness of soft layer and continuous layer controls the interlayer exchange coupling and the intergranular exchange coupling enhances the nucleation field, thermal stability and the switching field distribution of the films. However, the combination and optimization of the interactions is very complicated and it is required to understand the mechanism of magnetisation reversal. From Table 5.6 it clear that ECO2 $_h$  and ECPO2 $_h$  with the thinnest soft layers of  $t_s \sim 2$  nm and the thickest  $t_c \sim 7$  nm in each group provide the lowest  $H_C$  and the highest  $H_n$ . A further semi-quantitative measure of the intergranular exchange interaction is the slope of loop at  $H_C$  [36]. The gradients for ECO2 $_h$  and ECPO2 $_h$  are steeper than those for the other samples by about 30%. This implies that the switching field distribution is narrow. By comparison with the ECC samples with high oxide levels (EO $_h$  and EPO $_h$ ), the coercivity of samples which have a continuous layer on top is lower than that of the ECC samples. In particular,  $H_C$  of ECO2 $_h$  and ECPO2 $_h$  which have the thickest continuous layers with good and poor orientation respectively are reduced by about 30% compared to the ECC sample and the slope of loop at  $H_C$  is higher by 35%.

Nolan *et al.* [14] showed the effect of composite designs of ECC and CGC media by modelling the hysteresis loops using a Voronoi grain structure with the Landau-Lifshitz-Gilbert (LLG) equation to optimise the interactions. They assumed that the single grains of the soft and hard layers are segregated from each other. The magnetisation

reversal process showed grains switching independently leading to a wide switching field distribution. With a CGC layer which has strong intergranular coupling on top, the ECC layer acts to control the magnetisation reversal of the hard layer. The magnetisation of the grains of the storage layer will rotate and switch when the torque from CGC layer is transferred across the interface. Therefore, ECC/CGC media can reduce the coercivity and the switching field distribution.

## 5.3 Easy Axis Distributions

### 5.3.1 Experimental Studies

There have been a number of attempts to investigate the easy axis distribution by measuring the crystalline  $c$ -axis dispersion from the FWHM of X-ray rocking curves [147], [145]. However, magnetostatic and exchange interactions are not included in this measurement. Therefore, magnetic measurements are preferred for the characterisation of the *effective* easy axis distribution. The traditional remanence method [145–147] to measure the easy axis distribution for LRM cannot be used for PRM due to the effect of  $H_D$ .

We now present a new technique to extract the effective easy axis distribution from the variation of coercivity with angle [143, 144, 165] as discussed in section 4.2.3. The advantage of this technique is that the global demagnetising field is zero at the coercivity [28]. Due to the requirement to vary the angle between the sample plane and the applied field ( $\theta$ ) and the presence of SUL, conventional magnetometry and the simple polar MOKE cannot be used to make these measurements. Hence, an angular dependent MOKE at Seagate Media Research in Fremont was used.

The measurements were made at room temperature with a maximum applied field of 3.0 Tesla. The magnetisation curve for each sample was measured without correction for  $H_D$ . The sample was saturated with  $H_{sat} = \pm 15$  kOe and a field step of 50 Oe was used. The measurements were repeated varying the angle. The results were normalised to the maximum signal amplitude which is proportional to the saturation magnetisation.

Figure 5.6 shows typical normalised hysteresis loops at various angles from  $0^\circ$  to  $10^\circ$  for the ECO2<sub>h</sub> sample. Note that only 3 loops are shown for clarity but measurements were made at  $1^\circ$  intervals. The normalised remanence ( $M_R/M_S$ ) for all samples

does not change at these low angles. It does not change for angles up to  $10^\circ$ . There were a number of attempts to measure the effective easy axis distribution by the variation of remanence ratio ( $M_R/M_S$ ) with angle [145–147] which was the traditional characterisation for LRM. This technique originally was applied to measure PRM by Wu *et al.* [145]. The measurement was difficult to interpret due to the small change in  $M_R/M_S$  with angle ( $< 5\%$ ) and the fact that the true zero field cannot be determined due to the demagnetising field  $H_D$  in PRM. The internal  $H_D$  was calculated by micromagnetic simulation leading to increased error for this technique. In 2005, Voznyuk *et al.* [147] also reported the measurement of the easy axis distribution CoCr<sub>18</sub>Pt<sub>12</sub> alloy using the traditional remanence method. Moreover, the anisotropy dispersion,  $\Delta\theta_K$  and the crystal orientation were determined by a Monte Carlo simulation using a Landau-Lifshitz-Gilbert formulation and X-ray rocking curve respectively in order to compare with the traditional  $M_R/M_S$ . They found that the results from the variation of remanence gave a wide distribution from  $15^\circ$  to  $29^\circ$ . There was no apparent correlation with the simulation results and  $\Delta\theta_{50}$  which varied from  $5.2^\circ$  to  $8.4^\circ$ . It is clear that this technique is not sensible and suitable for PRM characterisation. The variation of  $H_C$  provides a much larger change of up to 20% and hence gives a more sensitive measurement of the effect of orientation.

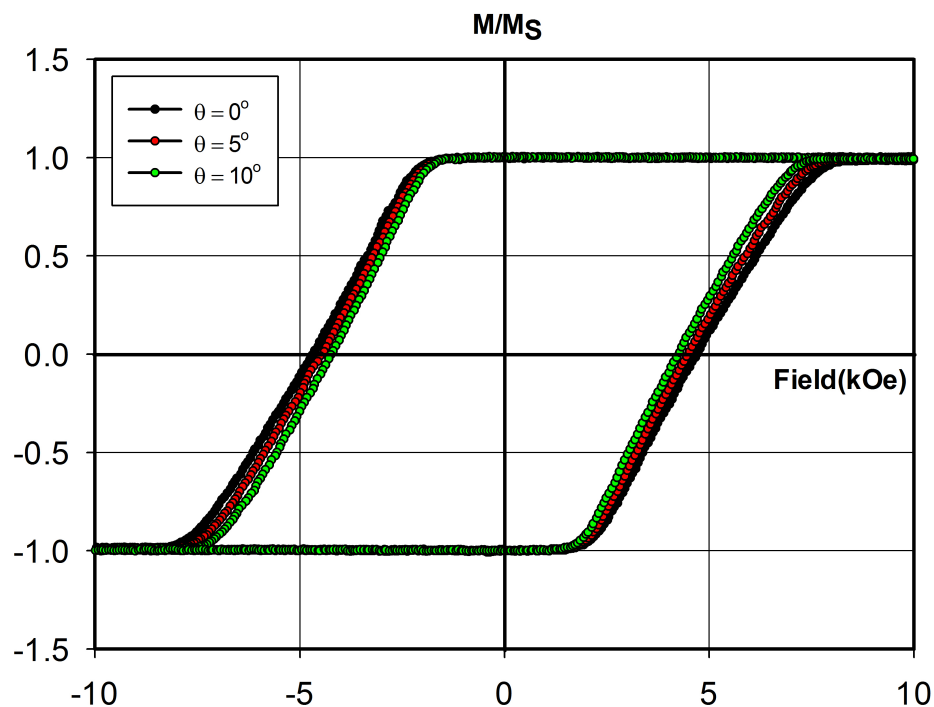


Figure 5.6: Typical magnetisation curves  $M(H)$  at different angles for sample ECO<sub>2h</sub>

The value of the coercivity is a maximum at zero degrees and decreases with increasing angle from  $0^\circ$  to  $10^\circ$ . A summary of the coercivity at different angles with a  $2^\circ$  step is shown in Tables 5.7 to 5.9 for granular, ECC and ECC/CGC media respectively.

## Granular Media

Table 5.7: Coercivity at different angles for granular samples.

Samples \ $H_C$ (kOe)	$H_C(0^\circ)$	$H_C(2^\circ)$	$H_C(4^\circ)$	$H_C(6^\circ)$	$H_C(8^\circ)$	$H_C(10^\circ)$
	$\pm 1\%$					
$GO_h$	8.60	8.19	7.86	7.56	7.35	7.03
$GO_m$	6.32	6.06	5.82	5.56	5.43	5.24
$GO_l$	4.22	4.14	4.02	3.90	3.80	3.70
$GPO_h$	6.71	6.27	5.93	5.74	5.53	5.33
$GPO_m$	5.04	4.92	4.76	4.61	4.49	4.37
$GPO_l$	3.07	3.02	2.98	2.96	2.90	2.85

## ECC Media

Table 5.8: Coercivity at different angles for ECC samples.

Samples \ $H_C$ (kOe)	$H_C(0^\circ)$	$H_C(2^\circ)$	$H_C(4^\circ)$	$H_C(6^\circ)$	$H_C(8^\circ)$	$H_C(10^\circ)$
	$\pm 1\%$					
$EO_h$	7.13	6.95	6.71	6.48	6.28	6.04
$EO_m$	5.72	5.57	5.39	5.18	5.03	4.87
$EO_l$	4.33	4.20	4.06	3.91	3.79	3.70
$EPO_h$	6.18	6.01	5.84	5.66	5.50	5.33
$EPO_m$	4.65	4.55	4.41	4.31	4.17	4.08
$EPO_l$	3.48	3.42	3.33	3.26	3.16	3.10

## ECC/CGC Media

Table 5.9: Coercivity at different angles for ECC/CGC samples.

Samples\H <sub>C</sub> (kOe)	H <sub>C</sub> (0°)	H <sub>C</sub> (2°)	H <sub>C</sub> (4°)	H <sub>C</sub> (6°)	H <sub>C</sub> (8°)	H <sub>C</sub> (10°)
	± 1%	± 1%	± 1%	± 1%	± 1%	± 1%
ECO1 <sub>h</sub>	5.70	5.59	5.45	5.31	5.17	5.05
ECO2 <sub>h</sub>	4.70	4.63	4.54	4.44	4.34	4.26
ECO3 <sub>h</sub>	6.55	6.40	6.22	6.00	5.84	5.67
ECPO1 <sub>h</sub>	5.18	5.09	5.00	4.86	4.74	4.62
ECPO2 <sub>h</sub>	4.54	4.47	4.39	4.29	4.19	4.10
ECPO3 <sub>h</sub>	5.85	5.76	5.63	5.45	5.30	5.18

From Tables 5.7 to 5.9, the maximum reduction of the coercivity at an angle of 10° was 19%, 16% and 13% for granular, ECC and ECC/CGC films respectively. The results agreed well with the previous work of Carter *et al.* [144] that showed the variation of coercivity of CoCrPt alloy PRM changed by 15% for  $\theta = 10^\circ$ .

### 5.3.2 Theoretical Calculations

In order to investigate the effect of the distribution of *c*-axis orientation, Stoner Wohlfarth calculations as discussed in section 4.4.1 have been used to compare with the MOKE results. Figure 5.7 shows the calculated variation of the normalized coercivity with angle from -10° to +10°. As seen in fig.5.7 the variation of H<sub>C</sub> follows the Stoner-Wohlfarth theory [15] in the case of  $\sigma_\phi = 0$  which is the aligned case which produces a highly peaked curve and the expected 30% reduction in H<sub>C</sub> at an angle of 10°. The variation is seen to broaden as the distribution of easy axis orientation increases.

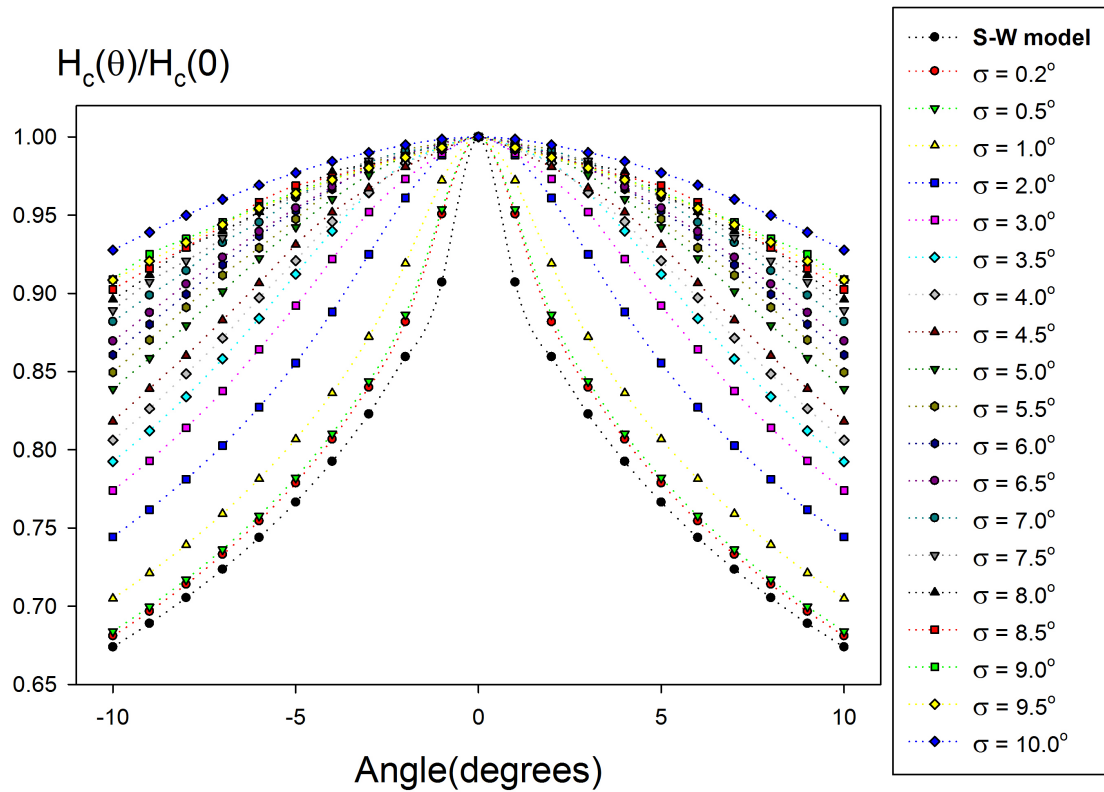


Figure 5.7: The Stoner Wohlfarth calculation of the variation of  $H_C(\theta)/H_C(0)$  for  $\sigma_\phi = 0$  to 10 degrees (courtesy of P. Chureemart)

In order to compare with the calculated values of  $H_C$  from the S-W model with a Gaussian distribution of easy axis orientation,  $f(\phi)$  for different values of  $\sigma_\phi$  from  $0^\circ$  to  $10^\circ$ , the values of coercivity from Table 5.7 to 5.9 were normalised to the maximum value of  $H_C$  at  $\theta = 0$ . Figure 5.8 shows the typical angular variation of  $H_C$  from the experimental and numerical results for the granular samples. The variation of  $H_C$  was examined for the granular films with the same functional layers but with different levels of oxide and also different orientations as shown in fig.5.8 a) and b) respectively. The variation of  $H_C$  for  $GO_l$  shows that the easy axis distribution is narrower than that for  $GPO_l$  which is consistent with the values obtained from X-ray rocking curves. The results from the calculations indicate the data correspond to value of  $\sigma_\phi$  lying between  $5^\circ$  and  $6^\circ$  for  $GO_l$  and about  $10^\circ$  for  $GPO_l$ . The crystal orientation dispersion  $\Delta\theta_{50}$  gave values of 3.33 and 3.92 for  $GO_l$  and  $GPO_l$  respectively. This shows that the distribution of magnetic easy axes does not depend solely on the crystalline orientation. Other factors and in particular exchange and dipole-dipole interaction affect the data. In general exchange interactions will keep the moments of the grains aligned parallel and

create an effective distribution of easy axes that is narrower than the physical spread. Dipole-dipole interactions will tend to broaden the effective distribution especially when determined at  $H_C$  where 50% of the grains are oriented in opposite directions. However the recording performance of a medium depends on its magnetic response which includes all the magnetic effects and not just the crystal orientation.

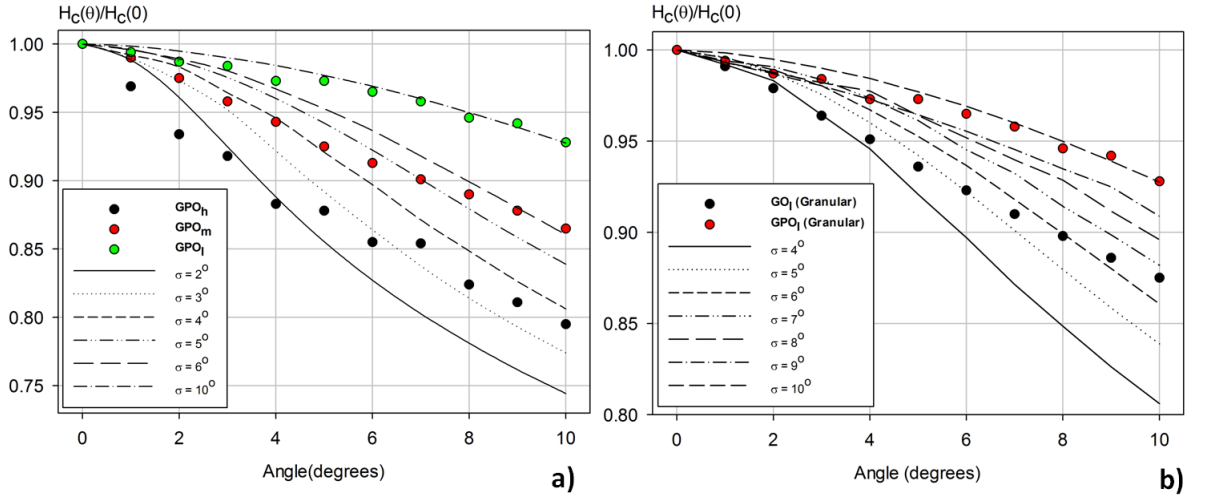


Figure 5.8: Angular variation of  $H_C$  from the experimental (dot) and numerical results (line) of granular samples; a) GPO at the different levels of  $\text{SiO}_2$  and b) GO and GPO at low  $\text{SiO}_2$

Fig.5.8 a) shows the comparison of the variation of  $H_C$  for the granular films with differing levels of silica. The results indicate that the width of the effective easy axis distribution decreases as the oxide content is increased. This is consistent with the effect of grain segregation by  $\text{SiO}_2$  leading to exchange decoupling [99]. The values of  $\Delta\theta_{50}$  from X-ray rocking curves were  $3.90^\circ$ ,  $3.80^\circ$  and  $3.92^\circ$  from high to low levels of oxide. These results do not differentiate the samples in terms of the different levels of  $\text{SiO}_2$ . This again shows that the measurement of coercivity as a function of angle provides a more sensitive and appropriate measurement [143].

In a previous work [143], we demonstrated that the coercivity technique for the measurement of the effective easy axis distribution comparing measurements with a S-W model integrated across a distribution. We found that the results were in good agreement for exchange decoupled CoCrPt alloy granular media. This technique has now been used to study the orientation distribution in various media structures such as  $\text{GO}_h$ ,  $\text{EO}_h$  and

$\text{ECO}_{2h}$  with a good orientation and a high level of  $\text{SiO}_2$ .

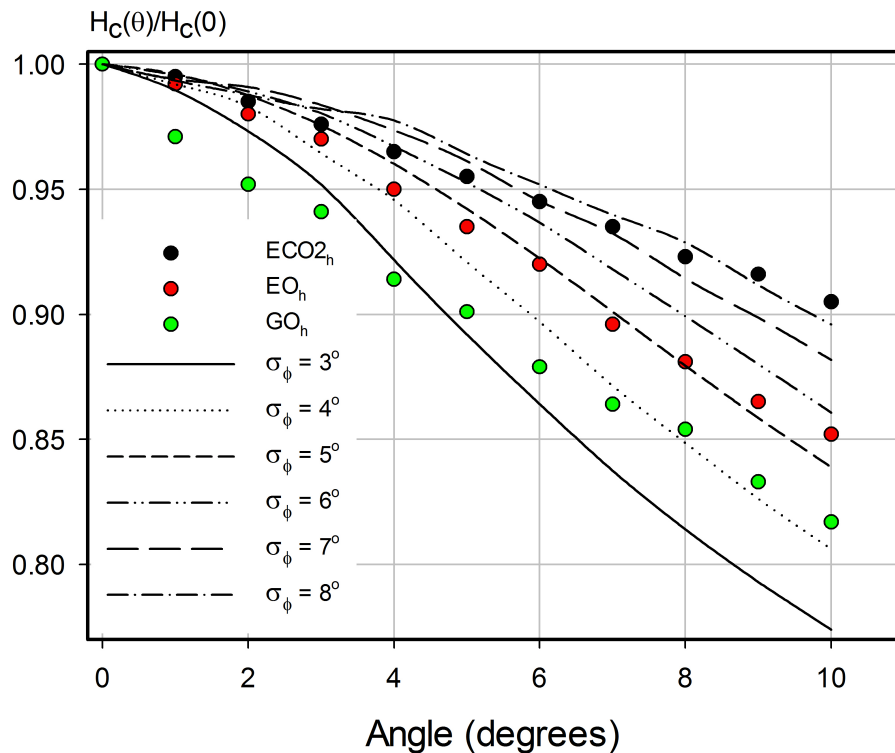


Figure 5.9: Angular variation of  $H_C$  from the experimental (dot) and numerical results (line) for the various structures with high  $\text{SiO}_2$

Figure 5.9 shows the angular variation of coercivity for the different structures together with the calculated values. Note the high resolution on the  $H_C$  axis. The variation of  $H_C(\theta)$  for the granular medium,  $\text{GO}_h$  shows that the easy axis distribution is narrow with  $\sigma_\phi = 3^\circ$ . The experimental data does not lie directly on any of the calculated lines. However the result indicates the data correspond to values of  $\sigma_\phi$  lying between  $3^\circ$  and  $4^\circ$ . This may be due to the actual distribution not following a Gaussian form. However there is no evidence that this is the case. Another possible explanation is that this may be due to intergranular coupling effects. TEM analysis, shown in fig.5.10 shows that whilst this sample has a high degree of  $\text{SiO}_2$  segregation, it is far from perfect. Hence some degree of intergranular exchange coupling may still be present.

A further possibility is that because the energy barrier of a given grain is strongly dependent on angle, the time dependence at higher angles may be significantly larger than at angles close to  $0^\circ$ . This would lead to an increase in the sweep-rate dependence

of coercivity particularly for the samples with the best orientation such as  $GO_h$ . For all measurements a constant sweep rate of 2500 Oe/s was used. However as discussed below, similar effects are not seen for the other samples even though all the distributions have values of  $\sigma_\phi$  of less than  $8^\circ$ . Hence this effect is relatively small and the most likely cause of the relatively poor fit for sample  $GO_h$  remains intergranular coupling.

The distribution of easy axes for the ECC medium,  $EO_h$  gives an excellent fit to the theory for  $\sigma_\phi = 5^\circ$ . This implies that the distribution is close to a Gaussian. Inspection of fig.5.10 shows that the grain segregation by  $SiO_2$  is almost perfect in this sample. We believe that these grains are almost perfectly exchange decoupled. This result also supports the contention that the poorer fit for sample  $GO_h$  is a result of exchange coupling.

The  $ECO_2h$  medium shows a much wider distribution with  $\sigma_\phi = 8^\circ$ . The distribution as measured also appears not to be Gaussian as the measured values cross the curves for standard deviations ranging from  $5^\circ$  to  $8^\circ$ . The structure of the  $ECO_2h$  sample is the most complex of all the media studied. The TEM image in fig.5.10 c) seems to indicate that the silica segregation is not as complete as that in the  $EO_h$  film. However the CGC over-layer has no silica segregation and will be exchange coupled. This may lead to an indirect exchange coupling between the grains in the ECC layer and may distort the distribution.

In order to examine the effect of  $SiO_2$  segregation on the measured distribution, in-plane bright field (BF) TEM images and the grain size distribution were obtained. Figure 5.10 shows the TEM images and the measured size distribution for all samples. The  $SiO_2$  boundary for the  $GO_h$  sample is thinner than for the other media. The in-plane structure of  $ECO_2h$  shows uniform grains but incomplete grain boundary segregation by  $SiO_2$ . In principle the physical orientation of the  $ECO_h$  grains should be the same as that for the ECC sample but the CGC layer creates coupling and widens the distribution. The median diameter  $D_m$  of the grains for the  $GO_h$  and  $ECO_2h$  samples were 11.6 nm and 6.32 nm with the standard deviations of the lognormal distributions  $\sigma_{lnD} = 0.16$  and 0.14 respectively. For the  $EO_h$  sample,  $D_m$  was 6.70 nm with  $\sigma_{lnD} = 0.11$  which is the smallest standard deviation of all the media studied. For each sample more than 600 grains were measured to obtain the distribution to high resolution. Cross-section TEM samples were also prepared to observe the uniformity of the silica segregation as shown in fig.5.1. It is clear again that the ECC medium shows well segregated columnar grains

whereas the  $\text{SiO}_2$  of the granular medium is thinner than that for the other media. For  $\text{ECO}_2h$  media the boundary between columnar grains and the CGC layer is clear.

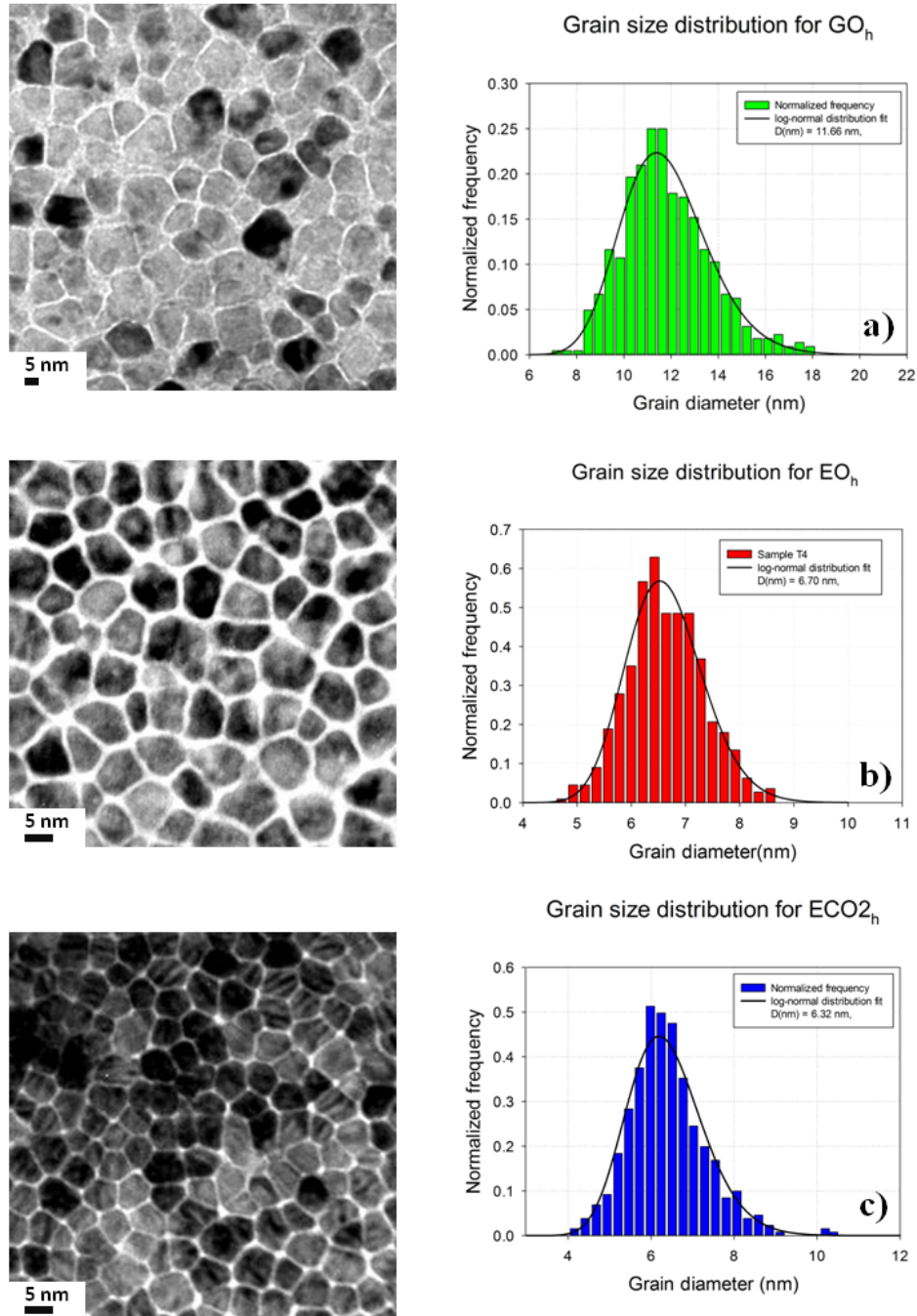


Figure 5.10: Bright Field (BF) in-plane images and normalised grain size distributions a) granular media,  $\text{GO}_h$ , b) ECC media,  $\text{EO}_h$  and c) ECC/CGC media,  $\text{ECO}_2h$

### 5.3.3 Coercivity of Complex Structures

The effective easy axis distribution of the most advanced type of ECC/CGC media with a high level of SiO<sub>2</sub> and good orientation was also investigated by comparison to the integrated S-W model as shown in fig.5.11. The experimental results do not lie directly on any of the calculated lines. The results indicate that the ECO2<sub>h</sub> medium with a maximum thickness of CGC layer of about 7 nm shows a much wider distribution corresponding to a value of  $\sigma_\phi$  between 5° and 8° whereas the ECO3<sub>h</sub> sample with the thinnest CGC layer of 3 nm shows a narrow distribution with  $\sigma_\phi = 5^\circ$  to 6°. This indicates that the wider distribution most probably comes from the effect of the CGC layer via the strong exchange coupling between CGC and ECC layers. However, the magnetic properties of ECO2<sub>h</sub> sample such as the thermal stability, nucleation field and gradient of the loop at H<sub>C</sub> are improved as shown in Table 5.6.

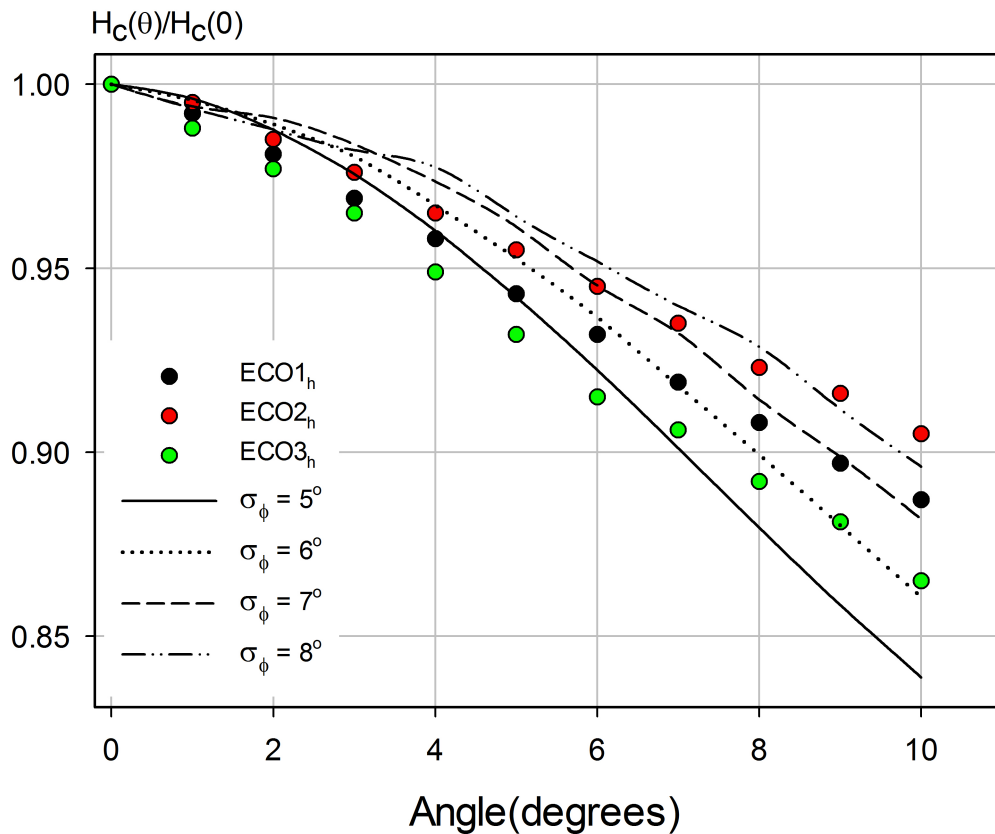


Figure 5.11: Angular variation of H<sub>C</sub> from the experimental (dot) and numerical results (line) for ECO samples with the different thickness ratios and high SiO<sub>2</sub> content

The results are consistent with the simulation of hysteresis loops with the thickness of CGC layer by Nolan *et al.* [14]. They showed that the loop squareness increases and  $H_C$  reduces as the thickness of  $t_c$  is increased due to the increase in the lateral exchange coupling,  $H_{ex}$  [14]. This can lead to a much wider distribution of easy axis orientations.

For advanced ECC/CGC recording media a further complication arises due to the different coercivities in the ECC and CGC layers. For this system the coercivity of the overall sample will be a combination of the reversal in each of the layers. In a normal single layer and ECC media there is little if any reversible component of the magnetisation. Hence, the coercivity is given by the criterion

$$\int_0^{\Delta E_C(H_C)} f(\Delta E) d\Delta E = \int_{\Delta E(H_C)}^{\infty} f(\Delta E) d\Delta E \quad (5.2)$$

where  $f(\Delta E)d(\Delta E)$  is the distribution of energy barriers often described via the switching field distribution (SFD). For the case of the ECC/CGC media, the soft CGC layer must be included, so the coercivity is now

$$\int_0^{\Delta E_C(H_C)} f(\Delta E)_{soft} d(\Delta E)_{soft} + \int_0^{\Delta E_C(H_C)} f(\Delta E) d(\Delta E) = \int_{\Delta E(H_C)}^{\infty} f(\Delta E) d\Delta E \quad (5.3)$$

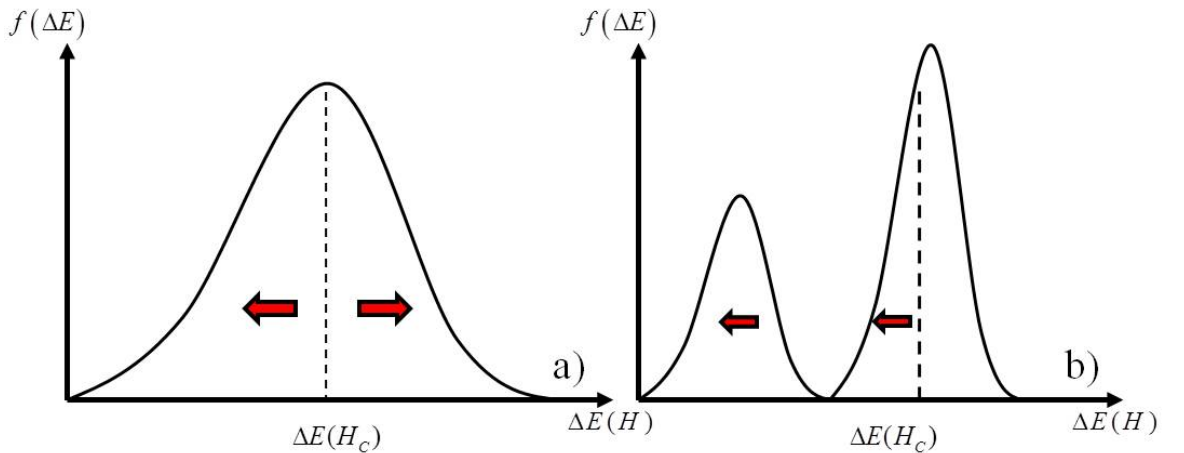


Figure 5.12: Schematic of the distribution of the energy barriers for a) a normal granular of ECC media, b) the ECC/CGC medium

These two criteria are shown schematically in fig. 5.12 a) and b). Because the CGC layer is soft it is likely to be saturated, or nearly so, at  $H_C$ . This will distort the value of  $H_C$  and may not be uniform with angle, even at the small angles used in this study. Hence an alternative technique based on the measurement of the remanent coercivity,  $H_{cr}$  may be required. The measurement of the variation of  $H_{cr}$  will be described in section 5.3.4.

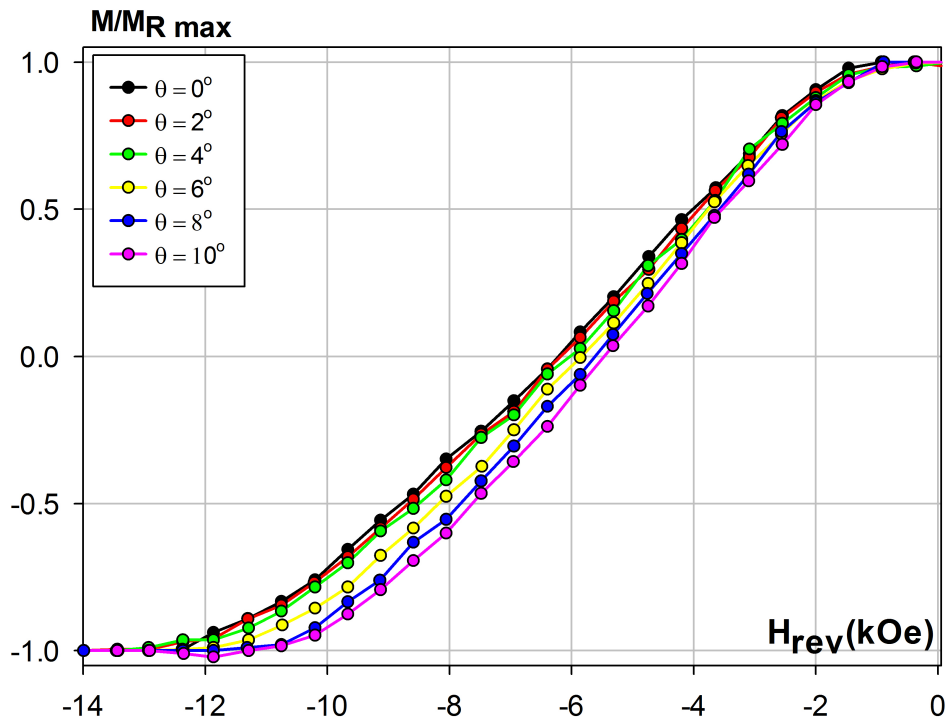
#### 5.3.4 The Easy Axis Distribution by the Variation of $H_{cr}$

It was decided to investigate the remanent coercivity  $H_{cr}$  as a function of angle.  $H_{cr}$  is the coercivity from a DCD curve as described in section 4.2.2. However the difficulty is now the demagnetisation field which means that the field values are no longer known.

Remanence curve measurements provide only the irreversible component of magnetisation and give no signal from the soft CGC layer. The measurement of the variation of  $H_{cr}$  as a function of angle was determined using the rotational MOKE and the DCD method.  $H_{cr}$  can be obtained from the median switching field by differentiating the remanence curve [36] [151]. But due to  $H_D$ ,  $H_{cr}$  cannot be determined directly from the differential method.  $H_{cr}$  was taken as the point at which  $M_{irr} = 0$ .

The measurements were made at room temperature with a maximum applied field of 15 kOe. A reverse field was applied in steps of 500 Oe. The reverse field and remanent magnetisation were recorded. The measurements were repeated by increasing the reverse field steps up to -15 kOe. The results were normalised to the signal amplitude at the maximum value of  $M_R$  which is proportional to the remanence. The measurements were repeated varying the angle between the sample plane and the applied field from  $0^\circ$  to  $10^\circ$  in  $1^\circ$  steps.

Figure 5.13 shows normalised remanence curves at various angles for the sample  $\text{ECO3}_h$ . Results are shown only for  $2^\circ$  steps but measurements were made at  $1^\circ$  intervals. The trend of the DCD curves is to be shifted to lower fields as the angle increases. The DCD curve for  $\text{ECO3}_h$  sample shows a wider switching region than expected. This may be due to the absence of a correction for  $H_D$ . Several points around the remanence were fitted using a linear regression in order to determine  $H_{cr}$ . The results of the measurements of  $H_C$  and  $H_{cr}$  with the angles in steps of  $2^\circ$  are shown in Table 5.10.

Figure 5.13: Typical DCD curves at different angles  $\theta$  for sample  $\text{ECO3}_h$ Table 5.10: Comparison of  $H_C$  and  $H_{cr}$  at different angles for the ECO samples.

Samples \ $H_C$ (kOe)	$H_C(0^\circ)$ $\pm 1\%$	$H_C(2^\circ)$ $\pm 1\%$	$H_C(4^\circ)$ $\pm 1\%$	$H_C(6^\circ)$ $\pm 1\%$	$H_C(8^\circ)$ $\pm 1\%$	$H_C(10^\circ)$ $\pm 1\%$
$\text{ECO1}_h$	5.70	5.59	5.45	5.31	5.17	5.05
$\text{ECO2}_h$	4.70	4.63	4.54	4.44	4.34	4.26
$\text{ECO3}_h$	6.55	6.40	6.22	6.00	5.84	5.67
Samples \ $H_{cr}$ (kOe)	$H_{cr}(0^\circ)$ $\pm 1\%$	$H_{cr}(2^\circ)$ $\pm 1\%$	$H_{cr}(4^\circ)$ $\pm 1\%$	$H_{cr}(6^\circ)$ $\pm 1\%$	$H_{cr}(8^\circ)$ $\pm 1\%$	$H_{cr}(10^\circ)$ $\pm 1\%$
$\text{ECO1}_h$	5.54	5.47	5.37	5.23	5.04	4.92
$\text{ECO2}_h$	4.57	4.51	4.43	4.34	4.23	4.16
$\text{ECO3}_h$	6.23	6.15	6.04	5.88	5.65	5.45

From Table 5.10, the comparison between of  $H_C$  and  $H_{cr}$  shows that the values of  $H_{cr}$  were less than  $H_C$  for any angles due to the elimination of the reversible component from the CGC layer as expected. All samples of the ECC/CGC type have a high level of  $\text{SiO}_2$ . The effect of exchange coupling between the grains is unlikely to be the cause.

In the previous section, the  $\text{ECO3}_h$  and  $\text{ECO1}_h$  samples showed easy axis distributions not following a Gaussian form as the measured values crossed the curves,  $\sigma_\phi$  between  $5^\circ$  and  $6^\circ$  for  $\text{ECO3}_h$  and  $\sigma_\phi$  from  $5^\circ$  to  $7^\circ$  for  $\text{ECO1}_h$ . The  $\text{ECO2}_h$  sample had a much wider distribution with the worst fit to the theory for  $\sigma_\phi$  from  $5^\circ$  to  $8^\circ$ . For the variation of remanent coercivity method, the agreement between the experimental data and the integrated Stoner-Wohlfarth calculation was improved. The variations of  $H_{cr}$  were compared with the Stoner Wohlfarth calculation as shown in figure 5.14. Good agreement was found for all samples in particular samples  $\text{ECO3}_h$  and  $\text{ECO1}_h$  showed an excellent fit to the theory which is consistent with  $\sigma_\phi$  lying between  $6^\circ$  and  $7^\circ$  respectively. This result confirms the hypothesis of the distortion from the  $H_C$  measurement coming from the soft CGC layer as discussed in section 5.3.3. The  $\text{ECO2}_h$  sample showed a wider distribution corresponding to a value of  $\sigma_\phi$  between  $7^\circ$  and  $8^\circ$ . However the results show a better fit compared with the coercivity technique.

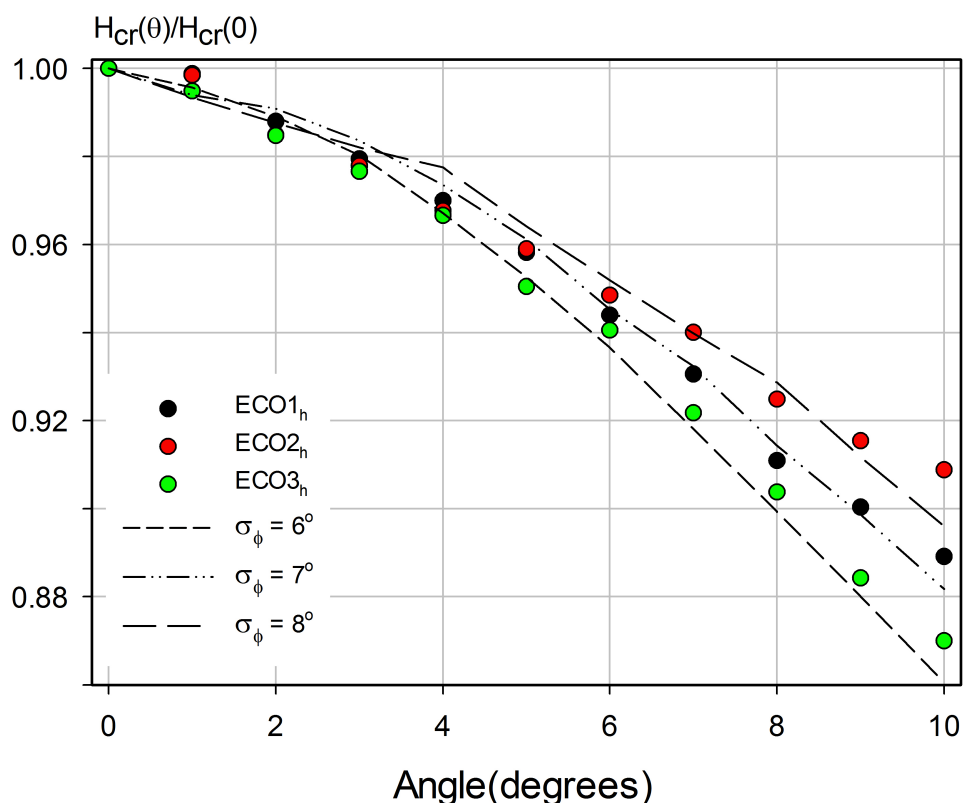


Figure 5.14: Angular variation of  $H_{cr}$  from the experimental data and numerical results for ECO samples with different thicknesses of the CGC layer

These results show that the values of the effective easy axis distribution were similar to those obtained from the  $H_C$  technique for all samples. However, the advantage of this new technique is that it gives an excellent fit between the experimental results and the integrated Stoner Wohlfarth calculation. Therefore, the measurements of remanent coercivity as a function of angle provides a sensitive measure of the effective easy axis distribution which includes the effect of exchange and dipolar coupling between the grains in the complex structure of advanced recording media.

## 5.4 Time Dependence in Thin Film Media

### 5.4.1 Time Dependence of Magnetisation

The time evolution of the switching of the magnetisation in thin film media can be used to characterise the effect of thermal activation on the thin film. The characterisation of the time dependence can provide a measurement of the activation volume  $V_{act}$  [63] which is an essential parameter for the improvement of the performance of advanced recording media.  $V_{act}$  represents the smallest entity that reverses coherently in a single step and gives the smallest unit that can be reversed.

The measurement of  $V_{act}$  was investigated using the measurement of the fluctuation field [77] where the relation between  $H_f$  and  $V_{act}$  is shown in equation 2.69. The waiting time method proposed by El-Hilo *et al.* discussed in section 2.4.4 was used for this measurement.

The effect of the level of  $\text{SiO}_2$  on the activation volume for identical structures of exchange coupled composite (ECC) media [12] [48];  $EO_h$ ,  $EO_m$  and  $EO_l$  has been studied and compared to the physical grain volume. Again a MOKE magnetometer was required for magnetic measurements due to the presence of the SUL.

The measurements were made at room temperature with a maximum applied field of 12 kOe. The sample was first magnetised in a saturating field and a constant reverse field,  $H_{rev}$  was then applied. The decay of magnetisation was measured for 600 seconds. This process was repeated with increasing reverse fields as required by equation 5.4. Due to the drift of the laser signal the hysteresis loop was measured before increasing  $H_{rev}$  in order to obtain the maximum signal amplitude as a reference signal.

$$H_{rev}^n = H_{rev} + n \cdot \Delta H \quad (5.4)$$

where  $H_{rev}^n$  is the new reverse field,  $n$  is the number of steps and  $\Delta H$  is the field step  $\sim 80$  Oe. The range of  $H_{rev}$  was chosen to cover the entire range of the switching field distribution. The chosen value of  $M$  for the determination of  $V_{act}$  is generally  $M = 0$  so that  $H_f$  is determined at the coercivity  $H_C$  in order to remove the effect of  $H_D$ . Figure 5.15 shows typical time dependence measurements over a 600 second interval for the  $EO_h$  sample with a high level of  $SiO_2$ .

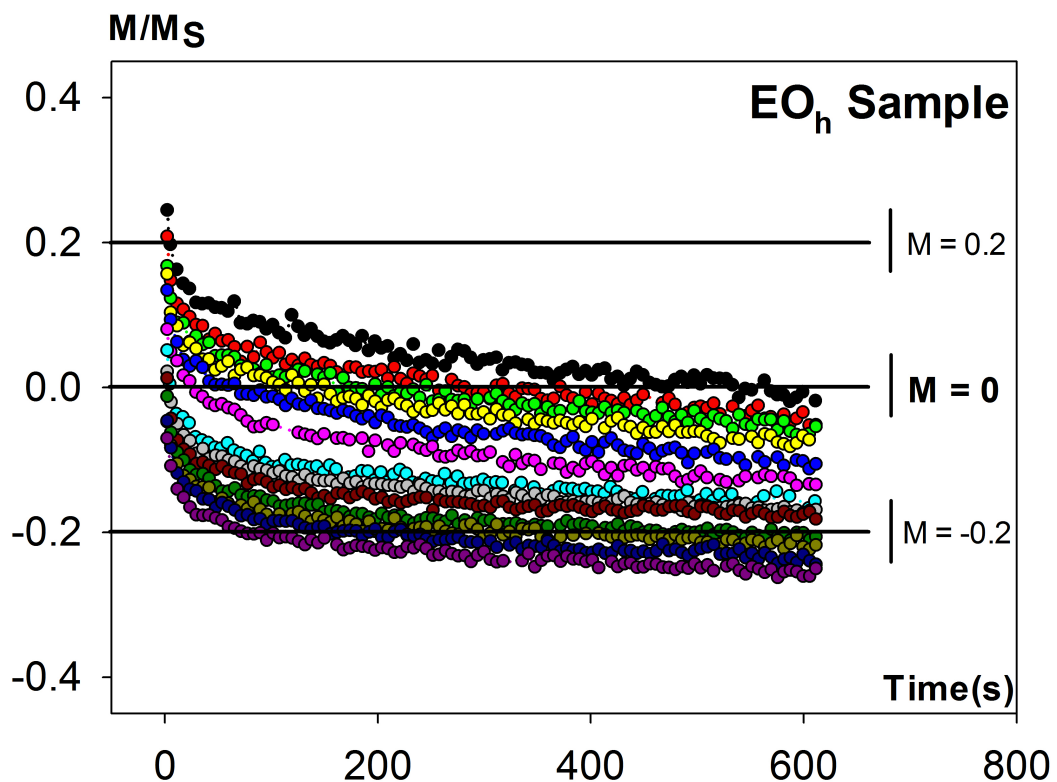


Figure 5.15: Typical time dependence of magnetisation decay for sample  $EO_h$

For the waiting time method, a number of different reverse field values and the values of  $\ln(t_1/t_2)$  where the value  $M$  falls to zero were obtained. Given the accuracy of the results the curves were fitted to a power series expansion of magnetic viscosity coefficients proposed by El-Hilo *et al.* [77] following equation 5.5.

$$M(t) = M_o \pm S_1 \ln(t) \pm S_2 \ln^2(t) \pm \dots \quad (5.5)$$

Fig.5.16 and 5.17 show the results of the magnetisation decay with time and  $\ln(t)$  respectively. It is obvious that the magnetisation decay with  $\ln(t)$  of the ECC samples exhibits non-linear  $\ln(t)$  behaviour. The concave downwards and concave upwards variations of the magnetisation with  $\ln(t)$  appear at high and low value of  $H_{rev}$ . This implies that the distribution of energy barriers is narrow [72]. Given the high levels of  $\text{SiO}_2$  in this sample the grain size distribution is narrow and the anisotropy constant highly uniform due to the use of heated substrates. Also the values of  $\sigma_\phi$  at  $5^\circ$  give a very narrow distribution of energy barriers as shown by equation 2.45

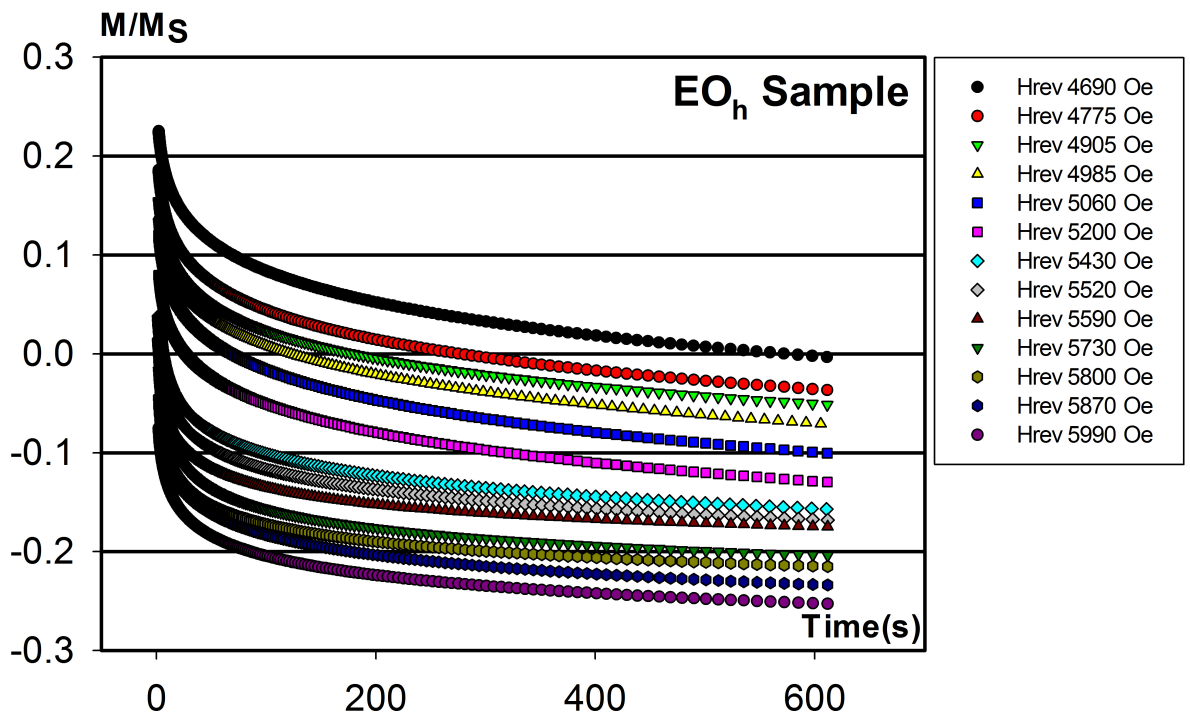


Figure 5.16: The variation of the time dependent magnetisation with  $t$

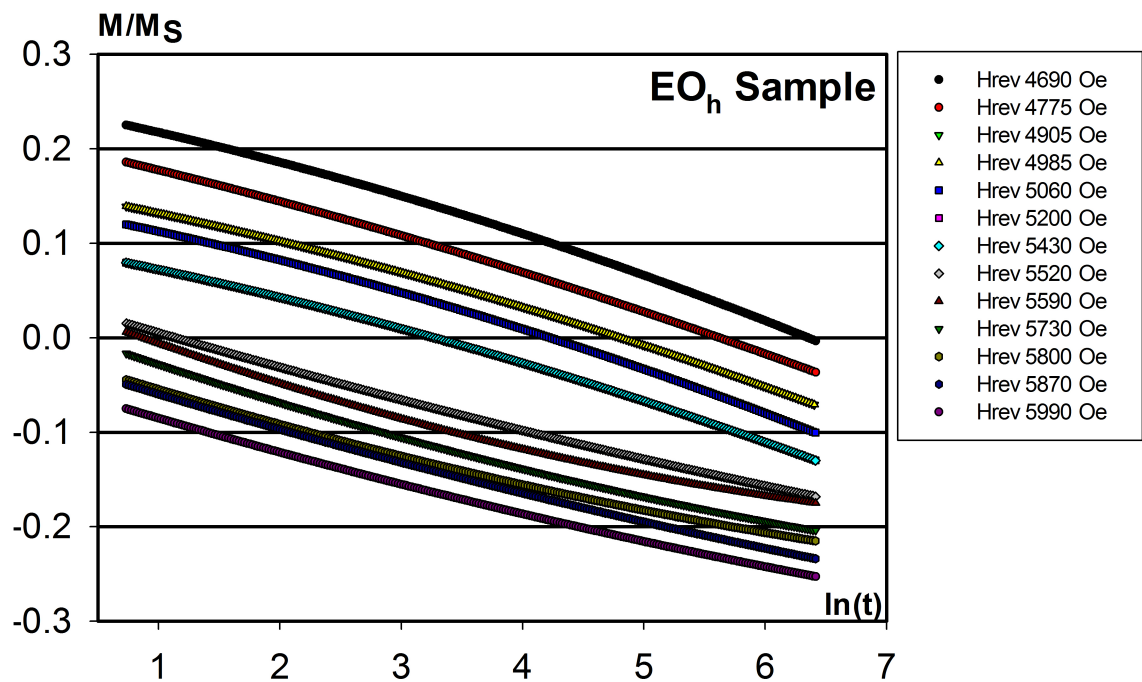


Figure 5.17: The variation of the time dependent magnetisation with  $\ln(t)$

#### 5.4.2 Determination of the Fluctuation Field and Activation Volumes

As discussed in section 2.4.4,  $H_f$  can be determined from the values of  $t_1$  and  $t_2$  which are the times taken for the magnetisation to fall to the same constant value of  $M$  in the presence of different reverse fields,  $H_{rev1}$  and  $H_{rev2}$  [77]

$$H_f = \frac{\Delta H}{\ln(t_2/t_1)} \Big|_M \quad (5.6)$$

A graph of  $\Delta H$  versus  $\ln(t_2/t_1)$  was drawn using as many crossing points at  $M = 0$  as possible.  $H_f$  was determined directly from the gradient of a graph of the reverse field ( $H_{M=0}$ ) and  $\ln(t_1/t_2)$ . The accuracy of the linear regression determined from  $r^2$  was  $> 0.99$  for all samples. Fig.5.18 shows the variation of  $H_{M=0}$  with  $\ln t$  for samples  $EO_h$ ,  $EO_m$  and  $EO_l$ .

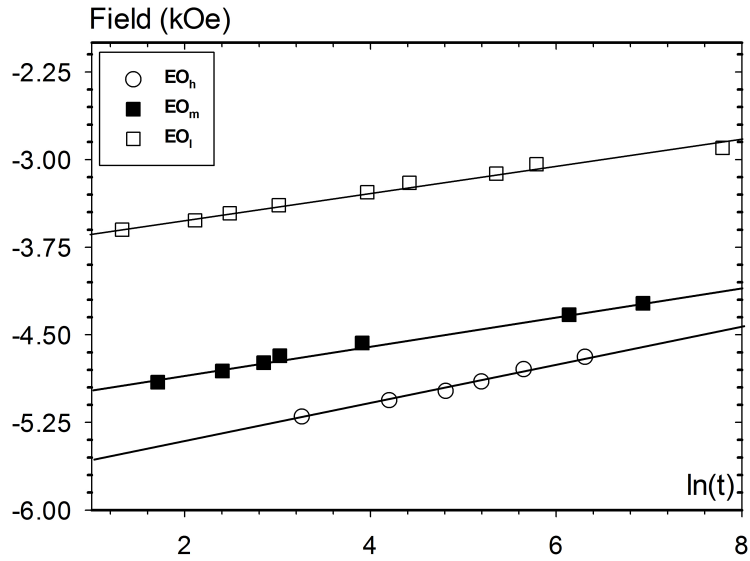


Figure 5.18: The variation of the reverse field with  $\ln(t)$  for all samples

As predicted by equation 5.6 an excellent linear variation is observed. The error bars lie within the symbols. The values of  $H_f$  obtained are shown in Table 5.11. The values of  $H_C$  and the slope of the magnetisation curve at  $H_C$  are also summarised in Table 5.12.

Table 5.11: Summary of physical properties,  $H_f$  and  $V_{act}$ .

Sample	SiO <sub>2</sub>	$D_m$ (nm)	$\sigma_D$	$H_f$	$V_{TEM} \times 10^{-19}$	$V_{act} \times 10^{-19}$
		$\pm 1\%$	$\pm 1\%$	$\pm 5\%$	(cc) $\pm 1.4\%$	(cc) $\pm 3\%$
EO <sub>h</sub>	High	6.70	0.11	170	4.94	5.09
EO <sub>m</sub>	medium	7.81	0.13	127	6.52	7.32
EO <sub>l</sub>	low	8.16	0.13	114	7.21	8.20

Table 5.12: Summary of magnetic properties of ECC set.

Sample	SiO <sub>2</sub>	$D_m$ (nm)	$H_C$ (kOe)	slope at $H_C \times 10^{-4}$	$M_S$
		$\pm 1\%$	$\pm 1\%$	(Oe <sup>-1</sup> ) $\pm 1\%$	(emu/cc)
EO <sub>h</sub>	High	6.70	6.75	1.95	480
EO <sub>m</sub>	medium	7.81	5.41	2.27	450
EO <sub>l</sub>	low	8.16	3.97	3.00	450

The value of the activation volume was obtained from the relationship between the thermal energy and the fluctuation field

$$V_{act} = \frac{k_B T}{M_S H_f} \quad (5.7)$$

where  $k_B$  is Boltzmann's constant,  $T = 300$  K and  $M_S$  is the saturation magnetisation of the composite film. There is one significant difficulty with this calculation because a value for the saturation magnetisation  $M_S$  is required. This value of  $M_S$  is that of the grain rather than that of the film. This value cannot be measured and may also vary if there is  $\text{SiO}_2$  contamination within a grain which may also vary from grain to grain. In order to overcome this difficulty the value of  $M_S$  used was that of the bulk alloy which may differ slightly from thin film form. The magnetisation of the bulk material was determined using the VSM as discussed in section 5.2. It is noted that the variation in composition of the two layers of the ECC media is small and any change in  $M_S$  will, we believe, be less than that between the bulk and the thin film sample. Hence a single value of  $M_S$  as shown in Table 5.12 has been used. Another source of error is due to the accuracy of the measurement of the volume. Cross-section TEM for all samples was used to measure the recording layer thickness in order to reduce errors. Hence the value of  $V_{act}$  presented in 5.11 may be subject to a systematic error in addition to the random errors quoted.

The values of  $V_{act}$  shown in Table 5.11 show the expected trend as the exchange decoupling increases for higher  $\text{SiO}_2$  levels. The results for the ECC media are in accordance with the previous works regarding the reduction of the activation volume for conventional CoCrPt- $\text{SiO}_2$  media with increasing levels of oxide as reported by Dutson *et al.* [166] and Inaba *et al.* [127]. The reduction of  $V_{act}$  as the oxide content is increased is due to the reduction of the intergranular exchange coupling due to the  $\text{SiO}_2$  segregation at the grain boundary. A further semi-quantitative measurement of the intergranular exchange coupling can be seen via the slope of the loop at  $H_C$  [36] given in Table 5.12. If co-operative reversal occurs then the gradient of the loop will be steeper. El-Hilo *et al.* [72] showed that the activation volume is also a measure of co-operative reversal. Since  $V_{act}$  is that volume of the material that reverses in a single step, a co-operative event will increase  $V_{act}$ . These results show that decreasing the  $\text{SiO}_2$  content increases the slope of the loop for samples such as  $\text{EO}_l$  which has a larger activation volume.

### 5.4.3 Correlation of Activation and Physical Grain Volumes

The activation volume has been compared to the physical volume of the grains in order to study the correlation between  $V_{act}$  and the grain volume. The grain volume of recording media can be estimated from the cylindrical volume of a single grain,  $V_{TEM}$ . The columnar structure of the ECC media can be observed clearly in the cross-section TEM image shown in fig.5.1. In order to determine  $V_{TEM}$  the median grain size for all samples was measured from in-plane TEM images. The SiO<sub>2</sub> content at the grain boundaries was also observed by cross-section high resolution scanning transmission electron microscope (HR-STEM) imaging. For the grain size distribution in-plane images were taken from various areas of the sample using a JEOL 2011 TEM. For each sample 600 grains were measured using an equivalent circle method via a light box with an adjustable aperture. The data were fitted to a log-normal distribution function of diameter of the form

$$f(D)dD = \frac{1}{\sqrt{2\pi}\sigma_{\ln D}D} \exp \frac{-(\ln D - \overline{\ln D})^2}{2\sigma_{\ln D}^2} dD \quad (5.8)$$

Here  $\overline{\ln D}$  is the mean value of  $\ln D$  so that the median diameter  $D_m = \exp(\overline{\ln D})$ .  $\sigma_{\ln D}$  is the standard deviation of  $\ln D$ . Therefore,  $V_{TEM}$  was calculated from the grain area assuming a constant film thickness,  $t_{total}$  including the soft and hard layers of ECC media. From fig.5.1, the cross-section of the ECC medium shows this approximation to be valid. It should be noted that  $\sigma$  is now  $2\sigma_{\ln D}$  because the standard deviation is that of the log of the area of the grains.

$$V_m = \pi D_m^2 t_{total} / 4 \quad (5.9)$$

Cross-section images were obtained using a JEOL JEM-2200FS double Cs-corrected TEM at bright field (BF) HR-STEM and high angle annular dark-field (HAADF) mode. The HAADF mode detects only electrons which are incoherently scattered as discussed in section 4.3.3. Z-contrast was used to analyse the composition distribution at the grain boundaries. Examples of the bright field TEM images are shown in fig.5.19 together with the fits to the lognormal distribution function of diameter. The size distribution parameters for both diameter and volume are shown in Table 5.11. From the data in Table 5.11,  $V_{TEM}$  decreases as the SiO<sub>2</sub> content increases. This is consistent with the values of  $V_{act}$ .

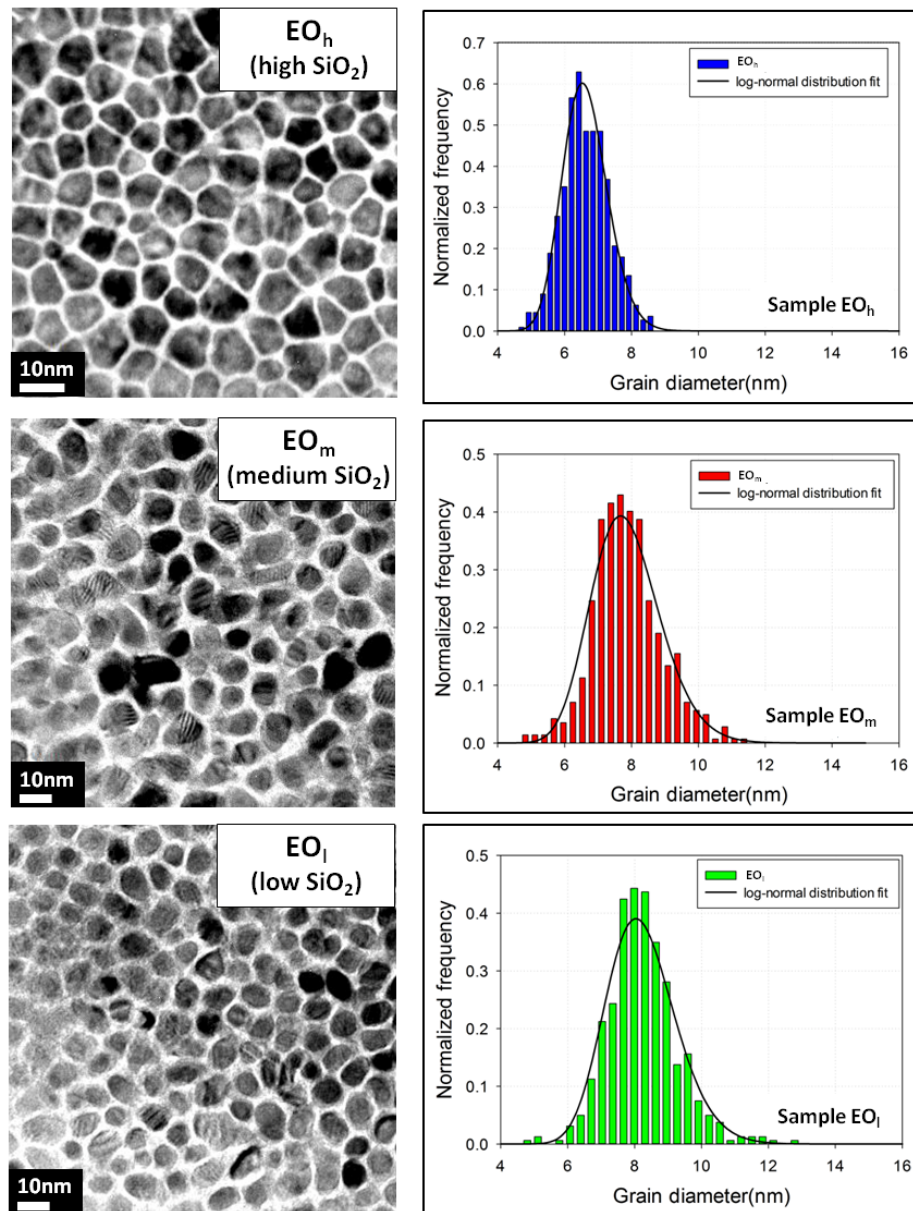


Figure 5.19: BF in-plane image and normalised grain size distributions for ECC samples with good orientation and different oxide levels.

In ECC media the concept of the grain volume is ambiguous due to the two layer structure. However the two layers are strongly exchange coupled via a direct exchange mechanism because they both consist of CoCrPt. Only slight variations in the level Pt are required to vary the anisotropy and hence the lattice match in the basal plane is essentially the same. Hence magnetically, the grains will reverse coherently and the required grain volume is that of the two layers.

The data in figure 5.20 shows excellent agreement between  $V_{act}$  and  $V_{TEM}$  for sample  $EO_h$ . This is a critical result because it indicates that for this sample single grain reversal occurs. This also implies that the intergranular exchange coupling has been reduced to near zero so that it has very little or no effect on the magnetisation reversal. The similarity of these values also indicates that the value of  $M_S$  used to calculate  $V_{act}$  is, at worst, a good approximation. The values of  $V_{act}$  for samples  $EO_m$  and  $EO_l$  were significantly larger than the value of  $V_{TEM}$ . This indicates the effect of co-operative reversal of the grains due to incomplete exchange decoupling from the lower level of  $SiO_2$ . The effect of the level of  $SiO_2$  in controlling the median grain size and the value of  $\sigma_{lnD}$  is also clear.

The increasing disparity between  $V_{TEM}$  and  $V_{act}$  with falling  $SiO_2$  content indicates that the level of  $SiO_2$  in the film is a critical parameter in controlling the intergranular exchange coupling [127]. However the lowest level of  $SiO_2$  in sample  $EO_l$  only gave rise to a value of  $V_{act}$  which was 15% greater than  $V_{TEM}$  indicating that a significant degree of exchange decoupling was achieved. For samples without  $SiO_2$  decoupling such as those which previously relied on Cr segregation, values of  $V_{act}$  indicated many grains reverse co-operatively [164]. The result here for  $EO_h$  indicates that it is an almost ideal single grain reversal medium.

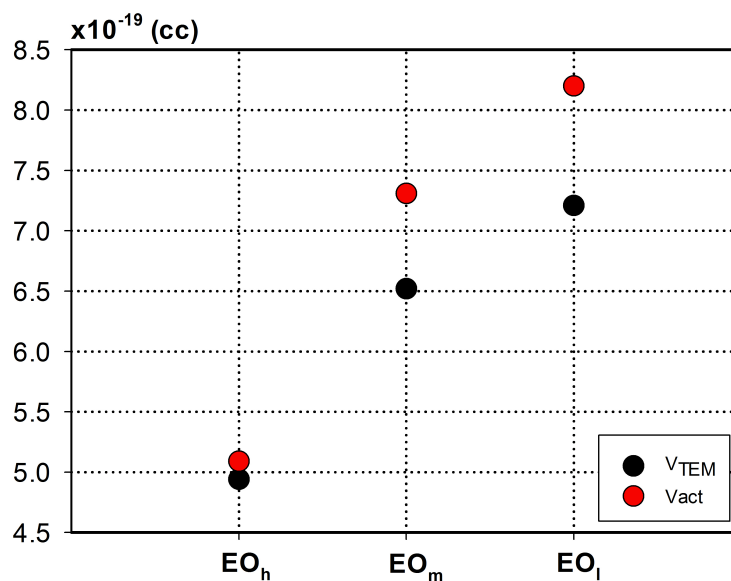


Figure 5.20: Comparison between activation volumes,  $V_{act}$  and  $V_{TEM}$

It is difficult to quantify the degree of exchange coupling in perpendicular media. Techniques such as  $\Delta M$  cannot be used because of the demagnetising field. However the effect of the interactions can be seen from the data in Table 5.12. The CoCrPt alloy used in all 3 samples is the same, and the difference in  $H_C$  between sample  $EO_h$  with a high level of  $SiO_2$  and sample  $EO_l$  with a low level is almost 3kOe. This reduction is in part due to exchange coupling. However the difference in grain size of 1.46 nm corresponds to a difference in volume of almost a factor 1.5. Hence the contribution of thermal activation to the reduction in  $H_C$  will be approximately half the overall reduction in coercivity. That would imply that the exchange interaction produces an equivalent field of the order of 1kOe.

It is somewhat surprising that the resulting cluster size is only 15% greater for the sample with a low level of  $SiO_2$  than that for the film with a high level. In previous work on longitudinal media much larger clusters were found in exchange coupled films. However the perpendicular orientation automatically results in repulsive dipole-dipole effects which will reduce cluster size as the exchange interaction will need to overcome anisotropy and dipole-dipole effects. In order to study the effect of the  $SiO_2$  at the grain boundaries, high resolution in-plane TEM images were obtained. The in-plane structure shows that the grain segregation for the  $EO_h$  sample is almost perfect with grain segregation in the range  $\sim 0.5$  to 1 nm. For samples  $EO_m$  and  $EO_l$ , the  $SiO_2$  segregation is not as complete as in the  $EO_h$  sample due to the lower  $SiO_2$  content. Hence,  $V_{act}$  appears to be in the same range as the median grain volume.

To observe the composition distribution along the grain boundaries BF HR-STEM and HAADF STEM imaging has been used as shown in fig.5.21 a) and b) respectively for sample  $EO_h$ . Figure 5.21 a) shows a very sharp grain boundary in good agreement with the in-plane image for this sample. Fig.5.21 a) shows that the width of the  $SiO_2$  is approximately 1 nm but varies and in places is of the order of 0.5 nm. However the critical observation is that the  $SiO_2$  is continuous. Given that intergranular exchange coupling is an indirect interaction mediated by conduction electrons, this is an important observation which explains why this sample appears to have almost perfect exchange decoupling.

In the HAADF STEM image 5.21 b), the brighter areas indicate heavy metal scattering and darker areas indicate light metal scattering (Z-contrast). The HAADF image clearly shows the dark area along the grain boundary and the brighter atoms in the

---

grain. This image confirms the continuity of the  $\text{SiO}_2$  layer. The comparison between BF HR-STEM and HAADF images for the same area shows that the  $\text{SiO}_2$ , which is light metal, predominantly segregates between the grains at high  $\text{SiO}_2$  content. Whilst the images in figure 5.21 are typical of the observations made of the grain boundaries, it should be noted that extensive observations were made over many areas and a continuous layer of  $\text{SiO}_2$  was found everywhere and no breaks in the  $\text{SiO}_2$  could be found. From this analysis the origin of the correlation between  $V_{act}$  and the grain volume is clear. Hence, this result implies that the activation volume in advanced recording media can be estimated via the correlation to the grain size.

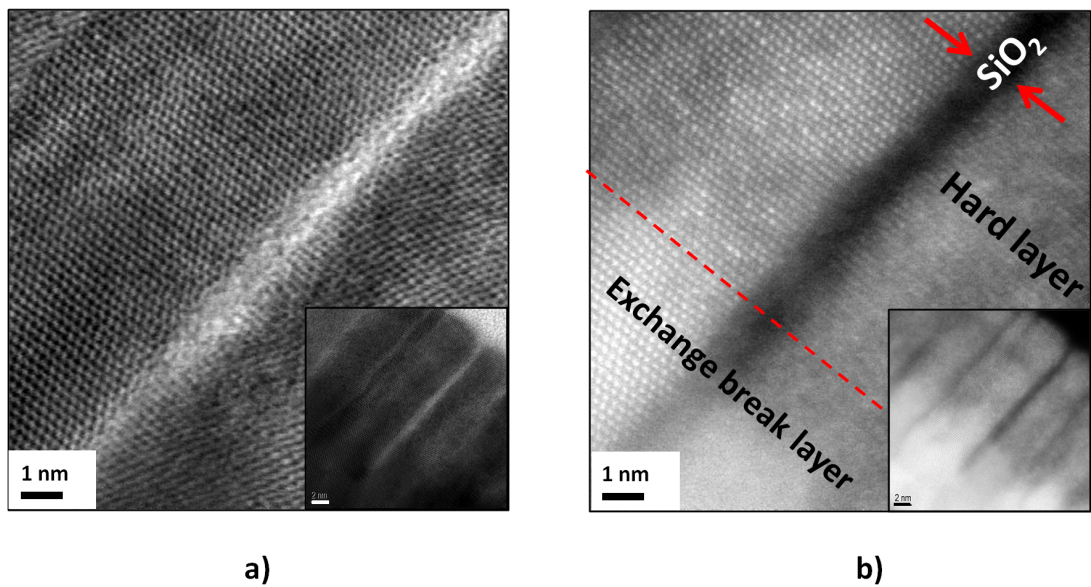


Figure 5.21: a) Typical BF-HR-STEM cross-section image and b) high angle annular dark field (HAADF)-STEM for sample  $\text{EO}_n$  (courtesy of Dr. L. Lari)

## CHAPTER VI

### Conclusions and Future Work

#### 6.1 Conclusions

In this work the value of advanced magnetic measurements and their use in understanding processes in advanced thin film media has been demonstrated. A number of techniques have been developed and used on new composite perpendicular recording media with different structures. The development and demonstration of the use of those techniques have provided valuable insights for my industrial collaborators in Seagate Media Research. The techniques are also being adopted by other major media manufacturers. Hence the techniques are valuable for the study of current media and will support future media development.

The main objective of this work was to investigate the effective easy axis distribution and study the effect of the oxide content on thermal stability. One of the most critical parameters in perpendicular recording media is the distribution of switching fields within the medium. The largest contributor to the switching field distribution is the variation in the orientation of the easy axis of the grains. This leads to a distribution of the intrinsic switching fields. The variation of coercivity technique was originally proposed by Carter *et al.* [144]. This technique has now been made quantitative via comparison with modelling results. Due to the efficiency of SiO<sub>2</sub> segregation at the grain boundaries leading to intergranular exchange decoupling, a simple model assuming coherent magnetisation reversal of each grain has been developed. The model gives excellent agreement with the experimental data. The advantage of the coercivity method is that it can measure  $\sigma_\phi$  with a resolution of less than 1 degree.

The requirement for this technique is a rotational system for the magnetometry. Due to the presence of the soft underlayer a rotational MOKE is required. This MOKE design is only currently available at Seagate Media Research. The coercivity technique can differentiate the effective easy axis distribution for different media structures and

---

different levels of SiO<sub>2</sub>. The values of crystallographic orientation  $\Delta\theta_{50}$  from X-ray rocking curves for all samples were not able to do this always giving values, of about 3°.

From the coercivity method the effect of intergranular exchange decoupling from the SiO<sub>2</sub> dominated the distribution. The granular medium with high intergranular exchange coupling showed a wide distribution with  $\sigma_\phi$  of 9° whereas it was only 3° for the sample with low exchange coupling. The effect of crystal orientation in identical structures was also observed giving a difference in  $\sigma_\phi$  of 9° and 6°. The  $\Delta\theta_{50}$  technique could not differentiate these samples.

The coercivity method was also applied to complex structures such as ECC media. The effective easy axis distribution showed similar results for the coupling effect and different crystal orientation as for the granular media. For the comparison with granular media the value of  $\sigma_\phi$  was slightly wider but showed an excellent fit to the theory for  $\sigma_\phi = 5^\circ$ . The TEM analysis showed that the grain segregation by SiO<sub>2</sub> was almost perfect. This implies that the larger value of  $\sigma_\phi$  was not due to exchange coupling.

Most advanced media are complex structures due to the presence of the continuous layer. The calculations from the S-W model cannot be matched perfectly to the experimental results due to the contribution of the reversible component of the magnetisation. The variation of remanent coercivity ( $H_{cr}$ ) is required. The variation of  $H_{cr}$  gave a good fit to the theory with  $\sigma_\phi = 6^\circ$  for the thinnest CGC layer. For the thickest CGC layer  $\sigma_\phi = 8^\circ$ . This is a much broader distribution compared to the other sample. Hence the CGC layer should be as thin as possible.

Another main topic studied is the thermal stability for alternative perpendicular recording media. This is a major limiting factor for the extension of areal density. In order to achieve a high density, the most important factor is the reduction of the median grain size controlled via the level of co-sputtered silica deposited with the CoCrPt alloy. The grain size is a critical parameter because small grains lead to thermal loss of data which affects all forms of data storage. The significant parameter is the activation volume which was investigated via time dependence studies.

These measurements indicated that all ECC samples with different levels of silica have a narrow switching field distribution. This implies that the easy axis distribution is an important factor because the distribution of grain size  $\sigma_D$  and the anisotropy distribution  $\sigma_K$  were small. The decay of magnetisation near the coercivity was observed for 600 seconds. The magnetisation reduced by about 0.2 M/M<sub>S</sub> during this time interval

---

for all samples. Due to the presence of the narrow SFD the waiting time method gives an accurate measure of the fluctuation field  $H_f$ .  $H_f$  was determined directly from the gradient of a number of intercept points of the variation of the reverse field with  $\ln(t_2/t_1)$  at  $M = 0$ . An excellent linear variation was observed giving  $H_f$  to  $\pm 5\%$ .  $H_f$  increased as the exchange coupling was reduced as expected.

$V_{act}$  was determined directly from the fluctuation field and  $M_S$ .  $V_{act}$  decreased as the  $\text{SiO}_2$  level was increased due to a decrease in the grain volume but also due to the exchange coupling between the grains being reduced.  $V_{act}$  was found to be the same as the median grain volume for a sample with a high level of  $\text{SiO}_2$ . Cross-sectional TEM analysis has been carried out to investigate the composition distribution at the grain boundaries. The images showed excellent grain segregation at the grain boundaries which was continuous through to the intermediate layer. This implies that near perfect exchange decoupling between the grains should occur as confirmed by the activation volume results. However, the dipole dipole interaction is still present.

## 6.2 Future Work

The variation of coercivity as a function of angle provides a sensitive technique to determine the effective easy axis distribution. It can also show the effects of intergranular exchange coupling on the dispersion. The technique is a simple and reliable experimental method taking the effect into account. If a rotational MOKE is available further work would be to use this technique to measure the distribution of easy axis orientation for future recording media such as bit patterned media and FePt media for HAMR technology. This technique would be applicable for the characterisation of future media due to the coherent magnetisation reversal of each single domain grain.

In order to interpret this data meaningfully high resolution micromagnetic computer modelling will be required to simulate more realistic media. The calculation of the coercivity value should take the effects of exchange and dipolar coupling between the grains into account. Voronoi grain structures can be controlled using the actual grain size from in-plane analysis in order to simulate the real system. Monte Carlo simulations can calculate the magnetisation curve including the anisotropy field, grain size distribution and exchange and dipolar coupling in the system. Figure 6.1 a) and b) show an example of a Voronoi grain structure and the variation of the coercivity calculated using a Monte

---

Carlo simulation and compared to the experimental results and the Stoner Wohlfarth model respectively. The results show an improved correlation due to the inclusion of exchange interactions.

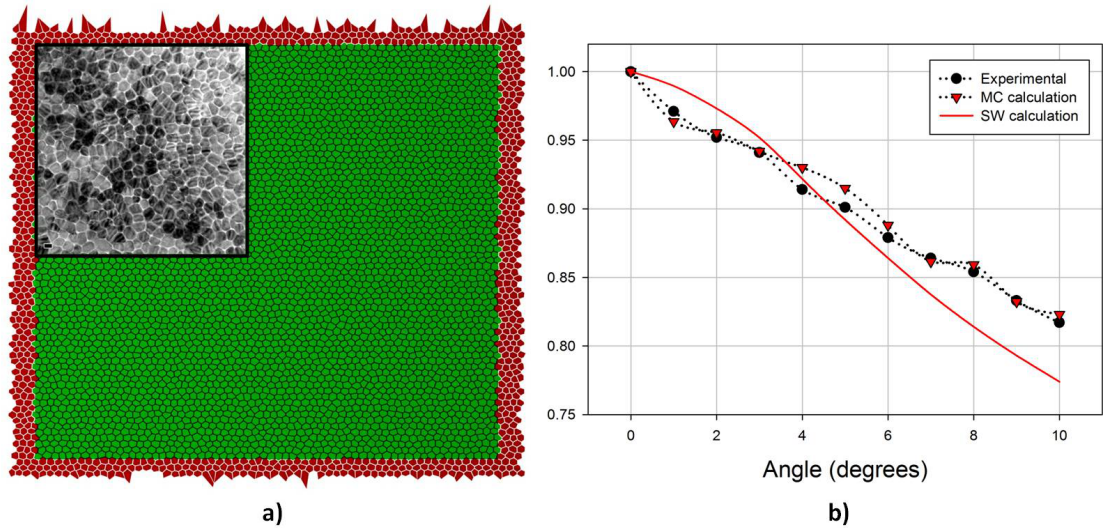


Figure 6.1: a) Comparison between Voronoi simulation grains and the recording grains and b) angular variation of  $H_C$  from experimental results, S-W and Monte Carlo calculations provided by P. Churemart and R.W. Chantrell.

The activation volume measurement has also shown the value of high resolution magnetic measurements. It can be used as a qualitative indicator of the exchange coupling between the grains. This will be equally applicable to HAMR media where cooperative reversal will remain a key issue.

The technique will also be valuable for bit patterned media. It has been proposed that bit patterned media can be fabricated from films with exchange coupled grains. As has been shown in this work this will reduce the coercivity and the activation volume will be several grains but perhaps not an entire element. In such small entities a magnetic force microscope will not be able to image the magnetisation reversal and perhaps only a technique such as that used here will be able to establish the mechanism.

---

## PUBLICATIONS AND PRESENTATIONS

### List of Publications

- **Magnetic Orientation in Advanced Recording Media**  
J. Chureemart, P. Chureemart, RFL Evans, RW Chantrell and K O' Grady  
Journal of Physics D: Applied Physics, vol. 44, no. 45, pp. 455002, 2011.
- **Media Design and Orientation in Perpendicular Media**  
J. Chureemart, P. Chureemart, J. Pressesky, T. Nolan and K O' Grady  
IEEE Transactions on Magnetics, vol. 49, no. 7, pp. 3592-3595, 2013.
- **The Effect of SiO<sub>2</sub> Content on Activation Volumes in Exchange Coupled Composite Media**  
J. Chureemart, L. Lari, T. P. Nolan and K O' Grady  
Journal of Applied Physics, vol. 114, no. 8, pp. 083907, 2013.

### List of Presentations

- **Easy Axis Orientation in Advanced Recording Media**  
J. Chureemart, P. Chureemart, RFL Evans, RW Chantrell and K. O' Grady  
The Current Research in Magnetism CRIM, July 2010, Manchester, UK.
  - **Magnetic Orientation in an Advanced Recording Media**  
J. Chureemart, P. Chureemart, RFL Evans, RW Chantrell and K. O' Grady  
INTERMAG 2011, April 2011, Taipei, Taiwan.
  - **Composite Perpendicular Recording Media**  
J. Chureemart and K. O' Grady  
The Current Research in Magnetism CRIM, June 2011, Durham, UK.
  - **Characterisation of Interface Spin Clusters in Exchange Bias Systems**  
N. C. Cramp, R. Carpenter, J. Chureemart, and K. O' Grady  
INTERMAG 2012, May 2012, Vancouver, Canada.
-

- 
- **Magnetic Measurements of Angular Dispersion in Recording Media**  
**J. Chureemart**, J. Pressesky, T. Nolan and K. O' Grady  
CMP Workshop, July 2012, York, UK.
  
  - **The Effect of Media Design on Orientation in Perpendicular Recording**  
**J. Chureemart**, P. Chureemart, J. Pressesky, T. Nolan and K. O' Grady  
The 12th **Joint MMM/Intermag Conference**, January 2013, Chicago, USA.
  
  - **The Effect of SiO<sub>2</sub> Content on Activation Volumes in ECC Media**  
**J. Chureemart**, L. Lari, T. P. Nolan and K. O' Grady  
Joint European Magnetic Symposia JEMS13, August 2013, Rhodes, Greece.
-

---

**LIST OF SYMBOLS**

$\alpha$	Orientation of grains factor
$\bar{D}_m$	Median diameter
$\Delta\theta_{50}$	Full width half maximum
$\chi_{irr}$	Irreversible susceptibility
$\Delta M$	Degree of intergranular exchange interaction
$\delta$	Thickness of medium
$\epsilon$	Induced voltage
$\epsilon_K$	Elipticity angles
$\lambda$	Wavelength of the X-rays
$\lambda_{me}$	Magnetostriction constant
$\mu$	Magnetic permeability
$\omega$	Angular frequency
$\phi_m$	Magnetic flux
$\sigma$	Tensile stress
$\sigma_\phi$	Standard deviation
$\sigma_{\ln D}$	Standard deviation of $\ln D$
$\tau$	Relaxation time
$\theta_{hkl}$	Bragg's angle
$\theta_K$	Rotation of polarisation plane
$\theta_{me}$	Angle between the magnetisation and $\sigma$
$\xi$	Ratio of the energy barrier $\Delta E$ to the switching field
$A$	Area of the magnetic sample

---

---

$a_o$	Transition width parameter
$a_{WC}$	Williams-Comstock transition width parameter
$AFC$	Antiferromagnetically coupled media
$B_m$	Magnetic flux density
$BPM$	Bit patterned media
$CGC$	Coupled granular continuous media
$d_{hkl}$	Lattice spacing or interplanar spacing
$d$	Magnetic spacing between the medium and the write head
$D_{av}$	Average grain diameter
$DCD$	DC-demagnetisation curve
$E_K$	Magnetocrystalline anisotropy energy
$E_a$	Anisotropy energy
$E_d$	Dipolar interaction energy
$E_{ex}$	Interfacial exchange energy
$E_{max}$	Maximum energy of a single domain particle
$E_{ms}$	Magnetostatic energy
$E_p$	Potential energy
$E_T$	Total energy
$ECC$	Exchange coupled composite media
$EDX$	Energy dispersive X-ray
$f(\Delta E)$	Function of the energy barrier
$f_o$	Frequency factor
$H$	Uniform magnetic field
$H^{spin}$	Heisenberg Hamiltonian

---

---

$H_f$	Fluctuation field
$H_{ac}$	Microwave ac field
$H_A$	Applied field
$H_{contral}$	Corrected applied field
$H_{cr}$	Remanence coercivity
$H_C$	Coercivity
$H_D$	Demagnetising field
$H_{ex}$	Exchange field
$H_i$	Internal field
$H_K$	Anisotropy field
$H_n$	Negative nucleation field
$H_{rev}$	Constant reverse field
$H_{rev}^n$	New reverse field
$H_{sat}$	Saturated field
$H_S$	Switching field
$H_W$	Writing field
$HAADF$	High angle annular dark field
$HAMR$	Heat assisted magnetic recording
$IRM$	Isothermal remanent magnetisation curve
$J_{ij}$	Exchange coupling constant
$K$	Anisotropy constant
$k_B$	Boltzman's constant
$K_{ms}$	Magnetoelastic constant
$LRM$	Longitudinal recording media

---

---

$M$	Magnetisation
$m$	Magnetic moment
$M_{irr}$	Irreversible magnetisation
$M_{rev}$	Reversible magnetisation
$M_R$	Remanence magnetisation
$M_S$	Saturation magnetisation
$MAMR$	Microwave assisted magnetic recording
$MOKE$	Magneto-optical Kerr effect
$N$	Number of turns in the detection coil
$N_a$	Demagnetising factor along the short axis
$N_c$	Demagnetising factor along the long axis
$N_D$	Demagnetising factor
$PRM$	Perpendicular recording media
$PW_{50}$	Width of the signal pulse at 50%
$Q_{\perp}$	Head field gradient
$S_i, S_j$	Spin angular momenta of atoms $i$ and $j$
$S_q$	Squareness of hysteresis loop
$SFD$	Switching field distribution
$SNR$	Signal to noise ratio
$STEM$	Scanning transition electron microscopy
$T$	Temperature constant
$T_C$	Curie temperature
$TEM$	Transition electron microscopy
$V$	Grain volume in the medium

---

---

$V_{act}$	Activation volume
$V_{TEM}$	Physical single grain volume
$VSM$	Vibrating sample magnetometer
$Z$	Atomic number
$\Delta E_C$	Energy barrier at remanence
$\Delta E$	Energy barrier
$\Delta E(H_C)$	Energy barrier at coercivity
$g(H)$	Langevin function factor

---

---

**BIBLIOGRAPHY**

- [1] G. Binasch, P. Grünberg, F. Saurenbach, and W. Zinn, “Enhanced magnetoresistance in layered magnetic structures with antiferromagnetic interlayer exchange,” *Phys. Rev. B*, vol. 39, pp. 4828–4830, Mar 1989.
  - [2] M. N. Baibich, J. M. Broto, A. Fert, F. N. Van Dau, F. Petroff, P. Etienne, G. Creuzet, A. Friederich, and J. Chazelas, “Giant Magnetoresistance of (001)Fe/(001)Cr Magnetic Superlattices,” *Phys. Rev. Lett.*, vol. 61, pp. 2472–2475, Nov 1988.
  - [3] A. Moser, K. Takano, D. T. Margulies, M. Albrecht, Y. Sonobe, Y. Ikeda, S. Sun, and E. E. Fullerton, “Magnetic recording: advancing into the future,” *Journal of Physics D: Applied Physics*, vol. 35, no. 19, p. R157, 2002.
  - [4] S. Iwasaki and Y. Nakamura, “The magnetic field distribution of a perpendicular recording head,” *Magnetics, IEEE Transactions on*, vol. 14, no. 5, pp. 436–438, 1978.
  - [5] S. Charap, P.-L. Lu, and Y. He, “Thermal stability of recorded information at high densities,” *Magnetics, IEEE Transactions on*, vol. 33, no. 1, pp. 978–983, 1997.
  - [6] B. D. Cullity and C. D. Graham, *Introduction to magnetic materials*, 2nd ed. John Wiley and Sons Ltd., Inc., Hoboken, New Jersey., 2009.
  - [7] R. Wood, “Magnetic recording.” Presented as IEEE magnetics society summer school, 2011.
  - [8] R. Rottmayer, S. Batra, D. Buechel, W. Challener, J. Hohlfield, Y. Kubota, L. Li, B. Lu, C. Mihalcea, K. Mountfield, K. Pelhos, C. Peng, T. Rausch, M. A. Seigler, D. Weller, and X. Yang, “Heat-assisted magnetic recording,” *Magnetics, IEEE Transactions on*, vol. 42, no. 10, pp. 2417–2421, 2006.
  - [9] B. D. Terris and T. Thomson, “Nanofabricated and self-assembled magnetic structures as data storage media,” *Journal of Physics D: Applied Physics*, vol. 38, no. 12, p. R199, 2005.
-

- 
- [10] J.P. Liu, *et al.*, *Bit Patterned Magnetic Recording: Nanoscale Magnetic Islands for Data Storage, Nanoscale Magnetic Materials and Applications*. US: New York; Springer, Chapter 9, 2009.
- [11] Y. Sonobe, D. Weller, Y. Ikeda, M. Schabes, K. Takano, G. Zeltzer, B. Yen, M. E. Best, S. Greaves, H. Muraoka, and Y. Nakamura, "Thermal stability and snr of coupled granular/continuous media," *Magnetics, IEEE Transactions on*, vol. 37, no. 4, pp. 1667–1670, 2001.
- [12] R. Victora and X. Shen, "Composite media for perpendicular magnetic recording," *Magnetics, IEEE Transactions on*, vol. 41, no. 2, pp. 537–542, 2005.
- [13] D. Suess, T. Schrefl, S. Fahler, M. Kirschner, G. Hrkac, F. Dorfbauer, and J. Fidler, "Exchange spring media for perpendicular recording," *Applied Physics Letters*, vol. 87, no. 1, p. 012504, 2005.
- [14] T. Nolan, B. Valcu, and H. J. Richter, "Effect of composite designs on writability and thermal stability of perpendicular recording media," *Magnetics, IEEE Transactions on*, vol. 47, no. 1, pp. 63–68, 2011.
- [15] E. C. Stoner and E. P. Wohlfarth, "A mechanism of magnetic hysteresis in heterogeneous alloys," *Phil. Trans. R. Soc. Lond.*, vol. 240, no. 826, pp. 599–642, May 1948.
- [16] S. N. Piramanayagam, "Perpendicular recording media for hard disk drives," *Journal of Applied Physics*, vol. 102, no. 1, p. 011301, 2007.
- [17] Y. Hirayama, M. Futamoto, K. Kimoto, and K. Usami, "Compositional microstructures of CoCr-alloy perpendicular magnetic recording media," *Magnetics, IEEE Transactions on*, vol. 32, no. 5, pp. 3807–3809, 1996.
- [18] Y. Hirayama, Y. Honda, T. Takeuchi, and M. Futamoto, "Recording characteristics of single-layer perpendicular media using ring-shaped heads," *Magnetics, IEEE Transactions on*, vol. 35, no. 5, pp. 2766–2768, 1999.
- [19] H. Uwazumi, T. Shimatsu, Y. Sakai, A. Otsuki, I. Watanabe, H. Muraoka, and Y. Nakamura, "Recording performance of CoCrPt-(Ta, B)/TiCr perpendicular recording media," *Magnetics, IEEE Transactions on*, vol. 37, no. 4, pp. 1595–1598, 2001.
-

- 
- [20] T. Shimatsu, H. Sato, T. Oikawa, Y. Inaba, O. Kitakami, S. Okamoto, H. Aoi, H. Muraoka, and Y. Nakamura, "High-potential magnetic anisotropy of CoPtCr-SiO<sub>2</sub> perpendicular recording media," *Magnetics, IEEE Transactions on*, vol. 41, no. 2, pp. 566–571, 2005.
- [21] T. Oikawa, Y. Ajishi, and H. Uwazumi, "Perpendicular magnetic recording media with glass substrate," *Fuji Electric Review*, vol. 55, no. 1, pp. 11–16, Nov 2009.
- [22] R. C. O'Handley, *Modern magnetic materials principles and applications*. John Wiley and Sons Ltd., Inc., Hoboken, New Jersey., 2000.
- [23] M. T. Johnson, P. J. H. Bloemen, F. J. A. den Broeder, and J. J. de Vries, "Magnetic anisotropy in metallic multilayers," *Reports on Progress in Physics*, vol. 59, no. 11, p. 1409, 1996.
- [24] C. A. Ross, M. E. Schabes, R. Ranjan, G. Bertero, and T. Chen, "The role of stress-induced anisotropy in longitudinal thin film magnetic recording media," *Journal of Applied Physics*, vol. 79, no. 8, pp. 5342–5344, 1996.
- [25] J. Bain, B. Clemens, S. Brennan, and H. Kataoka, "X-ray diffraction characterization of stress and crystallographic texture in thin film media," *Magnetics, IEEE Transactions on*, vol. 29, no. 1, pp. 300–306, 1993.
- [26] A. Kawamoto and F. Hikami, "Magnetic anisotropy of sputtered media induced by textured substrate," *Journal of Applied Physics*, vol. 69, no. 8, pp. 5151–5153, 1991.
- [27] E. O. Samwel, P. R. Bissell, and J. C. Lodder, "Remanent magnetic measurements on perpendicular recording materials with compensation for demagnetizing fields," *Journal of Applied Physics*, vol. 73, no. 3, pp. 1353–1359, feb 1993.
- [28] J. Wu, L. Holloway, H. Laidler, K. O'Grady, S. Khizroev, J. Howard, R. Gustafson, and D. Litvinov, "Magnetic characterization of perpendicular recording media," *Magnetics, IEEE Transactions on*, vol. 38, no. 4, pp. 1682–1686, jul 2002.
- [29] T. Deakin, C. Bunce, S. Wu, and K. O'Grady, "Remanence and Coercivity Measurements of Perpendicular ECC Media," *Magnetics, IEEE Transactions on*, vol. 44, no. 11, pp. 3515–3518, nov. 2008.
-

- 
- [30] T. Deakin, F. Garcia-Sanchez, S. Wu, O. Chubykalo-Fesenko, and K. O'Grady, "Magnetization reversal in exchange-coupled composite media-experiment and modeling," *IEEE Transaction on*, vol. 45, no. 2, pp. 856–861, 2009.
- [31] R. van de Veerdonk, X. Wu, and D. Weller, "Switching field distributions and  $\Delta M$  measurements for perpendicular media," *Magnetics, IEEE Transactions on*, vol. 38, no. 5, pp. 2450 – 2452, sep 2002.
- [32] R. J. M. Van de Veerdonk, X. Wu, and D. Weller, "Determination of switching field distributions for perpendicular recording media," *Magnetics, IEEE Transactions on*, vol. 39, no. 1, pp. 590–593, 2003.
- [33] K. Le Phan and C. Lodder, "Iterative method for intrinsic viscosity measurements on perpendicular recording media," *Magnetics, IEEE Transactions on*, vol. 38, no. 5, pp. 2003–2005, 2002.
- [34] H. J. Richter, "Recent advances in the recording physics of thin-film media," *Journal of Physics D: Applied Physics*, vol. 32, no. 21, p. R147, 1999.
- [35] M. L. Williams and R. L. Comstock, "An analytic model of the write process in digital magnetic recording," *AIP Conf. Proc.*, vol. 5, pp. 738–742, 1971.
- [36] R. W. Chantrell and K. O'Grady, "Magnetic characterization of recording media," *Journal of Physics D: Applied Physics*, vol. 25, no. 1, p. 1, 1992.
- [37] D. Weller and A. Moser, "Thermal effect limits in ultrahigh-density magnetic recording," *Magnetics, IEEE Transactions on*, vol. 35, no. 6, pp. 4423–4439, 1999.
- [38] B. A. E., E. Kneller, P.-L. Lu, and Y. He, "Magnetism and metallurgy," *Academic press, New York*, no. 2, p. 523.
- [39] A. de Witte, M. El-Hilo, K. O'Grady, and R. Chantrell, "Sweep rate measurements of coercivity in particulate recording media," *Journal of Magnetism and Magnetic Materials*, vol. 120, no. 13, pp. 184 – 186, 1993.
- [40] H. J. Richter, "The transition from longitudinal to perpendicular recording," *Journal of Physics D: Applied Physics*, vol. 40, no. 9, p. R149, 2007.
- [41] T. W. McDaniel, "Ultimate limits to thermally assisted magnetic recording," *Journal of Physics: Condensed Matter*, vol. 17, no. 7, p. R315, 2005.
-

- 
- [42] R. F. L. Evans, R. W. Chantrell, U. Nowak, A. Lyberatos, and H. J. Richter, “Thermally induced error: Density limit for magnetic data storage,” *Applied Physics Letters*, vol. 100, no. 10, p. 102402, 2012.
- [43] F. E. Luborsky, “Development of elongated particle magnets,” *Journal of Applied Physics*, vol. 32, no. 3, pp. S171–S183, 1961.
- [44] C. Tannous and J. Gieraltowski, “The Stoner-Wohlfarth model of ferromagnetism,” *European Journal of Physics*, vol. 29, no. 3, p. 475, 2008.
- [45] G. F. Hughes, “Magnetization reversal in cobalt–phosphorus films,” *Journal of Applied Physics*, vol. 54, no. 9, pp. 5306–5313, 1983.
- [46] J. G. Zhu and H. N. Bertram, “Micromagnetic studies of thin metallic films (invited),” *Journal of Applied Physics*, vol. 63, no. 8, pp. 3248–3253, 1988.
- [47] J. G. Zhu and H. N. Bertram, “Recording and transition noise simulation in thin film media,” *Magnetics, IEEE Transactions on*, vol. 24, no. 6, pp. 2706–2708, 1988.
- [48] R. H. Victora and X. Shen, “Exchange coupled composite media for perpendicular magnetic recording,” *Magnetics, IEEE Transactions on*, vol. 41, no. 10, pp. 2828–2833, 2005.
- [49] N. Ashcroft and N. Mermin, *Solid State Physics*. Philadelphia: Saunders College, 1976.
- [50] P. I. Mayo, K. O’Grady, P. E. Kelly, J. Cambridge, I. L. Sanders, T. Yogi, and R. W. Chantrell, “A magnetic evaluation of interaction and noise characteristics of CoNiCr thin films,” *Journal of Applied Physics*, vol. 69, no. 8, pp. 4733–4735, 1991.
- [51] P. E. Kelly, K. O’Grady, P. I. Mayo, and R. Chantrell, “Switching mechanisms in cobalt-phosphorus thin films,” *Magnetics, IEEE Transactions on*, vol. 25, no. 5, pp. 3881–3883, 1989.
- [52] R. W. Chantrell, N. Walmsley, J. Gore, and M. Maylin, “Calculations of the susceptibility of interacting superparamagnetic particles,” *Phys. Rev. B*, vol. 63, p. 024410, Dec 2000.
-

- [53] H. Kronmuller and S. Parkin, *Handbook of Magnetism and Advanced Magnetic Materials*, 2nd ed. John Wiley and Sons Ltd., 2007.
- [54] S. Iwasaki and Y. Nakamura, "The magnetic field distribution of a perpendicular recording head," *Magnetics, IEEE Transactions on*, vol. 14, no. 5, pp. 436–438, 1978.
- [55] T. Shimatsu, H. Sato, T. Oikawa, K. Mitsuzuka, Y. Inaba, O. Kitakami, S. Okamoto, H. Aoi, H. Muraoka, and Y. Nakamura, "CoPtCr-SiO<sub>2</sub> perpendicular media for high density recording with a high order magnetic anisotropy energy term," *Magnetics, IEEE Transactions on*, vol. 41, no. 10, pp. 3175–3177, 2005.
- [56] S. J. Greaves, H. Muraoka, Y. Sonobe, M. Schabes, and Y. Nakamura, "Pinning of written bits in perpendicular recording media," *Journal of Magnetism and Magnetic Materials*, vol. 235, pp. 418–423, Oct. 2001.
- [57] Y. Sonobe, H. Muraoka, K. Miura, Y. Nakamura, K. Takano, A. Moser, H. Do, B. Yen, Y. Ikeda, N. Supper, and W. Weresin, "Thermally stable CGC perpendicular recording media with Pt-rich CoPtCr and thin Pt layers," *Magnetics, IEEE Transactions on*, vol. 38, no. 5, pp. 2006–2011, 2002.
- [58] Y. Sonobe, H. Muraoka, K. Miura, Y. Nakamura, K. Takano, H. Do, A. Moser, B. K. Yen, Y. Ikeda, and N. Supper, "Coupled granular/continuous perpendicular recording media with soft magnetic underlayer," *Journal of Applied Physics*, vol. 91, no. 10, pp. 8055–8057, 2002.
- [59] H. Laidler, K. O'Grady, T. M. Coughlin, and J. H. Judy, "Demagnetising field reduction in keepered media," *Journal of Magnetism and Magnetic Materials*, vol. 193, pp. 262–264, Mar. 1999.
- [60] Y. Sonobe, K. Tham, L. Wu, T. Umezawa, C. Takasu, J. A. H. Dumaya, T. Onoue, P. Leo, and M. Liao, "CGC Perpendicular Recording Media With CoCrPt-SiO Alloy as Granular Layer," *Magnetics, IEEE Transactions on*, vol. 42, no. 10, pp. 2351–2353, 2006.
- [61] E. P. Wohlfarth, "The coefficient of magnetic viscosity," *J. Phys. F: Met. Phys.*, vol. 14, pp. L155–159, 1984.
-

- [62] M. L. Plumer, E. K. Van, and D. Weller, *The physics of Ultra-High-Density magnetic recording*. Springer Publishers, 2001, vol. 41.
- [63] L. Neel, “Thorie du trainage magnétique des ferromagnétiques en grains fines avec applications aux terres cuites,” *Ann. Geophys.*, vol. 5, pp. 99–136, 1949.
- [64] R. Street and J. C. Woolley, “A study of magnetic viscosity,” *Proc. Phys. Soc.*, pp. 562–572, 1949.
- [65] K. O’Grady, R. Chantrell, J. Popplewell, and S. Charles, “Time dependent magnetization of a system of fine cobalt particles,” *Magnetics, IEEE Transactions on*, vol. 17, no. 6, pp. 2943–2945, 1981.
- [66] S. Uren, K. Walker, K. O’Grady, and R. W. Chantrell, “Magnetic viscosity and switching field distribution,” *Magnetics, IEEE Transactions on*, vol. 24, pp. 1808–1810, 1988.
- [67] P. Gaunt, “Magnetic viscosity and thermal activation energy,” *Journal of Applied Physics*, vol. 59, pp. 4129–4132, 1986.
- [68] A. Aharoni, “Time dependence of magnetization decay in spin glasses,” *Journal of Applied Physics*, vol. 57, no. 10, pp. 4702–4705, 1985.
- [69] R. V. Chamberlin, G. Mozurkewich, and R. Orbach, “Time decay of the remanent magnetization in spin-glasses,” *Phys. Rev. Lett.*, vol. 52, pp. 867–870, Mar 1984.
- [70] I. Yeung, W. Ruan, and R. Roshko, “Magnetization measurements on very dilute spin glasses,” *Journal of Magnetism and Magnetic Materials*, vol. 74, no. 1, pp. 59 – 66, 1988.
- [71] M. El-Hilo, K. O’Grady, and R. W. Chantrell, “The origin of non-linear  $\ln(t)$  behaviour in the time dependence of magnetisation,” *Journal of Magnetism and Magnetic Materials*, vol. 109, pp. L164–L168, Mar. 1992.
- [72] M. El-Hilo, K. O’Grady, and R. W. Chantrell, “Demagnetised states and activation volumes in thin-film media,” *Journal of Magnetism and Magnetic Materials*, vol. 120, pp. 244–246, 1993.
- [73] L. Neel, “Thorie du trainage magnétique des substances massives dans le domaine de Rayleigh,” *J. Phys. Radium*, vol. 11, pp. 49–61, 1950.
-

- [74] A. M. de Witte and K. O'Grady, "Oxygen effect on the microstructure and magnetic properties of binary CoPt thin films for perpendicular recording," *IEEE Trans. Magn.*, vol. 26, pp. 1810–1812, 1990.
- [75] I. S. Jacobs and C. P. Bean, "An approach to elongated fine-particle magnets," *Phys. Rev.*, vol. 100, pp. 1060–1067, Nov 1955.
- [76] M. P. Sharrock, "Time dependence of switching fields in magnetic recording media (invited)," *Journal of Applied Physics*, vol. 76, no. 10, pp. 6413–6418, 1994.
- [77] M. El-Hilo, K. O'Grady, and R. W. Chantrell, "Fluctuation fields and reversal mechanisms in granular magnetic systems," *Journal of Magnetism and Magnetic Materials*, vol. 248, pp. 360–373, Aug. 2002.
- [78] Y. Estrin, P. G. McCormick, and R. Street, "A phenomenological model of magnetisation kinetics," *Journal of Physics: Condensed Matter*, vol. 1, no. 29, p. 4845, 1989.
- [79] K. O'Grady, P. Dova, and H. Laidler, "Determination of critical volumes in recording media," *Mater. Res. Soc. Symp. Proc.*, vol. 517, pp. 231–242, 1998.
- [80] A. Lyberatos and R. W. Chantrell, "The fluctuation field of ferromagnetic materials," *Journal of Physics: Condensed Matter*, vol. 9, no. 12, p. 2623, 1997.
- [81] Wikipedia. IBM 305 RAMAC, <http://en.wikipedia.org/wiki/IBMRAMAC>.
- [82] B. Dieny, V. S. Speriosu, S. S. P. Parkin, B. A. Gurney, D. R. Wilhoit, and D. Mauri, "Giant magnetoresistive in soft ferromagnetic multilayers," *Phys. Rev. B*, vol. 43, pp. 1297–1300, Jan 1991.
- [83] Seagate Reaches 1 Terabit per square inch milestone in hard drive storage with new technology demonstration, <http://www.seagate.com/about/newsroom/press-releases/terabit-milestone-storage-seagate-master-pr/>, 19/03/2012.
- [84] Hitachi GST Storage Technologies, <http://www.hgst.com/hdd/research/images/pmimages/conventionalpatternmedia>, 12/06/2013.
- [85] Seagate hits 1 terabit per square inch, <http://www.xbitlabs.com/articles/storage/display/seagatemomentus>.
- [86] R. Wood, "Future hard disk drive systems," *Journal of Magnetism and Magnetic Materials*, vol. 321, pp. 555–561, Mar. 2009.
-

- [87] B. Marchon, T. Pitchford, Y. T. Hsia, and S. Gangopadhyay, "The head-disk interface roadmap to an areal density of 4 Tbits/in<sup>2</sup>," *Advances in Tribology*, pp. 1–8, 2013.
- [88] D. E. Laughlin, Y. Feng, D. N. Lambeth, L.-L. Lee, and L. Tang, "Design and crystallography of multilayered media," *Journal of Magnetism and Magnetic Materials*, vol. 155, no. 13, pp. 146 – 150, 1996.
- [89] L. L. Lee, D. E. Laughlin, L. Fang, and D. N. Lambeth, "Effects of Cr intermediate layers on CoCrPt thin film media on NiAl underlayers," *Magnetics, IEEE Transactions on*, vol. 31, no. 6, pp. 2728–2730, 1995.
- [90] R. Schaller, "Moore's law: past, present and future," *Spectrum, IEEE*, vol. 34, no. 6, pp. 52–59, 1997.
- [91] E. Abarra, B. R. Acharya, A. Inomata, and I. Okamoto, "Synthetic ferrimagnetic media," *Magnetics, IEEE Transactions on*, vol. 37, no. 4, pp. 1426–1431, 2001.
- [92] S. N. Piramanayagam, J. Wang, X. Shi, S. Pang, C. K. Pock, Z. Shan, and T. Chong, "Magnetic properties and switching field control of antiferromagnetically coupled recording media," *Magnetics, IEEE Transactions on*, vol. 37, no. 4, pp. 1438–1440, 2001.
- [93] S. S. P. Parkin, N. More, and K. P. Roche, "Oscillations in exchange coupling and magnetoresistance in metallic superlattice structures: Co/Ru, Co/Cr, and Fe/Cr," *Phys. Rev. Lett.*, vol. 64, pp. 2304–2307, May 1990.
- [94] J. P. Wang, Z. Shan, S. N. Piramanayagam, and T. Chong, "Anti-ferromagnetic coupling effects on energy barrier and reversal properties of recording media," *Magnetics, IEEE Transactions on*, vol. 37, no. 4, pp. 1445–1448, 2001.
- [95] S. Iwasaki and K. Takemura, "An analysis for the circular mode of magnetization in short wavelength recording," *IEEE Trans. Magn.*, vol. 11, pp. 1173–1175, 1975.
- [96] S. N. Piramanayagam and K. Srinivasan, "Recording media research for future hard disk drives," *Journal of Magnetism and Magnetic Materials*, vol. 321, pp. 485–494, Mar. 2009.
-

- 
- [97] J. Desserre, "Crucial points in perpendicular recording," *Magnetics, IEEE Transactions on*, vol. 20, no. 5, pp. 663–668, 1984.
- [98] K. Tanahashi, R. Arai, and Y. Hosoe, "Exchange-biased soft underlayers for perpendicular recording," *Magnetics, IEEE Transactions on*, vol. 41, no. 2, pp. 577–580, 2005.
- [99] G. Choe, M. Zheng, E. Abarra, B. Demczyk, J. Zhou, B. Acharya, and K. Johnson, "High-performance CoPtCrO perpendicular media: optimizing exchange coupling and anisotropy orientation dispersion," *Journal of Magnetism and Magnetic Materials*, vol. 287, no. 0, pp. 159 – 166, 2005.
- [100] J. W. Park, Y. K. Kim, T. H. Lee, H. S. Oh, and B. K. Lee, "Optimization of Ru intermediate layer in CoCr-based perpendicular magnetic recording media," *physica status solidi (a)*, vol. 201, no. 8, pp. 1763–1766, 2004.
- [101] N. Honda, J. Ariake, K. Ouchi, and S. Iwasaki, "Low noise Co-Cr-Nb perpendicular recording media with high squareness," *Magnetics, IEEE Transactions on*, vol. 34, no. 4, pp. 1651–1653, 1998.
- [102] J. Yasumori, Y. Sonobe, S. J. Greaves, and K. K. Tham, "Approach to High-Density Recording Using CGC Structure," *IEEE Transactions on Magnetics*, vol. 45, pp. 850–855, Feb. 2009.
- [103] Y. Sonobe, D. Weller, Y. Ikeda, K. Takano, M. Schabes, G. Zeltzer, H. Do, B. Yen, and M. Best, "Coupled granular/continuous medium for thermally stable perpendicular magnetic recording," *Journal of Magnetism and Magnetic Materials*, vol. 235, no. 13, pp. 424 – 428, 2001.
- [104] T. Shimatsu, H. Muraoka, Y. Nakamura, Y. Sonobe, Y. Satodate, K. Muramatsu, and I. Watanabe, "High thermal stability in CoPrTb/CoCrTa composite perpendicular media," *Journal of Applied Physics*, vol. 91, no. 10, pp. 8061–8063, 2002.
- [105] K. Tham, Y. Sonobe, and K. Wago, "Magnetic and Read/Write Properties of Coupled Granular/Continuous Perpendicular Recording Media and Magnetization Reversal Process," *Magnetics, IEEE Transactions on*, vol. 43, no. 2, pp. 671–675, 2007.
-

- [106] H. Muraoka, Y. Sonobe, K. Miura, A. M. Goodman, and Y. Nakamura, "Analysis on magnetization transition of CGC perpendicular media," *Magnetics, IEEE Transactions on*, vol. 38, no. 4, pp. 1632–1636, 2002.
- [107] Y. Y. Zou, J. P. Wang, C. H. Hee, and T. C. Chong, "Tilted media in a perpendicular recording system for high areal density recording," *Applied Physics Letters*, vol. 82, no. 15, pp. 2473–2475, 2003.
- [108] K. Z. Gao and H. Bertram, "Transition jitter estimates in tilted and conventional perpendicular recording media at 1 Tbit/in<sup>2</sup>," *Magnetics, IEEE Transactions on*, vol. 39, no. 2, pp. 704–709, 2003.
- [109] J. P. Wang, Y. Y. Zou, C. Hee, T. Chong, and Y. F. Zheng, "Approaches to tilted magnetic recording for extremely high areal density," *Magnetics, IEEE Transactions on*, vol. 39, no. 4, pp. 1930–1935, 2003.
- [110] J. P. Wang, W. Shen, and J. Bai, "Exchange coupled composite media for perpendicular magnetic recording," *Magnetics, IEEE Transactions on*, vol. 41, no. 10, pp. 3181–3186, 2005.
- [111] A. Kikitsu, "Prospects for bit patterned media for high-density magnetic recording," *Journal of Magnetism and Magnetic Materials*, vol. 321, pp. 526–530, Mar. 2009.
- [112] H. J. Richter, A. Dobin, O. Heinonen, K. Gao, R. J. M. Van de Veerdonk, R. Lynch, J. Xue, D. Weller, P. Asselin, M. Erden, and R. Brockie, "Recording on Bit-Patterned Media at Densities of 1 Tbit/in<sup>2</sup> and Beyond," *Magnetics, IEEE Transactions on*, vol. 42, no. 10, pp. 2255–2260, 2006.
- [113] O. Hellwig, A. Berger, T. Thomson, E. Dobisz, Z. Z. Bandic, H. Yang, D. S. Kercher, and E. E. Fullerton, "Separating dipolar broadening from the intrinsic switching field distribution in perpendicular patterned media," *Applied Physics Letters*, vol. 90, no. 16, p. 162516, 2007.
- [114] D. Weller, O. Mosendz, G. Parker, S. Pisana, and T. S. Santos, "L10 FePtXY media for heat-assisted magnetic recording," *physica status solidi (a)*, 2013.
- [115] S. Granz, K. Barmak, and M. Kryder, "Granular L10 FePt:X (X = Ag, B, C, SiO<sub>x</sub>, TaO<sub>x</sub>) thin films for heat assisted magnetic recording," *The European Physical Journal B*, vol. 86, no. 3, pp. 1–7, 2013.
-

- [116] B. X. Xu, Z. J. Liu, R. Ji, Y. T. Toh, J. F. Hu, J. M. Li, J. Zhang, K. D. Ye, and C. W. Chia, "Thermal issues and their effects on heat-assisted magnetic recording system (invited)," *Journal of Applied Physics*, vol. 111, no. 7, p. 07B701, 2012.
- [117] A. Lyberatos and J. Hohlfeld, "Model of thermal erasure in neighboring tracks during thermomagnetic writing," *Journal of Applied Physics*, vol. 95, no. 4, pp. 1949–1957, 2004.
- [118] J. Sayama, T. Shimatsu, H. Nemoto, S. Okamoto, O. Kitakami, and H. Aoi, "Temperature dependence of the magnetic properties of L11-type Co–Ni–Pt ordered alloy films for thermally assisted recording media," *Journal of Applied Physics*, vol. 110, no. 1, p. 013918, 2011.
- [119] R. F. L. Evans. Heat Assisted Magnetic Recording (HAMR) media, <http://www-users.york.ac.uk/~rfl500/research/heat-assisted-magnetic-recording/>.
- [120] X. Wang, K. Gao, H. Zhou, A. Itagi, M. Seigler, and E. Gage, "HAMR Recording Limitations and Extendibility," *Magnetics, IEEE Transactions on*, vol. 49, no. 2, pp. 686–692, 2013.
- [121] A. Wu, Y. Kubota, T. Klemmer, T. Rausch, C. Peng, Y. Peng, D. Karns, X. Zhu, Y. Ding, E. Chang, Y. Zhao, H. Zhou, K. Gao, J. U. Thiele, M. Seigler, G. Ju, and E. Gage, "HAMR Areal Density Demonstration of 1+ Tbps on Spinstand," *Magnetics, IEEE Transactions on*, vol. 49, no. 2, pp. 779–782, 2013.
- [122] J. G. Zhu, X. Zhu, and Y. Tang, "Microwave assisted magnetic recording," *Magnetics, IEEE Transactions on*, vol. 44, no. 1, pp. 125–131, 2008.
- [123] Y. Shiroishi, K. Fukuda, I. Tagawa, H. Iwasaki, S. Takenoiri, H. Tanaka, H. Mutoh, and N. Yoshikawa, "Future Options for HDD Storage," *Magnetics, IEEE Transactions on*, vol. 45, no. 10, pp. 3816–3822, 2009.
- [124] S. Okamoto, M. Igarashi, N. Kikuchi, and O. Kitakami, "Microwave assisted switching mechanism and its stable switching limit," *Journal of Applied Physics*, vol. 107, no. 12, p. 123914, 2010.
- [125] S. Foner, "Versatile and sensitive vibrating-sample magnetometer," *Review of Scientific Instruments*, vol. 30, no. 7, pp. 548–557, 1959.
-

- [126] K. O'Grady, R. Chantrell, and I. Sanders, "Magnetic characterisation of thin film recording media," *IEEE Trans. Magn.*, vol. 29, no. 1, pp. 286–291, Jan 1993.
- [127] Y. Inaba, T. Shimatsu, H. Muraoka, J. Dutson, and K. O'Grady, "Activation volumes in CoPtCr-SiO<sub>2</sub> perpendicular recording media," *Magnetics, IEEE Transactions on*, vol. 41, no. 10, pp. 3130 – 3132, October 2005.
- [128] J. Dutson, J. Wu, K. O'Grady, N. Woolsey, Y. Kubota, and C. Platt, "Time dependence in perpendicular media with a soft underlayer," *Magnetics, IEEE Transactions on*, vol. 40, no. 4, pp. 2504 – 2506, July 2004.
- [129] J. Dutson, D. Litvinov, M. Gibbs, Y. Inaba, K. Muraoka, and K. O'Grady, "Magnetisation reversal in media with perpendicular anisotropy," *J. Magn. Magn. Matter*, vol. 304, p. 51, 2006.
- [130] T. Thomson, G. Hu, and B. Terris, "Intrinsic distribution of magnetic anisotropy in thin films probed by patterned nanostructures," *Phys. Rev. Lett.*, vol. 96, p. 257204, Jun 2006.
- [131] J. Kerr, "On rotation of the plane of polarisation by reflection from the pole of a magnet," *Philos. Mag.*, vol. 3, no. 19, p. 321, 1877.
- [132] J. Kerr, "On reflection of polarised light from the equatorial surface of a magnet," *Philos. Mag.*, vol. 5, no. 30, p. 161, 1878.
- [133] M. Faraday, *Diary*, vol. 4, p. 7434, August 1845.
- [134] M. Faraday, *Diary*, vol. 4, p. 7504, September 1845.
- [135] Z. Q. Qiu and S. D. Bader, "Surface magneto-optic Kerr effect," *Review of Scientific Instruments*, vol. 71, no. 3, pp. 1243–1255, 2000.
- [136] P. Weinberger, "John Kerr and his effects found in 1877 and 1878," *Phil. Mag. Lett.*, vol. 88, p. 897, 2008.
- [137] P. N. Argyres, "Theory of the Faraday and Kerr Effects in Ferromagnetics," *Phys. Rev.*, vol. 97, pp. 334–345, Jan 1955.
- [138] R. Atkinson, "Single layer equivalence of magneto-optic multilayers for normal incidence (i)," *Journal of Magnetism and Magnetic Materials*, vol. 95, no. 1, pp. 61 – 68, 1991.
-

- [139] J. Dutson, "Characterisation of media with perpendicular magnetic anisotropy for thin film recording," Ph.D. dissertation, Department of Physics, University of York, 2005.
- [140] L. Saharan, C. Morrison, J. J. Miles, T. Thomson, T. Schrefl, and G. Hrkac, "Angle dependence of the switching field of recording media at finite temperatures," *Journal of Applied Physics*, vol. 110, no. 10, p. 103906, 2011.
- [141] C. Morrison, L. Saharan, G. Hrkac, T. Schrefl, Y. Ikeda, K. Takano, J. J. Miles, and T. Thomson, "Inter/intra granular exchange and thermal activation in nanoscale granular magnetic materials," *Applied Physics Letters*, vol. 99, no. 13, p. 132507, 2011.
- [142] W. M. Li, X. L. Huang, J. Z. Shi, Y. J. Chen, T. L. Huang, and J. Ding, "Angular dependence and temperature effect on switching field distribution of Co/Pd based bit patterned media," *Journal of Applied Physics*, vol. 111, no. 7, p. 07B917, 2012.
- [143] J. Chureemart, P. Chureemart, R. Evans, R. W. Chantrell, and K. O'Grady, "Magnetic orientation in advanced recording media," *Journal of Physics D: Applied Physics*, vol. 44, no. 45, p. 455002, 2011.
- [144] A. Carter, L. Fernandez-Outon, Y. Inaba, S. Greaves, H. Muraoka, and K. O'Grady, "Anisotropy dispersion in  $(\text{CoCrPt-SiO}_2)_x$  perpendicular recording media," *Journal of Magnetism and Magnetic Materials*, vol. 320, no. 18, pp. 2269 – 2272, 2008.
- [145] X. Wu, H. Zhou, R. van de Veerdonk, T. Klemmer, and D. Weller, "Measurement of the magnetic easy axis dispersion in perpendicular media," *Journal of Magnetism and Magnetic Materials*, vol. 278, pp. 285 – 288, 2004.
- [146] X. Wu, H. Zhou, D. Weller, and H. Richter, "Measurement of angular-dependent hysteresis loops in perpendicular magnetic recording media," *Journal of Magnetism and Magnetic Materials*, vol. 303, no. 1, pp. 5 – 8, 2006.
- [147] V. G. Voznyuk, A. Misra, W. D. Doyle, P. B. Visscher, and R. W. Chantrell, "Angular dispersion of the anisotropy in perpendicular media," *Journal of Applied Physics*, vol. 97, no. 10, p. 10N508, 2005.
-

- [148] D. Hasegawa, S. Saito, N. Itagaki, S. Meguro, Y. Konishi, E. Yanagisawa, K. Akahane, and M. Takahashi, "Angular-dependent remanent magnetization curve for perpendicular magnetic recording media determined by precise polar-Kerr detection system," *Journal of Magnetism and Magnetic Materials*, vol. 320, no. 22, pp. 3027 – 3031, 2008.
- [149] C. L. Platt, J. K. Howard, A. G. Roy, and D. E. Laughlin, "Influence of stress on nucleation field of CoCrPt perpendicular media," *Journal of Applied Physics*, vol. 91, no. 2, pp. 772 –774, jan 2002.
- [150] T. Keitoku, A. J., N. Honda, and K. Ouchi, "Preparation of Co-Cr-Pt alloy film with high perpendicular coercivity and large negative nucleation field," *Journal of Magnetism and Magnetic Materials*, vol. 235, pp. 34 – 39, 2001.
- [151] K. O'Grady, R. Chantrell, and I. Sanders, "Magnetic characterisation of thin film recording media," *Magnetics, IEEE Transactions on*, vol. 29, no. 1, pp. 286 –291, jan 1993.
- [152] K. O'Grady and H. Laidler, "The limits to magnetic recording - media considerations (invited)," *Journal of Magnetism and Magnetic Materials*, vol. 200, pp. 616–633, Oct. 1999.
- [153] B. D. Cullity and S. R. Stock, *Elements of X-ray diffraction*, 3rd ed. Rrentice Hall, 2001.
- [154] K. Inaba, "X-ray thin-film measurement techniques," *The Rigaku Journal*, vol. 24, no. 1, pp. 10–15, 2008.
- [155] D. B. Williams and C. B. Carter, *Transmission electron microscopy*, 2nd ed. Springer Publishers, Aug 2009, vol. 1-4.
- [156] Electron microscope (EM) <http://www.vcbio.science.ru.nl/en/fesem/info/principe>, 15/03/2013.
- [157] P. J. Goodhew, F. J. Humphreys, and R. Beanland, *Electron microscopy and analysis*, 2nd ed. London Taylor, Francis, Aug 2001.
- [158] E. Muller and A. R. D., "Preparation of cross-section samples for transmission electron microscopy," *Swiss Federal Institute of technology Zurich*, vol. 37, no. 4, pp. 1426–1431, 2001.
-

- [159] S. N. Piramanayagam, H. K. Tan, M. Ranjbar, S. K. Wong, R. Sbiaa, and T. C. Chong, "Magnetic interaction in perpendicular recording media with synthetic nucleation layers," *Applied Physics Letters*, vol. 98, no. 15, p. 152504, 2011.
- [160] C. G. Granqvist and R. A. Buhrman, "Ultrafine metal particles," *Journal of Applied Physics*, vol. 47, no. 5, pp. 2200–2219, 1976.
- [161] C. V. Thompson, "Grain growth in polycrystalline thin films," *Mat. Res. Soc. Symp. Proc.*, vol. 343, pp. 3–12, 1994.
- [162] K. O'Grady and A. Bradbury, "Particle size analysis in ferrofluids," *Journal of Magnetism and Magnetic Materials*, vol. 39, pp. 91 – 94, 1983.
- [163] D. Carpenter, J. Codner, K. Barmak, and J. Rickman, "Issues associated with the analysis and acquisition of thin-film grain size data," *Materials Letters*, vol. 41, no. 6, pp. 296 – 302, 1999.
- [164] C. Mee and E. D. Daniel, *Magnetic Recording Technology*, 2nd ed. New York: McGraw-Hill, Aug 1996.
- [165] J. Churemart, P. Churemart, J. Pressesky, T. Nolan, and K. O'Grady, "Media design and orientation in perpendicular media," *Magnetics, IEEE Transactions on*, vol. 49, no. 7, pp. 3592–3595, 2013.
- [166] J. Dutson, M. Hashimoto, Y. Inaba, S. Greaves, H. Muraoka, and K. O'Grady, "Magnetic and Recording Properties of  $(\text{CoCrPt})_{1-x}(\text{SiO}_2)_x$  Media," *Magnetics, IEEE Transactions on*, vol. 43, no. 2, pp. 814–818, 2007.
-